

Automated Speckle Tracking in Ultrasound Images of Tendon Movements

Ahmad Sufri Azlan Mohamed

Ph.D. Thesis

2015

Automated Speckle Tracking in Ultrasound Images of Tendon Movements

Ahmad Sufri Azlan Mohamed

School of Computing, Science and Engineering
University of Salford, Salford, UK

Submitted in Partial Fulfilment of the Requirements of the
Degree of Doctor of Philosophy, July 2015

Table of Contents

Title Page	
Table of Contents	i
List of Tables	v
List of Figures	vi
List of Equations	xiv
List of Publications	xvi
Acknowledgments	xvii
Abbreviations	xviii
Abstract	xix
Chapter 1 - Introduction	1
1.1 Fundamental Steps in Image Processing	1
1.2 Image Acquisition	2
1.2.1 Light Radiation Based Imaging	3
1.2.2 Acoustic Based Imaging	4
1.3 Pre-processing	4
1.4 Segmentation	5
1.5 Feature Selection	5
1.6 Recognition	5
1.7 Interpretation	6
1.8 Knowledge Base	6
1.9 Image Tracking in Digital Video	7
1.10 General Applications of Object Tracking	8
1.11 Motivation of This Work	10
1.12 Aims and Objectives	11
1.13 Outline of The Thesis	12
Chapter 2 - Literature Review	15
2.1 Biomedical background: Tendon Structure and Function	15
2.1.1 Tendon Structure	16

2.1.2	Tendon Function	17
2.1.3	Tendon Injury and Risk	20
2.1.3.1	Acute Tendon Injury	21
2.1.3.2	Chronic Tendon Injury	23
2.2	Medical Imaging in Biomechanical Applications	24
2.2.1	X-ray Imaging	25
2.2.2	Bone Scintigraphy Imaging	26
2.2.3	Computed Tomography (CT) Scan	26
2.2.4	Magnetic Resonance Imaging (MRI)	27
2.2.5	Ultrasound Imaging	29
2.2.5.1	A-mode (Amplitude)	33
2.2.5.2	B-mode (Brightness)	34
2.2.5.3	M-mode (Motion)	35
2.2.5.4	Doppler Based Ultrasound Imaging	36
2.3	Ultrasound Speckle Tracking and Its Clinical Applications	39
2.4	Motion Estimation of Speckle Tracking	41
2.4.1	Gradient Based Optical Flow	43
2.4.1.1	Lucas-Kanade Algorithm (LK)	46
2.4.2	Block-Matching Algorithm (BMA)	49
2.4.2.1	Mean Square Error (MSE)	52
2.4.2.2	Normalised Cross-Correlation (NCC)	53
2.6	Summary	55
Chapter 3 - Materials and Methods		57
3.1	Methodology	57
3.2	Manual Measurement Based on Standard Method	60
3.3	Study 1: Algorithm Validation Experiment	60
3.3.1	Participant	61
3.3.2	Tracking Region	61
3.3.3	Hardware and Software Setup	62
3.3.3.1	Patella Tendon Assessment Setup	66
3.3.3.2	Medial Gastrocnemius Tendon Assessment Setup	68
3.4	Study 2: Two Regions of Interest (ROI) Tracking Experiment	71
3.4.1	Hardware and Software Setup	72

3.5	Study 3: In-Vivo Experiment Using Multiple Layers Tracking	77
3.5.1	Participants	77
3.5.2	Tracking Regions	77
3.5.3	Hardware and Software Setup	78
3.6	Speckle Tracking Software Design and Implementation	81
3.6.1	Software Design and Implementation Overview	81
3.6.2	The Graphical User Interface (GUI)	83
3.6.3	The Speckle Tracking Algorithms	87
3.6.3.1	MSE	87
3.6.3.2	NCC	90
3.6.3.3	LK	93
3.6.3.4	NCCMSE	95
3.6.4	Individual Error Analysis	98
3.6.4.1	Stationary Movement Error	98
3.6.4.2	Irregular Movement Error	99
3.7	Summary	100
Chapter 4 - Evaluation of The Four Tracking Algorithms		101
4.1	Evaluation of The Tracking Algorithms	101
4.2	Tracking Accuracy During Passive Tendon Movement	102
4.3	Tracking Accuracy During Active Tendon Movement	105
4.4	Tracking Reliability During Passive tendon Movement	112
4.5	Tracking Reliability During Active Tendon Movement	117
4.6	Discussion	121
4.7	Summary	124
Chapter 5 - Automatic Measurement using Normalised		
	Cross Correlation	125
5.1	Region of Interest (ROI) Block Size Comparisons	125
5.1.1	Patella Tendon	126
5.1.2	Medial Gastrocnemius Tendon	129
5.2	Tracking Algorithm Threshold Level Comparisons	132
5.2.1	Patella Tendon	132

5.2.2	Medial Gastrocnemius Tendon	133
5.3	Automatic Tracking using Two Regions of Interest (2-ROI)	135
5.3.1	Patella Tendon	136
5.3.1.1	Passive Movement	136
5.3.1.2	Active Movement	137
5.3.2	Medial Gastrocnemius Tendon	138
5.3.2.1	Passive Movement	138
5.3.2.2	Active Movement	139
5.4	Summary	141
Chapter 6 - In Vivo Experiments: Multiple Layer Automatic		
	Tracking to Determine Human Tendon Mechanical Properties	142
6.1	In-Vivo Strain Comparison	142
6.2	Proximal Strain Results	143
6.3	Distal Strain Results	144
6.4	Comparisons Between Proximal and Distal Layers	145
6.5	Summary	148
Chapter 7 - Summary and Conclusions		150
7.1	Summary	150
7.2	Conclusions and Recommendations for Future Works	155
	References	157
	Appendix A: Journal Publication I	172
	Appendix B: Journal Publication II	180
	Appendix C: Conference Abstract (SPARC 2011)	191
	Appendix D: RISE magazine column	194
	Appendix E: Conference Paper (IGNITE 2014)	195
	Appendix F: Matlab Source Code (NCC)	202
	Appendix G: Matlab Source Code (MSE)	206
	Appendix H: Matlab Source Code (NCCMSE)	210
	Appendix I: Matlab Source Code (LK)	214

List of Tables

Table 4.1	Mean displacement of 10 samples and difference (in millimetres) of each tracking algorithm against the standard manual measurement of passive movement at the patella tendon.	102
Table 4.2	Mean displacement of 10 samples and difference (in millimetres) of each tracking algorithm against the standard manual measurement of passive movement at the medial gastrocnemius tendon.	104
Table 4.3	Mean displacement of all passive movements of the tendon for each algorithm and the difference of each algorithm against the manual measurement.	122
Table 4.4	Mean displacement of all active movements of the tendon for each algorithm and the difference of each algorithm against the manual measurement.	122
Table 4.5	Total mean of computational cost for each algorithm on both active and passive tests.	123
Table 4.6	Total mean of tracking errors for each algorithm.	123
Table 6.1	Instantaneous mean strain for all layers at both proximal and distal regions of the patella tendon at 50% and 100% force levels.	146

List of Figures

Figure 1.1	Fundamental steps in digital image processing (Gonzalez, 1992)	2
Figure 1.2	Types of imaging and their application areas (Gonzalez, 2002)	3
Figure 1.3	Example of a video motion.	7
Figure 1.4	Examples of object tracking used in various applications: a) surveillance camera (from http://ben.benfold.com/research.html), b) traffic control management, c) cardiovascular strain estimation and d) tendon tracking (from http://www.ultrasoundcases.info/).	9
Figure 2.1	Structure of tendon with each layer bounded together to form a single tendon (Kannus, 2000).	17
Figure 2.2	Generalised stress-strain ($\sigma - \epsilon$) curve illustrating the tendon behaviour (Barfod, 2014).	18
Figure 2.3	A schematic illustration of energy absorption in a tendon during the coil-recoil process (Barfod, 2014).	19
Figure 2.4	Illustration of length-tension relationship of skeletal muscle (Pearson, 2010).	20
Figure 2.5	Example of tendon rupture with arrow indicating the rupture area (from http://www.ultrasoundcases.info/).	22
Figure 2.6	Different levels of tendinopathy illustrating (a) normal tendon, (b) enlarged tendon areas, and (c) Hypoechoic areas (Archambault et al. 1998).	24
Figure 2.7	Example of an X-ray of the medial upper leg visualising (a) the patella (kneecap), femur and tibia, and the X-ray of the lateral lower leg (b) the tibia, fibula and the calcaneus (from http://www.ultrasoundcases.info/).	25
Figure 2.8	Example of bone scintigraphy imaging of the medial upper leg visualising (a) the patella (kneecap), femur and tibia, and the lateral lower leg (from http://imgkid.com/bone-scan-images.shtml) (b) the tibia, fibula and the calcaneus (Karasick, 1996).	26

Figure 2.9	CT images of the lateral upper leg visualising (a) the patella (kneecap) with its (b) axial view and (c) the tibia, fibula and calcaneus with its axial view (d) . (Balke, et. al, 2010)	27
Figure 2.10	Examples of MRI images of the lateral upper leg visualising (a) the patella (kneecap) with its (b) axial view (from http://www.garylongmuir.com/quality-reports/knee_mri/) and (c) the tibia, fibula and the calcaneus with its axial view (d) (from http://mrimusculoskeletalsection.blogspot.com/).	28
Figure 2.11	An illustration of ultrasound sound waves emitted in pulses from the probe transducer and being reflected at 'a', 'b' and 'c'. The reflected pulse gives information of the reflected signal measured in amplitude and the time it takes to reach the probe. The incoming wave at 'a' is the full amplitude, while the incoming wave at 'b' is the wave transmitted through 'a'. The incoming wave at 'c' transmitted from 'b' [Støylen, 2010].	29
Figure 2.12	The positioning of the structure surface determines the directions of the scatters [Støylen, 2010]	30
Figure 2.13	Examples of ultrasound images of (a) Achilles tendon, (b) patella tendon (c) (from http://philschatz.com/physics-book/) blood flow of neck arteries (d) heart structure (from http://emergencyultrasoundteaching.com).	32
Figure 2.14	Example of an A-Mode image with y-axis represents the amplitude and x-axis represents the depth. The amplitude spikes of A and B represents the boundaries of solid objects found (from http://www.battlesnake.co.uk/_uni/ultra.htm).	33
Figure 2.15	Example of a B-mode image with small dots at (x,y) coordinates representing the echo intensity with different shades of grey.	34
Figure 2.16	Example of a M-mode image shows a wave-like motion where y-axis representing the depth of the tissue and x-axis represents the movement over time.	35

Figure 2.17	Examples of Doppler based ultrasound imaging. (a) Colour Flow Doppler Imaging (CFI), (b) Pulse Wave Doppler (PWD), (c) Continuous Wave Doppler (CWD) and (d) Tissue Doppler imaging (from http://www.criticalecho.com/content/tutorial-2-modes-ultrasound).	37
Figure 2.18	Three primary planes illustrated from anatomical position of human body.	38
Figure 2.19	B-mode image of the knee (from Knee Pro III, 3D4Medical.com) (I) with the patella tendon (a), and (II) the ankle (from http://achillestendon.com/) with tendons at gastrocnemius (b) and Achilles (c).	39
Figure 2.20	Illustration of two frames from a video sequence of a tendon, (a) is the initial frame, (b) is the next frame and (c) is the graphical representation of a displacement with arrow showing the motion vector.	41
Figure 2.21	Different types of motion estimation techniques.	42
Figure 2.22	Basic concept of optical flow. Red arrows indicating the origin of flow vectors and black arrow indicating the velocity vector.	44
Figure 2.23	Examples of Lucas-Kanade method (a) with its flow vector (b) and Horn-Schunck (c) and its flow global flow vector (d) .	46
Figure 2.24	Lucas-Kanade motion estimation illustrated with B-mode tendon data.	49
Figure 2.25	Illustration of a BMA with a predefined search window and image block (Barjatya, 2003).	50
Figure 2.26	Illustration of a block matching algorithm (BMA) matching from the image in frame k to the block within the search window in target frame $k+1$ (Purwar, et al., 2010).	51
Figure 2.27	Illustration of a Mean Square Error (MSE) similarity measurement.	53
Figure 2.28	Illustration of a Normalised Cross Correlation (NCC) similarity measurement.	55

Figure 3.1	Three stages of experiment for the tracking ultrasound images.	59
Figure 3.2	Example of Ultrasound imaging of patella tendon with regional areas within the tendon band.	61
Figure 3.3	Example of Ultrasound imaging of medial gastrocnemius with the regional tendon areas within the tendon band.	62
Figure 3.4	An example of a B-Mode ultrasound system and a 40mm prober transducer.	63
Figure 3.5	An example of isokinetic dynamometer Kin Com type 125 AP.	63
Figure 3.6	A typical equipment setup for the experiments.	64
Figure 3.7	Participant positioned for the assessment of patella tendon.	64
Figure 3.8	Participant positioned for the assessment of medial gastrocnemius tendon.	65
Figure 3.9	a) Example of ultrasound probe positioned in the sagittal plane over the patella tendon with echo-absorptive placed. b) The ultrasound image generated showing the proximal region of inferior pole of patella tendon and the marker.	66
Figure 3.10	A) An example of passive contraction of the tendon. The ROI node was shown moving from its starting position in the initial frame and moved to another position in all successive frames. B) An example of an active contraction of the tendon, which the ROI nodes at every percentage level of voluntary contraction (MVC). The displacements for both experiments were measured starting from the initial position (<i>I</i>) to the last position of (<i>P</i>).	68
Figure 3.11	a) Example of the ultrasound probe positioned in the sagittal plane over the myotendinous junction of the medial head of the gastrocnemius muscle with echo-absorptive placed. b) The ultrasound image generated showing the myotendinous junction of	69

the medial gastrocnemius tendon and the marker.

- Figure 3.12 (A) an example of passive contraction of the medial gastrocnemius. 70
The ROI node was shown moving from its starting position in the initial frame and moved to another position in all successive frames. (B) An example of an active contraction of the medial gastrocnemius, which the ROI nodes change at every percentage level of voluntary contraction (MVC). The displacements for both experiments were measured starting from the initial position (*I*) to the last position of (*P*).
- Figure 3.13 Example electrode placement for EMG recordings from Biceps 72
Femoris (Hamstring) and tibialis anterior. The illustration (right) shows where Biceps Femoris is located.
- Figure 3.14 Example output from the electronic signal generator to allow 73
temporal alignment between the (A) torque and EMG trace, and (B) the ultrasound image.
- Figure 3.15 Example of 2-ROI nodes on both A: patella tendon, where ROI 74
node, P1 was placed on the echo-absorbent marker and P2 on the regional tendon just distal to the patella, and B: medial gastrocnemius, where ROI node, P2 was placed on the regional tendon at the myotendinous junction.
- Figure 3.16 Example of 2-ROI nodes on both A: patella tendon and B: medial 76
gastrocnemius, where ROI node, P1 was placed on the echo-absorbent marker and P2 on the regional tendon area just distal to the patella, at 50%, and 100% MVC, both ROI nodes of *P1* and *P2* moved along the tendon elongation. *I1* and *I2* showed the initial position of the ROIs. The arrows indicated the path of the ROIs has taken. At 100% MVC, the distance of *P1* and *P2* were measured (*d1*), and the initial distance of the ROI nodes (*I1*, *I2*) were measured (*d2*). The difference between *d1* and *d2* gave the relative

displacement.

Figure 3.17	Example of patella tendon and regions being investigated.	77
Figure 3.18	Comparisons between a) 40mm probe transducer and b) 100 mm probe transducer. Image produced by the latter probe has a higher depth and broader viewing range.	78
Figure 3.19	Regional tracking of the patella tendon.	81
Figure 3.20	The module structure for the speckle tracking software.	82
Figure 3.21	The graphical user interface (GUI) for the main window of the tracking software.	84
Figure 3.22	The graphical user interface (GUI) for the scale unit.	85
Figure 3.23	The settings (GUI) of the tracking software.	86
Figure 3.24	Schematic diagram of MSE.	89
Figure 3.25	Schematic diagram of NCC.	92
Figure 3.26	Schematic diagram of LK.	94
Figure 3.27	Schematic diagram of NCCMSE.	97
Figure 4.1	Total mean computational cost for both experiments (in seconds) between the algorithms.	105
Figure 4.2	Mean displacement of 10 samples (in millimetres) of each algorithm against the manual measurement at every 10% intervals (from 10% to 100%) of the total frames on the active movement of patella tendon. For example, the individual displacement was measured from 0-10% and followed by 10-20%.	106
Figure 4.3	Mean displacement of 10 samples (in millimetres) of each algorithm against the manual measurement at every 10% intervals (from 10% to 100%) of the total frames on the active movement of medial gastrocnemius tendon. The individual displacement was measured from 0-10% and followed by 10-20%.	109
Figure 4.4	Total mean of computational cost for both experiments (in seconds)	112

	between the algorithms	
Figure 4.5	Stationary movement errors of passive movement at patella tendon.	113
Figure 4.6	Irregular movement error of passive movement at patella tendon.	114
Figure 4.7	Stationary movement error of passive movement at medial gastrocnemius tendon.	115
Figure 4.8	Irregular movement error of passive movement at medial gastrocnemius tendon.	116
Figure 4.9	Stationary movement error of active movement on patella tendon.	117
Figure 4.10	Irregular movement error of active movement at patella tendon.	118
Figure 4.11	Stationary movement error of active movement at medial gastrocnemius tendon.	119
Figure 4.12	Irregular movement error of active movement at medial gastrocnemius tendon.	120
	Mean displacement of each ROI block size from patella tendon	
Figure 5.1	Mean displacement of ROI sizes and manual measurement of active movement of the patella tendon, relative to their starting position to the final position.	126
Figure 5.2	Mean time (in seconds) of each ROI block size of the patella tendon.	128
Figure 5.3	Mean displacement of ROI sizes and manual measurement of active movement of the medial gastrocnemius tendon, relative to their starting position to the final position.	129
Figure 5.4	Curve fitting of mean time (in seconds) of each ROI block size of the medial gastrocnemius tendon.	131
Figure 5.5	Mean displacement (in millimetre) of threshold level at every 0.05 intervals and the manual measurement (red bar) of active movement of the patella tendon.	132
Figure 5.6	Mean displacement (in millimetre) of threshold level at every 0.05 intervals and the manual measurement (red bar) of active movement of the medial gastrocnemius tendon.	134
Figure 5.7	Comparisons graph between various sizes of ROI and manual tracking for passive movement at the patella.	136
Figure 5.8	Comparisons graph between various sizes of ROI and manual	137

	tracking for active movement at the patella.	
Figure 5.9	Comparisons graph between various sizes of ROI and manual tracking for passive medial gastrocnemius measurement.	138
Figure 5.10	Comparisons graph between various sizes of ROI and manual tracking for active medial gastrocnemius movement.	140
Figure 6.1	Strain value (%) for all measured proximal regions (mean \pm SEM) accumulated at 10-100% force.	143
Figure 6.2	Strain values for all measured distal regions (mean \pm SEM) accumulated at 10-100% force.	144
Figure 6.3	Instantaneous strain values for all layers at both proximal and distal regions of the patellar tendon at 50% and 100% force.	146

List of Equations

Equation 2.1	41
Equation 2.2	44
Equation 2.3	44
Equation 2.4	44
Equation 2.5	44
Equation 2.6	45
Equation 2.7	46
Equation 2.8	47
Equation 2.9	47
Equation 2.10	47
Equation 2.11	47
Equation 2.12	48
Equation 2.13	51
Equation 2.14	52
Equation 2.15	52
Equation 2.16	54
Equation 2.17	54
Equation 2.18	54
Equation 2.19	54
Equation 3.1	70
Equation 3.2	71
Equation 3.3	71
Equation 3.4	74
Equation 3.5	75
Equation 3.6	75
Equation 3.7	80
Equation 3.8	80
Equation 3.9	95
Equation 3.10	95
Equation 4.1	103
Equation 4.2	103

Equation 6.1	145
Equation 6.2	145

List of Publications

Mohamed, A.S.A, (2011) Ultrasound Image Research. RISE Magazine August/September 2011 Edition: p153.

Mohamed, A.S.A., Pearson, S.J., and Ritchings, T. (2011) Image tracking using normalized cross-correlation to track and analyse mechanical tendon properties. SPARC 2011. 2: p10-11.

Pearson, S.J., Mohamed, A.S.A., and Ritchings, T., (2012). The Use of Normalized Cross Correlation Analysis For Automatic Tendon Excursion Measurement in Dynamic Ultrasound Imaging. Journal of Applied Biomechanics. 29(2): p165-73.

Pearson, S.J., Mohamed, A.S.A., and Ritchings, T., (2013). Regional Strain Variations in The Human Patellar Tendon. Med Sci. Exer. 46: p1343-1351.

Mohamed, A.S.A., Pearson, S.J., and Ritchings, T. (2014). Automated Speckle Tracking in Ultrasound Images of Tendon Movements. Int. Conf. of Global Network for Innovative Technology. 2: p112-117.

Acknowledgements

I would like to convey my sincere gratitude to Professor Tim Ritchings and Dr. Stephen Pearson for their exceptional guidance and support throughout the supervision of my PhD, for providing a great source of knowledge and expertise and always making time to answer my questions. By continually challenging my ideas and thinking both supervisors have enhanced my critical awareness and understanding no end for that I am extremely grateful.

Special thanks go to the many colleagues who have provided help and support. With particular reference to Ahmed Hamouda who has helped me through with good times and bad. Many thanks to the Malaysian Community in Manchester for providing help on financials and accommodations. Thanks also to all the people who participated in the works of this thesis, your time and commitment was greatly appreciated, this work could not have gone ahead without you.

Special thanks to my beloved wife, Siti Suhaily Surip, with all the supports throughout my PhD years and patiently waiting for my returns. Your love, encouragement and belief in my abilities have kept me going. Finally, I would like to say a huge thank you to both my brother and sister-in-law as well as to my father for putting up with me throughout my study years! I would also like to dedicate this thesis to my mother who saw the beginning and had every faith that I would see the end.

Abbreviations

ABMA	Adaptive block matching algorithm
BF	Biceps femoris
BMA	Block matching algorithm
CSA	Cross-sectional area
DV	Digital video
ECM	Extracellular matrix
EMG	Electromyography
GUI	Graphical user interface
ICCs	Intraclass correlation coefficients
LK	Lucas-Kanade
MRI	Magnetic resonance imaging
MSE	Mean square error
MVC	Maximum voluntary contraction
NCC	Normalised Cross Correlation
NCCMSE	Normalised Cross Correlation & Mean Square Error
PC	Personal computer
RFD	Rate of force development
RMS	Root mean square
ROI	Region of interest
SEM	Standard error of mean
SNR	Signal-to-noise ratio
USA	United States of America
UK	United Kingdom

Abstract

The central aim of this thesis was to develop new tracking software employing various image tracking algorithms for tracking the speckled movement of the tendon image captured using dynamic B-mode ultrasound imaging. The algorithms were selected based on the literature related to the tracking of images captured using ultrasound imaging. Experiments were carried out to validate these tracking algorithms in order to enable development of the tracking software. The experiments conducted paralleled the objectives in designing, developing, experimenting and implementing the image-tracking algorithm to track movement of the human tendon in vivo within the speckled ultrasound images. The development of the tracking software focuses on solving the problems of tracking the ultrasound images as well as analysing the tracking movement frame-by-frame to produce useful measurements that can be used to describe the localised mechanical and structural properties of the human tendon.

The algorithms tested were Normalised Cross Correlation (NCC), Mean Square Error (MSE), optical flow – Lucas-Kanade (LK) and combination of NCC and MSE (NCCMSE) selected by signal-to-noise ratio (SNR) and were tested on both active and passive movements of the patella tendon (knee) and the medial gastrocnemius tendon (ankle). The comparison of the algorithms led to the identification of a single algorithm giving optimal result. The results from all tested algorithm showed NCC to be the closest match to the standard manual measurement. NCC was also the fastest among the algorithms tested and contained fewer errors in tracking.

For NCC algorithm, various sizes of the region of interest (ROI) block were also tested and found that 15x15 pixels ROI block size gave the optimum measurement, which was close to the standard manual measurement. The threshold levels also indicated that >0.90 to be the optimum level for optimum tracking. The 2-ROI tracking analysis were also explored to look at the tracking performances when tracking at two different regional sites of the tendon simultaneously, and again the

NCC performed better with 15x15 ROI block size and comparable to the results obtained from the standard manual measurement.

Lastly, multiple layers of the tendon were also explored to look at the excursion of the anterior, midsection and posterior layers of the tendon during ramped isometric contraction. This experiment uses all the settings found from previous experiment results, and applied to look at the mechanical properties of the human tendon. The experiments showed that the anterior gave the highest mean strain followed by the mid section and the smallest mean strain was found at the posterior proximal. The experiment also looked at the distal strain, with the result showing that the posterior gave the highest mean strain followed mid section and anterior layer gave the smallest mean strain. The experiment also looked at the performance of posterior layers and distal layers at 50 and 100% force levels.

The experimental results showed that the NCC to be the optimum-tracking algorithm. The method described here has the potential to improve clinical knowledge relating to the tendon mechanical properties. The information generated by the tracking algorithm could help to give further insight into the aetiology of tendon injury, repair, response to various training interventions and the time course of tissue adaptation with disease.

Chapter 1

Introduction

Overview

This chapter gives a brief introduction to the role of digital imaging techniques, particularly in the domain of computer vision and is supported by various applications that use these techniques and followed by the motivation of the work done in this thesis. Finally, the aims and objectives of this study are presented, and the contents of each chapter are outlined covering the introduction, literature review, methodology, experiments, findings and conclusions.

1.1 Fundamental Steps in Image Processing

Human beings have no difficulties recognising every geometric object in a simple image scene. Also, human beings can distinguish them from one another with little difficulty. For example, the human brain can differentiate various forms and sizes of objects and in addition can also assess the distances, colours and shapes with the help of individual senses such vision, touch and sound.

These complex activities that occur within the human brain are the primary goal of duplicating the same ability in digital image processing so that it can be digitized, manipulated and processed with endless possibilities. A typical digital image processing system consists of five fundamental modules (Figure 1.1); it is a cycle of processes that modifies an analogue signal into a digital reproduction with the purpose that it can be enhanced, extracted and interpreted into a much more useable format (Gonzalez, 1992). These modules are interchangeable between each

other, as the computer system learns and applies rules to make every transition of the steps easier, and more accurate.

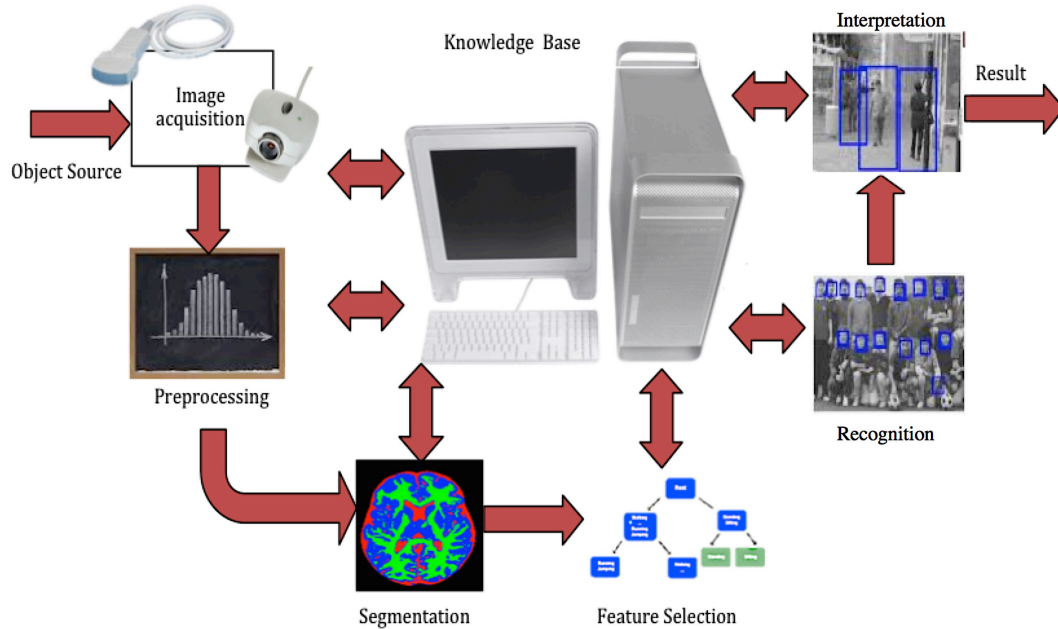


Figure 1.1: Fundamental steps in digital image processing (Gonzalez, 1992).

1.2 Image Acquisition

The very first module of the digital image processing is the image acquisition consisting of a sensory device (such as CCD camera, ultrasound probe transducer or sonar resonance) that illuminates (visual) or reflects sound waves (acoustic) towards the scene. The analogue signals can be captured by the imaging sensor and converted it into its digital representation. The signals are stored as digital image or digital video so that it can be manipulated within the computer system (Gonzalez, 1992). Figure 1.2 shows how an image can be captured or obtained in various ways according to its application.

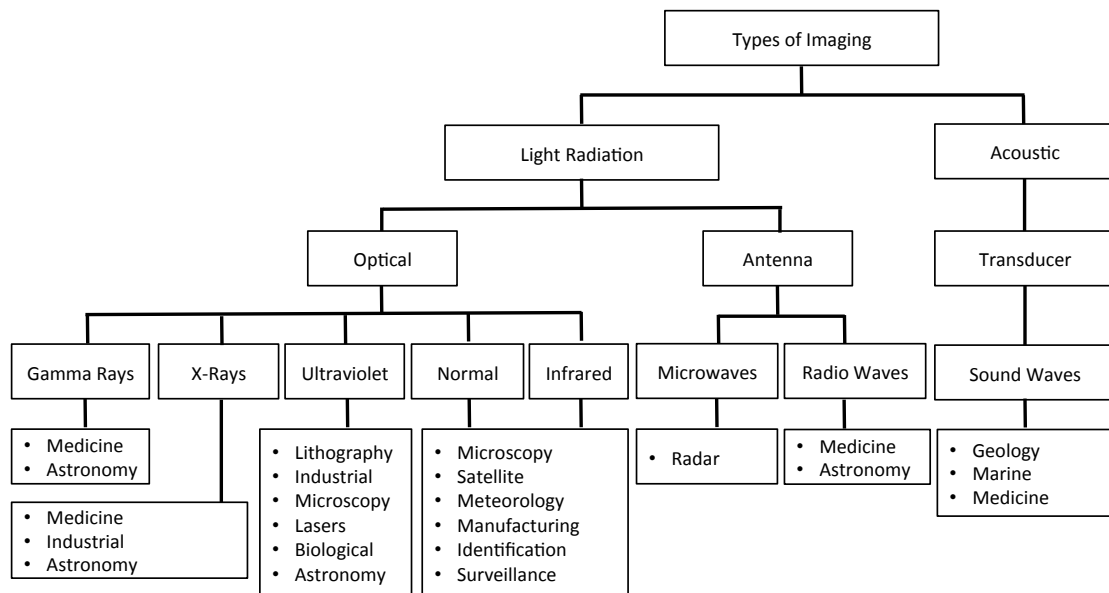


Figure 1.2: Types of imaging and their application areas (Gonzalez, 2002).

1.2.1 Light Radiation Based Imaging

Visual type image acquisition usually uses an optical sensor to capture the image scene (Gonzalez, 1992). This captured scene is often the result of the energy produced (e.g. photon, the sound wave or radiation) at the surface of the intended object or scene within the image space (Efford, 2000). The energy is absorbed by the sensory device and converted it into a digital representation. This radiation energy can be captured using an optical sensor to capture the radiated light. Such applications can be found in nuclear medicine and X-ray tomography. However, in astronomical use, special telescopes are used to capture either the gamma rays or X-rays released from stars. X-rays are also used in industrial use and recently extended to other areas such as archaeology. The next imaging technique involves visible light, which occurs naturally in most everyday applications (Gonzalez, 2002). Light sources can include the near-visible parts of the electromagnetic spectrum, such as the ultraviolet and infrared. In all cases, the light energy is detected by appropriate sensory device and converted to digital form.

Another image acquisition device is the antenna (Gonzalez, 2002). The antenna captures the propagated wave signal. Wave signals can travel through liquid

and solids and some wave signals are capable of penetrating obstacles such as the clouds and seawater, thus making them capable of travel further than the energy produced by the light signal. The wave signals can be either in the form of microwave or radio waves. Microwave is a form of electromagnetic radiation (Gonzalez, 2002). The wave energy is lower than the light rays but higher than radio wave. Radar imaging is the only example that uses the microwave technique extensively. The waves created from the radar can penetrate most objects. Microwave signals are useful for generating images of geological and marine observations.

Radio wave is another form of electromagnetic radiation that uses the smallest amount energy. In astronomical applications, a radio telescope is used to capture the radio waves generated from the stars (Gonzalez, 2002). In medical imaging, radio waves are used in magnetic resonance imaging (MRI), where short pulses of radio waves passes through the patient's body, and the responding pulse of radio waves are captured by the sensory devices to produce 3-dimensional picture of a section of the patient (Gonzalez, 2002).

1.2.2 Acoustic Based Imaging

Another imaging technique can be found in acoustic form whereby short pulses of sound waves are distributed to the scenery surface and captured as they are reflected to the sensor. It works almost similarly to the microwaves and radio waves, but with the exception that it uses sound as its medium (Gonzalez, 2002). The intensity and speed of the reflected pulses tell the distance of the object in the scene. This method can be found in the areas such as medicine (ultrasound), maritime and geological applications.

1.3 Pre-processing

Once the image is obtained, the next stage is to improve the image using various techniques such as increasing or decreasing its brightness and contrast,

changing its sharpness or enhancing by using noise removal (Gonzalez, 1992). Since the image is in its digital form, the data is stored in a matrix array consisting of row and column indices. Manipulation of this matrix array can be done easily by using appropriate mathematical functions (filters) resulting in a modified image according to the filtering applied.

1.4 Segmentation

In the segmentation stage, the image is partitioned into multiple segments of parts or objects. The aim of segmentation is to segment an image until the object of interest in an image scene has been isolated (Gonzalez, 1992). There are several segmentation techniques such as Hough Transforms (Ballard, 1981), where objects are segmented into various geometrical shapes, Harris Corner Detector (Harris, 1988) where objects are segmented by its corner, and object segmented by their edges (Canny, 1986).

1.5 Feature Selection

Next, in the feature selection stage, the raw data generated from the process of segmentation will be utilized as a medium for extracting features so that useful data from the image scene can be quantified, classified and differentiated from each other (Gonzalez, 1992). The image correlation algorithm is one of the examples typically used to measure and extract features in a digital image (Cafforia, 1976, Ryan, 1980, Forstner, 1986, Shi, 1994).

1.6 Recognition

Once features are extracted, the next step of the digital imaging processing is the recognition (Gonzalez, 1992). The recognition is the process that assigns label to object based on the information provided by the feature selection (Gonzalez, 1992). A

method such as feature matching uses the pattern vector containing the numerical features that represent some feature descriptors and statistically measure a score for similarity prediction (Liu, 1998). Another method of recognition is the matching by correlation where the object pattern is correlated with the feature template to measure its similarity (Ryan, 1980). For example, in identifying a car, the feature descriptions such as edges and lines are used as the collective knowledge and with similarity measurement technique; the object of interest can be identified as a car.

1.7 Interpretation

The knowledge gathered from all image-processing processes are later interpreted to describe the object of interest its size, shape, tone, colour, pattern, shadow, context and functions (Gonzalez, 1992). For example, a car can be described as moving in a moving scene, where the shape, colour and size are being observed to shift from one frame to another. This process involves descriptive techniques such as predicate logic using mathematical notation (automata) or semantic network using graph representing the relationships between nodes (Gonzalez, 1992).

1.8 Knowledge Base

The information gathered from the steps of the digital imaging process is controlled and set by the central unit known as the knowledge base where controls such as limiting the searching to the interested areas and interactions between each module are done in this central unit (Gonzalez, 1992). In general, it is the main interface containing the rules for managing the functions of the modules, as well as to facilitate the necessary programming codes and algorithms guiding the whole operation of a successful digital imaging and displays the necessary results to the end user.

1.9 Image Tracking in Digital Video

These five fundamental processes are the foundation of how the image is acquired, processed and presented. However, over time, the technology of acquiring a set of moving objects has been developed, as the technology behind it gets better and more advanced. Furthermore, with the advance in technology, more affordable digital videos are readily available, and they have become part of everyday life. Unlike still images, video sequences provide more information describing the objects and scenarios changes over time. This sequence of images is updated at a set rate (Guan, 2001). Figure 1.3 shows how an image at the initial frame 1 with a single dot moves to a different position with each frame. Towards the end of frame 5 the location of a single dot has shifted to a different position and this, when combined and arranged at a particular rate gives an apparent motion movement.

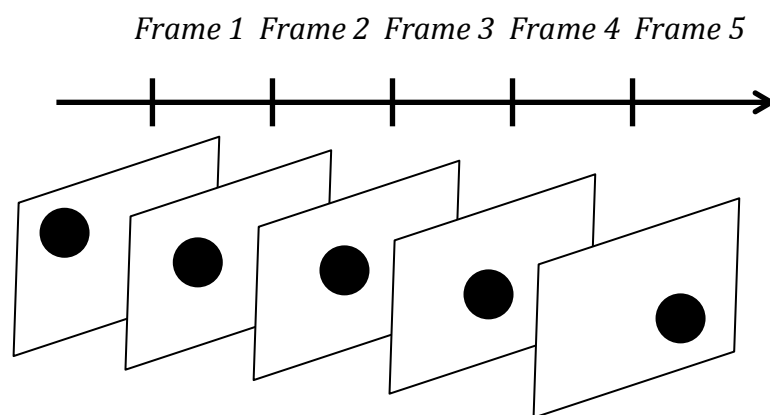


Figure 1.3: Example of a video motion.

Processing of an image sequence takes huge amount of processing and computational time. Estimating motion and tracking objects within the image sequence could give valuable data describing the characteristics of an object within the motion picture. Understanding the problem domain will help the development of suitable algorithms for tracking objects in the images.

The problem areas of a successful tracking can be divided into three categories:

- Tracking of rigid objects
- Tracking of articulated objects
- Tracking of non-rigid objects

All geometrical shape objects such as cube, sphere or balls that have no joints interconnecting between them are known as a rigid object. Articulated objects are rigid objects that contain multiple joints interconnecting between the rigid object such as person, cabinet doors and drawers, or room and garage doors. Objects that can deform and constantly change shape are known as non-rigid objects (e.g. clothes, human muscle). Objects that are active within the scene are usually differentiated by their edge, shape, size and colour. Measuring their translation and rotations is the main objective of the tracking algorithm. An example of a tracking method is by observing the edges of a 3D wireframe model in the image (Drummod, 2002).

1.10 General Applications of Object Tracking

The use of object tracking can be found in many areas involving object recognition in the areas of surveillance systems and medical applications (Foresti, 1998). For example, in automated surveillance systems, object tracking is a vital step in recognising people and identifying motions and patterns in order to provide a better sense of security (Stauffer, 2000, Li, 2004, Benfold, 2009). Object tracking is also used for traffic surveillance to detect vehicles and to observe the traffic flow (Zang, 2003, Foresti, 2005, Yu, 2006). Meanwhile, in medical application, object tracking is used for identifying an organ behaviour and tissue disease (e.g. breast lesions, tendon ruptures, cardiovascular diseases) by observing the flow of blood vessel and tissue behaviour (Støylen, 1993, Swillens, 2010).

Furthermore, in recent studies, living human tendons were used to study tendon force and strain during active tendon load (Dilley, 2001, Revell, 2003,

Bruhn, 2005, Jan-Wiebe, 2010, Pearson, 2012) where in comparisons, isolated animals or cadavers were used in vitro (Benjamin, 1995, Léjard, 2007). The advancement of the ultrasound technology has benefited non-invasive imaging that enables researchers to study different parts of tissue organs for the detection of diseases (Garra, 1997, Hall, 2002).

This method of using ultrasound analysis has increasingly been the interest of researchers to study and understanding tendon properties for both static and dynamic situations (Fukunaga, 1996, Narici, 1999, Loram, 2006, Onambele, 2007). Figure 1.4 shows some of the examples of applications that utilized object tracking.

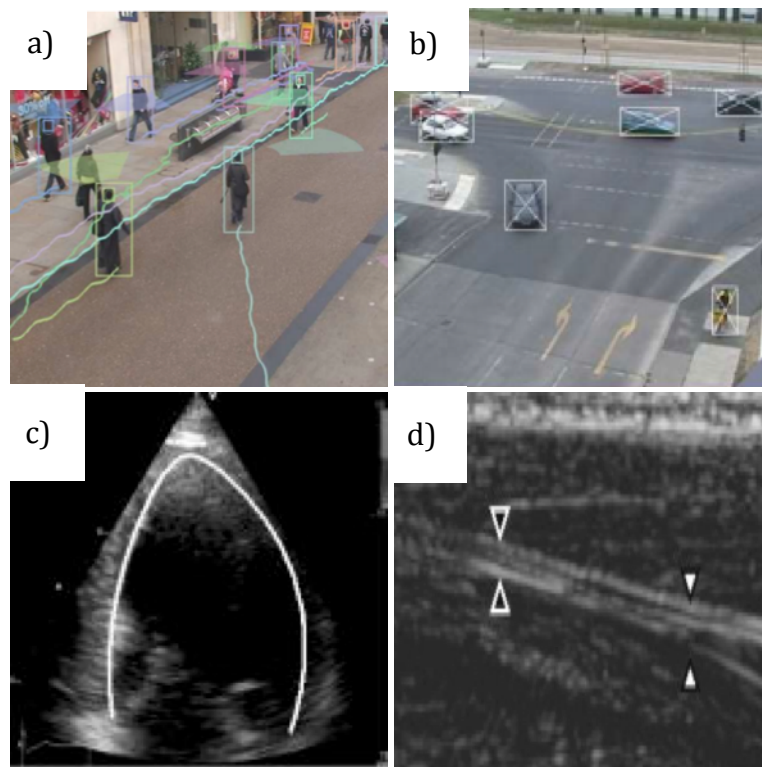


Figure 1.4: Examples of object tracking used in various applications: **a)** surveillance camera (from <http://ben.benfold.com/research.html>), **b)** traffic control management, **c)** cardiovascular strain estimation and **d)** tendon tracking (from <http://www.ultrasoundcases.info/>).

The real challenge of tracking ultrasound data is to make the algorithm intelligent enough to recognise the changes in the pattern. Since human tissue deforms and changes its density throughout the entire video frames, it reduces the possibility of tracking efficiently. The use of synthetic material as a marker is also introduced to

improve the tracking procedure (Lee, 2006, Lee, 2008). However, this does not reflect the natural behaviour of the tendon and might affect the speckle signature. Until now, there are no similarity measure algorithms that can accurately track the motion of the tissue fibre.

The work presented in this thesis focuses on improving the robustness of existing algorithms to analyse ultrasound images of the tendinous area and accurately estimate the motion of the tendon tissue. The displacements of the motion are then calculated and compared to the standard manual measurement (Onambele, 2007) for validation. The study also uses the algorithms to track various depth of the tendon tissue simultaneously so that strain at each level of depth (layer) of the tendon can be calculated.

1.11 Motivation of This Work

Tracking moving objects in a sequence of digital images has attracted a great deal of interest and has been a fundamental problem in computer vision as it requires a vast amount of visual data representing the real world. Furthermore, most objects in the real world are also dynamic and constantly influenced by changing elements such as variations of lighting conditions, changes in viewpoint, occlusions, and many other factors that could be viewed as “noise” in computer vision. Thus, developing a robust tracking algorithm is a challenging task. Nevertheless, it is the goal of every computer vision algorithm to be able to search within the image space and produce a visual interpretation describing the object such as its posture, movement, and spatial relation. The amount of computation required to successfully match and track the target object would also be a problem, as the computation time would grow over time (Gonzalez, 1992, Gonzalez, 2002).

Estimating the motion of the object in an image space normally involves comparing two image frames. The first frame (initial frame) contains the object of interest while the second frame (target frame) contains the possible movement of the object of interest and the difference is measured to estimate the displacement (Efford,

2000). Once, compared the immediate next frame is used as a reference frame. In each frame, every pixel motion is calculated and finally, if tracking is found to be tracked at wrong tracking path or wrong location in the next frame, this is then corrected based on the previous path and coordinate locations from the previous frame.

1.12 Aims and Objectives

The main objectives of this study are to develop an improved image tracking software for tracking the speckle in ultrasound. A detailed model of the workflow is also laid out to give better understanding of the algorithms and comparisons are conducted with existing tracking algorithms to select the best algorithm for this application. The tracking measurements should be generated to improve clinical knowledge relating to the tendon mechanical properties to help determine how and why these differences in strain may affect the aetiology of disease and effects of training rehabilitation.

Therefore, the aims and objectives of this study are:

- To identify the stages in the ultrasound tracking process starting from data acquisition of the subjects tested, to the development and evaluation of the software required for the study.
- To implement and validate optimum tracking algorithms to track ultrasound images of a tendon region with the optimum size of template block and threshold value.
- To extend the algorithm to track at different depths of the tendon to visualize and quantify differential strains between layers of the tendinous areas.
- To generate useful information from the tracking output for clinical knowledge of the tendon such as understanding the level of forces and strains that relates to tendon rupture during loading.

1.13 Outline of The Thesis

To sum up, Chapter 1 introduces the rationale for the study described in this thesis. The role of image processing mainly image based tracking solving various tracking problems is briefly discussed including its fundamentals and processes involved. Finally, the aims and objectives of this study are presented. The chapters of the thesis are arranged as follows:

Chapter 2 provides detailed background of biomedical properties related to tendon structures and functions as well as applications and experiments related to the ultrasound imaging and tracking in biomedical areas. The background of tracking imaging within the domain of ultrasound imaging is also described with details of the algorithms that have previously been used to track ultrasound images for medical purposes. This understanding of the tracking algorithms and its area of interest related to the mechanics of tendon are defined for the parameter identification and motion estimation with respect to ultrasound imaging with random speckle formation.

Chapter 3 describes the experimental setup in detail to validate the effectiveness of the tracking algorithms using the tendon tissue data in-vivo. In these experiments, different tracking algorithms are compared to the standard manual measurement (Pearson, 2006) in the later chapter. The hardware used, and the method of image acquisition is explained as well as the test subjects including areas of interest within the tendon muscle, and what kind of output to be expected. Software design and implementation is also covered in this chapter showing how results are achieved and what kinds of algorithms are used within the software environment. Details of software modules are defined here related to the software development, techniques used for each experiment also are modelled and described here, and finally, various models of the algorithms selected based on the literature discussed in Chapter 2 are described here in detail.

Chapter 4 describes the tracking algorithms: Normalised cross correlation (NCC), mean square error (MSE), optical flow – Lucas-Kanade (LK) and combination of NCC and MSE (NCCMSE) selected by peak signal-to-noise ratio (SNR). The validation of the algorithms leads to a single algorithm to be identified

and selected as the optimum algorithm. The mean displacement measurements generated were approximately similar to the ones measured using standard manual measurement and validated the tracking algorithm as capable of handling the randomness of the speckle pattern in any conditions (active or passive) on two different tendon areas (knee and ankle). Error analysis and computational time comparisons were also investigated to understand further the performance of each algorithm. Single region of interest (1-ROI) was used throughout the experiments in this chapter.

Chapter 5 describes normalised cross correlation (NCC) algorithm with various settings and properties to improve the accuracy of the tracking. The analysis looked at each ROI block size with comparisons performed against standard manual measurement. Time comparisons for each ROI block were also investigated. The threshold levels were also tested to identify the threshold levels that improve the accuracy of the tracking in matching between two image regions, again comparisons being made were between the levels against the manual measurement. Finally, two regions of interest (2-ROI) analysis was investigated in which the two markers were placed along the elongation of the tendon areas to look at relative movement of the two ROI markers and compared to the manual measurement. The experiments were conducted on both passive and active movements from both knee and ankle tendon area.

Chapter 6 examines and compares localized proximal strain at both the anterior and posterior regions of the patella tendon using 2-ROI tracking on multiple layers of anterior, posterior and mid section in vivo. The measurements obtained from the tracking were then converted into mean strain to look at the interactions between the layers of the tendon. The algorithm used for the tracking was normalised cross correlation (NCC), which was selected based on the analysis conducted in Chapter 4 and the tracking settings were based on the analysis performed in Chapter 5. The experimental setup for the experiments was described in Chapter 3. This chapter also explores the use of the selected algorithm to track the tendon tissue at multiple regional layers. Comparisons for both proximal and distal areas of the tendon while the tendon experiences voluntary contractions at 10% interval of forces were also evaluated. The outcome of this study shows how the algorithm can be implemented

to observe and analyse tendon and what kind of results it should generate suitable for understanding the working aetiology of human tendon.

Chapter 7 summarizes each chapter and the results from each experiment. Finally, in this chapter, aims and objectives of the study are investigated again to identify what has been achieved and lay out what was done and presents the future work to improve the tracking accuracy and to understand the tendon mechanical properties.

Chapter 2

Literature Review

Overview

This chapter provides a detailed background of tendon structure and function, as well as applications and experiments related to ultrasound imaging and tracking in biomedical areas. The background of tracking within the context of ultrasound imaging is also described with details of the tracking algorithms that have been developed primarily for biomedical applications.

2.1 Biomedical Background: Tendon Structure and Function.

Tendons connect muscle and bone in such a way that they allow muscle forces to be used to execute complex movements and actions such as the neck, shoulders, biceps, triceps, forearm elbow, hand, fingers, knee and ankle (Benjamin, et al., 1995). Their shape and length also depend on the area where a tendon resides, and normally found (Benjamin, et al., 1997). When a muscle contracts or shortens, it is the corresponding tendon that pulls the bone of the muscle attachment to create movement. Their tough and rigid characteristics provide joint stability at the articulation where two bones meet. This adaptable and viscoelastic affects the ability for it to accomplish tasks that involve high rates of force development, enabling a person to perform various ranges of physiological loading (Pearson, et al., 2006). The elastic energy of the tendon is produced when it is stretched and then recoils, resembling how a rubber band's elasticity works. This is because the kinetic and potential energy during locomotion was lost at one stage and stored as elastic strain energy and returned later in a recoil (Alexander, 2002).

2.1.1 Tendon Structure

The tendon is made up of a tough band of fibrous connective tissue and its primary role is to connect muscle to bone. The gross structure can be rounded cords, strap-like bands of flattened ribbons, which when healthy appear to be white and have a fibroblastic texture. Tendons are made up of two cells: tenoblast and tenocytes which are arranged and held together in a network of extracellular matrix (ECM) (Magnusson, et al., 2003, Kjaer, 2004). ECM consists of a range of collagens (primarily type I), proteoglycans and water (Kannus, 2000, Magnusson, et al., 2003). The type I collagen lends the strength to the tendon structure, while proteoglycans give the tendon its viscoelastic property. The tenoblast of the tendon contains both actin and myosin proteins that contribute to many important cellular processes (Sharma, et al., 2006). Actin filaments are responsible for many types of cell movements, while myosin is a type of protein that comprises of molecular motor (ATP), which generates force and movement by transforming chemical energy to mechanical energy (Jones, et al., 1990). Over time, tenoblasts become elongated and transform into tenocytes (Hampson , et al., 2008).

Tenocytes produce collagen molecules and are distributed throughout the tissue producing collagen fibrils and when compared to the tenoblasts contain lower metabolic activity (Chuen, et al., 2004). Tenocytes and tenoblasts lie between the collagen fibres along the axis of the tendon (Sharma, et al., 2006). The parallel fibres within the tendons are made up primarily of collagen (80-90% of the total dry mass), elastin (2%), proteoglycans (1-5%), and inorganic components (0.2%) such as copper, manganese, and calcium (Kjaer, 2004). The collagen part is made up of 97–98% type I collagen, with small quantities of other types of collagen (Kjaer, 2004). The collagen is the main structural protein in connective tissue and plays the main role in tissue development, while elastin is a protein that is elastic, allowing tissue to resume its shape after stretching and contracting. Figure 2.1 shows the illustration of the structure of the tendon (Kannus, 2000).

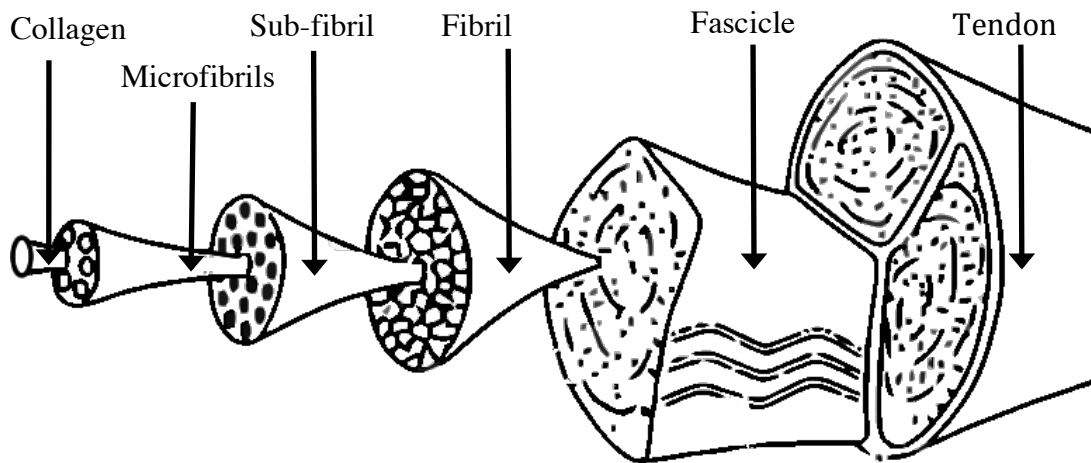


Figure 2.1: Structure of tendon with each layer bounded together to form a single tendon (Kannus, 2000).

The parallel fibres within the tendon are made up of collagen fibres closely packed together into microfibrils and sub fibrils that together form the fibrils. Fibrils are organised and held in parallel by a group of connective tissues called the fascicles. The collagen fibrils of the fascicles are arranged in a straight and parallel array interrupted by drastic changes in direction giving a wavy like structure or also known as “crimps”. The crimps allow the tendon to have some flexibility and low compressive stiffness (Diamant, et al., 1972). These groups of fascicles are held together by epitenon that forms the tendon appearance (Hulmes, 2002, Aslan, et al., 2008). The epitenon consists of loose, areolar tissue and permits the tendon to slide freely against adjacent tissue (Schatzker, et al., 1969).

2.1.2 Tendon Function

Tendons must be able to transmit high muscle forces to the bones for movement, and the parallel arrangement of the fibres is an important factor for this function. When a load is applied to the tendons, they exhibit changes in shape or configuration (deformation) and develop a tensile stress, thus making it demonstrate both viscous and elastic characteristics (viscoelastic). The viscoelastic properties make the tendon perform like a spring transmitting energy across the muscle and bone, as well as making it capable of storing and recovering the energy at high efficiency. The tendon also provides flexibility to the joints and enables muscles to

function with less change in length, allowing them to generate greater force, which gives the tendon the ability to adapt to influences such as mechanical loading and unloading. The tensile property of tendons allows them to resist rupture under normal loading capacity as well as handle compressive and shear forces when the tendon glides over the bony areas to utilise the moment arms, enabling the tendon to increase torque and transmit the kinetic energy to the bone.

Tendon tissue, when loaded, develops an internal resistance to loading or stress (σ), measured as force per unit area, while the deformation of the tissue is normally measured as strain (ϵ), defined as the change in length divided by the unloaded (rest) length (Whitting, et al., 2008a). The relationship between stress and strain operates according to Hooke's law, which suggests that in the normal operating regime stress and strain are linearly related (Whitting, et al., 2008a). The generalised stress-strain curve shown in Figure 2.2 illustrates the behaviour of the tendon (Pearson, 2010, Barfod, 2014). As the tendon experiences a gradually increasing tensile load, strains are developed due to the crimp structure of the collagen fibrils, but as this increases, the stress-strain curve becomes linear until the tendon starts failing, and microscopic tearing occurs (Pearson, 2010). If stress continued to increase, the tendon would ultimately rupture.

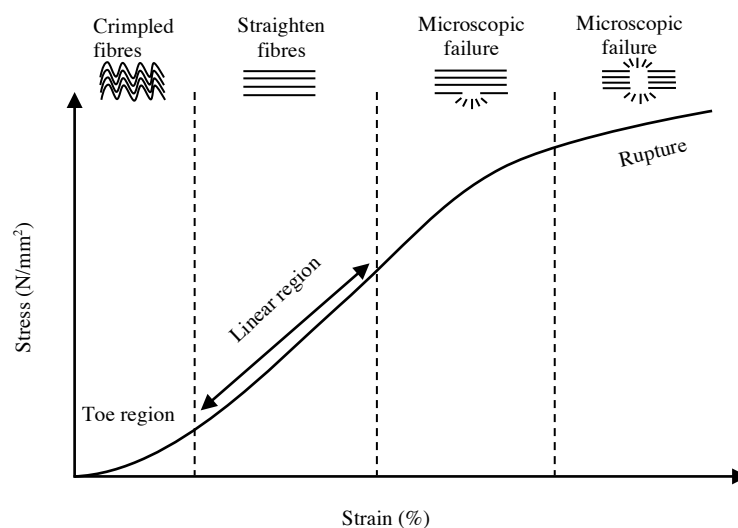


Figure 2.2: Generalised stress-strain ($\sigma - \epsilon$) curve illustrating the tendon behaviour (Barfod, 2014).

Figure 2.3 shows the slope of the curve represents the tendon stiffness and usually associated with the tendons' efficiency in storing and releasing energy (see Figure 2.3) (Barfod, 2014). The energy is released as it deforms during unloading. The ability of the tendon to store energy is the area under the loading stress-strain curve (Barfod, 2014). When unloaded the elastic property of the tendon releases its energy as it deforms (Whitting, et al., 2008a). However, energy loss (usually as heat energy) may occur when unloading and its recoil curve does not follow the same path as its loading curve (Whitting, et al., 2008a).

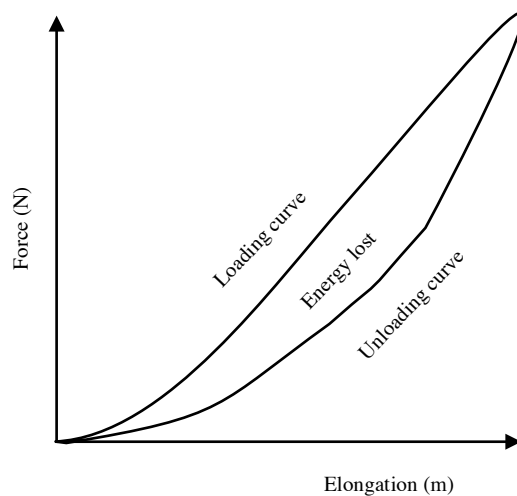


Figure 2.3: A schematic illustration of energy absorption in a tendon during the coil-recoil process (Barfod, 2014).

The ability of the tendon to store and release energy is extremely important for the stretch-shortening cycle; enabling movement to be carried out with higher efficiency than if the tendon did not stretch and then shorten (Barfod, 2014). An example of this could be where an athlete is sprinting or jumping, causing the tendon to store energy during stretch and releasing it during the shortening recoil period, thus giving potential increase of the power components as in jumping as or in running. The tendon also reduces the elastic strain energy by the muscle.

The mechanical properties of tendon can also affect the length of the contractile component of muscle (Pearson, 2010) and is described by its length-tension curve (see Figure 2.4) (Pearson, 2010). Here, muscle shortening occurs when a more compliant tendon is stretched under load, thus reduces the muscle force

generating capacity. However, any small increase or decrease in muscle length results in a large reduction in force generating capacity (Pearson, 2010).

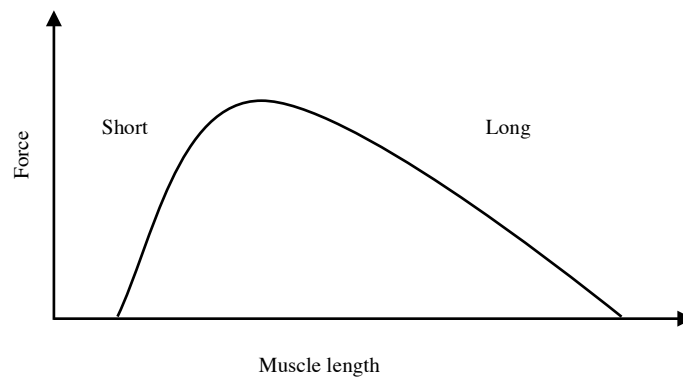


Figure 2.4: Illustration of length-tension relationship of skeletal muscle (Pearson, 2010).

Tendons are also adaptable to both training and disuse, where with exercise tendons can adapt to greater loads by becoming larger. Exercise increases the number and size of collagen fibrils and increases the cross-sectional area of the tendon when compared to a tendon without controlled training applied (Kjaer, 2004). It is also believed that exercises can lead to increased collagen synthesis and increased number of fibroblasts (Kjær, et al., 2006). Tendon disuse leads to rapid deterioration in tendon mechanical properties, which causes a net loss in strength and stiffness, leading to non-uniform orientation of the collagen fibrils, and a reduction of collagen cross links and extracellular water (Maganaris, C.N., et al., 2006).

2.1.3 Tendon Injury and Risk

In general, tendon injury can be described as damage caused by physical trauma sustained by the tendon, and the severity of injury depends to the amount of damage sustained (Whitting, et al., 2008b). Furthermore, in mild and moderate injuries, the tendon structure is partially disrupted, but although damaged, it is still able to accept load with a smaller magnitude than before the injury (Whitting, et al., 2008b). Complete failure of the tendon structure leads to inability to transmit load. Injuries that are minor and are ignored, with repeated loading may progress to more

severe injuries. Improper and inadequate treatment may also contribute to a more severe injury. This has an obvious implication for a range of activities ranging from normal activities that require movement to athletic performance where high levels of force and rate of force development are required (Pearson, 2010).

Tendon injury can result from a single insult (acute injury) or long-term abuse due to repeating loads (chronic injury) (Whitting, et al., 2008b). There are two factors leading to these injuries, referred to as either intrinsic or extrinsic (Lee, et al., 2008b, Pearson, 2010). Intrinsic is an injury caused by forces generated within the body such as tendonitis, muscle tears, ligament strains and stress fractures, while extrinsic is a type of injury caused by forces outside the body such as impact or contact caused by another person, inadequate equipment or training, or some other environmental factor (Sharma, et al., 2006, Seitz, et al., 2011).

2.1.3.1 Acute Tendon Injury

A complete or partial rupture of the tendon structure gives rise to an acute tendon injury. The injury usually occurs when a sudden force or torque applied to the tendon, resulting in a partial or complete tear to the tissue structure (Sharma, et al., 2006, Pearson, 2010). However, it has also been reported that there may be an intrinsic factor when strenuous activity is routinely carried out as cumulative damage may occur leading to a catastrophic failure to the tissue (Pearson, 2010).

Study reported that tendon injuries occurred more often to males than females (Clayton, et al., 2008). However, it is unclear if this is due to more participation in sport by males, which may explain a higher risk exposure to tendon injuries. A comparison between male and female showed that with similar strain limits, for a given force, females show a higher musculoskeletal injury risk with respect to the lower limb (Onambele, et al., 2007). This increase in injury risk may be associated with differences in stiffness of lower limb between the genders (Onambele, et al., 2007). It is also reported that certain classes of drugs can affect the collagen tissue directly, leading to weakened structures that may rupture under high loading

conditions (Sode, et al., 2007). Anabolic steroids are also shown to have an affect on the collagen matrix, which increased the abnormality and function of the connective tissue and tendon simply cannot keep pace and succumbs to injury. Recent evidence has indicated that certain specific gene polymorphisms may relate to tendon injuries. Each gene code plays specific roles to the structural component of the tendon and may be the cause for tendon injury rates (Mokone, et al., 2005, Mokone, et al., 2006).

There has been no agreement about the optimal method for repair and subsequent rehabilitation treatment of tendon ruptures (Pearson, 2010). However, there is increasing evidence to suggest that surgery treatment for active and able individuals may provide better functional capacity over non-operative options while, for less active individuals, non-invasive treatment may be encouraged (Pearson, 2010). Rehabilitation protocols may help for optimal healing after surgery, and with the use of ultrasound and magnetic resonance imaging (see Figure 2.5), an insight into the mechanical property of the injured tendon can be observed in vivo, and further rehabilitation can be planned and carried out.

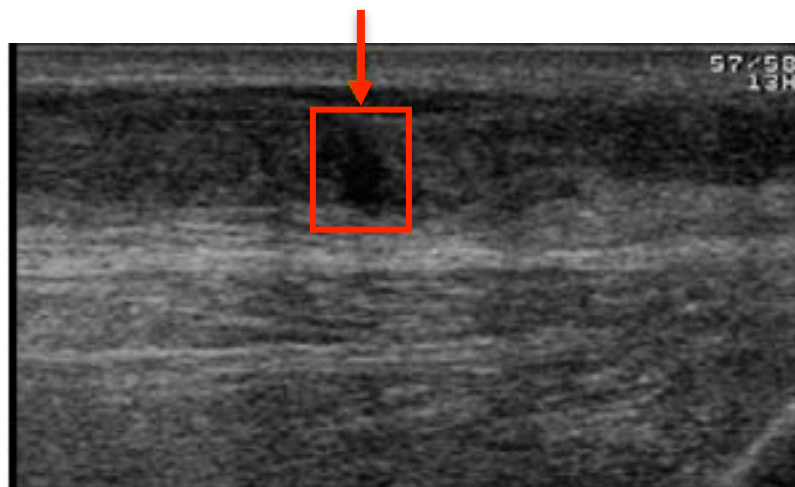


Figure 2.5: Example of tendon rupture with arrow indicating the rupture area (from <http://www.ultrasoundcases.info/>).

2.1.3.2 Chronic Tendon Injury

Chronic tendon injury is usually associated with overuse or degeneration of tendon. An overloaded tendon may become inflamed and lead to tendonitis, where the tendon is experiencing short-term inflammation and responds to treatments such as ice, reduction of activity, anti-inflammatory medications and physical treatment. If an injured tendon is repeatedly by overloaded, tendinopathy may develop where the tendon structure begins to minor rupture or tear, but becomes thickened and weakened with a range of chemicals released, which causes the inflammation. At this time, the blood supply required to provide necessary healing components is insufficient, and so the tendon may fail to recover from the trauma.

Some tendinopathy shows a high concentration of blood supply to the tendon with no association to a healing response (Sharma,et al., 2005). Previous study suggested that overuse injuries to the patella may be caused by tensile loading which affected the performance of the patella tendon and the angle of the knee for maximal loading, indicating localised tendon strain (Almekinders, et al., 1994, Almekinders, et al., 2002). Classically, tendinopathy pain has been attributed to inflammation; however, a recent study showed (Sharma, et al., 2006) that chronically painful Achilles and patella tendons show no indication of inflammation and many of the damaged tendon that are detectable on MRI or ultrasound are not painful. The pain, however, may originate from the mechanical breakdown of collagens (Sharma et al., 2006).

Medical imaging techniques such as MRI and ultrasound allow for the quantification of tendinopathy diagnosis, and these are typically used to determine tendon anomalies. Ultrasound has been used to characterise three different levels of tendinopathy (Archambault et al. 1998) (see Figure 2.6).

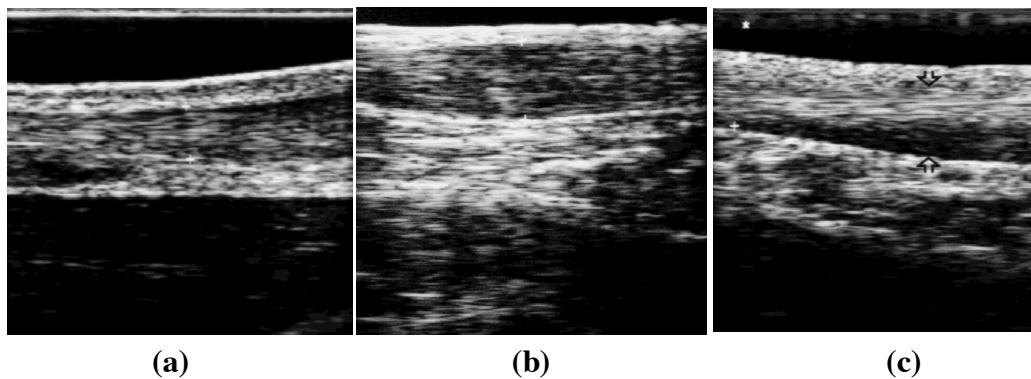


Figure 2.6: Different levels of tendinopathy illustrating (a) normal tendon, (b) enlarged tendon areas, and (c) Hypoechoic areas (Archambault et al. 1998).

To summarise, the tendon plays key roles for body motion, enabling the use of the muscle to transmit forces. However, the tendon can be injured either by external forces disrupting the mechanical behaviour of the tendon or internally due to excessive or sudden force to the tendon structure which leads to complete tendon rupture. Diagnosis with the aid of medical imaging has been utilised to observe tendon healing and to detect inflammation or damage for further rehabilitation. However, understanding of the aetiology of Tendinopathy is poor and as such treatment and rehabilitation modalities are not well defined.

2.2 Medical Imaging in Biomedical Applications

Medical imaging is widely used to provide information for giving clinical diagnosis, and by using the radiography technique and examination of the human body anatomy provides further understanding of their characteristics, non-invasively. The diagnostic radiography enables the acquisition of diagnostic information by the radiologist. The evaluation of bone structure, blood flow, cardiology, muscle and tendon are among those that benefit from the use of medical imaging procedures. There are several modalities that are currently available, including medical X-ray imaging, bone scintigraphy imaging, computed tomography (CT) scan, magnetic resonance imaging (MRI) and ultrasound imaging. These are described briefly in the

following sections, although since the thesis focuses on the use of ultrasound, its procedures are described extensively.

2.2.1 X-ray Imaging

X-ray imaging is a painless procedure that uses the ionising radiation to produce images of the inside of the body non-invasively, and is typically used to look at the bone structure. It helps diagnosis of disease and monitoring treatment. For example, X-rays can be used to view the bone fractures, dental decay, bone disease and tumours. X-rays are also useful in viewing the catheter tube being inserted into blood vessel to widen blocked coronary arteries. In some cases, X-rays are used together with a special fluid injected through the blood stream or swallowed before an X-ray is taken to highlight the tiniest details of the body structure such as the arteries. The images produced using X-rays show the parts of the body anatomy in different shades of black and white due to the different tissues absorbing different amounts of radiation. So, with X-ray imaging it will be difficult to produce a clear image of the fat and soft tissue (e.g. muscle and tendon) compared to the bone, where the calcium in the bone absorbs X-rays the most. Figure 2.7 shows examples of X-ray images taken at the part of upper and lower leg. The health risk using the X-ray is very low, although, high doses of the radiation may risk development of cancer.



Figure 2.7: Example of an X-ray of the medial upper leg visualising (a) the patella (kneecap), femur and tibia, and the X-ray of the lateral lower leg (b) the tibia, fibula and the calcaneus (from <http://www.ultrasoundcases.info>).

2.2.2 Bone Scintigraphy Imaging

Bone scintigraphy involves scanning the bone structure from the injection of a radioactive material known as technetium-99m (TC) methylene diphosphonate (MDP) into the blood vein of the arm, hand or foot. The scintillation camera produces a two-dimensional scintigraphy image of the bone from the emitted gamma rays (see Figure 2.8). The radioactive material can be seen clearly around the area where new bone tissue is formed (ossification) which is useful to detect lesions such as tumours, stress fractures, and infections. The radioactive material used in this procedure does pose health risk and leaves the body through kidneys and bladder in urine. When compared to X-rays, this method can detect bony abnormalities faster; however, it is unable to detect any changes of the soft tissue (Kahn, et al., 1987).

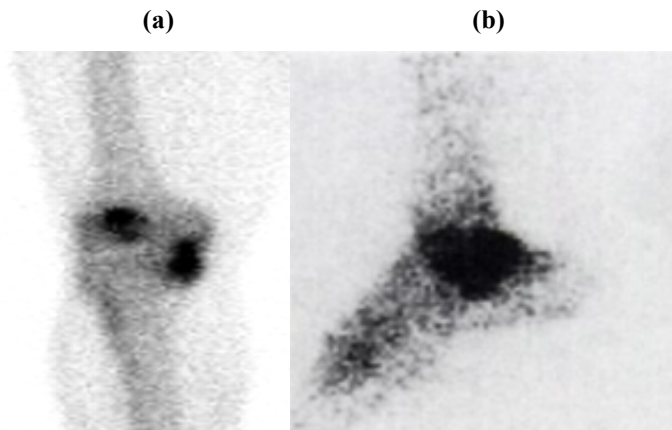


Figure 2.8: Example of bone scintigraphy imaging of the medial upper leg visualising (a) the patella (kneecap), femur and tibia, and the lateral lower leg (from <http://imgkid.com/bone-scan-images.shtml>) (b) the tibia, fibula and the calcaneus (Karasick, 1996).

2.2.3 Computer Tomography (CT) Scan

Computer tomography (CT) scanners use X-rays and computer technology to produce tomographic images, which take the form of cross-sectional slices of the scanned parts of the body allowing non-invasive insight of the body. The CT scanner consists of an X-ray source that rotates around the patient's body, and the bed where

the patient lies down is moved at a constant speed past the X-ray detector to image the designated part of the body. The image will then meshed together using digital reconstruction techniques to generate a 3D image of the scanned part of the body, CT scan offers better contrast resolution in soft tissue compared to the conventional X-Ray imaging. Figure 2.9 shows examples of CT images of upper and lower leg with each leg viewed either in lateral or axial (sliced) position.

CT scans are mainly used for screening diseases such as cancer, and detecting acute and chronic changes in the lung and diagnosing abdominal diseases. The advantages of CT scan over other 2D imaging techniques is that it produces high-contrast images, can show different layers of the tissue and can be viewed in the axial, coronal or sagittal planes, which when combined can be viewed as volumetric representation of the body. However, the quality of the finer details of the soft tissue are still not as good as to the images produced using MRI and ultrasound imaging, which are described in the following sections. The radiation risk of a CT scan is higher than X-ray due to higher dosage of ionising radiation.

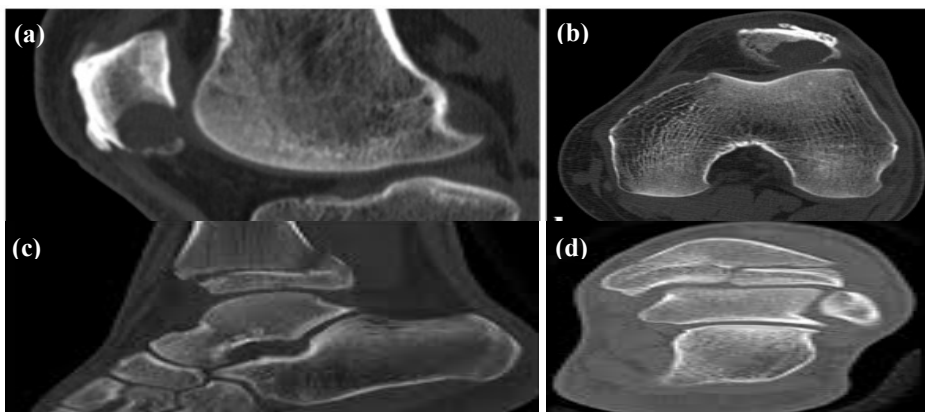


Figure 2.9: CT images of the lateral upper leg visualising (a) the patella (kneecap) with its (b) axial view and (c) the tibia, fibula and calcaneus with its axial view (d). (Balke, et. al, 2010)

2.2.4 Magnetic Resonance Imaging (MRI)

Magnetic resonance imaging (MRI) is a painless and safe medical imaging procedure that uses strong magnetic fields and radio waves to produce images of the

inside of the body with high spatial resolution with both bones, and soft tissues clearly visible. Unlike CT scans, MRI does not contain ionizing radiation although a standard MRI scanner normally consists of a fairly long tube or tunnel, which some patients might find claustrophobic. However, just like CT scan, MRI can produce virtual slices of the scanned body part in detail and can be viewed in three-dimensions (Figure 2.10).

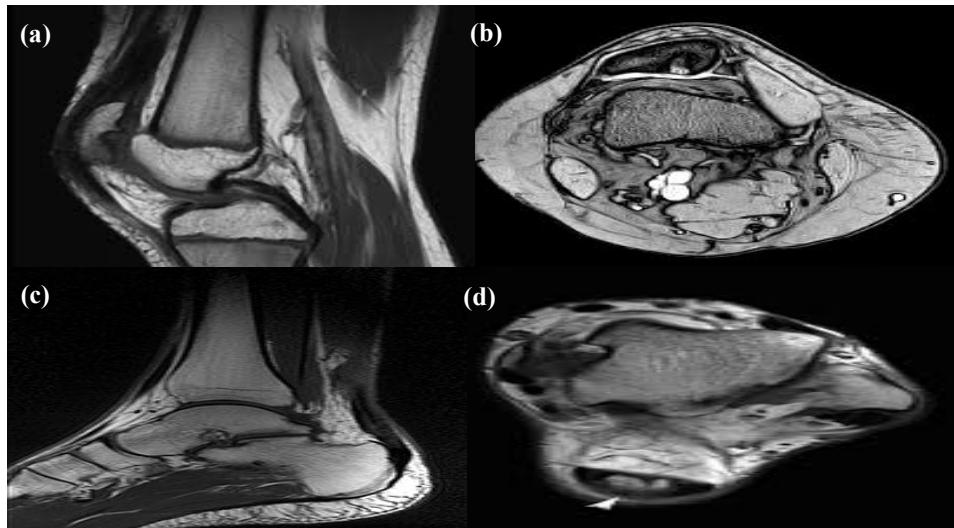


Figure 2.10: Examples of MRI images of the lateral upper leg visualising (a) the patella (kneecap) with its (b) axial view (from http://www.garylongmuir.com/quality-reports/knee_mri/) and (c) the tibia, fibula and the calcaneus with its axial view (d) (from <http://mrimusculoskeletalsection.blogspot.com/>).

MRI operates by sending a short burst of radio waves to designated areas of the body. The human body is made up primarily of water molecules, which consist of hydrogen and oxygen atoms and a proton sits at the centre of each hydrogen atom. The radio waves transmitted by the MRI knock these proton particles out of alignment and gets realign when the radio waves are turned off which is then picked up by the MRI receivers. The realignment of the protons provides information about the environment of the body. The speed of the realignment of the protons depends on the types of tissue, producing images of various types of the tissue in the body that are distinguishable.

MRI is widely used in many medical applications, particularly for investigating the brain for neurological cancers, and investigates brain activities,

assessment of various heart disease and functions, and assessment of joint disease and soft tissue tumours. MRI is also used for detecting and charactering lesions in various other internal organs. Compared to ultrasound imaging, MRI requires the patient to remain very still, thus dynamic testing and investigating of the soft tissue when put under stress is impossible. However, a special type of MRI (Cardiac MRI) is used to capture both still and moving image of the heart and blood vessels.

2.2.5 Ultrasound Imaging

Ultrasound imaging is a technique that involves propagating ultrasound pulses into tissue to visualise internal body structures such as tendons, muscles, joints, vessels and other internal organs by detecting their reflections. These ultrasound pulses consist of high-frequency sound waves generated from an ultrasound transducer (probe) and travel through body tissue. The different tissues absorb sound waves differently, and partial reflection of the body tissue occurs depending on the type of the tissue. The amount energy being reflected at different depths will have different amplitudes and the time of arrival of the reflected wave is proportional to the depth (see figure 2.11).

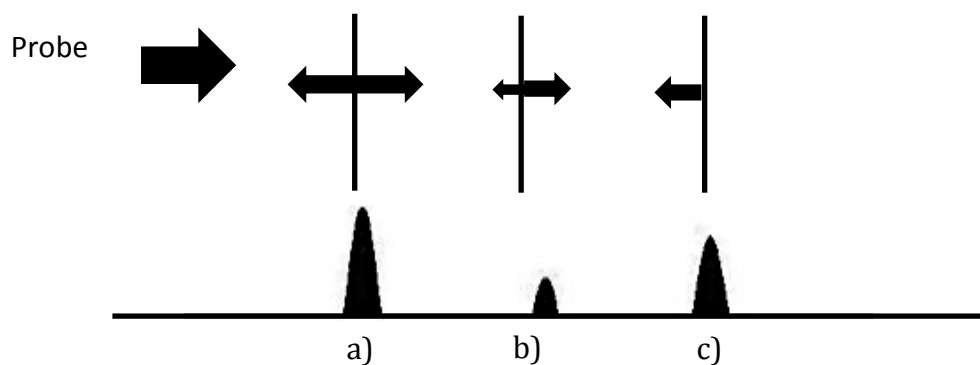


Figure 2.11: An illustration of ultrasound sound waves emitted in pulses from the probe transducer and being reflected at 'a', 'b' and 'c'. The reflected pulse gives information of the reflected signal measured in amplitude and the time it takes to reach the probe. The incoming wave at 'a' is the full amplitude, while the incoming wave at 'b' is the wave transmitted through 'a'. The incoming wave at 'c' transmitted from 'b' [Støylen, 2010].

The reflected structures normally scatter around in more than one direction. Figure 2.12 show that the amount of scattering depends on the reflection coefficient and direction of the reflected signals. If the reflecting surface is perpendicular to the ultrasound beam, more regular scattering will be produced compared to the scattering produced from irregular position of the surface where only portion of the scattering will reach back to the probe resulting in very low amplitude signals (Støylen, 2010).

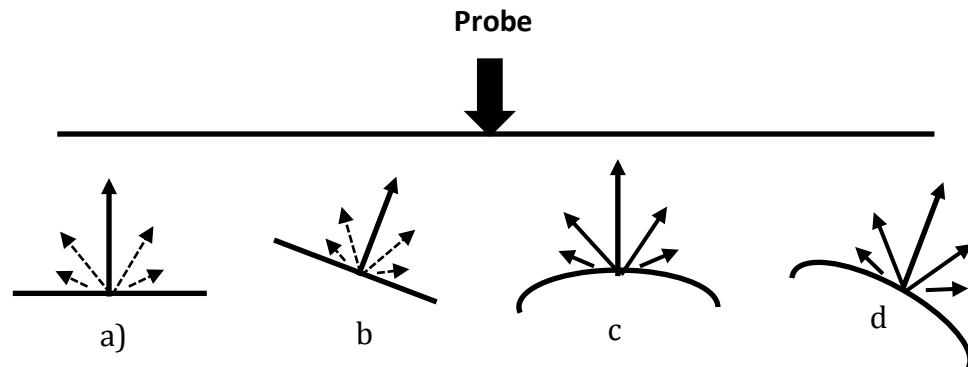


Figure 2.12: The positioning of the structure surface determines the directions of the scattering [Støylen, 2010].

For a curved surface, more energy being spread out in different directions, giving a lower amplitude signal oriented toward the probe beam, however if the curved surface is tilted towards the probe, more energy will be reflected. The reflected energy shows the density of the tissue when applying it to the muscle tissue (Støylen, 2010).

Tissues with high density will cause attenuation shadows while low density will appear brighter. This is simply because the wave energy being scattered or reflected will get attenuated when passing through tissue, which is a necessary technique building an image with various different density. An image is also built up from the result of the probe firing the sound wave beam vertically and waits for the returning sound wave. While maintaining the previous information, the probe fires a new line in a sequence of B-mode lines (Støylen, 2010). The reflected waves coming with random phases and amplitudes and tends to produce a uniquely random interference pattern known as speckle noise that scales from zero to maximum depending whether it is destructive or constructive (Oleg et. al., 2006).

The speckle patterns are seen as grayscale and the statistics of the speckle, can be useful to differentiate different compositions of the tissue, however, it is known that speckle noise tends to reduce the image contrast, obscure and blur image details, and hence decrease the quality and reliability of the tissue image (Wagner et. al., 1983, Sehgal, 1993). In comparison, speckle image from the ultrasound imaging does not produce images as good as the CT scan or MRI. The images produced using this technique are usually represented in greyscale and normally viewed as 2D images. However, recent advancement has introduced 3D ultrasound imaging using special types of transducer to capture the reflected echo-pulses at different angles, which are processed by a computer to reconstruct 3D images of volumes of the tissue.

Ultrasound equipment is less expensive and more portable in comparison to the other medical imaging modalities. It is also simple to use and able to produce a real-time moving image which is suitable for dynamic testing. The use of ultrasound imaging can be found in many areas of medical applications. For example, echocardiography is used to produce images of the heart structure, which is useful for diagnosing known heart diseases non-invasively (Stoylen, et al., 1999, Linguraru, et al., 2008). Medical ultrasound imaging is also widely used to diagnose various internal organs and is particularly useful for pregnant patients. Another usage of ultrasound can be found for diagnosing blood flow in the artery (Trahey, et al., 1988, Ophir, et al., 1999). The blood flow velocity is recorded by emitting a high-pitched sound wave from the probe, and at a specific frequency, the speed of the blood causes a frequency shift where the frequency is increased or decreased. The changed frequency of the blood flow is normally represented in colours by using colour Doppler technique (Gill, 1985, Pellerito, et al., 2012).

Ultrasound is also widely used for assessing and diagnosing the human musculoskeletal system that includes the bone, muscles, cartilage, tendons, ligament, joints and other connective tissues. Recent advancements have used feature recognition and segmentation algorithms to assess the deformable structures of each organ of the ultrasound medical imaging, which helps the physiologist to understand further its functions, diagnose diseases (Yeung, et al., 1998, Dilley, et al., 2001, Sharma, et al., 2010). These algorithms will be discussed further in detail. For this study, the availability of the ultrasound equipment, dynamic testing of the human

anatomy, cost and ease of use are the main factors as to why the ultrasound imaging was selected to be the means of data acquisition in this study. Figure 2.13 shows some of the examples of ultrasound imaging used in medical applications.

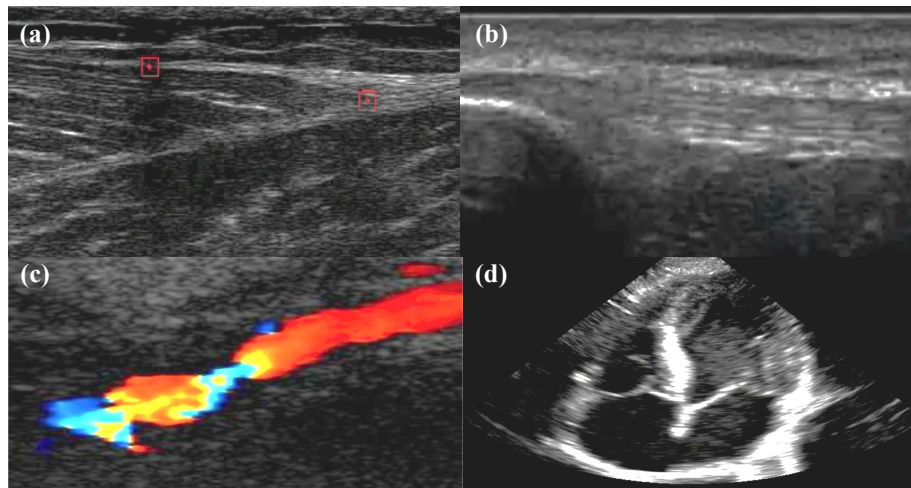


Figure 2.13: Examples of ultrasound images of (a) Achilles tendon, (b) patella tendon (c) (from <http://philschatz.com/physics-book/>) blood flow of neck arteries (d) heart structure (from <http://emergencyultrasoundteaching.com>).

Ultrasound imaging has been used in medical applications with an excellent safety record. Compared to X-rays and CT scans, it does not contain ionising radiation and the patient does not need to be injected with a radioactive element to emit the gamma rays used in bone scintigraphy technique. However, there are some slight effects when the ultrasonic sound wave enters the body that may heat the tissue slightly (Hayes, et al., 2004). Ultrasound scanner can operate at various operational modes. The mode is the state that is being operated using a method of channelling the sound pulses to the parts of the body such as the arterial system, heart, spinal cord, joint, and more. The common modes used in ultrasound applications are the A, B and M-mode. Each mode gives different types of results, and the chosen mode depends on the medical condition being investigated.

2.2.5.1 A-mode (Amplitude)

The simplest ultrasound mode is the A-mode, which scan the object with only a single line of sight from the transducer, and displays the amplitude spikes of different heights showing the range of the reflector. The transmitted sound pulses pass through tissues of difference consistency and hardness producing a spike like amplitude. This mode is used to measure the depth of organ. Figure 2.14 shows an example of A-mode display, where x represents the time taken after the sound pulse and y represents the amplitude of the amplified and demodulated echoes measure at that time. The amplitude peaks A and B indicate the spatial position of the object from the position of the transducer front face.

The amplitude spike represents the sharp boundary (e.g. bone), while a steady low line represents the homogenous structure (e.g. inside muscle). The real disadvantages of this mode of imaging are that it is hard to exactly know what the object generating the echo looks like, and knowing the exact direction of the object is impossible.

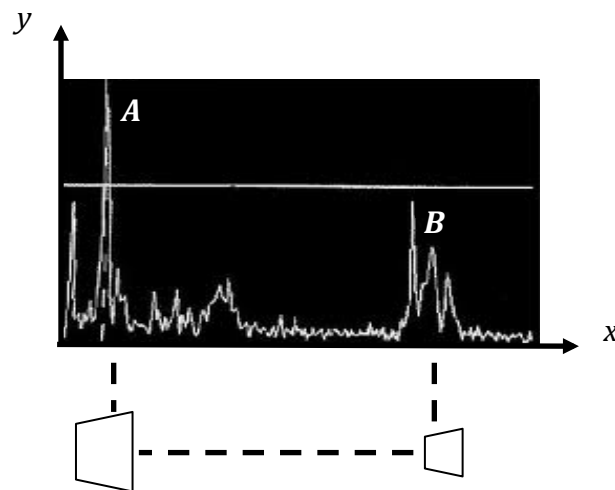


Figure 2.14: Example of an A-Mode image with y -axis represents the amplitude and x -axis represents the depth. The amplitude spikes of A and B represents the boundaries of solid objects found (from http://www.battlesnake.co.uk/_uni/ultra.htm).

2.2.5.2 B-mode (Brightness)

B-Mode imaging is the most common form of ultrasound imaging and uses brightness intensity as its base instead of vertical spikes. The transducer transmits a series of short pulses at regular intervals and in between listens for the reflected echoes. The time taken for each pulse to travel and reflected in between determines the distance of the reflector. The ultrasound machine then calculates the captured echoes by computing the distance from the probe to the reflector using the speed of sound of the tissue and the time taken of each echoes return. The intensity of the echoes depends on how much of the pulses' energy are reflected by the tissue.

The intensity of the echoes is represented in the form of random speckles consisting of large and small dots with different shades of grey, resembling the variations in the texture of internal organs. The calculated distances and intensities of the echoes are then formed to a viewable 2D map of grey scale of ultrasound image on the screen. The displayed image consists of 2D x,y coordinates of where the x-axis representing horizontal length of the transducer and y-axis as representing the depth (Figure 2.15).

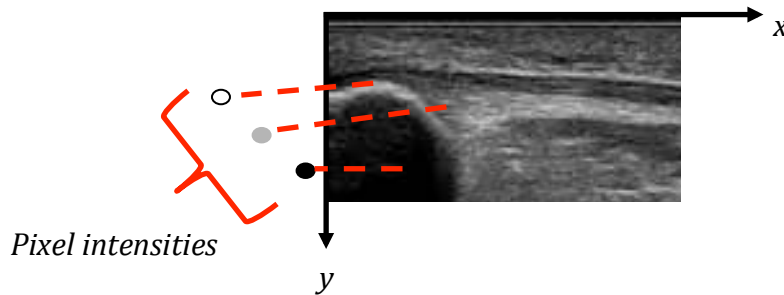


Figure 2.15: Example of a B-mode image with small dots at (x,y) coordinates representing the echo intensity with different shades of grey.

The different shades of grey represent the energy of the reflected pulses, giving sense the appearance of the tissue such as the skin to appear as smooth and bright, both fat and muscle appears to be bright or dark and tendons are typically bright. The bone structure can be identified as speckles of white dots while soft

tissues such as tendons are seen with various shades of greys speckle formations and fluids are seen as black. B-mode has the advantage over A-mode in that the direction and the shape of an object can be viewed in real-time.

Each complete scan is arranged into a series of frames within a timeline. Usage of B-mode ultrasound imaging has intensified over time and can be found in many medical applications for diagnostic purposes such as the evaluation of fetus development and other organs. B-Mode is also fast enough to capture real-time motion and is used to evaluate the motion of organs. Due to its wide use and availability, the ultrasound equipment used for this study is the B-mode imaging.

2.2.5.3 M-mode (Motion)

M-mode ultrasound imaging is a technique of displaying one-dimensional data to analyse moving body parts with depth and time. The procedure is achieved by transmitting a single sound beam from the ultrasound probe transducer with a moving reflector and recording the reflected echoes. The reflected echoes are presented along the y-axis, which essentially represents the depth of the tissue, while the x-axis represents time. Figure 2.16 shows the movements of a heart valve in cardiac imaging (Støylen, 2010). Because of its high sampling frequency (up to 1000 pulses per second), M-mode is useful in assessing the rates and motion, which are also useful to diagnose cardiac movement, as well as fetus development.

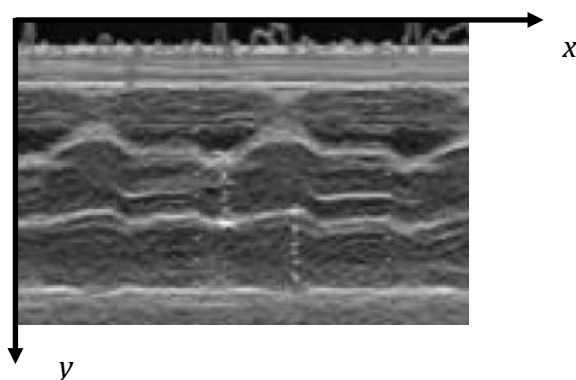


Figure 2.16: Example of a M-mode image shows a wave-like motion where y-axis representing the depth of the tissue and x-axis represents the movement over time.

2.2.5.4 Doppler Based Ultrasound Imaging

There are other types of ultrasound technique used in medical applications such as the Colour Flow Doppler Imaging (CFI), Pulse Wave Doppler (PWD), Continuous Wave Doppler (CWD) and Tissue Doppler. In contrast to traditional ultrasound imaging where the sound waves reflect the tissue, the sound waves in Doppler imaging are reflected off moving objects, such as blood, and are usually used to measure its flow and speed.

The CFI mode uses these Doppler waves and represents the reflecting echoes by colours superimposed on the 2D image (see Figure 2.17a). The colours are usually notated as red for flow coming toward the transducer probe and blue notated as flow moving away from the probe. CFI suffers the disadvantage of lower frame rate when compared to the standard ultrasound mode due to its technique of acquiring data sequentially one line at a time and transmitting many pulses in each scan line to generate these colours.

The PWD mode uses the Doppler pulses to transmit and to receive its reflection within a preset delay. The image produced contains a cursor showing the sample volume placed over the 2-D image at the region of interest (see Figure 2.17b). PWD has the disadvantage of being unable to measure high-velocity movement accurately and suffers from image aliasing, where different signals wrap around the waveform signals as noise, making it indistinguishable from noise that may exist in the signals.

The CWD mode in the other hand uses two parts of the transducer, one continuously transmitting the pulses, and the other continuously receiving the Doppler signals. The image produced contains an indicator placed on the image showing the continuity of the signals along the scan line (see Figure 2.17c). CWD gives good resolution of high velocities when compared to PWD, but unlike the standard ultrasound method, it does not give any information of the location of the signal.

The final example of Doppler mode imaging is Tissue Doppler imaging. This mode is normally used to measure the velocities of tissue movement. The velocity

rate used in this mode is lower than the one used in PWD mode, which is used to measure the velocity of blood flow. The image produced contains regions of interest placed on the image representing the sample volume and Doppler waveforms showing the velocities of the tissue movement (see Figure 2.17d).

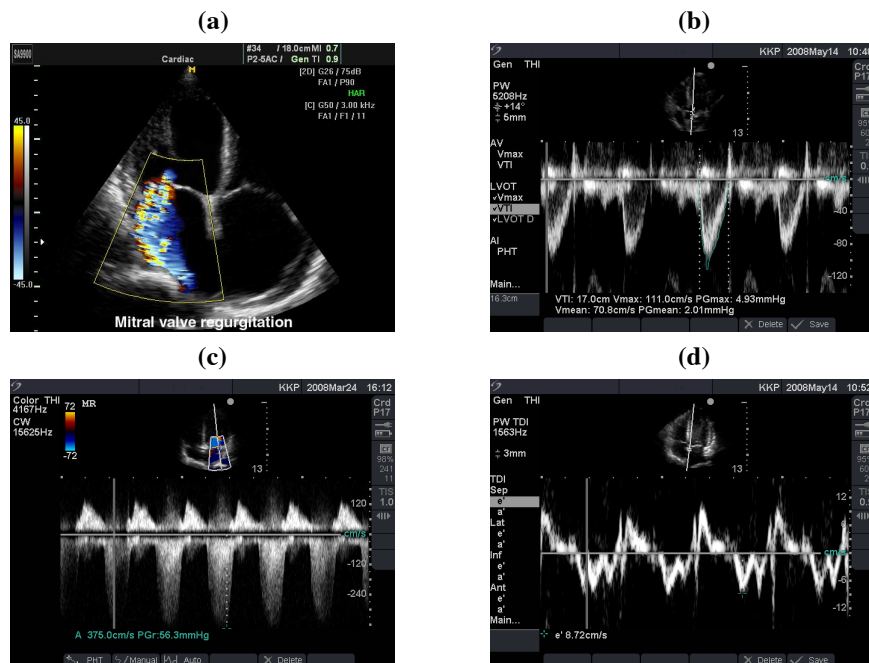


Figure 2.17: Examples of Doppler based ultrasound imaging. **(a)** Colour Flow Doppler Imaging (CFI), **(b)** Pulse Wave Doppler (PWD), **(c)** Continuous Wave Doppler (CWD) and **(d)** Tissue Doppler imaging (from <http://www.criticalecho.com/content/tutorial-2-modes-ultrasound>).

As indicated above, each of these modes is suited to specific medical applications. However, for tracking the tendon tissue, the B-Mode is the preferred option as it has the advantage of producing real-time images with a sampling rate that is suitable for tissue evaluation and can be carried out repeatedly. Also, the B-Mode to be the only mode that displays the location of the tissue with high resolution image which enhances the clarity of the image, and this is particularly useful for tracking tissue motion within an area of interest of the tissue. Furthermore, when using B-mode ultrasound imaging, the image can be produced in three different planes (sagittal, frontal or transverse) depending on the anatomical position of human body (see Figure 2.18). Thus, the image produced can be viewed either as lateral view

(frontal), anterior view (sagittal) or cross section view (transverse), which gives better understanding of the properties and functions of the tissues.

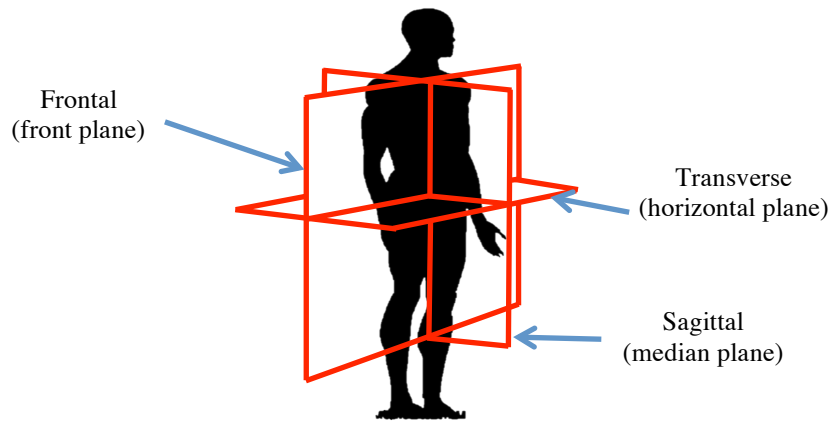


Figure 2.18: Three primary planes illustrated from anatomical position of human body.

Both A-mode and M-mode produce images that show only motion and its depth without the necessary shape of the body organs and its locations under the muscle area. The Doppler imaging modes however, gave extra information of flow movement with colours and sampling rate, but with the expense of images being reduced to a lower frame rate and no indication of the location of the signals.

In this Chapter it has been shown that B-mode ultrasound imaging and MRI produce image with higher resolution than the other imaging techniques. However, MRI scanners are costly and incapable of real-time scanning of body organ, whereas B-Mode ultrasound imaging is cheaper, portable, and provides good enough image resolution with real-time observation. Figure 2.19 illustrates the sample images of B-mode ultrasound imaging of lower limb at scanned over sagittal plane of the body showing the location of tendon at both knee and ankle.

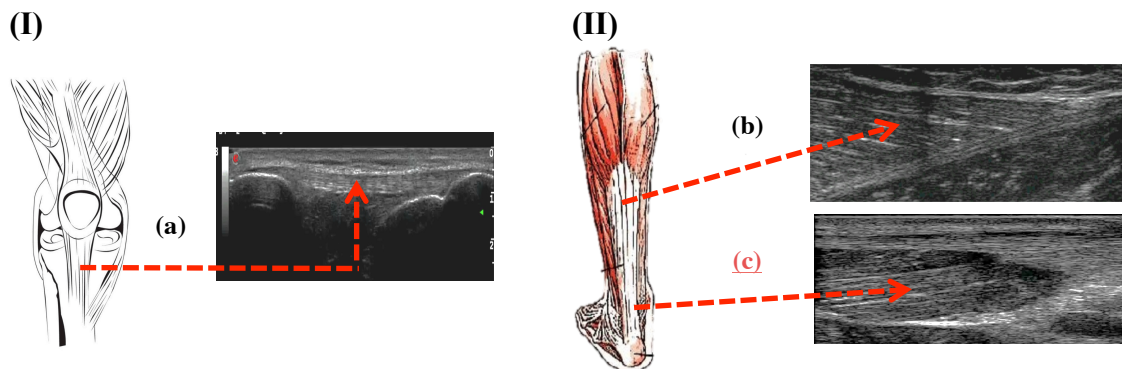


Figure 2.19: B-mode image of the knee (from Knee Pro III, 3D4Medical.com) **(I)** with the patella tendon **(a)**, and **(II)** the ankle (from <http://achillestendon.com/>) with tendons at gastrocnemius **(b)** and Achilles **(c)**

2.3 Ultrasound Speckle Tracking and Its Clinical Applications

The B-Mode image contains unique random speckle patterns, which are formed by the interference patterns of the waves reflected from the tissue structure. These patterns are deterministic, but they are not correlated to the structures in the image (Anderson, et al., 2006), which greatly reduces the ability to detect features in the image (Bamber, et al., 1986). Tracking the speckle movement has become a widely used method for accessing strain in 2D ultrasound imaging (Kaluzynski, et al., 2001, Helle-Valle, et al., 2005) and mainly found in studies related to the fluid flows and deformation of tissue organs. Such examples can be found in the related studies such as estimating the blood flow velocity (Chen, et al., 1989, Bohs, et al., 2000, Vray, et al., 2004), assessing the function of the heart (Suhling, et al., 2005, Vahid, et al., 2007, Vahid, et al., 2008), assessing the function of other tissue organs for cancer and tumours (Fabio, et al., 2006, Jonathan, et al., 2012), and analysis of tendon tissue working mechanisms for rehabilitation and injury prevention (Maganaris, C. N., et al., 1998, Yeung, et al., 1998, Dilley, et al., 2001).

Measuring the moving objects from 2D speckle patterns was first reported by Robinson, et al. (1982) who were interested in determining the velocity of propagation of ultrasound in tissue, and used cross-correlation to detect the apparent

shift within the region of interest. Later in 1987 this method was used for detection of blood flow (Trahey, et al., 1988). Then, the use of speckle tracking moved to track elasticity to assess stiffness and strain in various biological tissues to recognise diseases such as cancer (Fabio, et al., 2006, Jonathan, et al., 2012) and cardiovascular diseases (Fung, 1993, Suhling, et al., 2004, Sahba, et al., 2008, Vahid, et al., 2008).

The advancement of the ultrasound machine to provide real-time strain imaging has enable researchers to study various parts of tissues and organs to detect tissue anomaly such as breast lesions (Garra, et al., 1997, Hall, et al., 2002) or coronary artery diseases (Biering-Sorensen, et al., 2014). Muscles and tendon tissues were also studied to understand its properties and functions to identify possible damage non-invasively (Dilley, et al., 2001, Loram, et al., 2006, Lee, S., et al., 2008a, Farron, et al., 2009). The deterministic property of the speckle pattern also represents the changes of the speckle indicating the movements and deformations of the underlying tissue (Meunier, 1998), which is therefore useful for the tracking algorithms to detect its movement.

Studies of tendon tissues had been conducted a long time before ultrasound techniques were used in medical diagnosis. Most were carried out in vitro from isolated animals or a cadaver (Bennet, et al., 1986, Lieber, et al., 1991) and only recently on living human material (Rigby, et al., 1959, Butler, et al., 1978, Greaves, et al., 2008). However, there have been only a few reports on tendon mechanical properties under maximal physiological load and most studies referred to animal material testing that does not represent the ideal references to living human tissues. The earliest work that examined the dynamic of human muscles looked at the relation between the production of heat and shortening of human muscle in vivo (Hill, 1938).

B-mode ultrasound imaging was able to give a clearer insight into the tendon properties that can be assessed and measured in vivo in real-time while the tendon was loaded via means of isometric muscle contraction. Since then ultrasound analysis has become increasingly popular to study and understand the working of tendon properties for both static and dynamic situations (Fukunaga, et al., 1996, Onambebe, et al., 2007, Jan-Wiebe, et al., 2010, Kim, et al., 2011, Yoshii, et al., 2011, Pearson, et al., 2012).

2.4 Motion Estimation of Speckle Tracking.

Observing the motion of tendon deformations in successive speckle images is not a straightforward task, images needed to be analysed on a frame-to-frame basis and thus require complex image processing calculations (Gonzalez, et. al., 2002). Conventionally, a trained eye is needed to be able to identify the actual movement of the localised tissue (Fukunaga, et al., 1996, Hansen, et al., 2006, Pearson, et al., 2007). The estimation of the motion between two frames in the context of 2D ultrasound imaging is known as speckle tracking. In general, subtracting 8-bit grayscale images can produce 512 values:

$$I(x,y) = I_1(x,y) - I_2(x,y) \quad (2.1)$$

where I is the image difference resulting from the subtraction of I_1 and I_2 . The measurement is the basic operation used for change detection where the difference between the two frames can be extracted to estimate motion (see Figure 2.20).

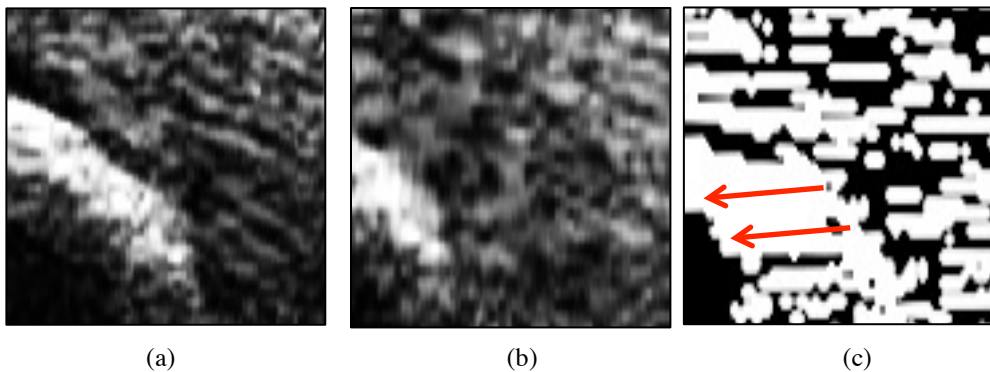


Figure 2.20: Illustration of two frames from a video sequence of a tendon, **(a)** is the initial frame, **(b)** is the next frame and **(c)** is the graphical representation of a displacement with arrows showing the motion vectors.

Several other improved methods have been proposed in the past for extracting motion between different images (Foresti, 1998, Dilley, et al., 2001, Loram, et al., 2006, Lee, S., et al., 2008a). These include block matching algorithm (BMA) methods (Zhu, et al., 1997, Barjatya, 2003) and gradient-based (optical flow) (Baker, et al., 2004, Bruhn, et al., 2005, Lee, S., et al., 2008a) methods. The BMA method finds

similar blocks between two image frames and assumes that intensity of the block between two frames is constant. The similarity between two blocks is based on the greyscale value of the image. There are many methods of observing the similarity such as Mean Square Error (MSE) (Revell, et al., 2004) and Normalised Cross Correlation (NCC) (Hii, et al., 2006). The searching strategy consists of exhaustive search, which is the oldest method, and newer searching strategies such as the steps search (3SS) and diamond search (Zhu, et al., 1997).

Another group of motion estimation methods is optical flow, which follows the movement of apparent objects such shapes, edges or surfaces within a virtual scene. Lucas-Kanade (Lucas, et al., 1981) and Horn-Schunck (Horn, et al., 1981) are the two most popular techniques used for the optical flow. These are similar to the BMA method in that both assume that the intensity is constant in consecutive frames. Figure 2.21 illustrates different types of motion estimation.

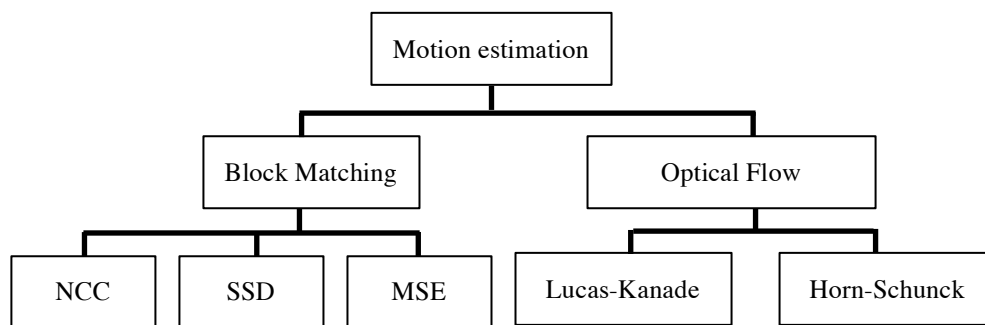


Figure 2.21: Different types of motion estimation techniques.

To improve the success of the motion estimation, the area to be tracked is defined by marking it manually and is usually referred to as the region of interest (ROI) and the selected area can be either bounded by rigid appearance (such as lines, corners, junctions) or non-rigid appearance (changing over time) (Kumar, et al., 2011). The ROI helps the algorithm to selectively process the desired subset of the image data for motion estimation (Kehtarnavaz, et al., 2006). A typical ROI for the tracking of localised tissue tends to undergo non-rigid transformation. The ROI usually contains a speckle pattern and is thus difficult to track (Dilley, et al., 2001, Korstanje, et al., 2010).

A reference landmark such as a tendon junction was used to improve the estimation of the tendon movement (Narici, et al., 2006, Lee, S., et al., 2008a). The displacement of the tissue is determined by locating the same unique pattern in consecutive frames (Hsu, et al., 2005). Most of the studies related to tendons use a single ROI marker with various range of ROI sizes to track the overall displacement of the tendon (Dilley, et al., 2001, Revell, J., et al., 2005, Lee, S., et al., 2008a), rather than looking at localised features of the tendon. The 2-ROI markers were used to observe the dynamic changes of the regional area of the tendon to calculate the localised stiffness and strain (Couppé, et al., 2008, Pearson, et al., 2012). The use of multiple ROIs to track multiple layers the tendon gave better comparisons between the layers (Pearson, et al., 2014).

2.4.1 Gradient Based Optical Flow

Optical flow is a method of following the motion of object pixels (i.e. shapes, surfaces, and edges) in a visual scene. It works by sampling spatially and temporally the light of two image frames so that a sequence of motion is generated. It is typically used in robotic applications to detect and to track an object. The application is customarily found in motion compensation and compression to track every pixel in a moving image so that estimating the motion between two video frames can be achieved. In a tissue motion application, the optical flow is commonly used to compute the dense displacement field on the assumption that the image intensities remain constant over time. An optical flow method calculates the motion between two image frames, which are taken at times t and $t + 1$ at every pixel location.

Figure 2.22 illustrates the basic concept of optical flow where motion of an object between two frames can be observed. Here, the object of interest located at coordinate (x,y) at time t moves to a new coordinate of $(x + u, y + v)$ in Frame 2 at time $t + 1$. The displacement (u,v) is used to calculate the velocity vector of the optical flow.

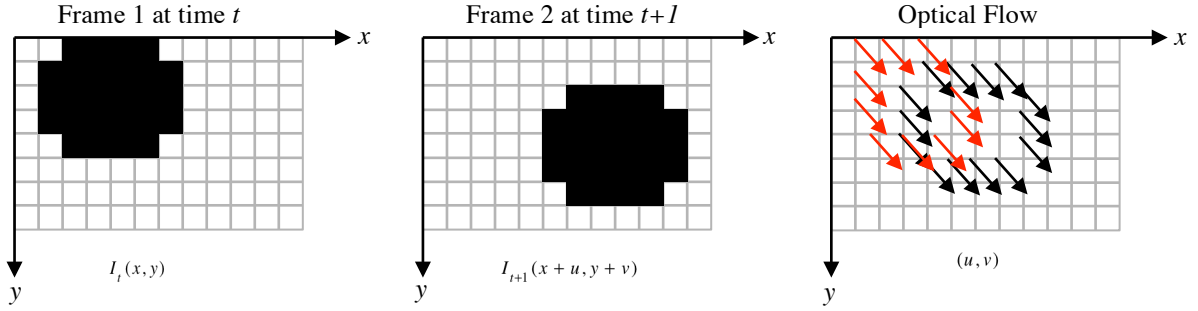


Figure 2.22: Basic concept of optical flow. Red arrows indicating the origin of flow vectors and black arrow indicating the velocity vector.

The example shown in Figure 2.22 can be expressed mathematically by considering a patch of a brightness pattern at location (x,y) that has the intensity of $I(x,y)$ at time t . Assuming the brightness of the patch remains constant, the displacement of the pattern in the x -direction and the y -direction from time t can be derived as:

$$I(x,y,t) = I(x+u, y+v, t + \Delta t) \quad (2.2)$$

By expanding Taylor series, the right-hand side of Equation 2.2 can be expressed as:

$$I(x,y,t) = I(x,y,t) + \frac{\partial I}{\partial x}u + \frac{\partial I}{\partial y}v + \frac{\partial I}{\partial t}\Delta t + \epsilon \quad (2.3)$$

where ϵ contains second and higher order terms in x and y . By subtracting $I(x,y,t)$ from both sides gave the following equation:

$$0 \approx \frac{\partial I}{\partial x}u + \frac{\partial I}{\partial y}v + \frac{\partial I}{\partial t}\Delta t \quad (2.4)$$

where (u,v) are the displacements or optical flow of (x,y,t) and $\frac{\partial I}{\partial x}, \frac{\partial I}{\partial y}, \frac{\partial I}{\partial t}$

are derivatives of the image at (x,y) in the corresponding directions. Assuming the limit $\Delta t \rightarrow 0$ to estimate the velocity of the displacement:

$$0 \approx \frac{\partial I}{\partial x} \frac{u}{\Delta t} + \frac{\partial I}{\partial y} \frac{v}{\Delta t} + \frac{\partial I}{\partial t} \frac{\Delta t}{\Delta t} \quad (2.5)$$

where $\frac{u}{\Delta t}, \frac{v}{\Delta t}$ are the velocities. Thus, a single linear equation in the two unknowns can be derived as:

$$\begin{aligned}\nabla I \cdot [u, v] + I_t &= 0 \\ \text{or} \\ \nabla I \cdot [u, v] &= -I_t\end{aligned}\tag{2.6}$$

where ∇I and I_t are the partial derivatives of the spatial gradient and temporal gradient with respect to x, y and t respectively.

It should be noted that it is not possible to determine the motion due to the nature of the equation as it provides only one equation for two unknowns (i.e. unknown flow vector) and is known as the aperture problems of the optical flow algorithms (Beauchemin, et al., 1995, Mesbah, 1999). To find the optical flow, another set of equations is needed, which involve some additional constraint. All optical flow methods introduce additional conditions for estimating the actual flow. The above simple method shows that the motion has to be sufficiently small, for the first-order Taylor's series expansion to be valid. Furthermore, the motion has to be constant throughout the neighbourhood for the estimation to work.

The above example is the basis of differential methods used in the Lucas-Kanade (Lucas, et al., 1981) and Horn-Schunck (Horn, et al., 1981) methods, which are described shortly. Both the Lucas-Kanade and Horn-Schunck methods assume that brightness does not change over time. The Lucas-Kanade method also assumes that the velocity is locally constant, and so neighbouring points belong to the same patch and have similar motion, while the Horn-Schunck method assumes that the flow field is globally smooth where neighbouring velocities are nearly identical. In comparison, Lucas-Kanade would produce less noise compared than the dense method of Horn-Schunck.

However, the global aspect of the Horn-Schunck method is computationally expensive compared to the local neighbouring method of Lucas-Kanade. Moreover, Horn-Schunck being a global method yields dense flow field and is less robust to noise (Bruhn et. al., 2005) thus making it less feasible to track the deformation of

localised area of the speckle representation of human tissue that is hard to track the localised areas of the tendon tissue. Figure 2.23 illustrates the Lucas-Kanade and Horn-Schunck methods with illustrating the Lucas-Kanade method containing the feature template T from the initial frame at time t (a) and the local flow vector in time $t+1$ (b). The Horn-Schunck is shown in (c) where the motion between I_t and I_{t+1} is shown as vectors in (d).

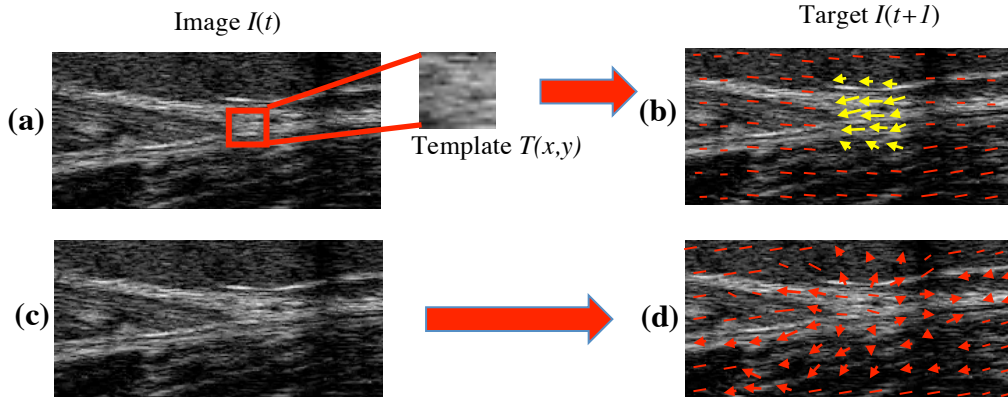


Figure 2.23: Examples of Lucas-Kanade method (a) with its flow vector (b) and Horn-Schunck (c) and its flow global flow vector (d).

2.4.1.1 Lucas-Kanade Algorithm (LK)

The Lucas-Kanade algorithm was initially developed to align a template image to an input image locally within the image space assuming that the brightness is constant, and the displacement between two frames is small. Using the standard optical flow equation (see Equation 2.2) all pixels can be grouped together within a window of $M \times N$ and written in a matrix form of minimum least square to compute the summation over all pixels in the $M \times N$ window:

$$\begin{bmatrix} \sum I_x I_x & \sum I_x I_y \\ \sum I_x I_y & \sum I_y I_y \end{bmatrix} \begin{bmatrix} u \\ v \end{bmatrix} = - \begin{bmatrix} \sum I_x I_t \\ \sum I_y I_t \end{bmatrix} \quad (2.7)$$

The matrix in Equation 2.7 holds all pixels within a window centred at p . If p^* is the best alignment, by using Taylor series approximation the similarity can be derived as:

$$p^* = \sum_x [I(W([x,y];p)) - T(x,y)]^2 \quad (2.8)$$

where $W([x,y];p)$ is the set of parameterised warps (geometrical transformation), $T(x,y)$ is the template model and p is a vector of parameters. $I(W([x,y];p))$ is the warped image obtained by interpolating the image I at the sub-pixel location $W([x,y];p)$. The displacement is then obtained by subtracting $I(W([x,y];p))$ from $T(x,y)$ where the point p is assumed to be a known parameter, which gives a linear equation of optimal increment:

$$\Delta p^* = \sum_x \left[I(W([x,y];p)) + \nabla I \frac{\partial W}{\partial p} \Delta p - T(x,y) \right]^2 \quad (2.9)$$

where Δp is the vector with increment parameter and ∇I is the gradient of image I evaluated at $I(W([x,y];p))$.

The term $\frac{\partial W}{\partial p}$ is the Jacobian of the warp:

$$\frac{\partial W}{\partial p} = \begin{bmatrix} \frac{\partial W_x}{\partial p_1} & \frac{\partial W_x}{\partial p_2} & \dots & \frac{\partial W_x}{\partial p_n} \\ \frac{\partial W_y}{\partial p_1} & \frac{\partial W_y}{\partial p_2} & \dots & \frac{\partial W_y}{\partial p_n} \end{bmatrix} \quad (2.10)$$

Minimizing the Equation (2.9) gives a least squares problem and has a closed form solution linear in Δp which can be derived as follows:

$$\Delta p^* = 2 \sum_{x,y} \left[\nabla I \frac{\partial W}{\partial p} \right]^T \left[I(W([x,y];p)) + \nabla I \frac{\partial W}{\partial p} \Delta p - T(x,y) \right] \quad (2.11)$$

where $\nabla I \frac{\partial W}{\partial p}$ is known as the steepest descent image (Baker, et al., 2004). Setting this expression to zero gives:

$$\begin{aligned} \Delta p &= \left[\sum_{x,y} \left(\nabla I \frac{\partial W}{\partial p} \right)^T \nabla I \frac{\partial W}{\partial p} \right]^{-1} \left[\sum_{x,y} \left(\nabla I \frac{\partial W}{\partial p} \right)^T (I(W([x,y];p)) - T(x,y)) \right] \\ &= H^{-1} \sum_{x,y} \left[\nabla I \frac{\partial W}{\partial p} \right]^T [I(W([x,y];p)) - T(x,y)] \end{aligned} \quad (2.12)$$

where H is Gauss-Newton approximation of the Hessian matrix. For this reason it can be seen that the above equation is the steepest descent parameter updates, and proves that Δp is the steepest descent parameter.

The point p is then continuously updated with parameters Δp until $\|\Delta p\| \leq \epsilon$, where ϵ is a threshold parameter. The process of the Lucas-Kanade method is illustrated in Figure 2.24 using a B-mode image of tendon data. Here, in Frame 1, a $M \times N$ size template is selected **(a)** and is then compared at every pixel to the warped image of Frame 2 **(b)**. At every position of the pixel is updated with the steepest descent parameter (summation of both gradient of warp x and warp y) until match is found and the displacement of the search object between the two frames represents its motion vector **(c)**.

There are two cases that will cause a poor match in Lucas-Kanade. The first case being that the point p falls outside of the tracked image and the other case when the image patch around the tracked point between image I and T varies too much (points disappear due to occlusion).

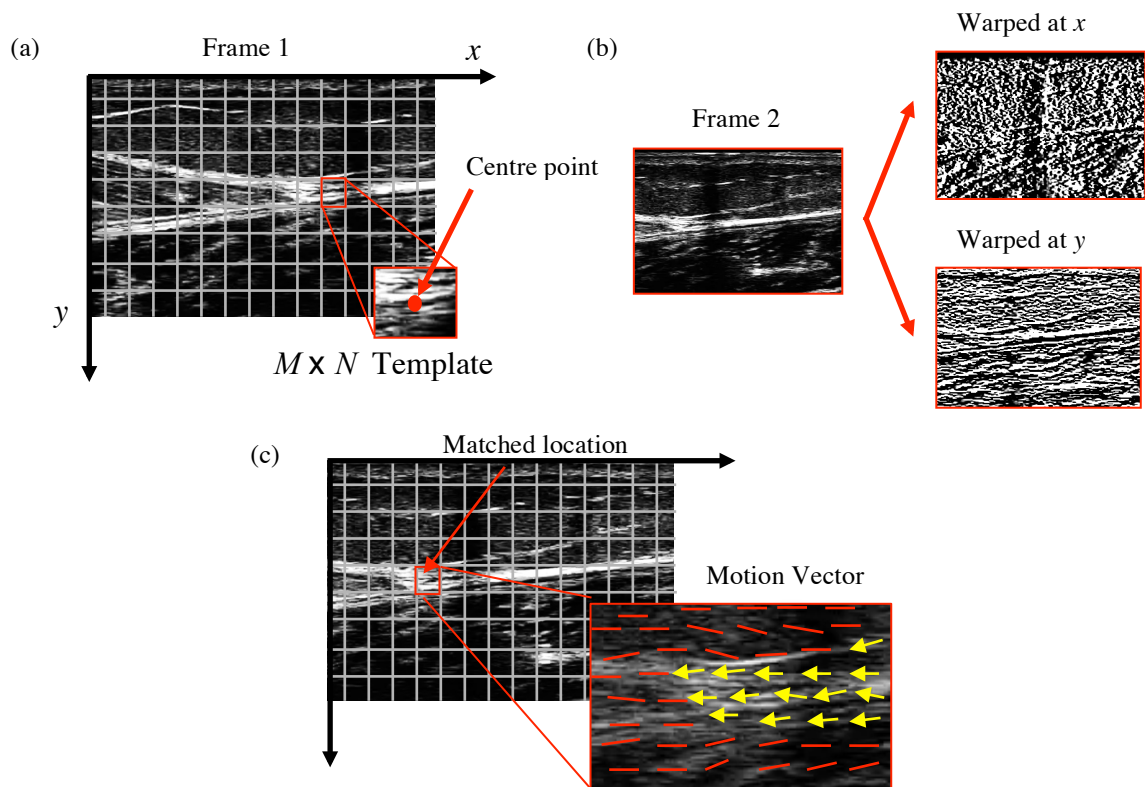


Figure 2.24: Lucas-Kanade motion estimation illustrated with B-mode tendon data.

2.4.2 Block-Matching Algorithm (BMA)

Block-matching algorithm (BMA) computes the local displacement between two images or portions of images on a pixel-by-pixel basis (Sun, et al., 2003). These methods have been extensively researched, and various developments based on the block-matching method have been developed to estimate the motion of speckle patterns in ultrasound images (Lin, et al., 1997, Barjatya, 2003, Hariharakrishnan, et al., 2005, Purwar, et al., 2010). The use of BMA was first introduced in discovering temporal redundancy in video sequences and video compression (Jan-Wiebe, et al., 2010) but has been applied to medical image processing (Ourselin, et al., 2000). The typical BMA consists of a fixed search window of size $M \times N$ pixels and a template image block of size $m \times n$ pixels. The motion displacement is measured by pixels (p) per frame (see Figure 2.25).

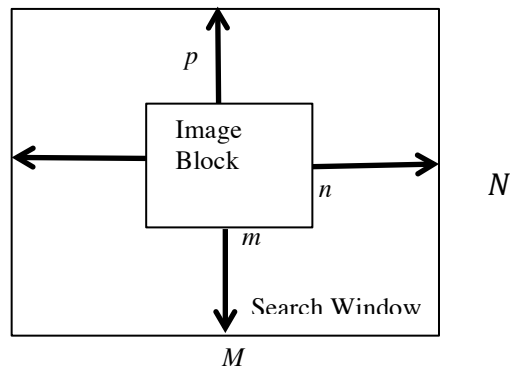


Figure 2.25: Illustration of a BMA with a predefined search window and image block (Barjatya, 2003).

The typical BMA search technique divides the image frames into non-overlapping blocks where each block from the initial frame (t) is matched into a block in target frame $t+1$ (see Figure 2.26). The search region is defined by its search window parameters. By using exhaustive search methods (Sun, et al., 2003) or newer methods such as the three-steps search (3SS) (Koga, et al., 1981) or the diamond search method (Zhu, et al., 1997), a new block location can be estimated. The exhaustive search method is a very time-consuming technique but gave more accurate results compared to the other newer search methods (Mohammad, et al., 2009).

Both the three-steps search and diamond search methods were developed to simplify the search and to reduce the computational cost of the exhaustive method. However, at the expense of accuracy, both methods become inefficient for small motion estimation, irregular data flow and high control overhead compared to the exhaustive search method (Lin, et al., 1997). The Block-matching algorithm (BMA) is based on Euclidean distance measurement. By using the Sum of Squared Distance (SSD), which is usually used in block-based motion estimation, the search window is sized appropriately for the tracked object (Beauchemin, et al., 1995) between $-w$ for minimum and $+w$ for maximum.

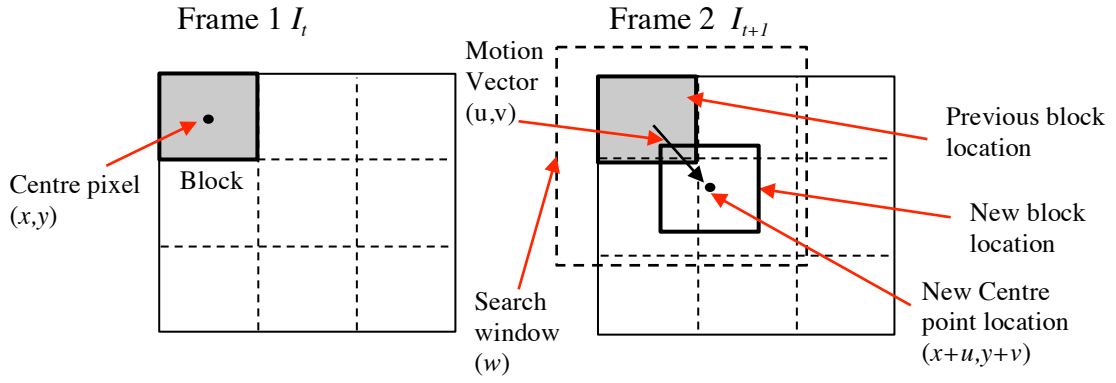


Figure 2.26: Illustration of a block matching algorithm (BMA) matching from the image in frame k to the block within the search window in target frame $k+1$ (Purwar, et al., 2010).

In general, the block-matching method searches for best matches from each block from the initial frame t within a search window of size $(2w + n) \times (2w + n)$ in the next frame $t+1$ within the maximum allowed displacement w and each block is measured in pixels n . SSD can be derived as:

$$SSD_{(u,v)} = \sum_{x=0}^{n-1} \sum_{y=0}^{n-1} [I_t(x,y) - T_{t+1}(x+u, y+v)]^2, \quad (2.13)$$

$$-w \leq u, v \leq w$$

where I_t is the initial block in frame t from the top left location of the image frame while T is the target block in frame $t+1$ within the search window of the target image and (w) is the maximum searched area. Neighbouring pixels give the central pixel and corresponding displacement vector (u,v) . The block with the least distortion is known as the “best match”.

The full search method computes SSD for all $(2w+n)^2$ positions of the target block. To improve accuracy of the estimation within a number of image frames, a technique known as adaptive block matching algorithm (ABMA) is used (Vermaut, et al., 2001) where the best match block of target frame is reassigned the initial block to be searched in the next frame. This procedure is repeated until the final frame. The basic correlation technique for similarity measurement used in the block-matching

search contains several problems; mainly the correlation value of $\sum(I,T)$ at a certain pixel in an image may produce a large value even though no good match exists and generate significant error when the window is too large.

The error produced will also be overwhelmed by background information, and thus, an undersized window can easily drift and lose the tracking area (Eltoukhy, et al., 2001). Several other similarity measurement techniques have been introduced such as Mean Square Error (MSE) (Zhu, et al., 1997, Chan, et al., 1998, ZhāNg, et al., 2000, Ulysses, et al., 2010) and Normalised Crossed Correlation (NCC) (Nillius, et al., 2002, Hii, et al., 2006, Pearson, et al., 2012) to overcome the problems found in block matching algorithm.

2.4.2.1 Mean Square Error (MSE)

Mean Square Error (MSE) is one of the similarity measurements that is used to measure the quality of the estimator (*error*) by squaring of the differences between the initial blocks and target blocks, summing them and averaging by the number of observations (dimension size of search window). MSE is defined as:

$$MSE(u,v) = \frac{1}{MN} \sum_{x=1}^M \sum_{y=1}^N [I(x,y) - T(u+x, v+y)]^2 \quad (2.14)$$

$$-w \leq u, v \leq w$$

where u, v are the displacements, $M \times N$ is the size of the template and w is the search area for the template T shifted by (u, v) steps. The MSE produces a value for displacement vector for a shift to pixel (u, v) .

The MSE is calculated for a displacement at every pixel position within the search range in the target frame, and the movement that gives the minimum value of MSE is chosen as the motion vector:

$$MSE(x,y) = \arg \min_{x,y} [MSE(u,v)], \quad (2.15)$$

$$\approx \min = 0$$

where $MSE(x,y)$ is the minimum difference (error) within the motion vector and with a perfect match indicated as zero and larger difference indicating poorer matches.

The search similarity measurement of MSE is illustrated in figure 2.27 using the B-mode tendon data. The similarity measurements between T and I are shown in greyscale using the BMA. The position of the closest match is also indicated in the figure 2.27. It is known that the MSE has the disadvantage of assigning more weight to large errors than small ones (Hibon, et al., 1995, Twomey, et al., 1996).

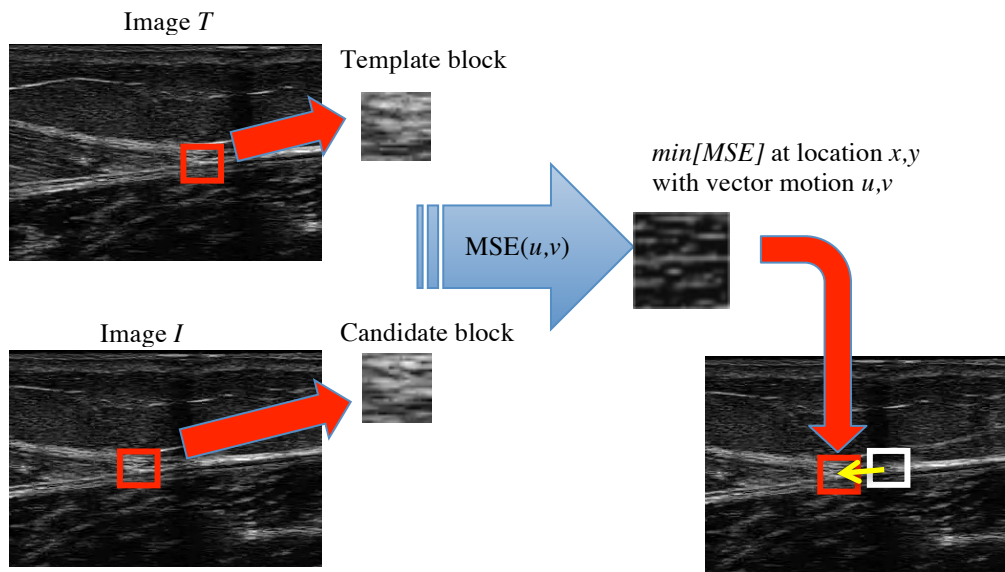


Figure 2.27: Illustration of a Mean Square Error (MSE) similarity measurement.

2.4.2.2 Normalised Cross Correlation (NCC)

Another widely used similarity measurement in BMA is the Normalised Cross Correlation (NCC), which is a simple template matching method that determines the location of the template block (T) inside the 2-dimensional target image (I). By using the BMA approach, the template was shifted pixel-by-pixel across the image, forming a correlation plane to indicate the location of the best match in the image. Unlike MSE, the intensity of the image is normalised to smaller unit length and the NCC value produces a small correlation coefficient between the target blocks and the initial block (Revell et al., 2004).

The correlation coefficient at the location (u,v) is defined as:

$$NCC(u,v) = \frac{\sum_{x=1}^M \sum_{y=1}^N [I(x,y) - \bar{I}_{u,v}] \sum_{x=1}^M \sum_{y=1}^N [T(x-u, y-v) - \bar{T}]}{\left\{ \sum_{x=1}^M \sum_{y=1}^N [I(x,y) - \bar{I}_{u,v}]^2 \sum_{x=1}^M \sum_{y=1}^N [T(x-u, y-v) - \bar{T}]^2 \right\}^{\frac{1}{2}}} \quad (2.16)$$

$$-w \leq u, v \leq w$$

where x,y are the pixel locations, $M \times N$ is the size of the template, and \bar{I} is the mean value of I within the search area w of the template T shifted to (u,v) and can be derived as zero mean image:

$$\bar{I}_{u,v} = \frac{1}{MN} \sum_{x=1}^{u+M} \sum_{y=1}^{v+N} I(x,y) \quad (2.17)$$

and \bar{T} is the mean value of the template T , defined as:

$$\bar{T}_{u,v} = \frac{1}{MN} \sum_{x=1}^{u+M} \sum_{y=1}^{v+N} T(x,y) \quad (2.18)$$

As the template T is shifted to n -th positions (u,v) where at every position, the zero mean image \bar{I} and the zero mean of the template \bar{T} have to be recalculated simultaneously, giving NCC the disadvantage of being computationally expensive. Due to the zero mean, NCC values are between 0 to 1, where 0 is assumed as a poor match and 1 to be the best match. It can be derived as:

$$NCC(x,y) = \arg \max_{x,y} [NCC(u,v)] \quad (2.19)$$

$$\approx \max = 1$$

where $NCC(x,y)$ is the maximum differences allowable for motion vector and if a match is determined with the difference (error) is 1, while smaller difference value indicating poor matches.

The search similarity measurement of NCC is illustrated in figure 2.28 using the B-mode tendon data. The similarity measurements between T and I are shown in greyscale with its zero mean functions. Using the block-matching algorithm, the

search shift pixel-by-pixel to find the closest match, which corresponds to the position u,v when the correlation value reaches the maximum value, which must be above a preset threshold. The new candidate or match is at new location of x,y with the vector path u,v is measured between previous and current frames.

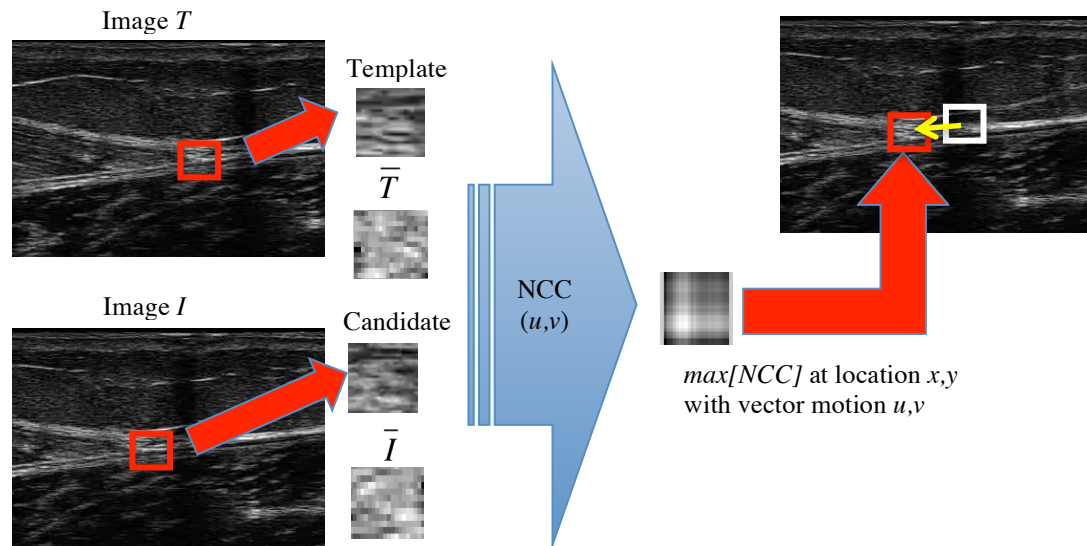


Figure 2.28: Illustration of a Normalised Cross Correlation (NCC) similarity measurement.

2.5 Summary

In this chapter the biomedical background related to tendon structures and functions has been described, as well as applications and experiments related to ultrasound imaging and tracking in biomedical areas. The background to tracking imaging within the domain of ultrasound imaging was also described, with details of the tracking algorithms that were predominantly used in biomedical applications. This understanding of the tracking algorithms and its area of interest within the mechanical tendon are essential for the parameter identification and motion estimation for the ultrasound imaging with random speckle formation, and will be used extensively in the following Chapters.

In the next chapter, the experiment setup used to validate the effectiveness of the tracking algorithms using the tendon muscle data in-vivo is explained. In these experiments, different algorithms are investigated and are compared to the standard manual measurements. The hardware used, and the method of image acquisition is explained as well as the test subjects, including areas of interest within the tendon muscle, as well the kind of output to be expected. Software design and implementation are also covered in this Chapter, showing how results are achieved and what kinds of algorithms are used within the software environment. Detailed discussions of tracking algorithms were discussed there. The algorithms tested were Normalised Cross Correlation (NCC), Mean Square Error (MSE), NCCMSE and optical flow – Lucas-Kanade (LK).

Chapter 3

Materials and Methods

Overview

In this chapter, the methodology used to validate the effectiveness of the tracking algorithms using the in-vivo tendon images is presented. Three studies are devised, and the experimental setup and planned experiments for each study are described. Finally, the design and implementation of the speckle tracking software that is required to support these studies, including the speckle tracking and pattern matching algorithms that have been identified in the previous Chapter, are also discussed.

3.1 Methodology

In order to meet two of the project's Objectives: determining the optimal image-tracking algorithm for in-vivo tendon images, and then extend this algorithm and identifying the optimum settings such as the region of interests (ROI) block size and the threshold range; and generating useful information from the tracking output such as the displacement and the motion path of the tendon region to calculate its stress and strain for a better clinical understanding of the tendon mechanical properties during dynamic excursion under load, a series of three studies were devised and conducted which built on the results of the previous one.

The first study was a pilot study and involved comparing the performance of the main speckle tracking algorithms for ultrasound images identified in the previous Chapter and validating them against the standard manual measurement (Pearson et al., 2006, Pearson et al., 2012). The standard manual measurement process is described in the following Section, and the experimental setup and planned

experiments for the pilot study are described in Section 3.3. The best performing speckle-tracking algorithm was chosen and used for the two remaining studies. In the second study, the chosen tracking algorithm was applied to two regions of interest (ROI) consisting of two markers placed at both proximal and distal ends of the regional areas of the tendon (Farron et al., 2009) to measure its strain against the standard manual measurement (Pearson et al., 2012).

The experimental setup and planned experiments for this study are described in Section 3.4. For the final experiments, the best tracking algorithm was chosen with ROIs placed at multiple areas of the regions of both proximal and distal ends on each layer of anterior, midsection and posterior, for tendon strain measurement at each layer (Pearson et al., 2014). The experimental setup and planned experiments for this study are described in Section 3.5. The study had the approval of the local University Ethics Committee and was in agreement with the World Medical Association's declaration of Helsinki describing ethical principles for medical research involving human subjects.

All participants were made aware of the study before any testing was carried out. All subjects gave their written informed consent to participate in this study. The testing took place in the Human Performance Laboratory at Salford University. Reliability estimates of the measures were determined by Intraclass correlation coefficients (ICCs) (two-way mixed model with absolute agreement). Each experiment in the studies can be considered to have three separate stages: the Input, Processing and Output (see Figure 3.1). The Input stage involved setting up the equipment in the lab to capture the ultrasound images from participants in-vivo using the ultrasound scanner probe. The images were digitized by the ultrasound system and stored as a sequence of images in uncompressed video file (DV) format at 25 frames per second (fps) into computer storage for further analysis. In the Processing stage, the speckle tracking software that has been developed read an Input video file, displayed it on screen, then allowed the user to select the regions to be tracked (Region of interest - ROI) as a marker in the initial frame, and finally let the user choose appropriate settings such as algorithm type and search block size through a graphical user interface.

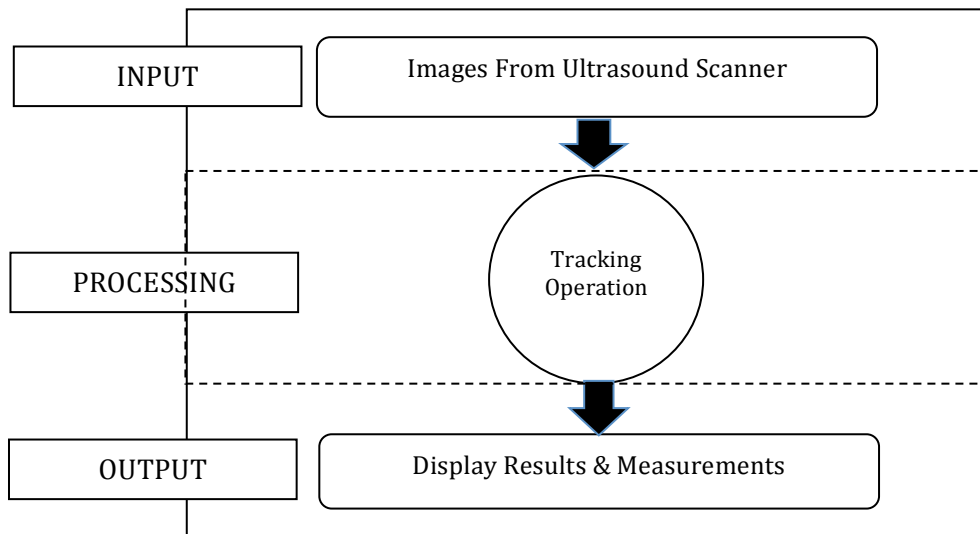


Figure 3.1: Three stages of experiment for the tracking ultrasound images.

Then the software tracked the speckle in the selected region as a single ROI (or both ROIs for the 2 ROI study) from one frame to another frame in the video, based on the selected settings, and computed the displacement of ROI marker(s) for each of the layers being studied. Finally, at the Output stage, the results were presented either in a sequence of images showing the path of the ROI marker(s) or saved into Excel spreadsheet format so that frame-by-frame measurements and displacements can be shown. This information could be used for further analysis to describe the characteristics of the subject, in this case the tendon, where stress and force could be calculated. The speckle tracking software that was developed for the Processing and Output stages is described in Section 3.6.

It should be noted that the speckle tracking software that was developed for the first two studies used the equipment that was available at that time. However, for the final study (tendon assessment in vivo), an upgraded version of ultrasound machine and computer system and development environment was available. The upgraded hardware gave a deeper depth in image resolution, an easier method of capturing and storing the data, and finally, better performance during the tracking process, although it was necessary to upgrade the software. With the new upgraded

system, the evaluation of the tendon could be done with more tracking features added to take advantage of the higher image resolution.

3.2 Manual Measurement Based on Standard Method

The manual measurement used for the study was based on the standardized method of measuring the tendon stress, strain and stiffness of patella tendon elongations during ramped isometric co-contractions (simultaneous contraction of both the agonist and the antagonist around the joint) using both proximal and distal tendon excursions (Onambele et al., 2007). The sequence of images was firstly captured and digitized. On each still image, the distance between the patella and the echo-absorptive marker was manually measured using the ImageJ software (<http://imagej.nih.gov/ij/>). The ultrasound image was calibrated, and measured distance converted from pixels to millimetres by using the ultrasound's depth measure as a calibration scale. Elongation was calculated by subtracting the distance measured at rest (0%) maximum voluntary contraction (MVC) from the measured distance at every 10% force interval. Each distance was measured three times and an average taken prior to the calculation of elongation. Mean differences between the short and long duration contractions for the calculated mechanical parameters were determined using paired t-tests. Alpha level was set to ($p < 0$).

3.3 Study 1: Algorithm Validation Experiment

For the pilot study, the equipment was setup to accommodate the experiment concerned with implementing several tracking algorithms, their performance compared and validated against the standard manual measurement.

3.3.1 Participant

A healthy recreationally active male aged 47 years with mass 91kg and height 1.81m participated in the study. Both left and right limb were investigated where the areas of interest were the localised tendentious regions of patella (knee) and gastrocnemius (ankle). Each tested area was captured repeatedly three times using similar testing method and configuration.

3.3.2 Tracking Region

The best algorithm is chosen and implemented to study the characteristics of the tendon muscle. Figure 3.2 shows the ultrasound imaging of the patella tendon with its properties visible. The region that was examined is the tendon band; the length of the tendon is notated as **(G)** and the height is notated as **(E)**. The band is attached to the peninsular bone of the knee, which is the proximal side of the tendon **(D)**. The band consists of three regional layers: anterior **(A)**, midline **(B)** and Posterior **(C)**. These are the regional layers that will be used in the assessment throughout the study. The echo-absorbent marker is notated as **(F)** and is used as a measuring point to measure the displacement of the tendon.

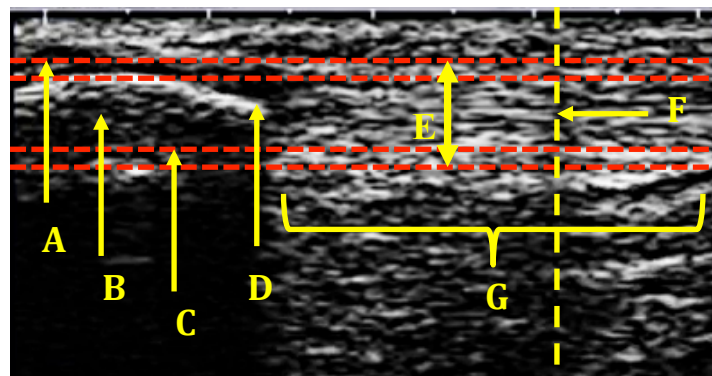


Figure 3.2: Example of Ultrasound imaging of patella tendon with regional areas within the tendon band.

In the case of the medial gastrocnemius, as shown in Figure 3.3, the regional tendon area is marked as **(A)**, which is the region for assessment through the study.

The myotendinous junction (**B**) is the site of connection between tendon and muscle. The echo-absorbent marker is notated as (**C**), and this will be the measuring point to measure the displacement of the tendon.

The results from both regions (i.e. patella and gastrocnemius) should give an overview of the best algorithm to be used for tracking such data, and how to treat the results generated from the experiments to describe the characteristics of the tendon mechanical properties.

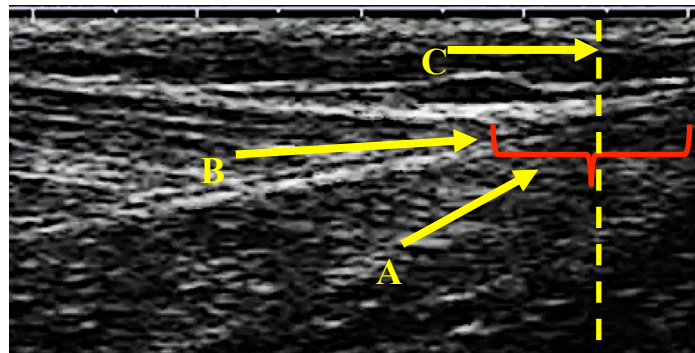


Figure 3.3: Example of Ultrasound imaging of medial gastrocnemius with the regional tendon areas within the tendon band.

3.3.3 Hardware and Software Setup

The hardware used for the experiment was the Esaote Biomedics B-mode ultrasound system (AU5) with a 7.5 MHz, 4cm linear array probe transducer (<http://www.esaote.com>). The probe setting for the both experiments was set to 49.3mm depth range with scanner gain was set at 51%. Images were captured using Quintic Biomechanics 9.03 v11 (<http://www.quintic.com/>) as DV format into PC via s-video at 25 frames per second (fps) with the size dimension 768x576 pixels for each image. Figure 3.4 shows a picture of the ultrasound machine and the probe transducer.



Figure 3.4: An example of a B-Mode ultrasound system and a 40mm probe transducer.

A Kin-Com isokinetic dynamometer (type 125 AP) was also used in the experiments (<http://kincom.com/>) as shown as in Figure 3.5.

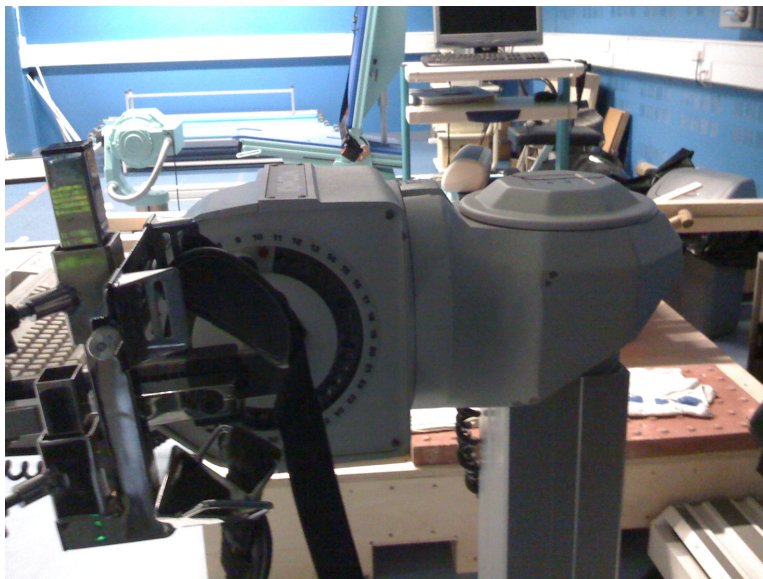


Figure 3.5: An example of isokinetic dynamometer Kin Com type 125 AP.

The typical setup for both ultrasound system and the isokinetic dynamometer is shown in Figure 3.6. For all experiments, the participant was required to strap across the chest, hip and thigh of the test limb to prevent any extraneous movement.



Figure 3.6: A typical equipment setup for the experiments.

For the assessment of the patella tendon, using a dynamometer, the knee was fixed at 90° flexion. The knee joint centre was aligned to the centre rotation of the dynamometer lever arm, and a lever attachment cuff was placed on the lower leg (see Figure 3.7).



Figure 3.7: Participant positioned for the assessment of patella tendon.

While for the assessment of the gastrocnemius, the foot was set in a neutral anatomical position, where the sole was at 90° to the tibia (see Figure 3.8). The ankle joint axis was aligned with the pivot point of the dynamometer lever arm, and the consequent lever arm length of the dynamometer noted. The foot was securely fastened to the dynamometer footplate with Velcro straps and straps were also fixed across the chest, hip and thigh of the test limb to prevent any extraneous movement.



Figure 3.8: Participant positioned for the assessment of medial gastrocnemius tendon.

The computer system used to run the speckle tracking software which is described later, was an Apple MacBook Pro, with a specification as follows:

- Intel Core i5 processor running at 2.4GHz
- 8GB 1600 MHz DDR3 RAM
- 256GB Solid State Drive (SSD)
- MAC OSX 10.9.2

The specification used was capable of handling more than 300 frames of the image sequence. A less powerful system was tested with 4GB RAM and was found to be only capable of processing 200 frames until it ran out of memory.

Scaling the images in pixels per mm was determined from ImageJ software (<http://imagej.nih.gov/ij/>) by using the known depth of field in the ultrasound images, (1 mm = 9.20 pixels or 1 pixel = 0.11 mm) and utilised as a calibration factor in the automated tracking software to ensure equivalent pixel to mm ratios. Other software used during the experiment was as follows:

- SPSS Statistics For Mac version 22 for statistical analysis (<http://www.ibm.com/>).
- Microsoft Excel and Microsoft Word for Mac 2011 (<http://www.microsoft.com/>) for both data analysis and documentation.

For the comparison analysis between the automatic and manual tracking methods, two sites were chosen based on those typically utilized in the literature. These were the patella and medial gastrocnemius tendon (Arampatzis, 2005, Pearson et al., 2007).

3.3.3.1 Patella Tendon Assessment Setup

For the assessment of the patella tendon, the probe was positioned in the sagittal plane over the proximal patella and patella tendon as shown in Figure 3.9a. An echo-absorptive marker was placed between the probe and the skin to act as a fixed reference from which manual measures of elongation could be made as shown in Figure 3.9b.

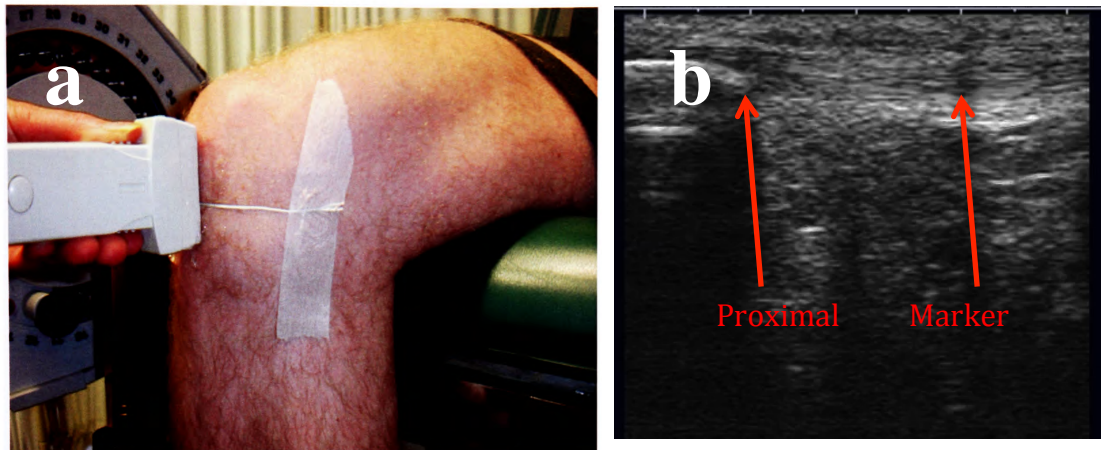


Figure 3.9: a) Example of ultrasound probe positioned in the sagittal plane over the patella tendon with echo-absorptive placed. b) The ultrasound image generated showing the proximal region of inferior pole of patella tendon and the marker.

Two experiments were performed for this study. The first one examined the passive tendon excursion where no tendon deformation would be expected. The probe was moved along the skin surface within a 20mm range, so that the tendon appeared to be moving but with no muscle contraction. The starting position was defined as frame zero and final position as frame $n-1$. The same criteria or frame range was used for three times for all similar trials. The purpose of this study was to test the capability of each algorithm to track movement along the tendon.

For the second experiment, the participant was instructed to perform maximal voluntary (MVC) isometric knee extension with gradually increasing force up to the maximum. Voluntary forces ramped manually over 3-4 seconds, and the probe captured the deformation of the tendon. This was used to test the tracking algorithm's ability to track a highly loaded tendon. The elongation of the tendon was measured by measuring the distance between the region just distal to the inferior pole of the patella (proximal) and the echo-absorption marker.

The same trials were performed three times. Figure 3.10 shows an example of a passive tendon movement **(A)** starting from its initial position (first frame) to 50% of the total frame and finally towards the final frame (100% of the total frame), as for active movement, **(B)** shows the initial position (tendon rest) gradually increasing to 50% maximum voluntary contraction (MVC) and finally towards 100% MVC. Both passive and active experiments were marked with ROI-nodes within the tendon region with I indicating its initial position in the first frame and P indicating its current position in successive frames.

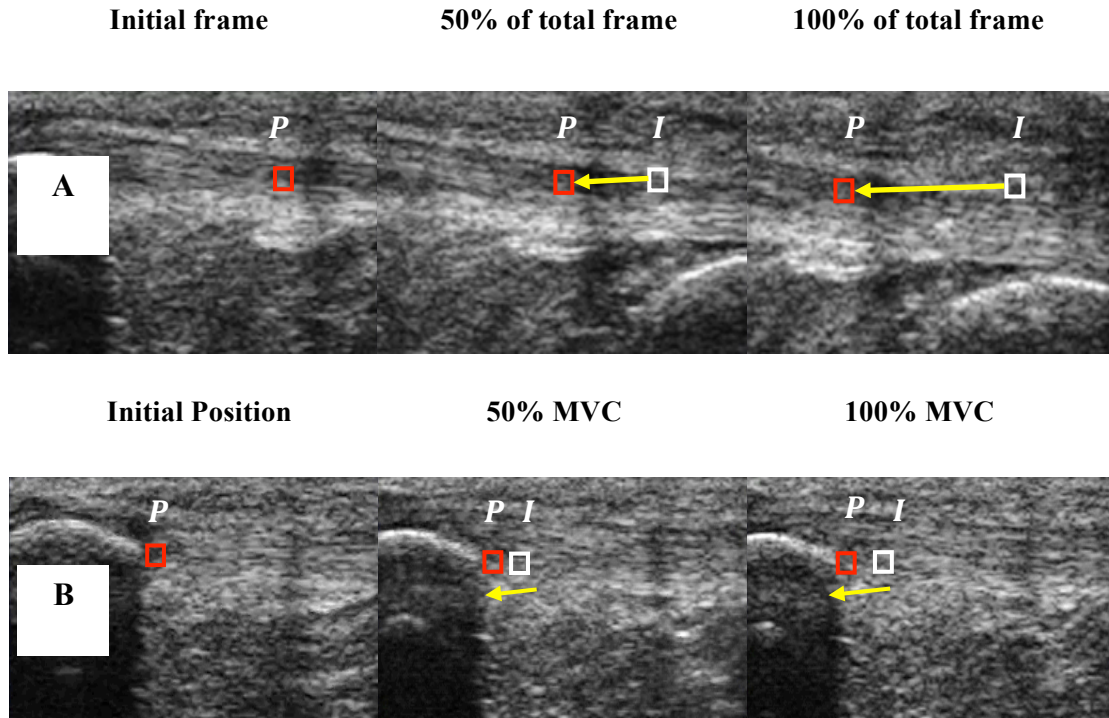


Figure 3.10: **A)** an example of passive movement of the tendon. The ROI node was shown moving from its starting position in the initial frame and moved to another position in all successive frames. **B)** An example of an active movement of the tendon, which the ROI nodes at every percentage level of voluntary contraction (MVC). The displacements for both experiments were measured starting from the initial position (*I*) to the last position of (*P*).

3.3.3.2 Medial Gastrocnemius Tendon Assessment Setup

For the assessment of the medial gastrocnemius, the probe was positioned in the sagittal plane over the myotendinous junction of the medial head of the gastrocnemius muscle as shown in Figure 3.11a. An echo-absorptive marker was placed between the probe and the skin to act as a fixed reference from which manual measures of elongation could be made as shown in Figure 3.11b. Similar to the patella tendon assessment, passive and active tendon excursions were examined. For the observation of the passive tendon, the probe was moved along the skin surface, with no contraction activity by the participant. For the active tendon assessment, the

participant was instructed to perform the same maximal voluntary (MVC) isometric plantar flexions with gradually increasing force, reaching over a 3-4s period. Both passive and active trials were repeated three times by the participant.

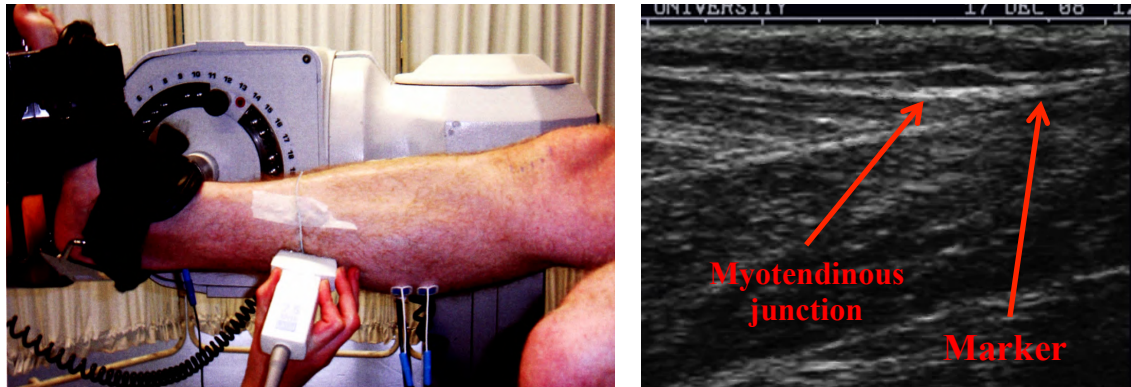


Figure 3.11: a) Example of the ultrasound probe positioned in the sagittal plane over the myotendinous junction of the medial head of the gastrocnemius muscle with echo-absorptive placed. b) The ultrasound image generated showing the myotendinous junction of the medial gastrocnemius tendon and the marker.

Figure 3.12 shows an example of a passive movement of the medial gastrocnemius starting from its initial positions in the first frame (A) and moved along to 50% of the total frame and finally towards the final frame (100% of the total frame). The echo-absorption marker shows the gradual movement and the tendon fiber shown as speckles has a non-rigid like movement. The initial position of the tendon during active movement assessment is seen in (B). The tendon is at rest (first position), and the participant gradually increase to 50% maximum voluntary contraction (MVC) and finally towards 100% MVC. Both passive and active experiments were marked with ROI-nodes within the tendon region with *I* indicating its initial position in the first frame and *P* indicating its current position in successive frames.

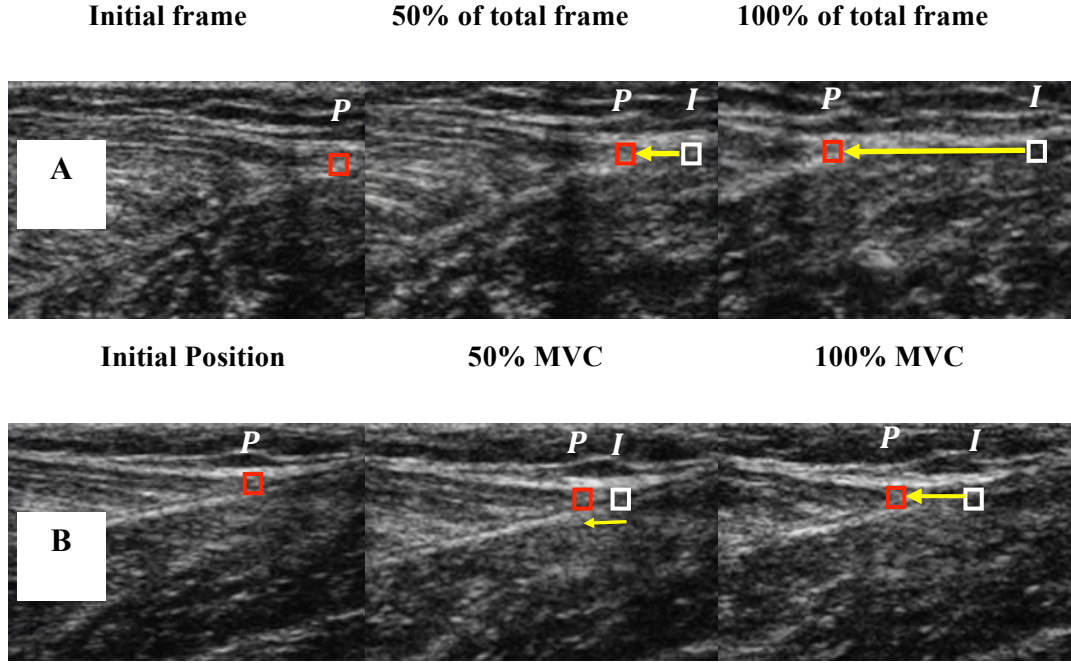


Figure 3.12: (A) an example of passive contraction of the medial gastrocnemius. The ROI node was shown moving from its starting position in the initial frame and moved to another position in all successive frames. (B) An example of an active contraction of the medial gastrocnemius, which the ROI nodes change at every percentage level of voluntary contraction (MVC). The displacements for both experiments were measured starting from the initial position (I) to the last position of (P).

The image data collected for both patella tendon, and medial gastrocnemius was then analysed using the tracking software and a single region of interest (ROI) was selected. The displacement is measured from the initial position I in the first frame and the position of the ROI-node in the final frame. The tendon displacement was observed frame-by-frame. The distance between the initial ROI node (I) and the ROI node at new location (P) in the latest frame (for passive movement) or at 100% MVC (for active movement) was measured using the two dimensional Euclidean distance as follows:

$$d(P,I) = \sqrt{(P_x - I_x)^2 + (P_y - I_y)^2} \quad (3.1)$$

where (P_x, P_y) is the position of current ROI node in successive frames, (I_x, I_y) is the position of initial ROI node, and $d(P,I)$ is the Euclidean distance between I and P .

3.4 Study 2: Two Regions of Interest (ROI) Tracking Experiment

The study used the same participant and equipment as the previous study but with the addition of recording the co-contraction torque using the electromyography (EMG) in the antagonist's muscle (Hamstrings and tibialis anterior) to determine the level of antagonistic muscle activity (Pearson et al., 2005). The net torque is calculated as follows:

$$\tau_{net} = \tau_e + \tau_f \quad (3.2)$$

where τ_{net} is the observed net torque, τ_e is the external torque output and τ_f is the antagonistic (hamstring) co-contraction torque. Tendon forces were subsequently calculated by dividing all net torques by the respective moment arms as follows:

$$F_{tend} = \frac{\tau_{net}}{MA_{tend}} \quad (3.3)$$

where F_{tend} is the force in the patella tendon, τ_{net} is the observed net torque, and MA_{tend} is the tendon moment arm and has a value of 44.7mm (Lindahl et al., 1967, Nisell et al., 1986, Yamaguchi et al., 1989, Herzog et al., 1993, Baltzopoulos, 1995, Lu et al., 1996, Wretenberg et al., 1996, Kellis et al., 1999). All excursion records were then determined at ten percent intervals of maximal voluntary force (MVC) up to the maximum.

Here only two ROI nodes were examined, whereby one region was put onto the echo-absorptive marker and the other on an identifiable landmark within the tendon (Gastrocnemius muscle-tendon junction and just distal to the inferior pole of the patella on the inferior aspect). A total of ten trials of active tendon movements were carried out for the 2-ROI experiments. For the active trials, the start was defined where the force was zero and end where a force plateau was reached. The results from the 2-ROI tracking were then compared to the standard manual measurement.

3.4.1 Hardware and Software Setup

In this study, both knee and ankle were fixed similarly to the previous experiments, and again, an echo-absorptive marker was placed between the probe and the skin. The same procedures were used here to capture and record the images using the ultrasound system with similar depth into the computer system. Additionally, the EMG in the antagonist's muscles was recorded and used to calculate the co-contraction torque.

A pair of self-adhesive Ag-AgCl electrodes ~15mm in diameter (type N10A, Medicotest, Rugmarken, Denmark), were placed in a bipolar configuration with a constant between-electrodes distance of ~20mm, at the proximal one-third of the length and in the mid-sagittal plane of the biceps femoris. The skin was prepared by shaving, abrading (Nuprep, SLE Ltd) and cleaned with an alcohol-based solution before placing the electrode in order to minimise the resistance. The reference electrode (Type Q-IOA) was placed on the lateral tibial condyle of the test limb. The EMG signal was sampled at 2000Hz, and pre-amplified (x2000) and band-pass filtered between 500Hz and 10Hz. (see Figure 3.13).

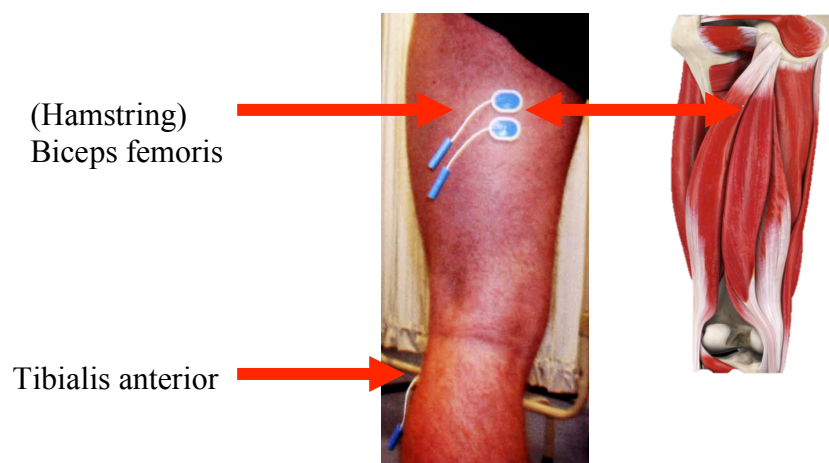


Figure 3.13: Example electrode placement for EMG recordings from Biceps Femoris (Hamstring) and tibialis anterior. The illustration (right) shows where Biceps Femoris is located.

All EMG and torque signals were displayed in real time in TestPoint software (Capital Equipment Corporation, Massachusetts, USA) via a PC. A series of four maximal flexion contractions were carried out to obtain the EMG value at maximal flexion torque. The root mean square EMG activity corresponding to the peak torque period was averaged for 1s period during the plateau of peak torque using AcqKnowledge® software version 3.72 (<http://www.biopac.com>).

The ultrasound output was synchronised using a DS7AH electrical stimulator (<http://www.digitimer.com>) with the torque and EMG records to allow temporal alignment (see Figure 3.14). Still images were then captured from the video output using Quintic Player version 3.09 (<http://www.quintic.com>). The trigger indicates the starting point of voluntary contraction intervals determined from the torque output trace using the AcqKnowledge® software (<http://www.biopac.com>). All excursion records were then determined at ten percent intervals of maximal voluntary force up to the maximum, and the torque output was subsequently converted to tendon force.

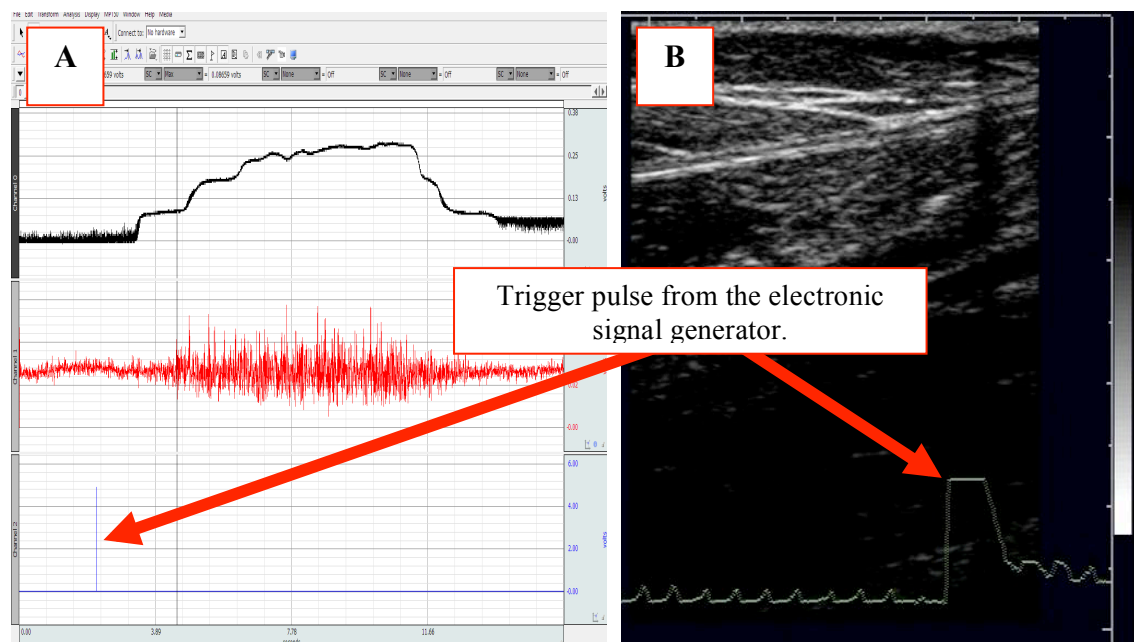


Figure 3.14: Example output from an electronic signal generator to allow temporal alignment between the (A) torque and EMG trace, and (B) the ultrasound image.

The speckle tracking software reads the stored data and two regions of interest (2-ROI) nodes were then selected on the tendon regions $P2$ and the echo-absorbent marker $P1$. Figure 3.15a shows the example of 2-ROI nodes selected for patella tendon and medial gastrocnemius (see Figure 3.15b). As for manual measurement, the ultrasound image was calibrated using the ultrasound's depth measure as a calibration scale, which converts the displacement measurement from pixels to millimetres, and manual measurement was done using ImageJ (<http://imagej.nih.gov/ij/>) for each image to measure the elongation of the tendon.

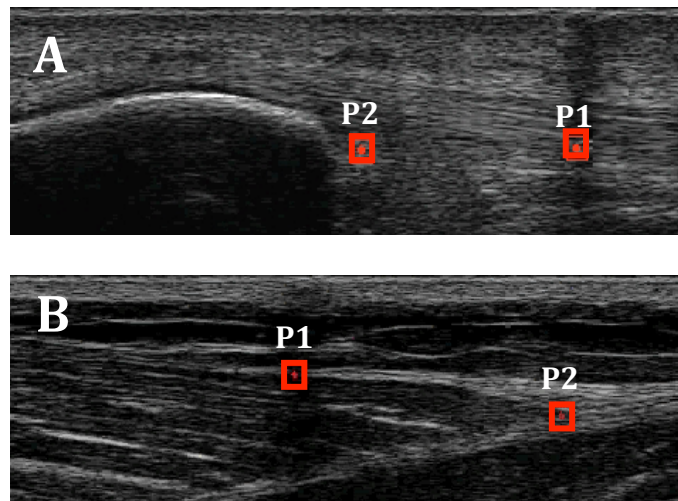


Figure 3.15: Example of 2-ROI nodes on both **A:** patella tendon, where ROI node, $P1$ was placed on the echo-absorbent marker and $P2$ on the regional tendon just distal to the patella, and **B:** medial gastrocnemius, where ROI node, $P2$ was placed on the regional tendon at the myotendinous junction.

Both ROIs ($P1$ and $P2$) moved along the elongation of the tendon. The distance is measured between the echo absorbent marker and the regional area of the tendon. By using the Euclidean distance measure, the current distance between $P1$ and $P2$ can be calculated as follows:

$$d1(P1, P2) = \sqrt{(P2_x - P1_x)^2 + (P2_y - P1_y)^2} \quad (3.4)$$

where $(P1_x, P1_y)$ is the current position of ROI node of the echo absorbent marker, $(P2_x, P2_y)$ is the current position of ROI node of the regional area of the tendon, and

$d1(P1,P2)$ is the Euclidean distance between $P2$ and $P1$ indicating the latest distance measurement of the ROIs. Also, the initial distance between the two ROIs can be measured as follows:

$$d2(I1,I2) = \sqrt{(I2_x - I1_x)^2 + (I2_y - I1_y)^2} \quad (3.5)$$

where, $(I1_x, I1_y)$ is the initial position of ROI node on the echo absorbent marker, $(I2_x, I2_y)$ is the initial position of ROI node of the regional tendon and $d2(I1, I2)$ is the Euclidean distance between $I1$ and $I2$ indicating the initial distance between the ROIs. The relative displacement is measured as follows:

$$Disp = d1 - d2 \quad (3.6)$$

where the difference of current distance of $P1$ and $P2$ ($d1$) was subtracted from the initial distances of $I1$ and $I2$ ($d2$) to give relative displacement.

The measurements are illustrated in Figure 3.16a for the patella tendon where the relative displacement includes the movement of the echo absorbent marker, indicating slight movement of the ultrasound probe. Since both ROIs were moving simultaneously, this did not affect the measurement and the arrows showed the movement of the ROIs at 50% and maximum voluntary contraction. For the medial gastrocnemius, the displacements for both ROIs were shown in Figure 3.16b. The placement of the ROI nodes was the same as the patella tendon experiment (i.e. from echo absorbent marker to regional tendon area), and the arrows show the movement of each ROI node. The relative displacement was measured by subtracting the last position of the ROIs ($d1$) with the initial distance of the ROIs ($d2$). The 2-ROI tracking is useful for measuring the localised tendon region to give its stiffness and strain efficiently, and in the next study, the same method of measuring two ROIs should be used to measure the strain and stiffness at different layers of the tendon.

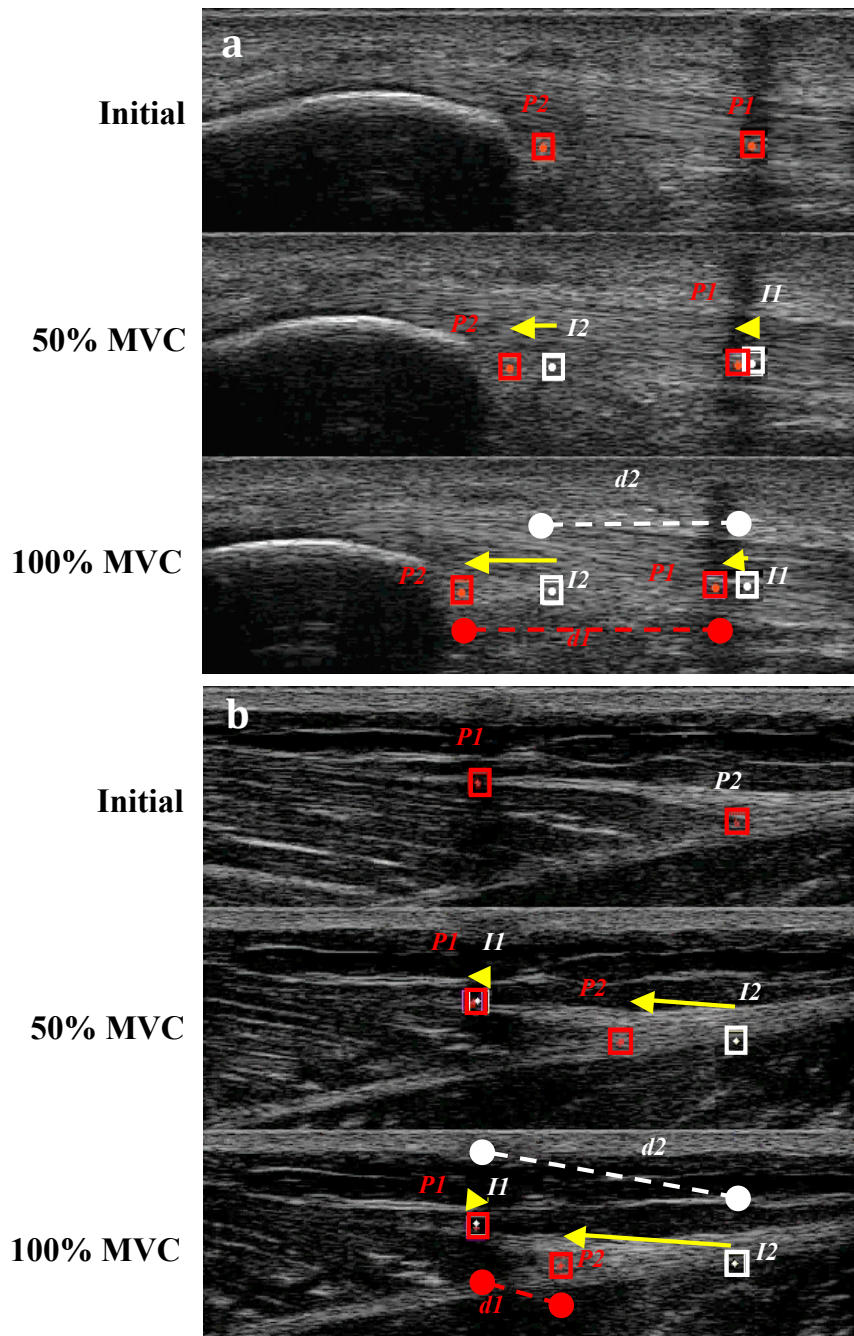


Figure 3.16: Example of 2-ROI nodes on both **A:** patella tendon and **B:** medial gastrocnemius, where ROI node, P1 was placed on the echo-absorbent marker and P2 on the regional tendon area just distal to the patella, at 50%, and 100% MVC, both ROI nodes of P1 and P2 moved along the tendon elongation. I1 and I2 showed the initial position of the ROIs. The arrows indicated the path of the ROIs has taken. At 100% MVC, the distance of P1 and P2 were measured ($d1$), and the initial distance of the ROI nodes (I1, I2) were measured ($d2$). The difference between $d1$ and $d2$ gave the relative displacement.

3.5 Study 3: In-Vivo Experiment Using Multiple Layers Tracking

This study examined local tendon strain across the anterior, middle, posterior at the proximal and the distal aspect of the patella tendon during ramped isometric contractions. The chosen automatic tracking algorithm (i.e. NCC) was used to track multiple regions of interests (ROI) simultaneously arranged in layers with the same block sizes and positions at each tendon layers. Unlike previous experiments, this study compares the results of each layer and the proximal and distal aspect of the patella tendon to initiate a much more detailed understanding of the tendon in injury, repair and also in response to various training interventions.

3.5.1 Participants

Sixteen healthy limbs were used for data collection in this study from healthy male subjects with an average age of 28.0 ± 6.3 years; height of 1.7 ± 0.04 m and body mass 79 ± 5.4 kg.

3.5.2 Tracking Regions

The whole length of the patella tendon was imaged (see Figure 3.17) and the thickness of the tendon was measured at 8–9mm (a). The regions being examined were at the proximal (b) and distal ends (c). The regional layers for each tendon end are divided into anterior, mid and posterior (d-f). The peninsula bone is located at the proximal ends (g) and tibia at the distal ends (h). The line at the top of the image is the skin layer (i).

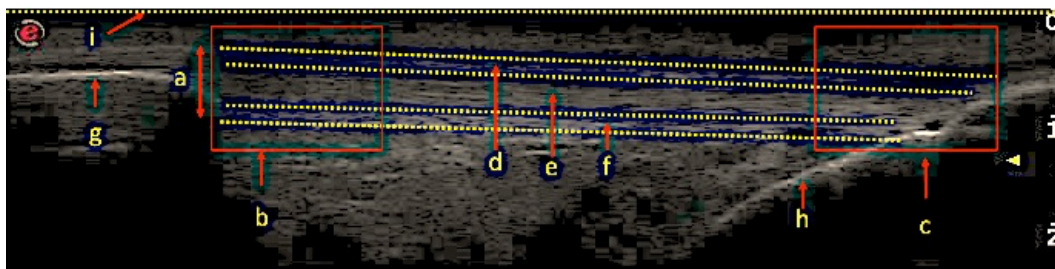


Figure 3.17: Example of patella tendon and regions being investigated.

3.5.3 Hardware and Software Setup

Unlike the previous study, an upgraded ultrasound system was used for this experiment (MyLab70, <http://www.esaote.com/>) with a 7.5 MHz 100mm linear array, B-mode ultrasound probe with a depth range of 67mm was used to image the patella tendon in the sagittal plane. The wider ultrasound probe was capable of capturing more width of the tendon compared to the earlier ultrasound probe (see Figure 3.18). The same setup as before was used for assessing the patella region. The images were then captured at 25 frames per second (fps) in DV format, with image size of 800x600 pixels, and stored locally into the storage memory. The captured frames were then transferred to the computer system for the tracking process. Again, as in the earlier experiments, scaling in pixels per mm was determined from ImageJ software by using the known depth of field in the ultrasound images, (1 mm = 11 pixels in the x and y directions) and utilised as a calibration factor in the automated tracking system to ensure equivalent pixel to mm ratios.

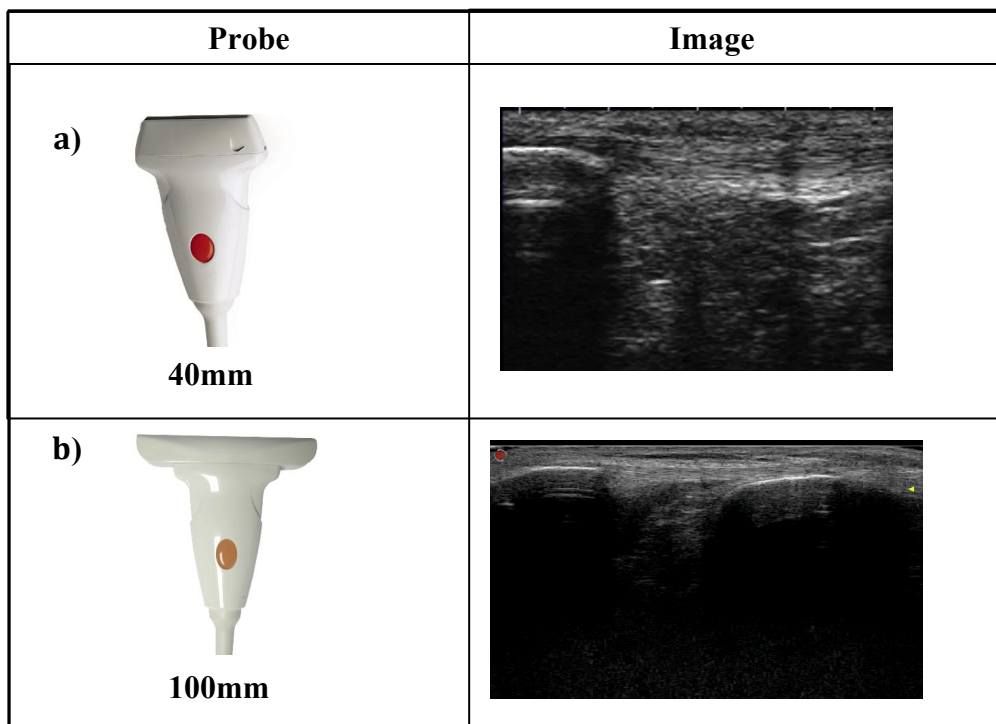


Figure 3.18: Comparisons between a) 40mm probe transducer and b) 100 mm probe transducer. Image produced by the latter probe has a higher depth and broader viewing range.

The transducer probe was fixed statically at the skin surface, similarly to the previous study. Also, the torque output during isometric quadriceps contraction was determined using an isokinetic dynamometer with the participant in a seated position. The same knee setup was set at 90° flexion and hip at 85°, and a lever attachment cuff was also placed on the lower leg at ~3cm just above the medial malleolus. The tendon was imaged during ramped voluntary isometric contractions (3-4 seconds). The maximal isometric quadriceps contraction efforts were repeated three times to ensure tendon preconditioning prior to the test. Participants performed ramped isometric contractions from 0% MVC (rest) to the maximum (100% MVC) over a 3s to 4s period. Three trials were repeated with 180s rest between contractions. The mean values of strain for the three contractions were used for subsequent analysis.

The EMG of the long head of the biceps femoris (BF) muscle was evaluated in order to determine the level of antagonistic muscle co-contraction during the isometric knee extension (S. Pearson et al., 2006). The assumptions were that BF was representative of its constituent muscle group (Carolan et al., 1992) and that the biceps femoris EMG relationship with knee flexor torque was linear (Lippold, 1952). Three maximal isometric knee flexion contractions were carried out obtaining the EMG at maximal flexion torque. The root mean square EMG activity of the biceps femoris during knee extension was divided by the maximal flexor EMG. Then the maximal flexion torque was multiplied by this value to determine co-contraction torque. The patella tendon force was finally determined by dividing the total torque by the patella lever arm as determined from the literature (Krevolin et al., 2004, Tsaopoulos et al., 2006).

Figure 3.19 shows the regional tracking of ROIs where R1 and R2 are the arbitrary pixel regions in the tendon arranged into layers; anterior (**a**), mid (**b**) and posterior (**c**). The ROIs are marked on a typical tendon excursion on both proximal (**A**), and distal (**B**) ends showing shift in ROI's from the resting tendon, at 50% and 100% MVC. The vertical dotted lines show the initial positions of the ROIs. The arrows show the movement of each ROI during the tracking experiment.

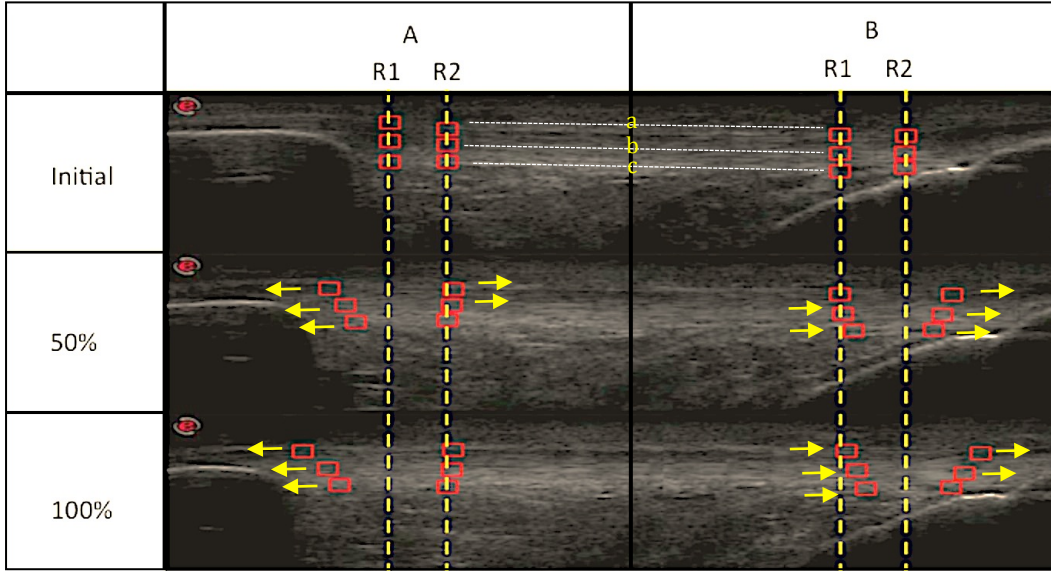


Figure 3.19: Regional tracking of the patella tendon.

The resultant displacement for each layer is measured as follows:

$$\Delta d = \left(\sqrt{(x_{R2} - x_{R1})^2 + (y_{R2} - y_{R1})^2} \right)_{f_n} - \left(\sqrt{(x_{R2} - x_{R1})^2 + (y_{R2} - y_{R1})^2} \right)_{f_1} \quad (3.7)$$

where Δd is the change of length, (x_{R1}, y_{R1}) is the position of first ROI, (x_{R2}, y_{R2}) is the position of second ROI, f_1 is the initial frame and f_n is the subsequent frame. The strain is measured as follows:

$$\varepsilon = \frac{\Delta d}{\Delta i} \quad (3.8)$$

where ε is the strain measurement, Δd is the change of length, Δi is the initial distance between R1 and R2. All the initial proximal and distal regions were aligned vertically to enable quantification of any differences in regional strain within a localised site of the tendon.

3.6 Speckle Tracking Software Design and Implementation

As described in Section 3.1 (see Figure 3.1), the speckle tracking software provided a framework to support the studies described in the previous Sections. In general, it loaded the captured ultrasound image sequence (Input). Then, it performed the speckle tracking operation frame-by-frame of the image sequence, using a selected tracking algorithm and user-defined parameters appropriate for a particular study (Processing). A new tracking algorithm (NCCMSE) is introduced by combining both the NCC and MSE algorithms with Signal-to-Noise Ratio (SNR) as the selector, and tested its effectiveness against the selected tracking algorithms. Further discussion of the algorithm is described in Section 3.6.3.4. Finally, it displayed the results of the tracking operation after each frame and the measurements at the end (output).

3.6.1 Software Design and Implementation Overview

The speckle tracking software was developed in Matlab version 8.1 R2013a for Apple Macs with the Image Processing Toolbox installed (<http://www.mathworks.com/>). In order to run the Matlab editor, version 6 (at least) of Java runtime is required. The Image Processing toolbox provides access to built-in functions such as importing and exporting images, displaying and exploring images and many more.

The user interface (GUI) of the tracking software was developed using the tool of GUI development environment (GUIDE). The component properties and behaviours were added using the Matlab scripting programming code giving GUI advanced functionality. All algorithms that were used and developed for the studies were programmed from scratch to give a better understanding of how each tracking algorithm worked and for more control over the algorithm. The design of the software was relatively straightforward as it allows the user to choose and inspect an ultrasound video, and manually mark the tracking region (ROI) by using the mouse pointer over the displayed tendon image. Also, the configuration settings can be

configured through the graphical user interface, before executing the selected tracking algorithm frame-by-frame on a chosen ultrasound video, and displaying the results after each frame.

Since the fibrous tendon was displayed as random speckles, which sometimes appears as a black patch causing the tracking algorithm to fail, some extra logic was required to handle this situation. This involved adding two markers to regions that are clearly visible such as the bone structure, or the skin layer. If the position of the matched value moved erratically, or out of the search window, the position was then compared to the movement of the visible landmark (e.g. tendon junction). In the worst-case scenario if no matched value existed within the threshold range, the position from the previous frame was then used as the updated position, thus, indicating that there was no movement between the images. If the software finds no movement within five successive frames, the tracking process stops. The software was designed in modular format or functions as where each function performs individual tasks and communicates with the other functions as shown in Figure 3.20.

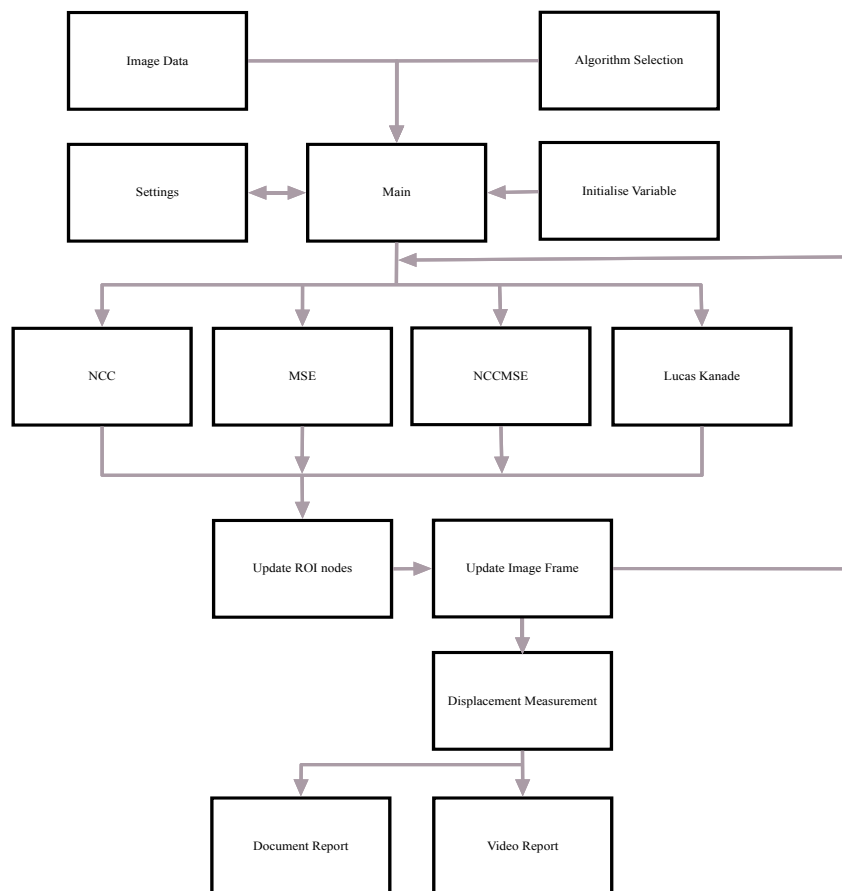


Figure 3.20: The module structure for the speckle tracking software.

The main function sits on top of the module life cycle, where all data related to the image being read and the configuration settings required for the tracking operation were gathered (i.e. images, settings, algorithm selections and variables). Then, from the main function these accumulated data were shared across the four modules containing the tracking algorithms that were to be investigated: NCC, MSE, NCCMSE and LK. At the end of each frame, the position of the ROIs were updated, and the displacements of the tracked regions recorded to the temporary computer memory so that the animation of the movement can be created and stored as a video. The positions of the ROIs and the frame-by-frame displacements are saved into a document, such as a spreadsheet giving the frame-by-frame displacements. These data are suitable to be used by other analysis software such as SPSS. A graphical user interface that was developed to control the operation of the speckle tracking software is presented in the next Section, and this is followed by implementation details for the four tracking algorithms.

3.6.2 The Graphical User Interface (GUI)

Figure 3.21 shows the main window of the graphical user interface (GUI) for the speckle tracking software. At the top of the main screen, is a menu bar containing the main options: the File **(A)**, Tools **(B)** and Report **(C)**. The File options include opening a video file, saving and recovering the configuration settings and exiting the software, while the Tools options allows the user to set the calibration scale (ultrasound depth) and to enable the ROI selection on the screen, and the Report options let the user specify whether to save the results to video format or save the displacement results frame-by-frame into a spreadsheet, which could be used by other analysis software such as SPSS. The main part of the tracking system is the viewing panel **(D)**, which occupies most of the main screen. The viewing panel displays the video ultrasound image and can be controlled frame-by-frame using the slider **(E)** or by using the buttons **(F)**.

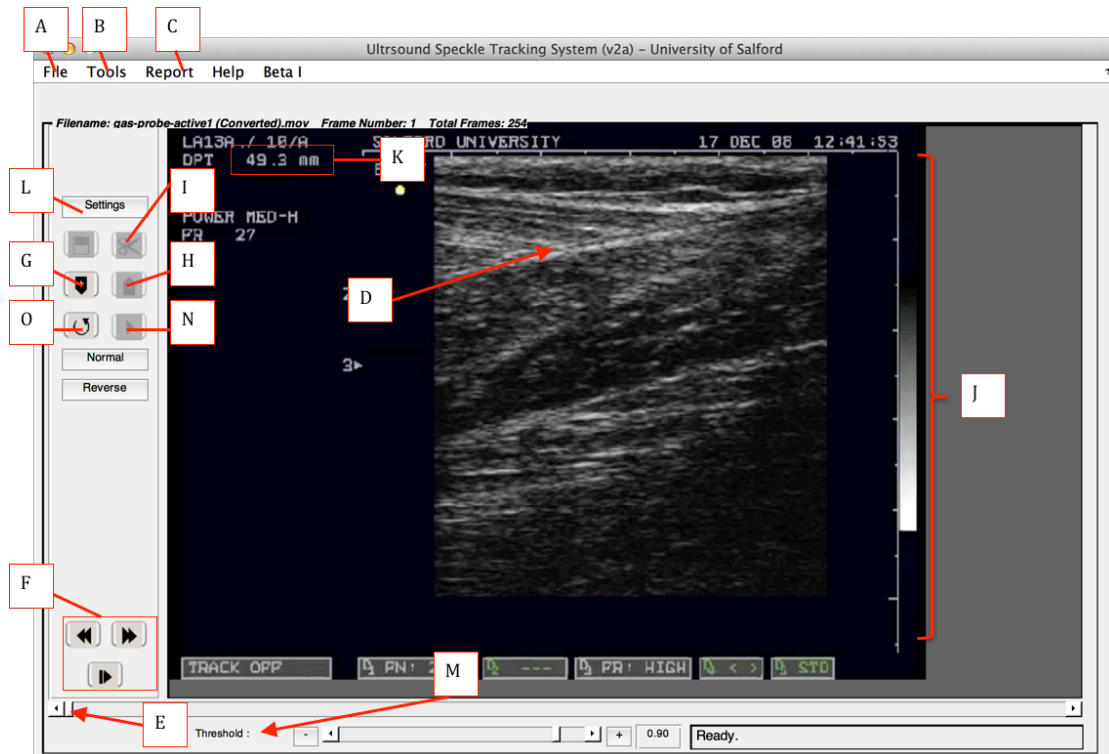


Figure 3.21: The graphical user interface (GUI) for the main window of the tracking software.

Ensuring the image data only displays the useful information for tracking is critical. The image is obtained manually by placing the ultrasound transducer probe over the skin surface. A slight change while handling the probe leads to inconsistent movements of the captured image during the experiment and may result in erroneous speckle scattered around the image rendering the frame useless for tracking. Based on this uncertainty, the software includes the ability to select the portion of the image frame with good tendon movement by using the frame slider (**E**) and set the starting keyframe using the provided button (**G**) to a feasible duration and set it as end keyframe (**H**). The trim button (**I**) trims the selected keyframes to the desired duration, giving only useful frames to be analysed.

The calibration of the measurement is set by the use of calibration tool from the Tool option (**B**). This enables the user to measure by moving the mouse cursor along the depth scale at the right side of the image (**J**). The calibration counts the number of pixels. A small window (see Figure 3.22) will appear prompting the user to key in the known distance which is the depth used for scanning and was set from the

ultrasound machine. The depth information is shown at the top left of the main image **(K)**. The pixel count is shown as pixel distance and will be used to calibrate the measure to pixels per mm.

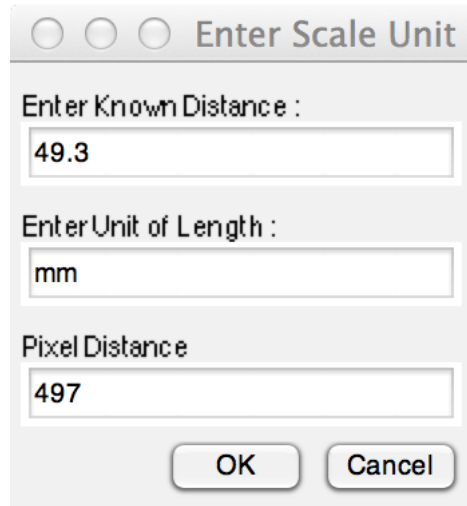


Figure 3.22: The graphical user interface (GUI) for the scale unit.

Selecting the setting button **(L)** displays the settings screen as shown in Figure 3.23, which allows the user to select and configure the tracking algorithm to be used in the tracking process. At the top of the setting screen, is the Tracking Algorithm drop-down **(a)** allows the user to select one of the four tracking algorithms being investigated in the present experiment (MSE, NCC, NCCMSE, Lucas-Kanade). The ROI size selection dropdown **(b)** controls the block size (in pixels), options available are 5x5, 11x11, 15x15, 21x21 and 25x25 (These options were primarily for the pilot study where the optimal block size was investigated). The Search Window **(c)** enables the user to set the size of the search window for the tracking process.

The Layers option **(d)** sets the number of layers for the ROI where the 1 Layer consists of only a single ROI; the 2 Layers consist of two 2-ROI end points while multi layers consists of multiple layers (maximum up to six layers) where each layer can be marked with 2-ROIs. However, in the case of tracking multiple region of the tendon only three layers were needed and this can be done by placing 2-ROIs at each distal ends (proximal and distal) for each layer. Information regarding the images

such as the file location, the sizes, and the calibration parameters were also displayed on the screen as shown (e). The Scale Setting showed the present scale parameters (f) used by the software; the user can store these parameters as global if the same scales are to be used for another tracking process.

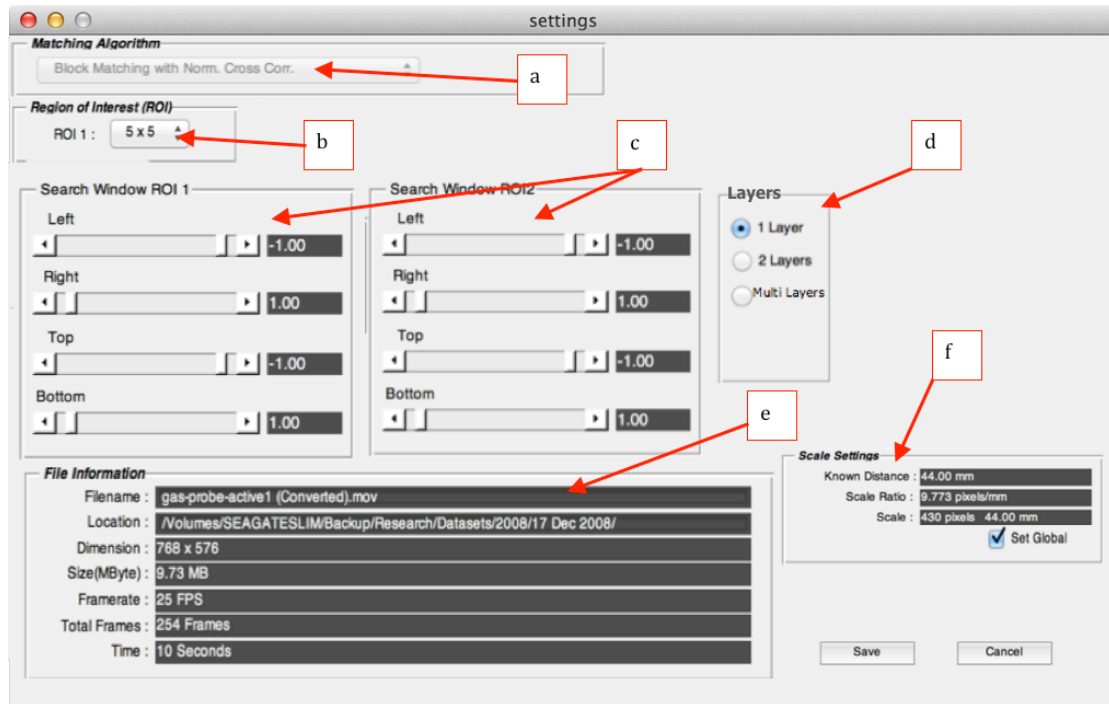


Figure 3.23: The settings (GUI) of the tracking software.

A threshold slider was set to eliminate poor matches (M) (see figure 3.21) in the movement between frames. The threshold setting was set to the default value of 0.9, although a higher threshold could be selected for greater accuracy. A lower threshold will result in a slower tracking process, while the highest threshold often leads to no movement being found since the image data are speckles. The value of 0.9 was found to be a good compromise. The good value of the threshold was obtained from the results covered in section 5.2 of chapter 5. Finally, the Start button (N) starts the tracking process, and Reset button (O) resets screen for new tracking operation.

3.6.3 The Speckle Tracking Algorithms

This section describes the implementation of the four speckle tracking algorithms (MSE, NCC, NCCMSE, LK) that were described in the previous Chapter.

3.6.3.1 MSE

This tracking algorithm as a block-matching algorithm uses the Mean Square Error (MSE) to give a measure of the difference between the blocks in the initial and target frames. The flow diagram for the implementation of this algorithm is shown in Figure 3.23. The algorithm starts with the *image A* assigned as a reference image from the initial frame K and *image B* assigned as the target image from frame $(K+1)$. The initial block (I) was then extracted from *image A* with the pixel size of the block set to *width x height* ($m \times n$). Using the BMA search method the search window was then set to $(M \times N)$ two times larger than the size of the initial block, similar to the description in Section 2.4.2 (Chapter 2). The search area starts from position $(x=1, y=1)$ and the motion vector starts from $(u=0, v=0)$.

The target block (T) of *width x height* ($m \times n$) size was extracted from *Image B* pixel by pixel within the search window while $x < M$ and $y < N$ with (x, y) and (u, v) values increased by 1 pixel. Next, the estimator (error) was calculated using MSE where the differences of the pixels in the initial block (I) and target block (T) were squared and averaged with the size of the template $(M \times N)$ and stored into memory vector. When the search window reached $(x = M, y = N)$, the lowest (minimum) error results from the memory vector were selected and compared with the Threshold, and if the error was less than the Threshold (error \leq Threshold), the algorithm then checks for the final location of frame K .

If frame K was not at the final location, the algorithm updates the target block (T) to be the initial block (I). The next frame $(K+1)$ was also updated to be a new target frame where the new target block (T) was extracted. The algorithm then checks for the position of the centre point p of previous initial block $I[(x, y); K; p]$ and

compared the difference with the current initial block $I[(x,y);K+1;p]$ to validate the correct position of the tracking point.

If a displacement of more than 15 pixels was observed, the next minimum error value from the memory vector was selected with its corresponding Target block $T(x,y)$ and assigned as the new initial block (Irregular Movement – see Section 3.6.4.2), or otherwise the algorithm proceeds with the same search process iterated and stopped when frame K reach to the final frame. If none of the estimator (error) results met the Threshold, the algorithm skips the current target frame (T) to the next frame ($K+count$) as a new target frame. The same search procedure was repeated up to five frames until the estimator (error) met the Threshold condition, however, if none of the results from the five frames reached the Threshold condition, the algorithm stops the search process (Stationary Movement – see Section 3.6.4.1).

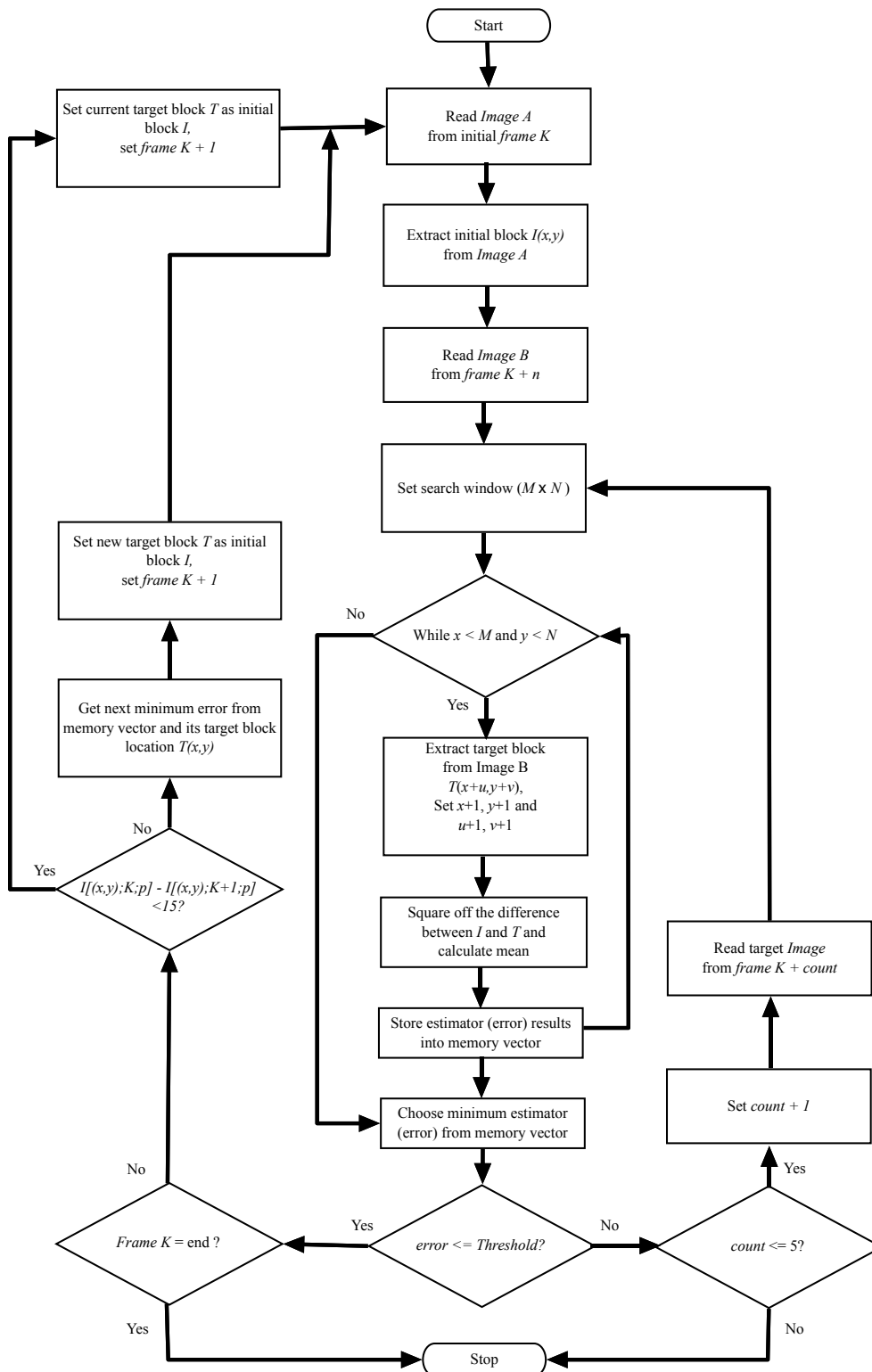


Figure 3.24: Schematic diagram of MSE.

3.6.3.2 NCC

This tracking algorithm as a block-matching algorithm uses the Normalised Cross Correlation (NCC) to give a measure of the average similarity between the blocks in the initial and target frames. The flow diagram for the implementation of this algorithm is shown in Figure 3.25. The algorithm starts with two images A and B that were used as the data input. The *Image A* was then designated as the reference image from the initial frame (K), and *image B* was assigned as the target image from frame ($K+1$). Next, the initial block (I) was extracted from *image A* and using the BMA search method, the target block (T) was then extracted from *image B*. The size of both initial and target were set to *width x height* pixels ($m \times n$). Meanwhile, the search window was set to ($M \times N$) two times larger than the size of the initial block, similar to the description in Section 2.4.2 (Chapter 2) and then, the search area starts from the position ($x=1, y=1$) with motion vector starting at ($u=0, v=0$).

The search stops when (x, y) reaches the maximum size of the search window ($M \times N$) twice the size of the target block. Next, the target block (T) was extracted from *Image B* pixel by pixel within the search window while $x < M$ and $y < N$ with (x, y) and (u, v) values were increased by 1 pixel. Both zero mean image of (I) and shifted zero mean templates of (T) were then calculated by subtracting their mean features \bar{I} and \bar{T} respectively. The numerator is then calculated to give mean function $d1$, and the denominator was calculated to give the standard deviation $d2$. Next, the correlation coefficient (corr) was calculated by dividing the mean function $d1$ by its standard deviation $d2$ and ($M \times N$) and stored into memory vector. When the search reaches ($x = M, y = N$), the maximum correlation results were selected from the memory vector and compared with the Threshold.

If the error was within the Threshold (error \geq Threshold), the algorithm then checks for the final position of frame K . If frame K was not at the final location, the algorithm updates the target block (T) as the initial block (I). Then, the algorithm checks for the position of the centre point p of previous initial block $I[(x,y);K;p]$ and compares the difference with the current initial block $I[(x,y);K+1;p]$ to validate the correct position of the tracking point. If more than 15 pixels difference were observed, the next minimum error value from the memory vector was selected with its corresponding target block $T(x,y)$. Then it is assigned as the new initial block (Irregular Movement – see Section 3.6.4.2); otherwise the next frame ($K+1$) was updated to be a new target frame where the new target block (T) was extracted.

The same search process was iterated and stopped when frame K reached the final frame. If none of the correlation (corr) results met the Threshold, the algorithm skips the current target frame (T) to the next frame ($K+count$) as a new target frame. The same search procedure was repeated up to 5 frames until the correlation (corr) value met the Threshold condition (Stationary Movement – see Section 3.6.4.1), however, if none of the results from the 5 frames met the Threshold condition, the algorithm stops the search process.

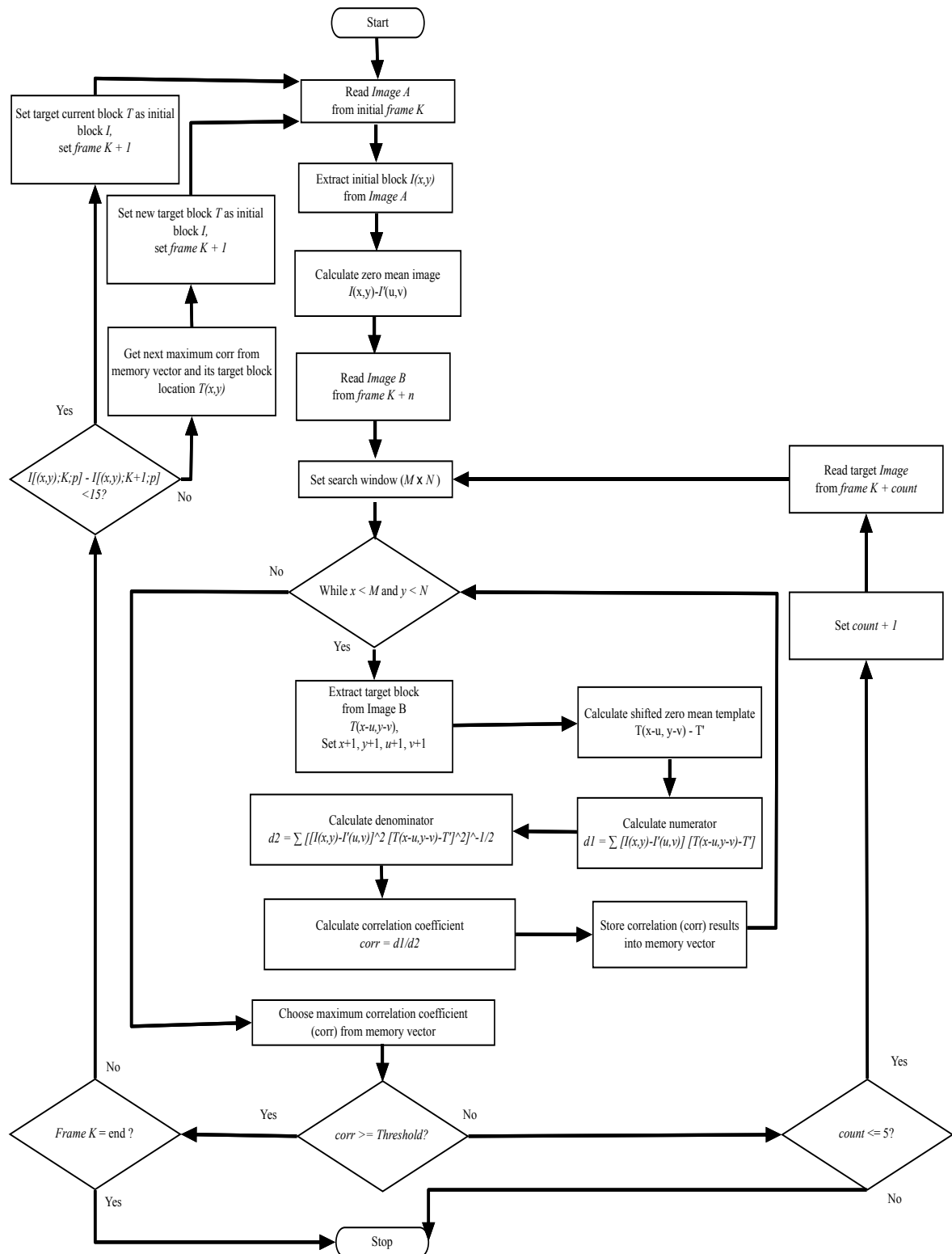


Figure 3.25: Schematic diagram of NCC.

3.6.3.3 LK

This tracking algorithm is an optical-flow algorithm that uses the Lucas-Kanade method to find the motion estimation between the image and the template. The flow diagram for the implementation of this algorithm is shown in Figure 3.27. The process starts with the input *image A* that was warped with a set of parameterized warps at sub-pixel locations $I(W([x,y];p))$ where p is the vector parameter. Next, the gradient value of *image A* was calculated giving the variable ∇I . *Image B* was then read from the frame $K+n$. Then, the template block $T(x,y)$ of size *width* x *height* pixels ($M \times N$) was extracted from *image B*. The algorithm then proceeds with subtracting the warped image A from the template block $T(x,y)$, giving the error value that indicated the best match found in *Image A*. In the next process, the steepest descent image $\nabla I \frac{\partial W}{\partial p}$ was calculated by multiplying the gradient *image A* (∇I) with the Jacobian of the warp $\frac{\partial W}{\partial p}$.

Next, the motion vector Δp was estimated by performing the Gauss-Newton approximation over the steepest descent image. In the next process, the algorithm compares Δp with the Threshold. If $\Delta p \leq \text{Threshold}$ was found, the algorithm proceeds by checking that Frame K was not positioned at the end of the frames, otherwise the search process stops. Then, the algorithm checks for the position of the vector point p with $p + \Delta p$ to validate the correct position of the tracking point. If more than 15 pixels difference were observed, the algorithm retains the current vector p (Stationary Movement – see Section 3.6.4.2) and proceeds with the next frame $K+1+n$, otherwise the program updates the motion vector $p \leftarrow p + \Delta p$ and the increases frame K by 1. The processes iterated until the pre-specified stopping criterion is met. If Δp did not meet the Threshold condition, the algorithm will retain the current motion vector p . The algorithm then proceeded with the next frame $K+\text{count}$ and iterated for five times until the Threshold condition was met; otherwise, the algorithm will stop the search process when count was more than five iterations (Stationary Movement – see Section 3.6.4.1).

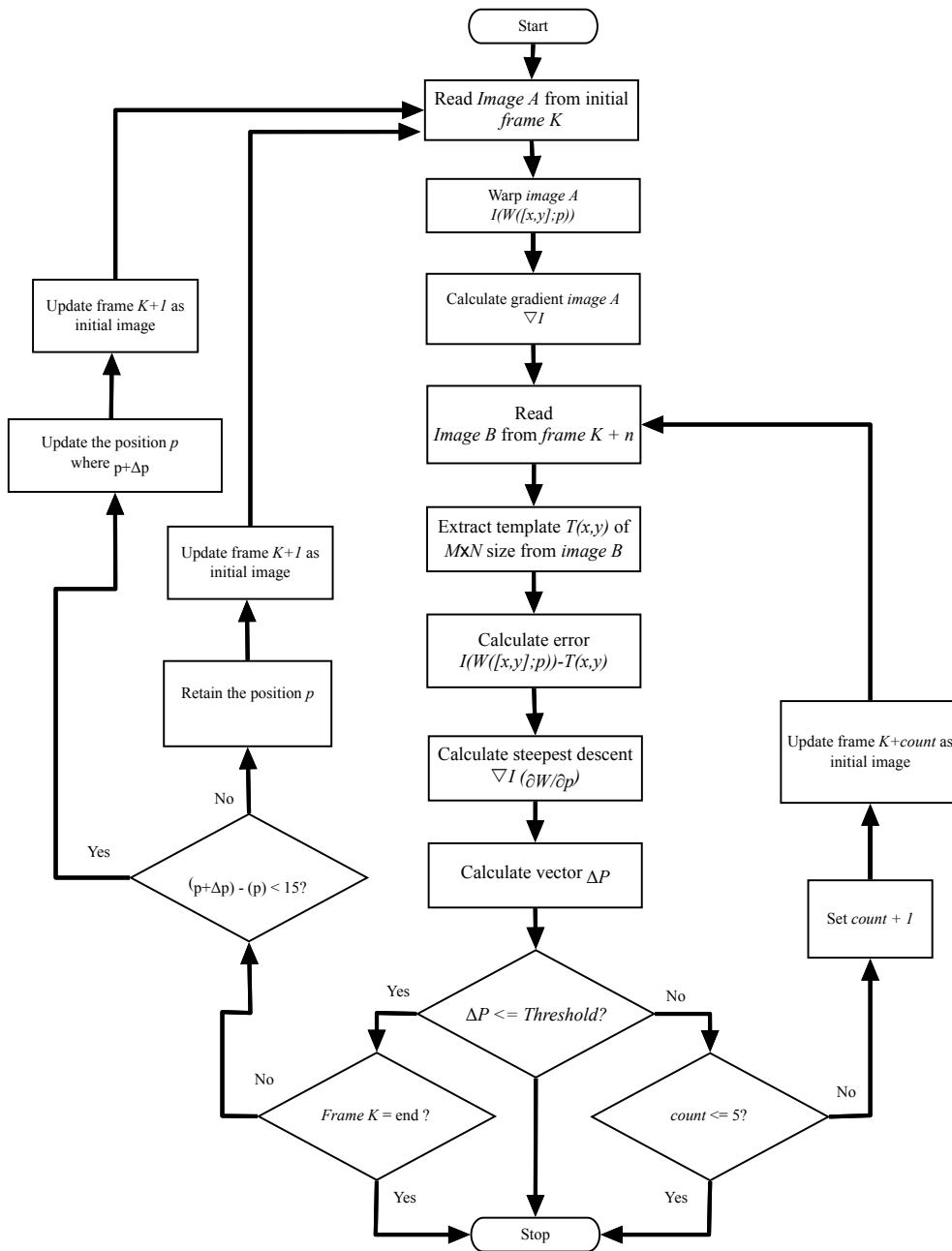


Figure 3.26: Schematic diagram of LK.

3.6.3.4 NCCMSE

Both NCC and MSE were claimed to be robust and suitable for tracking the ultrasound image constructed from speckle noise (Hibon et al., 1995, Twomey et al., 1996, Revell et al., 2004, Hii et al., 2006, Pearson et al., 2012). Since both algorithms used similar search method of block matching algorithm (BMA), the idea of combining the two algorithms to improve the tracking results can be carried out. Previous works have been attempted at using the Signal-to-Noise Ratio (SNR) as algorithm selector (Cohen et al., 2002, Revell et al., 2008). For this study, both algorithms were alternated based on the Signal-to-Noise Ratio (SNR) to examine if by combining these two algorithms the tracking improved. The SNR was measured using the coefficient of variation, which is commonly used in image processing. The mean value of initial block I is divided to the standard deviation of template block T and is notated as:

$$SNR = \frac{\mu(I)}{\sigma(T)} \quad (3.9)$$

where μ is the mean pixels of I and σ is the standard deviation of T over a given neighbourhood assuming that the pixels in T represent the noise in I .

When the standard deviation is equal to the mean of pixel, so its coefficient of variation is equal to 1. Therefore, when distribution of coefficient of variation is considered low variance (< 1) then MSE is selected. This is because when only fewer pixel formations exist, then more black patches formed around the speckle areas which tracks better using the MSE algorithm. However, if the distribution of coefficient of variation is considered high variance (≥ 1) then NCC is selected, due to its sensitivity towards the formation speckle patterns. The SNR value will be the decision factor of using MSE or NCC to improve the tracking method:

$$SNR \begin{cases} < 1 = MSE \\ \geq 1 = NCC \end{cases} \quad (3.10)$$

where the SNR implemented in the tracking system gave a range value of 0 to +inf.

Any SNR value less than 1 means that the image has low intensity, possibility fewer speckles were found but with darker patches around the searching area, then the tracking will proceed using the MSE algorithm. If the SNR value was equal to or greater than 1 showing that a high intensity with heavily speckled area was found then the tracking will proceed using the NCC algorithm.

The flow diagram for the implementation of this algorithm is shown in Figure 3.27. The process begins by reading both initial and target *images* (*A* and *B* respectively). Then, the initial block (*I*) was extracted from *image A* and using the BMA search method, the target block (*T*) was then extracted from *image B* and the size of both initial and target were set to *width x height* pixels ($m \times n$). The search window was then set to *width x height* ($M \times N$) two times larger than the size of the initial block and the search area starts from the position ($x=1, y=1$) with motion vector starts at ($u=0, v=0$). Both search method and initial estimation vector were then set to ($x=1, y=1$) and ($k=0, l=0$) respectively. Next, the target block (*T*) was extracted from *Image B* pixel by pixel within the search window while $x < M$ and $y < N$ with (x, y) and (u, v) values increased by 1 pixel.

The algorithm proceeds with calculation of Signal-to-Noise Ratio (SNR) as the decision selector to choose either MSE or NCC. If SNR value was ≥ 1 , then NCC will be chosen as its similarity measure; otherwise MSE will be chosen. The MSE similarity measurement description was described in Section 3.6.3.1 and NCC in Section 3.6.3.2. If the frame (*K*) was not at the final position, the target block (*T*) will be assigned as the new initial block (*I*) and next frame ($K + 1$) will be assigned as the new target frame. Finally, the algorithm will repeat the same procedure until the frame (*K*) reaches the final frame and stops.

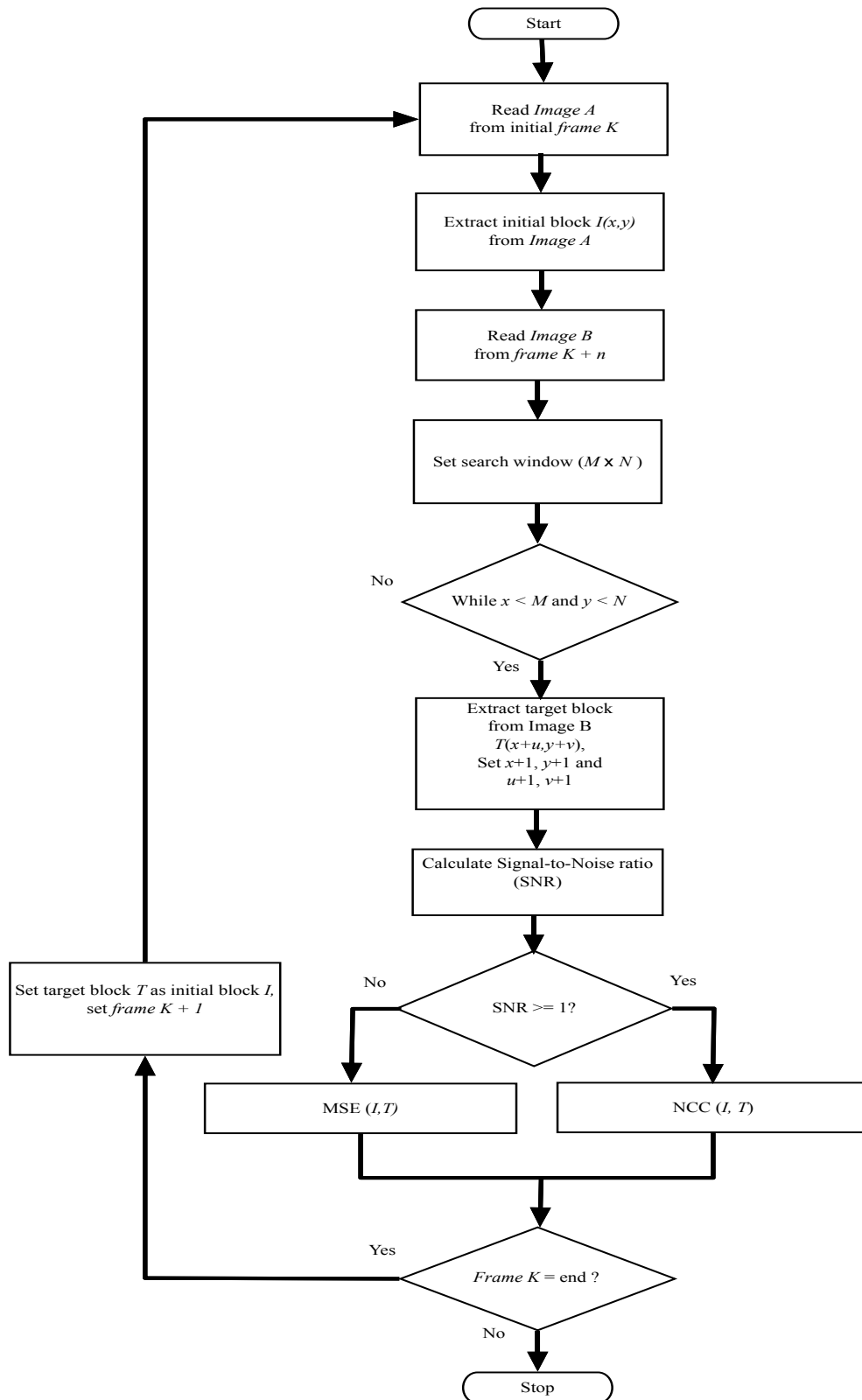


Figure 3.27: Schematic diagram of NCCMSE.

3.6.4 Individual Error Analysis

One of the biggest problems found with all speckle tracking algorithms were the errors that arise due to the inconsistency of speckle patterns that comes and go between frames. Eventually, all algorithms fail to track the correct ROI along successive frames when more errors occur. Two types of error were identified:

- Stationary movement error
- Irregular movement error

The causes of these and the solutions adopted are discussed in the following sections.

3.6.4.1 Stationary Movement Error

The error happened when tracking showed no movement and the algorithm fails to find any match that met the threshold condition between the two frames. To solve this problem, the tracking algorithm proceeded with analysing the images from the next frame and marked if no movement was found and the previously successful matched image was used as the image reference. This procedure was repeated for the next five frames, and if no movement was found after five-frame duration, the software algorithm would terminate. If more errors were found during the tracking process the tracking would appear to be no movement at all as no possible matches were found throughout the whole image sequences. The study conducted was to understand better how the algorithm deals with unmatched criteria. The study also helped in identifying the optimum algorithm to be used in the later stage of the analysis and integrated into the tracking software system as the primary tracking algorithm. Understanding the frequency of the errors also contributed to the enhancement of the algorithm so that any errors in movement can be repaired by the use of previous best match as recovery mechanism during the tracking process.

3.6.4.2 Irregular Movement Error

An error happened when the algorithm fails to match between the two blocks correctly causing the tracking to track a different region throughout the whole tracking process. The movement of the tracked ROI can be seen as if it is jumping around erratically and sometimes the movement appeared to move further than it should move or move in the direction opposite the tracking path. The movement was considered to be an error when the tracked ROI jumped 15 pixels more than the previous tracked movement. This anomaly triggered the software algorithm to recheck the path of the tracking system and reanalysed the tracking process by selecting the next lowest (MSE) or highest (NCC) estimation values, and the procedure proceeds until the best location was found.

For counting the errors, every movement that exceeded 15 pixels from the previous tracking path was counted and averaged to get the mean value so that mean differences can be identified between algorithms and plotted to illustrate the difference. Pairwise comparisons were also used to the p value between the algorithms to differentiate further the interactions between the data collected for each algorithm. As the previous analysis, the errors found from this section did not represent the total errors for the algorithm in failing to track the tendon regions of highly speckled ultrasound images. The analysis conducted here contributes another half of the two principal errors identified, which influences the ability of the tracking algorithm to follow the movement.

Similar to the previous analysis, the idea of analysing the errors was to understand better how the algorithm deals with unmatched criteria. The analysis also helped in identifying the optimum algorithm to be used in the later stage of the analysis and integrated into the tracking software system as the primary tracking algorithm. Understanding the frequency of the errors also contributed to the enhancement of the algorithm so that any errors in movement can be recovered by the use of last best match as a recovery mechanism during the tracking process.

3.7 Summary

In summary, this chapter is a descriptive chapter where the methodology of data collection and analysis of the tracking algorithms are presented. The evaluation of the four algorithms and planned experiments for each study are described in the next chapter. The design and implementation of the speckle tracking software that was required to support these studies area was also described including the description of the graphical user interface (GUI) and the three tracking algorithms (NCC, MSE, LK) that were identified in the previous chapter. A new method is introduced, which is the combination of the algorithms NCC and MSE and therefore named as NCCMSE algorithm. With the use of SNR as the decision selector, these two algorithms are alternated to improve the tracking based on the value of the SNR. The performance of the four selected tracking algorithms will be described in the following Chapter.

The tracking accuracy as well as the computational cost of each algorithm was compared to the standard manual measurement. Finally, the reliability of the tracking algorithms are also discussed where two kinds of errors are being described as stationary movement errors and irregular movement errors. These reliability factors are evaluated in the next following chapter.

Chapter 4

Study 1: Evaluation of The Four Tracking Algorithms

Overview

In this chapter, the results of the pilot study are presented. The main purpose of the study was to evaluate the four selected tracking algorithms against the standard manual measurement. Error analysis was also evaluated for each algorithm. The outcome of this study was to identify and select the best performing tracking algorithm for use in the two remaining studies.

4.1 Evaluation of The Tracking Algorithms

The main purpose of the evaluation was to evaluate the performance of the four selected tracking algorithms in terms of the accuracy as compared to the standard manual measurement and their tracking reliability. The algorithms were evaluated in a series of experiments that took both passive and active movements on the patella tendon and the medial gastrocnemius tendon. The experimental setup and procedures were described in Chapter 3. The tracking accuracy was quantified in terms of the mean error between the position derived from the standard manual measurement, and tracking algorithms. The results obtained for passive movements are given in Section 4.2 and for active movement in Section 4.3.

Reliability was assessed by averaging the number of tracking errors, which was observed in the tracking sequence. Two sources of error were identified in the previous Chapter, when the tracking algorithm could not find a matching region in the next frame (stationary movement). The threshold value was set to ≥ 0.90 and was

chosen based on the analysis conducted in Chapter 5). When the tracking algorithm finds the wrong target block (irregular movement), these errors were evaluated independently and, the results obtained for both the stationary and irregular errors during passive and active movements are given in Sections 4.4 and 4.5 respectively. All the results are discussed in Section 4.6 and the best performing algorithm identified.

4.2 Tracking Accuracy During Passive Tendon Movement

This experiment evaluates the performance of the four tracking algorithms when the tendon was relaxed at 0% maximum voluntary contraction (MVC), and the probe was moved over the sagittal plane of the patella tendon (knee) along the skin surface for a distance of approximately 2-3 cm. The areas of interest for this study were the tendentious areas of the patella (knee) and gastrocnemius (ankle). Two experiments took place as explained in Chapter 3.

The errors are calculated from the displacements of the ROI. In the first experiment, which involved the patella tendon, the mean displacement of the ROI from automatic tracking and manual measurement from ImageJ were shown in table 4.1.

Test	Mean Displacement (mm)				
	MSE	NCC	NCCMSE	LK	Manual
Knee Passive	14.50±1.38	15.79±1.57	14.90±1.30	13.48±1.02	15.35±1.22
Difference (mm)	0.85±1.84	-0.44±1.99	0.46±1.79	1.87±1.59	-

Table 4.1: Mean displacement of 10 samples and difference (in millimetres) of each tracking algorithm against the standard manual measurement of passive movement at the patella tendon.

The manual measurement is based on standard measurement method and each algorithm mean value is compared against the value from the manual measurement to give the difference between mean as shown in equation 4.1:

$$d = \overline{\text{man}} - \overline{\text{algo}} \quad (4.1)$$

where d is the difference between two means. The standard error of the difference between means is shown in equation 4.2:

$$\sigma_{\text{man-algo}} = \sqrt{\sigma_{\text{man}}^2 + \sigma_{\text{algo}}^2} \quad (4.2)$$

where σ is the variance of the sample, n is the sample size, $algo$ is the measurement using the algorithm and man is the manual measurement.

The NCC tracking algorithm gave very little difference against manual measurement with the difference value of -0.44 ± 1.99 mm while NCCMSE gave the difference of 0.46 ± 1.79 mm. The MSE tracking algorithm and manual measurement gave a difference of 0.85 ± 1.84 mm while the Lucas-Kanade tracking algorithm gave the highest difference of 1.87 ± 1.59 mm. However, multiple t-tests revealed no significant differences ($p > 0.05$) were found between the algorithms and the manual measurement. In this experiment, the NCC and NCCMSE tracking algorithms gave the closest values to the manual measurement compared to the MSE and LK.

In the second experiment, the passive movement of the myotendinous junction of the gastrocnemius tendon was tracked. The same apparatus and procedures (as previous experiments) were used in this study. An addition of EMG was employed to calculate co-contraction torque. The mean total displacements are plotted against manual measurement as shown in table 4.2.

Test	Mean Displacement (mm)				
	MSE	NCC	NCCMSE	LK	Manual
Gastrocnemius Passive	18.76±1.56	20.26±0.80	20.68±0.93	22.42±0.94	20.90±1.31
Difference (mm)	2.14±2.04	0.63±1.54	0.22±1.61	-1.53±1.62	-

Table 4.2: Mean displacement of 10 samples and difference (in millimetres) of each tracking algorithm against the standard manual measurement of passive movement at the medial gastrocnemius tendon.

Again, the manual measurement is based on standard measurement method and all algorithms are compared against the value from manual measurement. The same multiple t-tests were used for statistical analysis, and the results showed that the NCC and NCCMSE tracking algorithms were significantly different to both Lucas-Kanade and MSE tracking algorithm ($p < 0.05$). However, none of the algorithms was found to be significantly different ($p > 0.05$) to the manual measurement. The NCCMSE mean displacement value had the smallest difference of 0.22 ± 1.61 mm, followed by NCC at 0.63 ± 1.54 mm. Both NCC and NCCMSE tracking algorithms gave < 1 mm difference compared to LK with the value of -1.53 ± 1.62 mm and MSE tracking algorithm gave the worst difference with the value of 2.14 ± 2.04 mm.

The results showed that the LK tracking algorithm struggled to track the speckle images, particularly when tracked at the areas of the patella tendon, which had no significant identifiable feature such as edges or shapes. The results improved when tracked over the media gastrocnemius tendon due to the ‘Y’ shape existing between the intersection of muscle and the tendon. However, the MSE tracking algorithm proved to be poor in both experiments because it was less sensitive to the heavily formed speckle. Both the NCC and NCCMSE tracking algorithms however, gave little differences in terms of tracking at both patella and gastrocnemius tendon, but the NCCMSE tracking algorithm was shown to give the better tracking result.

The computational costs (measured in seconds) for both experiments were also recorded (see Figure 4.1). The figure showed that among all algorithms, the LK tracking algorithm was found to give the highest computational cost with overall

performance of 470 ± 30 seconds to complete the tracking process. The NCCMSE tracking algorithm performed better than the LK tracking algorithm, but because it consisted of an SNR decision selector, it required more computation operations, and showed a total mean time of 39 ± 1 seconds. The NCC tracking algorithm was shown to have the least mean computation cost of 13 ± 1 seconds while the MSE tracking algorithm gave a mean of 27 ± 1 seconds. The passive movement experiments showed the NCCMSE tracking algorithm gave the best results but with the cost of computational time. The NCC tracking algorithm however, has only $<5\%$ different than the NCCMSE tracking algorithm with less computational cost. The LK tracking algorithms were shown to be unsuitable in this experiment.

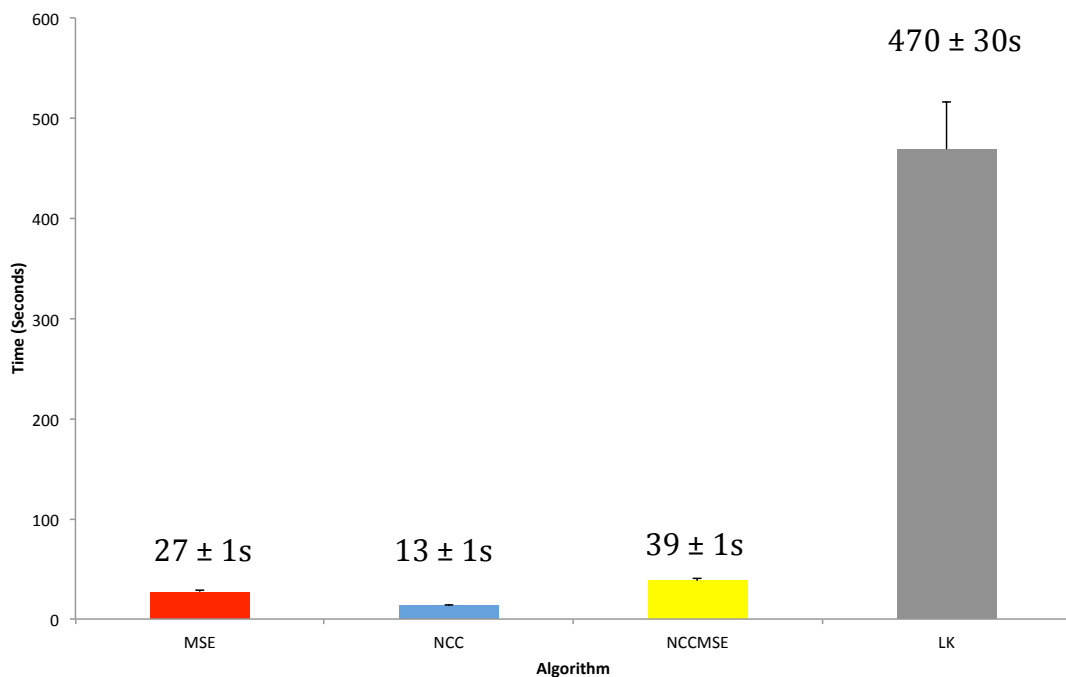


Figure 4.1: Total mean computational cost for both experiments (in seconds) between the algorithms.

4.3 Tracking Accuracy During Active Tendon Movement

The mean displacement of each tracking algorithm of the active movement of the patella tendon was measured at every 10% interval of total frames as shown in figure 4.2. For example, the individual displacement was measured from 0-10% and

followed by 10-20%. At 10%, MSE, NCC, NCCMSE and LK were shown to be not significantly different to ($p>0.05$) manual measurement with MSE gave lowest displacement value of 0.24 ± 0.19 mm when compared to manual measurement (0.37 ± 0.22 mm) and LK gave lower value of 0.30 ± 0.15 mm. Both NCC and NCCMSE gave higher displacement value of 0.45 ± 0.11 mm and 0.59 ± 0.21 mm respectively.

Again, no significant differences ($p>0.05$) were found of each algorithm against the manual measurement (1.29 ± 0.22 mm) at 20% of the frame with MSE gave the highest displacement value (1.61 ± 0.73 mm) and followed by NCC (1.48 ± 0.39 mm). NCCMSE gave lower displacement value of 0.94 ± 0.26 mm and LK gave the lowest displacement value (0.70 ± 0.30 mm).

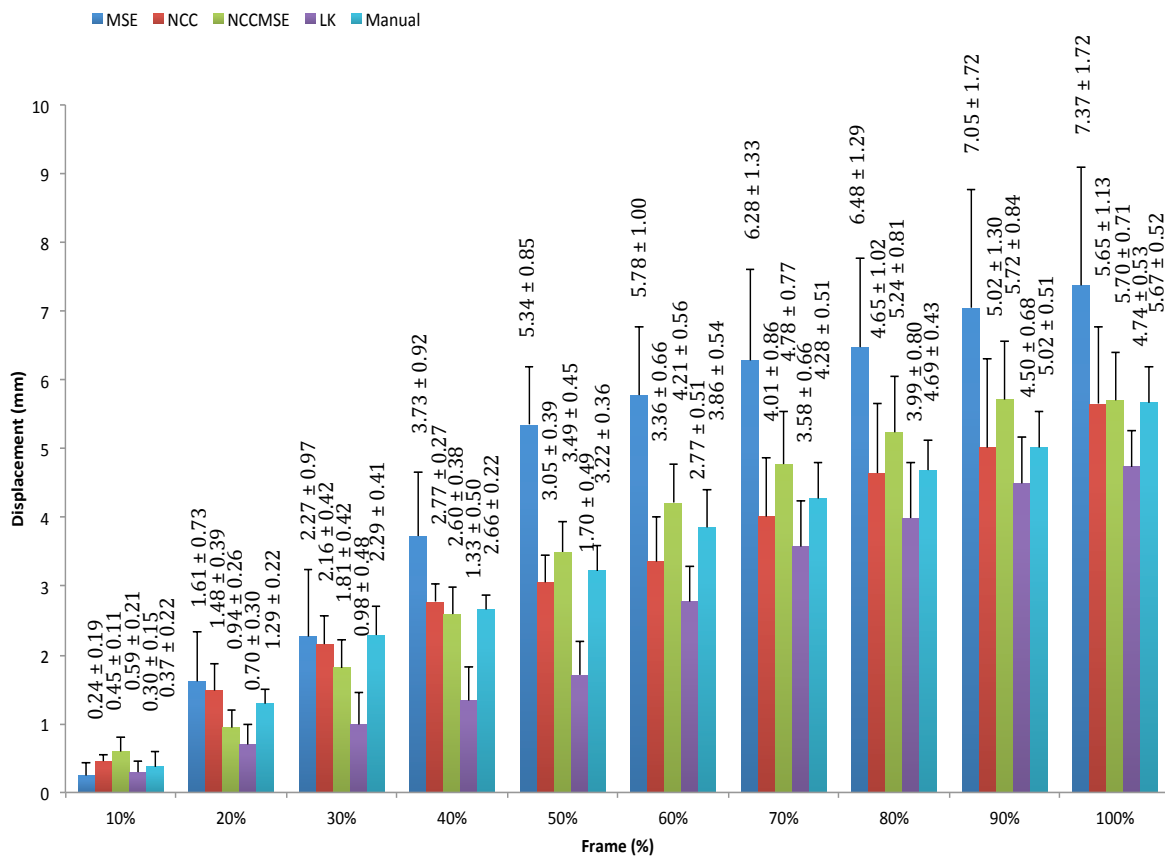


Figure 4.2: Mean displacement of 10 samples (in millimetres) of each algorithm against the manual measurement at every 10% intervals (from 10% to 100%) of the total frames on the active movement of patella tendon. The individual displacement was measured from 0-10% and followed by 10-20%.

At 30% of the frame, the algorithm MSE ($2.27\pm 0.97\text{mm}$), NCC ($2.16\pm 0.42\text{mm}$), NCCMSE ($1.81\pm 0.42\text{mm}$) and LK ($0.98\pm 0.48\text{mm}$) gave lower displacement value when compared to the manual measurement ($2.29\pm 0.41\text{mm}$) but only LK was significantly different ($p<0.05$) to the manual measurement. MSE and NCC gave higher values at 40%, each gave the displacement value of $3.73\pm 0.92\text{mm}$ and $2.77\pm 0.27\text{mm}$ respectively against the manual measurement ($2.66\pm 0.22\text{mm}$) while NCCMSE gave a lower value ($2.60\pm 0.38\text{mm}$) and LK gave the lowest value ($1.33\pm 0.50\text{mm}$). Again, only LK was significantly different ($p<0.05$) to the manual measurement.

MSE was shown to be significantly different ($p<0.05$) against manual measurement at 50% giving the highest displacement value of $5.34\pm 0.85\text{mm}$ and manual measurement gave the displacement value of $3.22\pm 0.36\text{mm}$. NCC, NCCMSE and LK showed no significant difference ($p>0.05$) to the manual measurement, NCC gave a lower value ($3.05\pm 0.39\text{mm}$) and NCCMSE gave a higher value ($3.49\pm 0.45\text{mm}$) while LK gave the lowest value ($1.70\pm 0.49\text{mm}$). MSE continued to give the highest value ($5.78\pm 1.00\text{mm}$) at 60% of the frame and LK continued to give the lowest value ($2.77\pm 0.51\text{mm}$) against the manual measurement ($3.86\pm 0.54\text{mm}$). NCC gave a lower value ($3.36\pm 0.66\text{mm}$) and NCCMSE gave a higher value ($4.21\pm 0.56\text{mm}$). However, only LK was significantly different ($p<0.05$) to the manual measurement.

At 70% all algorithms showed no significant difference ($p>0.05$) to the manual measurement. MSE continued to perform worst with the highest displacement value of ($6.28\pm 1.33\text{mm}$) against the manual measurement ($4.28\pm 0.51\text{mm}$). NCC and LK continued to decrease giving the values of $4.01\pm 0.86\text{mm}$ and $3.58\pm 0.66\text{mm}$ respectively while NCCMSE ($4.78\pm 0.77\text{mm}$) continued to increase with the value of $4.78\pm 0.77\text{mm}$. NCC performs better at 80% of the frame, giving the displacement value of $4.65\pm 1.02\text{mm}$ while the manual measurement gave the value of $4.69\pm 0.43\text{mm}$. MSE and NCCMSE continued to increase giving the value of $6.48\pm 1.29\text{mm}$ and $5.24\pm 0.81\text{mm}$ respectively while LK continued to drop to $3.99\pm 0.80\text{mm}$. However, all algorithms showed no significant difference ($p>0.05$) to the manual measurement.

NCC again performed better at 90% of the frame and gave the value of $5.02 \pm 1.30 \text{mm}$ while the manual measurement gave the value of $5.02 \pm 0.51 \text{mm}$. MSE performed worst with the displacement value of $7.05 \pm 1.77 \text{mm}$. NCCMSE gave the value of $5.72 \pm 0.84 \text{mm}$ and LK gave the lowest displacement value of $4.50 \pm 0.68 \text{mm}$. Again, no significant differences ($p > 0.05$) were found from the algorithms against the manual measurement. The final frame at 100% showed that NCC performed the best ($5.65 \pm 1.13 \text{mm}$) followed by NCCMSE ($5.70 \pm 0.71 \text{mm}$) when compared to the manual measurement ($5.67 \pm 0.52 \text{mm}$). MSE continued to perform the worst ($7.37 \pm 1.72 \text{mm}$) and followed by LK ($4.74 \pm 0.58 \text{mm}$).

The experiment has shown that MSE was an unsuitable tracking method when tracking on its own, but when combined with NCC, it performed better. The NCC tracking algorithm was found to perform the best however, slight increases were seen at the beginning of the frames but it improved subsequently. The NCC may struggle to track the movement of the speckle formation of the tendon due to the shakiness or quality of the image data but soon the tracking algorithm manages to track better from 70% onwards since the image data showed steady movement of the tendon. Finally, the LK tracking algorithm was found to be unable to track the speckle pattern of the patella tendon and keeps giving a displacement value lower than the manual measurement through out the frames.

Both MSE and LK failed to track successfully throughout the intervals. The NCC tracking algorithm, however, started higher at 10% and 20% and value was close enough to the manual measurement at 30-50%. 60-70% gave lower tracking result and improved at 80-100% with results close to the manual measurement. Similarly, NCCMSE started high at 10% and dropped at 20-30%. At 40% the value was close to the manual measurement and started to increase at 50-90%. At the final frame, the tracking value was close to the manual measurement.

Meanwhile, as for the medial gastrocnemius, the mean displacement of each tracking algorithm of the active movement the tendon was measured at every 10% interval of total frames as shown in figure 4.3. At 10% all algorithms showed no significant difference ($p > 0.05$) to the manual measurement, however all algorithms showed higher displacement values than the manual measurement ($0.37 \pm 0.23 \text{mm}$)

with MSE, NCC, NCCMSE and LK giving the value of $0.50\pm 0.23\text{mm}$, $0.61\pm 0.30\text{mm}$, $0.61\pm 0.18\text{mm}$ and $0.76\pm 0.27\text{mm}$ respectively. Again, no significant difference ($p>0.05$) was seen between the algorithms and the manual measurement at 20% of the total frames. MSE gave the displacement value of $1.35\pm 0.49\text{mm}$ and the manual measurement gave the value of $1.31\pm 0.41\text{mm}$. NCC gave slightly lower value ($1.24\pm 0.39\text{mm}$) and followed by NCCMSE with the lowest value ($1.05\pm 0.28\text{mm}$).

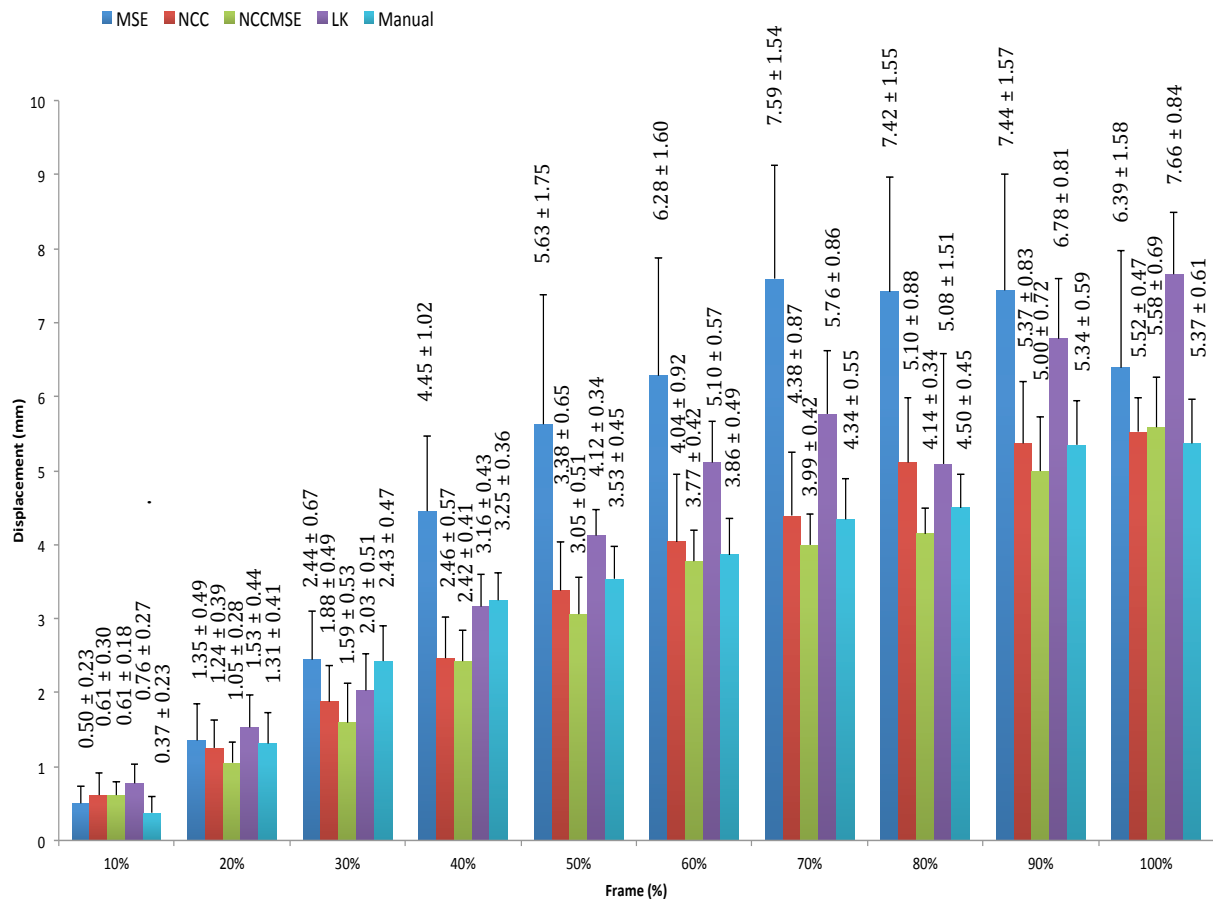


Figure 4.3: Mean displacement of 10 samples (in millimetres) of each algorithm against the manual measurement at every 10% intervals (from 10% to 100%) of the total frames on the active movement of medial gastrocnemius tendon. The individual displacement was measured from 0-10% and followed by 10-20%.

Meanwhile, at 30%, MSE, NCC and LK were shown to be not significantly different ($p>0.05$) to the manual measurement while only NCCMSE was shown to be significantly different ($p<0.05$) to the manual measurement. MSE gave a displacement value slightly higher ($2.44\pm 0.67\text{mm}$) than the manual measurement ($2.43\pm 0.47\text{mm}$). LK gave a lower value of $2.03\pm 0.51\text{mm}$, followed by NCC with a

value of $1.88\pm 0.49\text{mm}$, and NCCMSE gave the lowest displacement value ($1.59\pm 0.53\text{mm}$). At 40% MSE continued to give a higher displacement value ($4.45\pm 1.02\text{mm}$) than the manual measurement ($3.25\pm 0.36\text{mm}$), while LK gave a slightly lower value ($3.16\pm 0.43\text{mm}$), followed by NCC with a value of $2.46\pm 0.57\text{mm}$ and NCCMSE gave the lowest value ($2.42\pm 0.41\text{mm}$). Only NCCMSE was shown to be significantly different ($p < 0.05$) to the manual measurement.

At 50% of the frame, MSE continued to give the highest displacement value ($5.63\pm 1.75\text{mm}$) while manual measurement gave the displacement value of $3.53\pm 0.45\text{mm}$, followed by LK with the displacement value of $4.12\pm 0.34\text{mm}$. NCC performed slightly better with the displacement value of $3.38\pm 0.65\text{mm}$ and NCCMSE still remained giving the lowest value ($3.05\pm 0.51\text{mm}$). All algorithms were shown to be not significantly different ($p > 0.05$) to the manual measurement. MSE again at 60% of the frame, performed the worst with a value of $6.28\pm 1.60\text{mm}$ in comparison to the manual measurement ($3.86\pm 0.49\text{mm}$). Followed by LK, which gave the value of $5.10\pm 0.57\text{mm}$. NCC increases slightly with value of $4.04\pm 0.92\text{mm}$ while NCCMSE gave the closest value to the manual measurement with $3.77\pm 0.42\text{mm}$. Again, all algorithms showed no significant differences ($p > 0.05$) to the manual measurement.

At 70% of the frame, the manual measurement gave the displacement value of $4.34\pm 0.55\text{mm}$. The MSE gave the highest displacement value of $7.59\pm 1.54\text{mm}$, followed by LK with the value of $5.76\pm 0.86\text{mm}$. The NCC however, performed better giving the displacement value of $4.38\pm 0.87\text{mm}$ while NCCMSE gave the lowest displacement value of $3.99\pm 0.42\text{mm}$. All algorithms showed no significant differences ($p > 0.05$) to the manual measurement. Meanwhile at 80% of the total frame, the manual measurement gave the displacement value of $4.50\pm 0.45\text{mm}$. MSE again showed the highest difference with a displacement value of $7.42\pm 1.55\text{mm}$, followed by NCC and LK giving values of $5.10\pm 0.88\text{mm}$ and $5.08\pm 1.51\text{mm}$ respectively. NCCMSE again had the lowest value with $3.99\pm 0.42\text{mm}$. All algorithms also showed no significant difference ($p > 0.05$) to the manual measurement.

Moving further towards 90% of the total frame, the manual measurement was measured at $5.34\pm 0.59\text{mm}$. MSE gave the highest displacement value ($7.44\pm 1.57\text{mm}$) followed by LK ($6.78\pm 0.81\text{mm}$). NCC performed better with the displacement value

of $5.37\pm 0.83\text{mm}$ while NCCMSE gave the lowest value ($5.00\pm 0.72\text{mm}$). At the final frame (100% of the total frames), the manual measurement gave the value of $5.37\pm 0.61\text{mm}$, and LK gave the highest difference with the displacement value of ($7.66\pm 0.84\text{mm}$), followed by MSE ($6.39\pm 1.58\text{mm}$). NCC and NCCMSE gave values of $5.52\pm 0.47\text{mm}$ and $5.58\pm 0.69\text{mm}$ respectively. Also, all algorithms showed no significant differences ($p>0.05$) to the manual measurement.

It was evident that both MSE and LK failed to track successfully throughout the intervals. The NCC tracking algorithm, however, started higher at 10%, was lower at 20-50% and started to track close to the manual measurement from 60% onwards. Similarly NCCMSE started high at 10% and was lower at 20-90%. Displacement value was close to the manual measurement at 100%.

As for the active tendon movements, the computational costs (measured in seconds) for both experiments were also plotted as shown in Figure 4.4. The LK tracking algorithm was found to be the most demanding in terms of computational cost for both experiments, with an overall performance of 170 ± 30 seconds needed to complete the tracking process. The NCCMSE tracking algorithm performed better than the LK tracking algorithm, but because the algorithm consists of an SNR decision operation, it required more computation time (23 ± 3 seconds) than the MSE (15 ± 2 seconds) and NCC (8 ± 1 seconds) tracking algorithms. The active movement experiment shows that the NCC tracking algorithm took the least computational time. The LK tracking algorithms were shown to be unsuitable in this experiment.

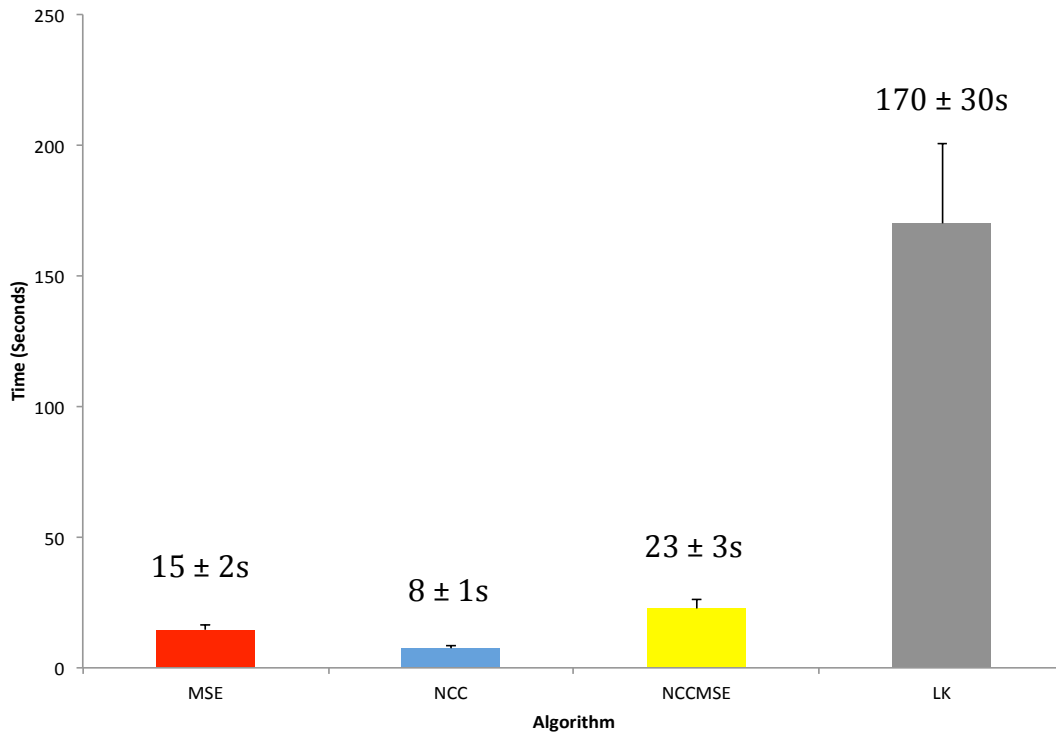


Figure 4.4: Total mean of computational cost for both experiments (in seconds) between the algorithms.

4.4 Tracking Reliability During Passive tendon Movement

The results were the mean number of errors obtained from 10 tests from each participant. The mean number of error count for stationary movement at the patella is shown in Figure 4.5 where it can be seen that LK tracking algorithm gave the highest mean number of error counts (13.00 ± 1.25) and followed by MSE (13.10 ± 1.32). NCC and NCCMSE gave 9.40 ± 1.07 and 9.70 ± 0.79 mean number of error counts respectively. However, no significant differences were found ($p > 0.05$) between the algorithms.

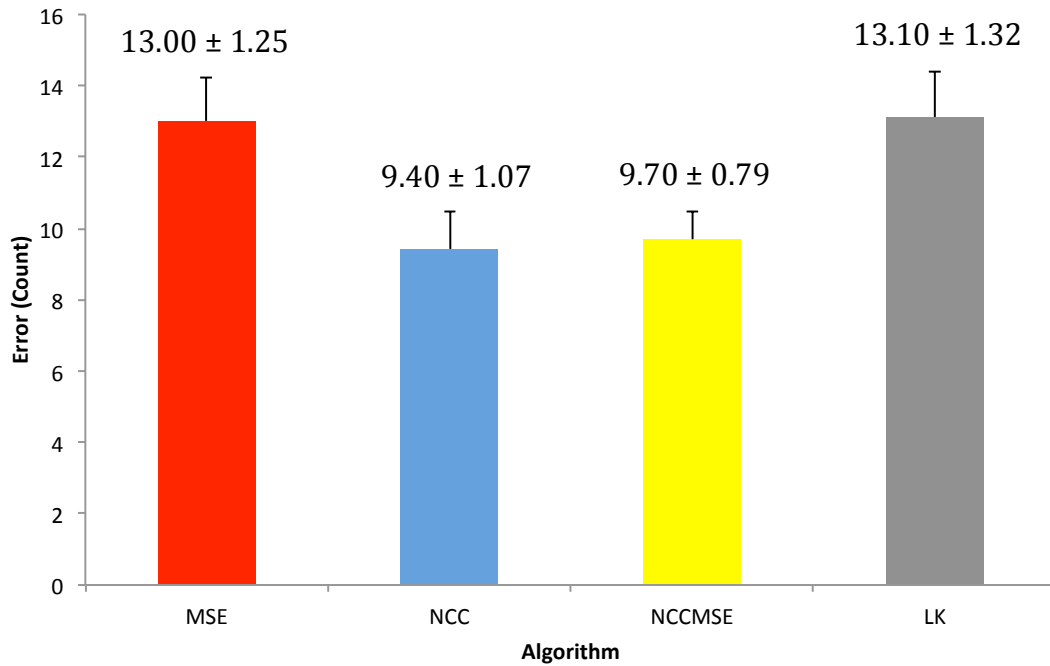


Figure 4.5: Stationary movement errors of passive movement at patella tendon.

In the case of the irregular errors, the results shown in Figure 4.6 indicate that the NCC tracking algorithm gave the least mean error count with the mean value of 0.50 ± 1.43 . The MSE algorithm was shown to have the most count of errors with the mean value of 4.10 ± 1.43 . Meanwhile, the NCCMSE tracking algorithm gave a higher mean value of 1.00 ± 0.33 compared to the NCC tracking algorithm, but lower than the mean value of the LK tracking algorithm (1.90 ± 0.31).

Pairwise comparisons of the error data indicated that only the NCC and LK tracking algorithms were found to be significantly different ($p < 0.05$). The rest of the algorithms showed no significant differences ($p > 0.05$). The results showed the MSE algorithm to be least suitable compared to the NCC, NCCMSE and LK algorithms. The NCC algorithm produced the smallest mean error followed by the NCCMSE algorithm. The LK algorithm showed higher error counts compared to NCC and NCCMSE algorithms but performed better than MSE algorithm.

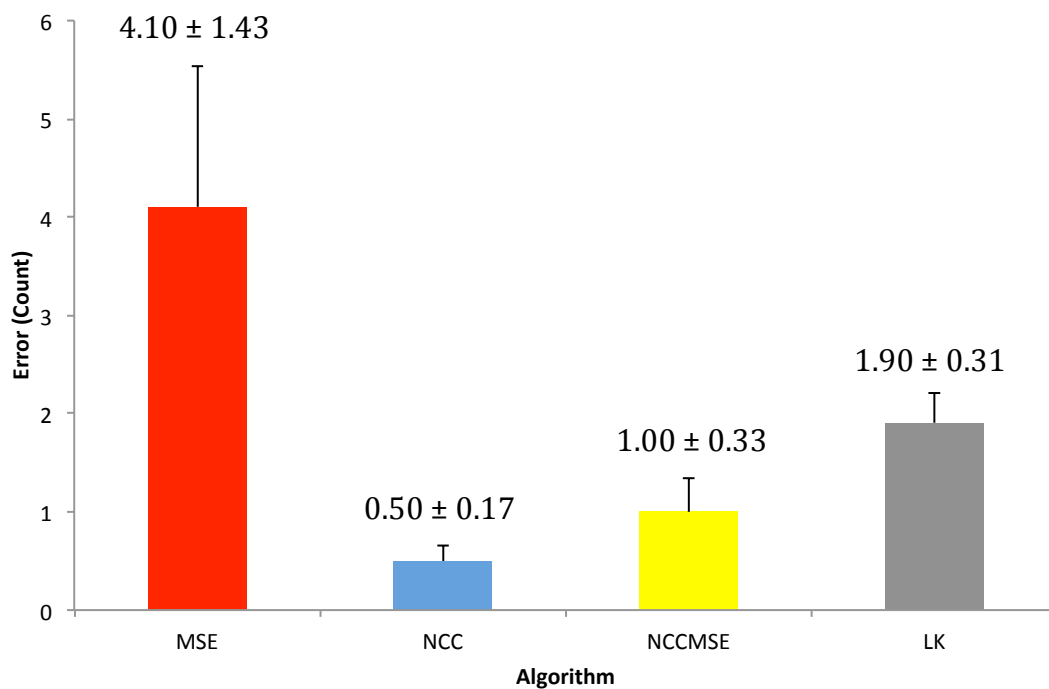


Figure 4.6: Irregular movement error of passive movement at patella tendon.

The results showed that the NCC algorithm was found to be the optimum algorithm when tracking the regional area of the patella tendon with less stationary and irregular errors during tracking. The MSE algorithm, however, was found to be the least favourable. The tracking pattern was seen to be non-consistent throughout the image sequence since it was found to be susceptible to the tightly formed speckled and performs better if the tracking has a well defined structure with darker grayscale value.

Figure 4.7 shows the stationary errors for medial gastrocnemius analysis indicates that there exists a decrease in the mean number of errors compared to the mean number of errors found in the patella tendon analysis. The reason for the decrease in mean errors for the medial gastrocnemius tendon tracking analysis was because of the nature of the tendon itself. The area being tracked on the patella tendon has a wider tendon band than the more defined band in the medial gastrocnemius. Even though the movement was uniform throughout the frame and there was no strain within the tendon, there were a large number of speckles coming and going, leading to the tracking being less reliable.

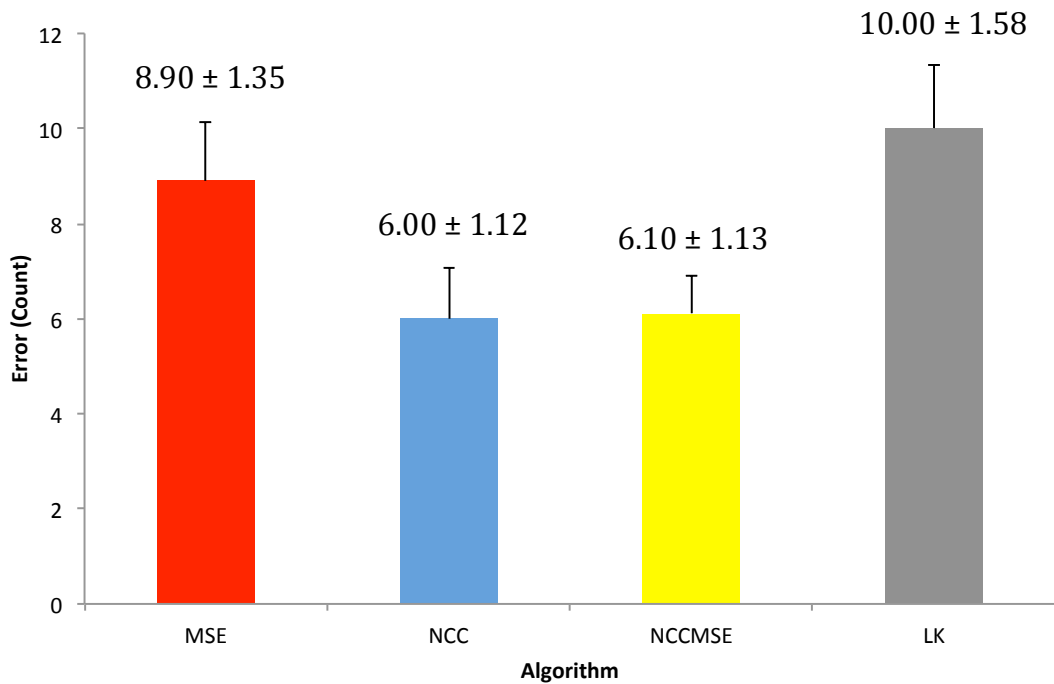


Figure 4.7: Stationary movement error of passive movement at medial gastrocnemius tendon.

Again, the LK tracking algorithm gave the most errors with a mean number of errors of 10.00 ± 1.58 , while NCC gave the least mean number of errors with the value of 6.00 ± 1.12 . Second highest is the MSE algorithm while second lowest is the NCCMSE with mean error counts of 8.90 ± 1.53 and 6.10 ± 1.13 respectively. T-test showed that there were significant differences between LK and NCC ($p < 0.05$), and similar significant difference was found between LK and NCCMSE ($p < 0.05$). No significant difference was found between LK & MSE ($p > 0.05$). However, the MSE tracking algorithm showed no significant difference from the NCC tracking algorithm ($p > 0.05$) and the NCCMSE tracking algorithm ($p > 0.05$).

Lastly, as expected, NCC and NCCMSE tracking algorithms showed no significant difference ($p > 0.05$) to each other. The reason for this may be because the SNR used in the tracking favoured the NCC algorithm rather than MSE algorithm. Both LK and MSE tracking algorithms however gave higher mean errors. In summary, pairwise comparisons indicated that for the patella tendon, none of the algorithms gave significantly different result ($p > 0.05$) while as for the medial gastrocnemius tracking analysis only the results for the LK tracking algorithm were significantly different to the NCC and NCCMSE tracking algorithms ($p < 0.05$).

In the case of the irregular errors, the error numbers found for the medial gastrocnemius showed an increase for all algorithms when compared to errors found in passive movement of the patella tendon (see Figure 4.8). The analysis showed that the MSE tracking algorithm gave a large number of errors with the mean value of 14.70 ± 1.25 followed by the LK tracking algorithm with a mean value of 2.50 ± 0.17 . The NCCMSE tracking algorithm gave a slightly lower number than the LK tracking algorithm with a mean value of 1.20 ± 0.73 and finally, the NCC tracking algorithm gave the least error count with the mean value of 0.50 ± 0.17 .

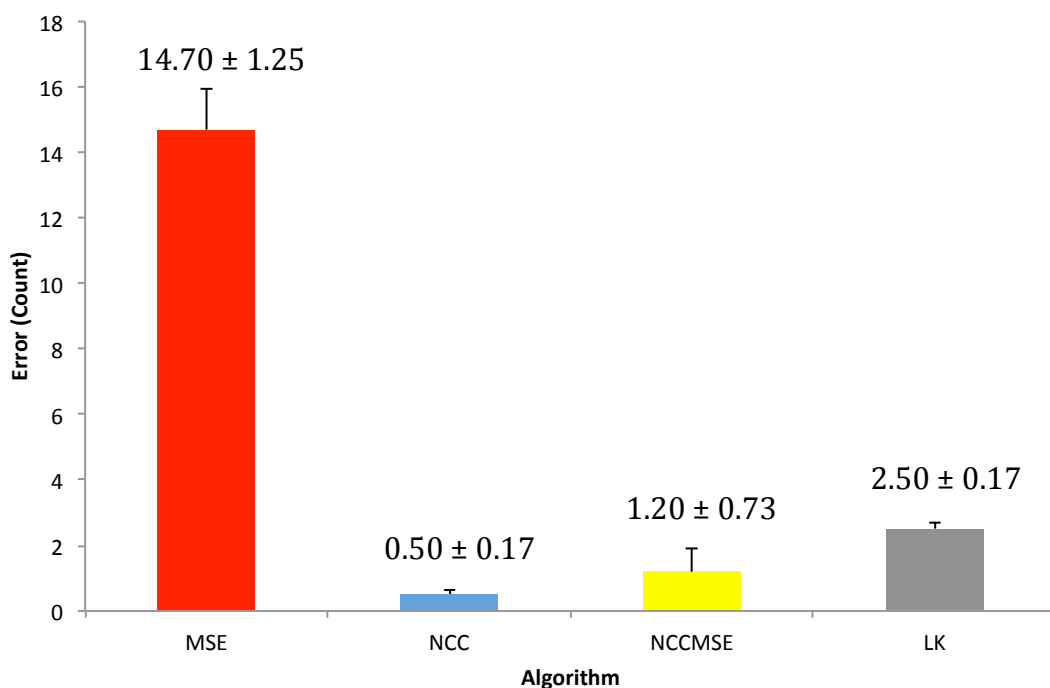


Figure 4.8: Irregular movement error of passive movement at medial gastrocnemius tendon.

The pairwise comparisons showed that no significant differences ($p > 0.05$) were found between the LK and NCCMSE tracking algorithms, and between the NCC and NCCMSE tracking algorithms. All other algorithms were found to be significantly different ($p < 0.05$) to each other. The results shown for the analysis indicated the MSE tracking algorithm to be the least reliable, while the NCC tracking algorithm gave the least mean number of error and has proven to be highly reliable. In conclusion, for both passive movement analysis of the patella tendon and medial gastrocnemius, all algorithms were found to be less prone to irregular movement error compared to the stationary tracking error. In both cases, the most reliable algorithms

were the NCC tracking algorithm, giving the best results for both stationary and irregular errors.

4.5 Tracking Reliability During Active Tendon Movement

The results for the patella show that MSE tracking algorithm had the highest count of stationary errors with the mean error count of 13.00 ± 1.89 . While NCC tracking algorithm had the lowest mean error of 9.40 ± 2.37 (see Figure 4.9).

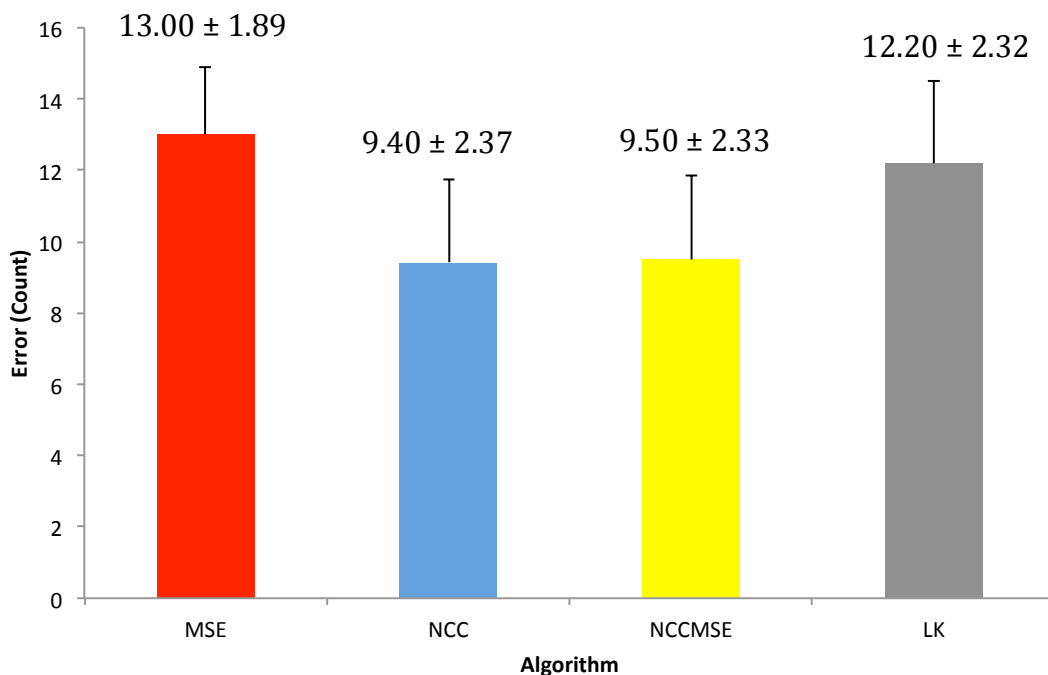


Figure 4.9: Stationary movement error of active movement on patella tendon.

The figure showed that for this experiment, the MSE algorithm was seen to be unsuitable along with the LK algorithm. The NCC tracking algorithm gave the lowest mean number of errors (9.40 ± 2.37), followed by the NCCMSE (9.50 ± 2.33). Pairwise comparisons of the data observed indicated that there were significant differences between MSE and NCC tracking algorithms ($p < 0.05$) algorithms and large differences between NCCMSE and LK tracking algorithms ($p < 0.05$). However, there was no significant difference ($p > 0.05$) between the MSE and the NCCMSE and LK tracking algorithms.

No significant difference ($p>0.05$) was found between the NCC and NCCMSE algorithms. The same observation was found between NCC and LK algorithms with no significant differences ($p>0.05$) observed. The comparison of results from the mean error values and pairwise comparisons of the tracking data indicated that both MSE and LK algorithms were unsuitable for tracking the active movement of the patella tendon. The NCC tracking algorithm still showed the best results with the lowest error counts followed by the NCCMSE tracking algorithm

The results for irregular movement errors during tracking are shown in Figure 4.10. The MSE algorithm again showed the highest mean count of 5.70 ± 1.19 , followed by the LK algorithm with mean count value of 3.30 ± 1.05 . Both NCC and NCCMSE algorithms gave small error means count values of 0.60 ± 0.22 and 0.70 ± 0.21 respectively.

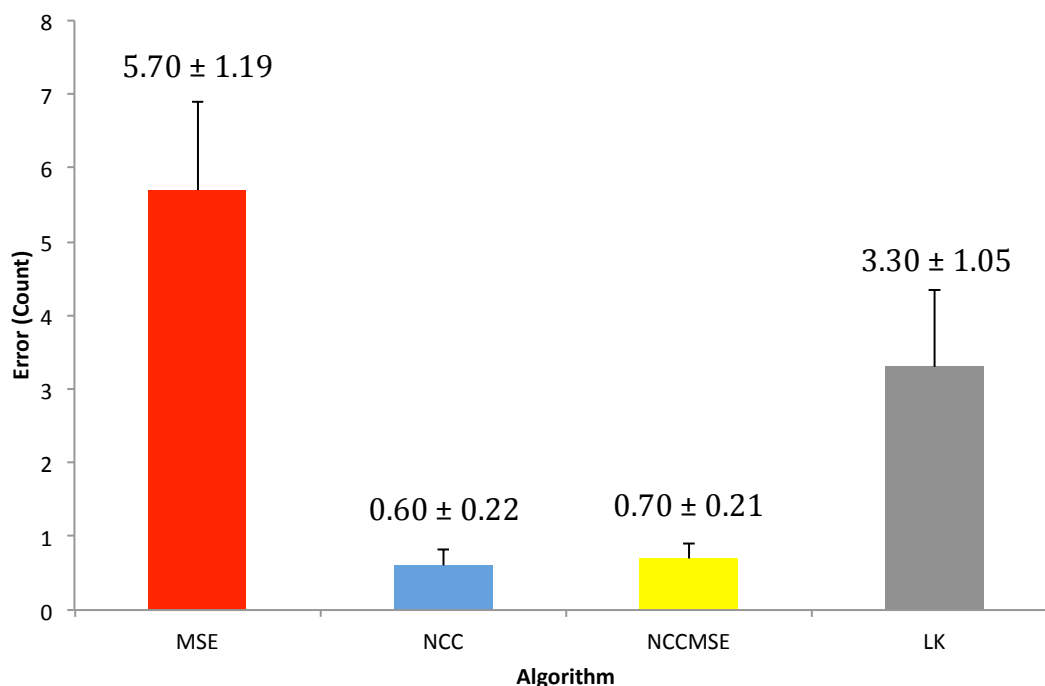


Figure 4.10: Irregular movement error of active movement at patella tendon.

The pairwise comparisons, however, showed that there were significant differences ($p<0.05$) between the MSE and NCC algorithms, and between the MSE and NCCMSE algorithms. The rest of the pairings showed no significant differences ($p>0.05$) between each other. The results again showed that the MSE algorithm was

unsuitable, and the error counts increased with the active tracking of the patella tendon. This was expected as the algorithm struggled to correctly estimate the actual movement of the ROI within the tendon band of the patella. The LK algorithm though, showed a lower error count compared to the MSE algorithm, which was seen to give a higher error count compared to the NCC and NCCMSE algorithms, indicating that tracking a regional area of the patella tendon was a failure.

NCC and NCCMSE, however, gave smaller error count compared to the MSE and LK algorithms, and NCC being the least error to be found, has proven to be the most reliable. NCCMSE, however, showed that the error count was not that far behind with error difference of 0.10 ± 0.93 . The tracking results for the stationary movement errors when tracking the medial gastrocnemius tendon are shown in Figure 4.11.

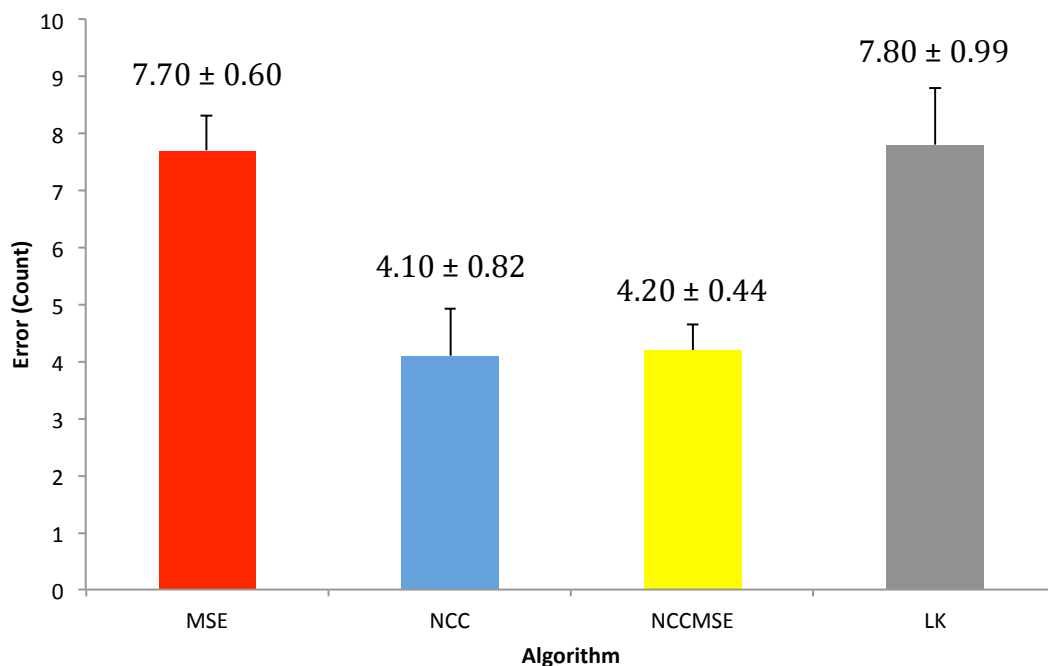


Figure 4.11: Stationary movement error of active movement at medial gastrocnemius tendon.

As for the other results, the LK tracking algorithm gave the highest error count with mean errors of 7.80 ± 0.99 and was followed by MSE tracking algorithm with a mean error of 7.70 ± 0.60 . The NCC tracking algorithm still showed the lowest error count with the mean error of 4.10 ± 0.82 and followed by NCCMSE tracking algorithm

with differences of only 0.10 ± 0.93 . The pairwise comparisons for this analysis showed that there were significant differences ($p < 0.05$) between MSE and NCC tracking algorithms, and between LK and NCCMSE tracking algorithms. However, no significant differences ($p > 0.05$) were found between LK and NCC tracking algorithm, and similarly for the LK and MSE tracking algorithms. Finally, the results between NCC & NCCMSE tracking algorithms showed no significant difference ($p > 0.05$).

The results for the irregular movement errors when tracking the medial gastrocnemius analysis are shown in Figure 4.12. It can be seen that the MSE tracking algorithm showed the mean error count of 6.70 ± 0.60 . Lucas-Kanade algorithm however, showed a lower error count compared to the MSE tracking algorithm with mean error count of 2.90 ± 0.95 . The NCC showed lowest error count with mean errors of 0.40 ± 0.16 while NCCMSE gave mean error count of 0.60 ± 0.16 .

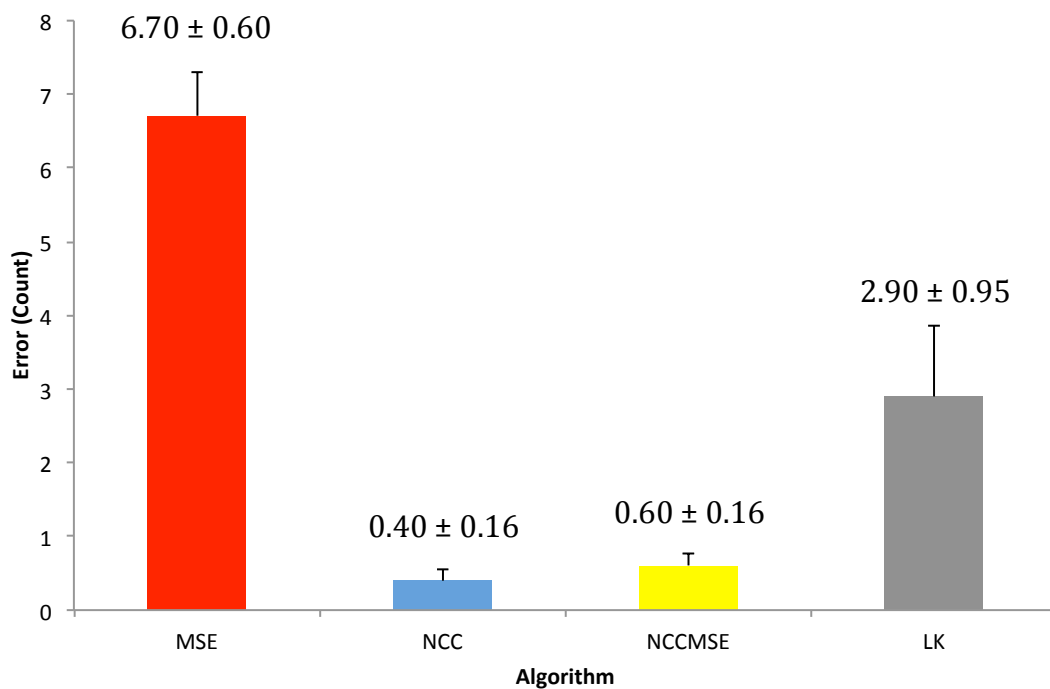


Figure 4.12: Irregular movement error of active movement at medial gastrocnemius tendon.

The t-test statistical comparisons indicated that LK and MSE algorithms were found to be significantly different ($p < 0.05$). Similarly, significant differences ($p < 0.05$) can be found between MSE and NCC tracking algorithms, and between

MSE and NCCMSE tracking algorithms. However, LK and NCC tracking algorithms were found to be not significantly different ($p>0.05$) to each other and also, no significant difference ($p>0.05$) was found between the LK and NCCMSE tracking algorithms. Lastly, NCC and NCCMSE tracking algorithms showed no significant difference ($p>0.50$).

The analysis showed that MSE algorithm gave the greatest error counts for both the stationary and the irregular errors and was unsuitable for tracking the active movement of the medial gastrocnemius tendon. Again, the reason for the failure of the MSE algorithm to track the regional area was because MSE tracking algorithm was not sensitive towards densely packed speckle patterns. The LK tracking algorithm also gave higher errors than the NCC and NCCMSE tracking algorithms, but smaller than the MSE tracking algorithm. The NCCMSE tracking algorithm, on the other hand, showed promising results with lower mean error counts compared to the LK algorithm and a slight improvement compared to the results found in the patella tendon analysis. Finally, the NCC tracking algorithm gave the best results with the lowest stationary and irregular errors.

4.6 Discussion

The experiments conducted in this section firstly evaluated the performance of the four algorithms in terms of tracking accuracy, as compared with the standard manual measurement and computational cost. Table 4.3 shows the total mean of all of the passive tests (patella and gastrocnemius) of each of the algorithm and the manual measurement. The difference of each algorithm against the manual measurement shows the level of accuracy of the algorithm, in this case the smallest difference is the optimum result. The total mean displacement of passive movement experiments (in millimetres) for the tendon located at both patella and gastrocnemius showed that NCC gave the closest mean displacement when compared to the manual measurement (0.10 ± 1.47 mm difference) while the MSE, gave the worst results with 16.63 ± 1.12 mm difference.

Test	Mean Displacement (mm)				
	MSE	NCC	NCCMSE	LK	Manual
Mean	16.63±1.12	18.03±1.00	17.79±1.02	17.95±1.23	18.13±1.08
Difference	1.50±1.56	0.10±1.47	0.34±1.49	0.18±1.64	

Table 4.3: Mean displacement of all passive movements of the tendon for each algorithm and the difference of each algorithm against the manual measurement.

Table 4.4 showed the total mean of all of the active tests (patella and gastrocnemius) for each of the algorithms and the manual measurement. The difference of each algorithm against the manual measurement showed the level of accuracy of the algorithm, in this case the smallest difference is the optimum result. The mean displacement of active movement experiments (in millimetres) at the final frames of the tendon located at both patella and gastrocnemius showed that NCC again gave the closest mean displacement when compared to the manual measurement with 0.07 ± 0.69 mm difference while the MSE again gave the worst result with 1.37 ± 0.18 mm difference.

Test	Mean Displacement (mm)				
	MSE	NCC	NCCMSE	LK	Manual
Mean	6.88±1.12	5.58±0.58	5.64±0.47	6.20±0.67	5.52±0.38
Difference	1.37±0.18	0.07±0.69	0.12±0.60	0.68±0.77	

Table 4.4: Mean displacement of all active movements of the tendon for each algorithm and the difference of each algorithm against the manual measurement.

The computational cost on both active and passive tests showed the results of NCC having the least time taken with a total mean time of 10 ± 1 seconds for all tests.

The LK, however, gave the most time taken for the tracking to complete with total mean time value of 320 ± 40 seconds for all tests (see Table 4.5).

Test	Mean Time (second)			
	MSE	NCC	NCCMSE	LK
Passive	27 ± 1	13 ± 1	39 ± 1	469 ± 33
Active	15 ± 2	8 ± 1	23 ± 3	170 ± 30
Mean	21 ± 2	10 ± 1	30 ± 3	320 ± 40

Table 4.5: Mean value of computational cost for each algorithm on both active and passive tests.

The tracking reliability of the four algorithms was investigated, and the average number of tracking errors calculated for both stationary and irregular movement errors, during both passive and active movements. The NCC tracking algorithm gave the best performance in each case. The overall tracking reliability of the four algorithms is shown in Table 4.6, where it can be seen that the NCC tracking algorithm gave the least total mean number of errors (3.86 ± 1.55).

Test	Mean Error (count)			
	MSE	NCC	NCCMSE	LK
Stationary Knee Passive	13.00 ± 1.25	9.40 ± 1.07	9.70 ± 0.79	13.10 ± 1.32
Stationary Gastrocnemius Passive	8.90 ± 1.35	6.00 ± 1.12	6.10 ± 1.13	10.00 ± 1.58
Stationary Knee Active	13.00 ± 1.89	9.40 ± 2.37	9.50 ± 2.33	12.20 ± 2.32
Stationary Gastrocnemius Active	7.70 ± 0.60	4.10 ± 0.82	4.20 ± 0.44	7.80 ± 0.99
Irregular Knee Passive	4.10 ± 1.43	0.50 ± 0.17	1.00 ± 0.33	1.90 ± 0.31
Irregular Gastrocnemius Passive	14.70 ± 1.25	0.50 ± 0.17	1.20 ± 0.73	2.50 ± 0.17
Irregular Knee Active	5.70 ± 1.19	0.60 ± 0.22	0.70 ± 0.21	3.30 ± 1.05
Irregular Gastrocnemius Active	6.70 ± 0.60	0.40 ± 0.16	0.60 ± 0.16	2.90 ± 0.95
Mean	9.23 ± 0.59	3.86 ± 1.55	4.13 ± 1.51	6.71 ± 1.83

Table 4.6: Mean value of the tracking errors for each algorithm.

In conclusion, the best performance in terms of tracking accuracy and tracking reliability was obtained using the NCC tracking algorithm. This algorithm was also found to have the lowest computational cost for both active and passive movements.

4.5 Summary

In this chapter, the results of the pilot study were presented and discussed. The performance of the four selected tracking algorithms was evaluated with tracking accuracy being analysed by comparisons, the standard manual measurement and computation costs. The errors analysis measures the reliability of each algorithm handling tracking error such as stationary movement errors and irregular movement errors. The results were obtained from experiments involved with speckle tracking during passive and active tendon movements. In all cases, the NCC tracking algorithms gave the best performance and will be used and enhanced in the two remaining studies. In the next Chapter, this algorithm will be used to select the optimum ROI size and most effective threshold ranges, and again compared with the standard manual measurement.

Chapter 5

Automatic Measurement using Normalised Cross Correlation

Overview

In this chapter, the Normalised Cross Correlation (NCC) tracking algorithm that was selected as the best performing tracking in the previous Chapter is explored further to identify the optimal ROI block size and threshold value. The results were then validated against the standard manual measurement. The computational cost for each ROI block and threshold size are also compared. Tracking experiments were conducted on both the patella and medial gastrocnemius tendon for active movement. The final study to validate the tracking algorithm utilised 2-ROI blocks to track two regional areas of the tendon simultaneously with both active and passive movements. The results from this study were compared to the standard manual measurement.

5.1 Region of Interest (ROI) Block Size Comparisons

The regional area of the tendon can be tracked using different ROI block sizes but choosing the optimal block size for the tracking algorithm search was an important factor in the performance of the algorithm. Various ROI block sizes were tested ranging from 5x5, 11x11, 15x 15, 21x21, 25x25 and 31x31 pixel dimensions for the ROI block. The size selections were based on other user's experience with the block matching method (Dilley et al., 2001, Revell et al., 2005, Lee et al., 2008a), as was described in Chapter 2. The experimental setup and software settings were based on the description outlined in Section 3.1.2 and 3.1.3 of Chapter 3.

10 participants were tested, and all sizes of ROIs were observed on both active movement of patella and medial gastrocnemius tendon. No passive movements were observed since all ROI sizes evaluated gave similar results. Both patella and gastrocnemius results were combined and averaged to look at the performance of each algorithm against the standard manual measurement. For each experiment, the ROI was placed within the regional area of the tendon as described in Chapter 3. T-test statistical analysis was used for comparing the results.

5.1.1 Patella Tendon

Six ROI block sizes of were tested during active movement of the patella tendon and also, the displacement of the manual measurement was also measured. The displacement value for each algorithm and manual measurement measures the displacement relative to their starting position in the initial frame to their final position in the final frame. Figure 5.1 shows mean displacement of each ROI size from the algorithm as well as the mean displacement from the manual measurement.

The manual measurement gave a mean displacement of 8.50 ± 0.51 mm. The 5x5 pixels ROI block was significantly different ($p < 0.05$) to the manual measurement with a mean value of 3.98 ± 0.66 mm, which was less than the mean displacement of manual measurement. Next, the 11x11 pixels ROI block was found to be not significantly different ($p > 0.05$) compared to the manual measurement with the mean value of 8.95 ± 0.76 mm, which was higher than the mean value of manual measurement.

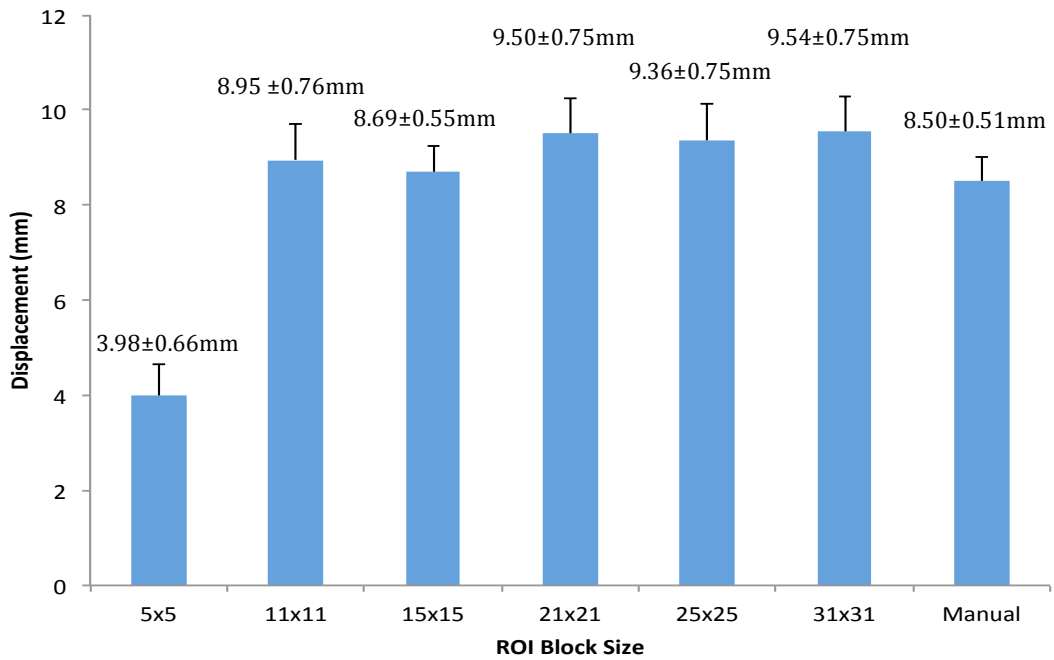


Figure 5.1: Mean displacement of ROI sizes and manual measurement of active movement of the patella tendon, relative to their starting position to the final position.

No significant difference to the manual measurement ($p>0.05$) was found for the 15x15 pixels with the mean value of 8.69 ± 0.55 mm and the rest of the results were also found to be not significantly different ($p>0.05$) to the manual measurement. The 21x21 pixels block size gave the mean value of 9.50 ± 0.75 mm, the 25x25 pixels block gave the mean value of 9.36 ± 0.75 mm and finally, the 31x31 pixels block size gave the mean value of 9.54 ± 0.75 mm. The experiments showed that the 5x5 pixel size was the least able to match the manual method. Meanwhile, the 15x15 pixel size gave the closest mean value to the manual measurement and was used for all evaluations in this study.

In order to investigate the computational time performance, Figure 5.2 shows the number of pixels contained in a block (ROI) with its relative computational time taken for a complete tracking process with coefficient of determination of $R^2=0.99$ with all block sizes were found to be significantly different ($p<0.05$) to each other.

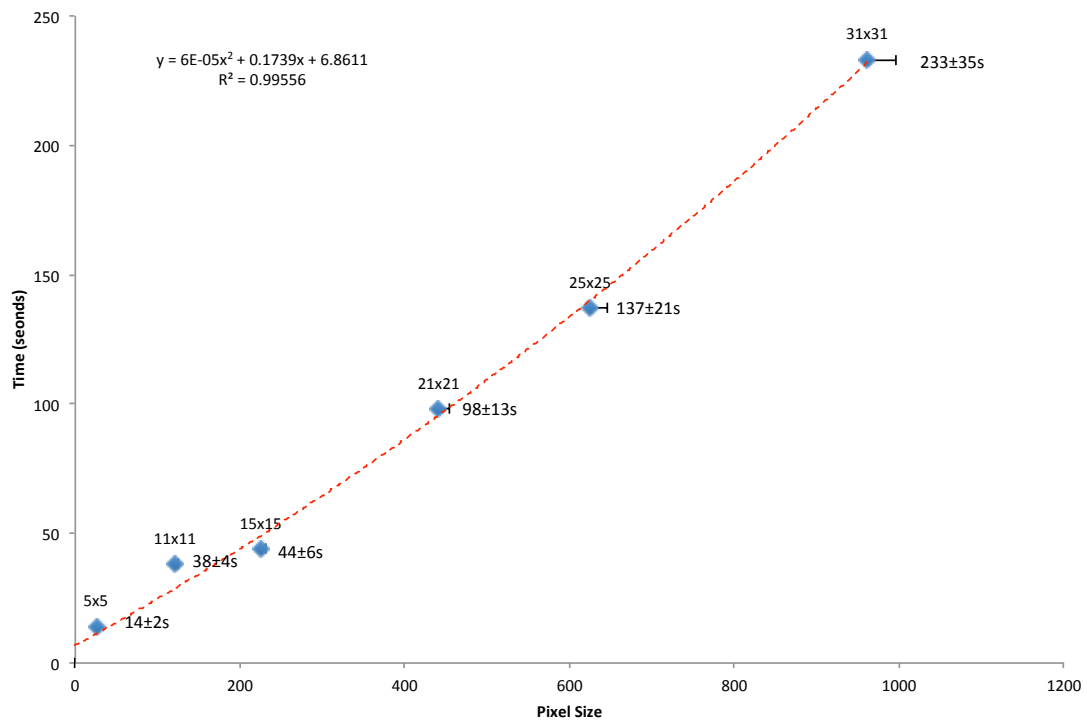


Figure 5.2: Mean time (in seconds) of each ROI block size of the patella tendon.

As expected, 5x5 gave the least mean time for tracking to complete with the mean time value of 14±2 seconds while 31x31 block size gave the highest computational time than the rest of the block sizes tested with the mean time value of 233±35 seconds to complete its tracking throughout the image sequence. 11x11, 15x15, 21x21 and 25x25 block size each respectively gave mean time of 28±4, 44±6, 98±13 and 137±21 seconds.

A parametric curve has been fitted to these measurements, as shown on the plot. This is in line with what is expected, as the dominant computation in the tracking process is the calculation of the NCC match. This should be proportional to the number of pixels in the block, and so vary linearly with the size of the block. The slight curve indicated that there is a small additional increase as the block size increases, and this is attributed to the number of tracking errors for this data and additional computations that had to be made.

5.1.2 Medial Gastrocnemius Tendon

Similar experiments were conducted on the medial gastrocnemius tendon data with six ROI block sizes evaluated. Figure 5.3 shows the results for each of the ROI block size with the mean displacement from the manual measurement (dashed line) set as the average. The manual measurement was measured at the start of the experiment and gave a mean displacement of $8.19 \pm 0.46 \text{mm}$.

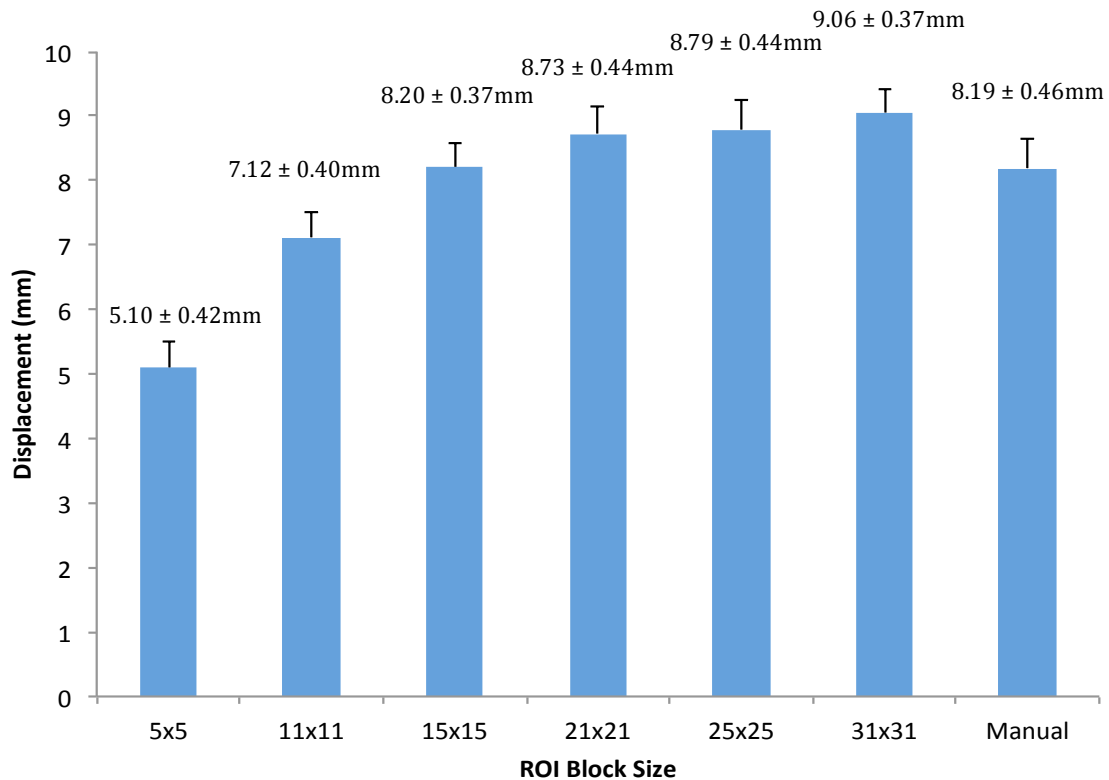


Figure 5.3: Mean displacement of ROI sizes and manual measurement of active movement of the medial gastrocnemius tendon, relative to their starting position to the final position.

The 5x5 block size showed significantly different ($p < 0.05$) displacements compared to the manual measurement, with a mean displacement of $5.10 \pm 0.42 \text{mm}$, which is lower than the manual measurement. Also, the result for the 11x11 ROI was found to be significantly different ($p < 0.05$) to the manual measurement with a mean displacement of $7.12 \pm 0.40 \text{mm}$, again lower than the manual measurement.

Meanwhile for the 15x15 pixel ROI block there was no significant difference ($p>0.05$) to the manual measurement with a mean displacement of 8.20 ± 0.37 mm. The result was close to the manual measurement with only 0.01 ± 0.59 mm difference. For the 21x12 pixel size ROI the results was found to be significantly different ($p<0.05$) and gave a mean value of 8.73 ± 0.44 mm.

The result for the 25x25 pixel block size however, was found to not be significantly different ($p>0.05$) to the manual measurement with only slight increases over the previous ROI size (8.79 ± 0.44 mm) while the 31x31 pixel size was found to be significantly different ($p<0.05$) to the manual measurement and gave the highest mean displacement (9.06 ± 0.37 mm) with both gave mean differences of 0.60 ± 0.64 mm and 0.86 ± 0.59 mm respectively. These results showed that bigger ROI blocks were less sensitive to speckle noise, which affected the performance of the tracking. From the results in figure 5.3, the 15x15 block size can be seen to give the most accurate result, as was the case for the patella experiment.

The timing results obtained for tracking the medial gastrocnemius tendon with different sizes of ROI is plotted to a quadratic fit with $R^2 = 1$ (see Figure 5.4). All timings of the ROIs were found to be significantly different ($p<0.05$) to each other. The line started with a curve with 5x5 and 11x11 block size with mean time of 10 ± 0 and 21 ± 1 seconds respectively. The curve begins to be linear with the 15x15 block size with time of 37 ± 3 seconds to complete the tracking and progresses with the 21x21 (67 ± 1 seconds), 25x25 (99 ± 6 seconds) and the longest time of completion with block size of 31x31, which took 142 ± 9 seconds to complete. Again, similarly to Figure 5.2, among the best-fit results (i.e. 15x15, 21x12, 25x25 and 31x31), the block size of 15x15 gave the optimum computational time.

The time performances for each number of pixels per blocks (ROI) are shown in figure 5.4 with coefficient of determination of $R^2= 1$ and all timings of the ROIs were found to be significantly different ($p<0.05$) to each other.

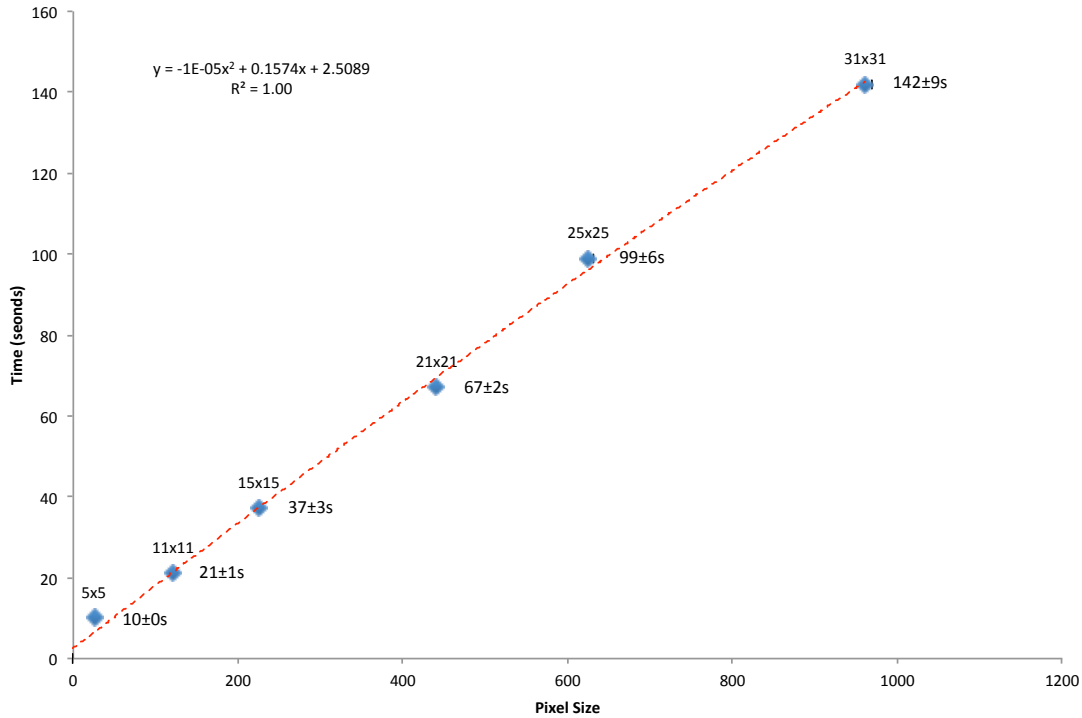


Figure 5.4: Curve fitting of mean time (in seconds) of each ROI block size of the medial gastrocnemius tendon.

Again, to look at the performance of each block size, 5x5 gave fastest the mean time of 10±0 and 31x31 gave the longest time with 142±9 seconds to complete. 11x11, 15x15, 21x21 and 25x25 each respectively gave the mean value of 21±1, 37±3, 67±2 and 99±6 seconds to complete. The figure exhibits the similar trend of time curve as in figure 5.2 expect that the variation is more linear, and does not show the slight additional increase in computation as the block size increases. This is considered to be due to fewer tracking errors for this data set, as observed in both Section 4.4 (passive movement) and 4.5 (active movement). In passive movement, for the NCC algorithm, the medial gastrocnemius tendon data gave a lower number of tracking errors compared to the errors found using the patella tendon data. Again, in active movement, for the NCC algorithm, medial gastrocnemius gave the least number of tracking errors compared to the patella tendon.

5.2 Tracking Algorithm Threshold Level Comparisons

For each frame, the tracking algorithm gave an array of correlation values for the ROI, which were sorted, to get the highest correlation which then are used as the starting position in the following frame. If the highest value was less than the threshold value pre-defined within the GUI selections, the software entered the stationary movement error recovery process. This experiment looks at various threshold values in order to compare and decide the optimum value for the speckle tracking. The experiment again looks at both active movements of patella and the medial gastrocnemius tendon regional area.

5.2.1 Patella Tendon

The first tests conducted for the threshold analysis was to look at every 0.05 interval ranging from 0 to 1 over the patella regions (see Figure 5.5). The displacement values were relative to their starting position in the initial frame to their final position in the final frame. The differences between intervals were minimal when compared to the manual measurement.

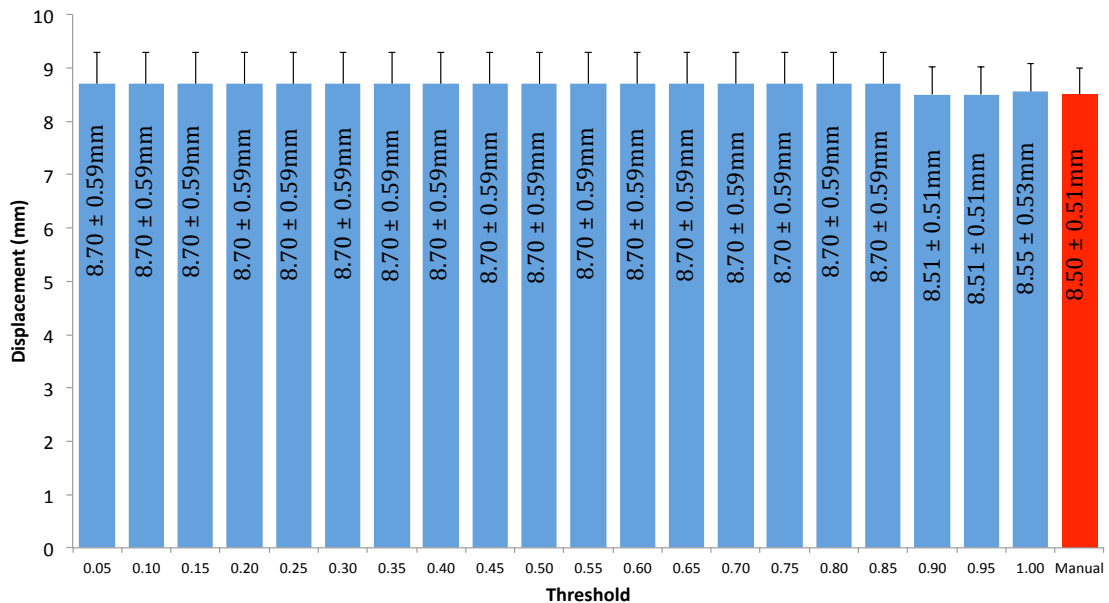


Figure 5.5: Mean displacement (in millimetre) of threshold level at every 0.05 intervals and the manual measurement (red bar) of active movement of the patella tendon. The displacement values were relative to their starting position in the initial frame to their final position in the final frame.

No significant differences ($p>0.05$) were found between the measured displacement at every interval and the manual measurement. However, the threshold value ranging from 0.05 to 0.80 gave the mean displacement of $8.70\pm 0.59\text{mm}$ compared to the manual measurement of $8.50\pm 0.59\text{mm}$. Meanwhile, the threshold value ranging from 0.90 to 0.95 gave the displacement value of $8.51\pm 0.51\text{mm}$, indicating that at >0.90 there was an improvement in tracking. Finally, the maximum threshold value of 1.00 gave a slightly higher threshold value, with the mean displacement of $8.55\pm 0.53\text{mm}$, which means that an exact match will not be possible since the tracking was looking at the movement of randomised speckle patterns. The experiment showed that the threshold values of 0.90 to 0.95 gave the closest measurement to the manual measurement but not significantly different ($p>0.05$).

5.2.2 Medial Gastrocnemius Tendon

The same experiment was conducted on the regional area of the medial gastrocnemius tendon to look at every 0.10 intervals of the threshold value. As shown in Figure 5.6, similarly to the results shown from patella tendon analysis, no significant differences ($p>0.05$) were found between the measurement of the threshold levels and the manual measurement. However, the threshold value ranging from 0.10 to 0.80 gave the percentage differences of $1.29\pm 9.75\%$ with mean displacement of $8.30\pm 0.36\text{mm}$ compared to the manual measurement with mean displacement of $8.19\pm 0.46\text{mm}$. Threshold level 0.90 gave the smallest percentage difference of $0.12\pm 0.07\%$ with the mean displacement of $8.18\pm 0.46\text{mm}$, and threshold level 0f 1.00 gave slightly higher percentage difference of $0.15\pm 4.36\%$ with the average displacement of $8.21\pm 0.42\text{mm}$.

Again, the experiment showed that the threshold value of 0.90 and 1.00 gave the closest measurements to the manual measurement. Further observation was conducted to look at the displacement value of the tracking using the threshold level of 0.90 to 1.00 at 0.01 intervals (see figure 5.6). The experiment indicated that the threshold levels, ranging from 0.90 to 0.96 gave the smallest percentage difference of $0.12\pm 0.07\%$ with mean displacement of $8.18\pm 0.46\text{mm}$. The threshold levels ranging

from 0.97 to 0.99 gave the highest percentage differences of $0.24 \pm 3.50\%$ with mean displacement of $8.17 \pm 0.35\text{mm}$. A threshold level of 1.00 gave slightly lower percentage difference of $0.15 \pm 4.36\%$ with mean displacement of $8.21 \pm 0.42\text{mm}$. All threshold levels were found to be not significantly different ($p > 0.05$) from the manual measurement.

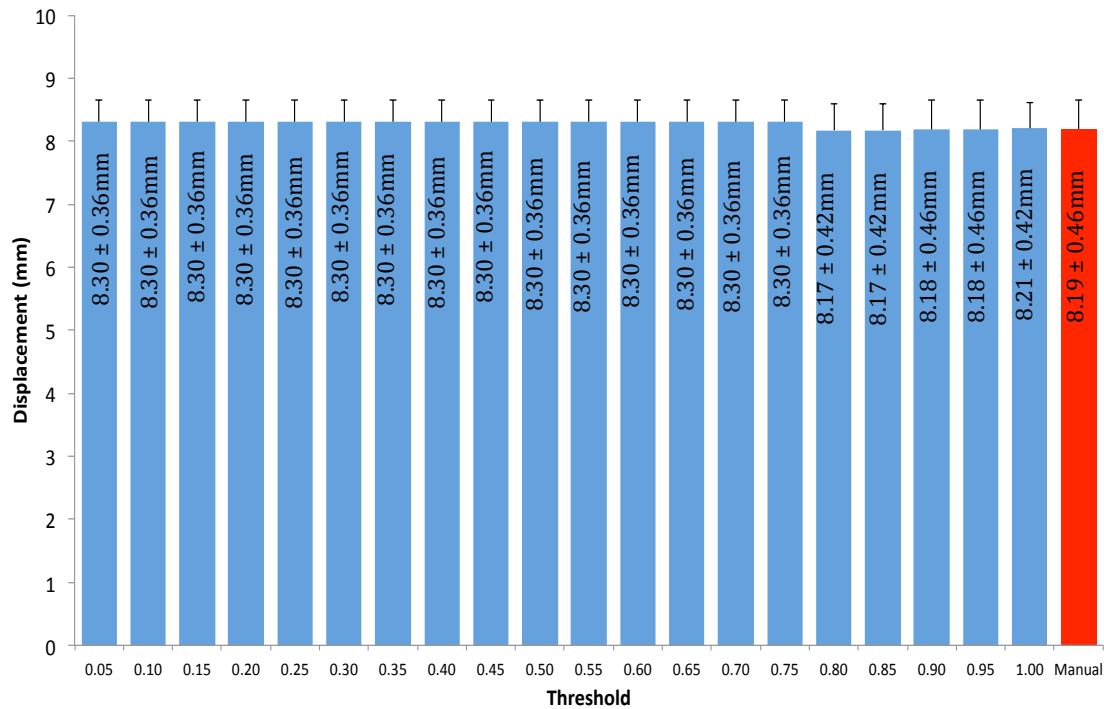


Figure 5.6: Mean displacement (in millimetre) of threshold level at every 0.05 intervals and the manual measurement (red bar) of active movement of the medial gastrocnemius tendon.

Both analyses showed that the threshold level of 0.90 onwards gave the closest mean displacement with the smallest percentage differences to the mean displacement using manual measurement. However, measurement depended on how the speckles formed within the image.

5.3 Automatic Tracking using Two Regions of Interest (2-ROI)

Since the Normalised Cross Correlation (NCC) was chosen as the algorithm for the tracking software, this section explored the performance of the tracking algorithm when two regions of interests (2-ROI). The 2-ROI consists of P1 (node 1) and P2 (node 2) placed in the first frame used as the initial nodes. The movement for both ROIs was then tracked until it reached the last frame. The position of the nodes in the last frame was then measured. The difference of the position of P1 and P2 of the first frame to the position of P1 and P2 of the last frame is the displacement value (see Figure 3.16). The 2-ROI markers were used to observe the dynamic changes of the regional area of the tendon to calculate the localised stiffness and strain (Couppé et al., 2008, Pearson et al., 2013) and the results were then compared to the standard manual measurement. The method and experimental setup was described in Section 3.4 of Chapter 3.

For the comparison analysis between the automatic tracking method and the manual tracking method, both patella and medial gastrocnemius tendon were chosen. Similarly to the previous analysis in Chapter 4, each site experimented with both passive and active tendon activity. 2-ROI markers were selected on two regional sites of the tendon (as described in Section 3.4 of Chapter 3). In the compared frame, the coordinates of the region of interest (ROI) are offset along the horizontal image plane and are shifted by a pixel at a time. Here a good match should be expected if the algorithm can give the closest difference with the manual measurements. Manual measurements used the same start reference point (P1, P2) in the first frame as the automated method and identified where it had moved to in the last frame by examination of the video as mentioned in Chapter 3 (see Figure 3.16).

Since the previous experiment showed that the 15x15 pixel ROI gave the closest match to the standard manual measurement, the same ROI size was selected to compare with the smallest ROI block (5x5 pixel ROI) and the largest ROI pixel block (31x31). The performance of 2-ROI was measured when tracking the dynamic tendon regions. For all repeat trials the initial position of the ROIs were the exact same reference point in the frame.

5.3.1 Patella Tendon

The first experiment looked at the knee area of the patella tendon using the 2-ROI-experiment setup described in Chapter 3, with both passive and active muscle movement tested. Both tests were on 10 participants and compared to the manual measurements.

5.3.1.1 Passive Movement

The 2-ROI passive tests for the patella tendon (knee) showed the 15x15 pixel ROI has the closest mean value to the manual measurement ($0.35 \pm 0.06\text{mm}$ vs. $0.30 \pm 0.07\text{mm}$). The 5x5 pixel ROI gave the largest displacement mean value ($1.62 \pm 0.64\text{mm}$). Comparisons between manual and 15x15 ROI indicated that there was no significant difference ($p > 0.05$). 5x5 pixel ROI was shown to be significantly different ($p < 0.05$) to the manual measurement. The results of the 2-ROI passive tests were illustrated as a graph in Figure 5.7.

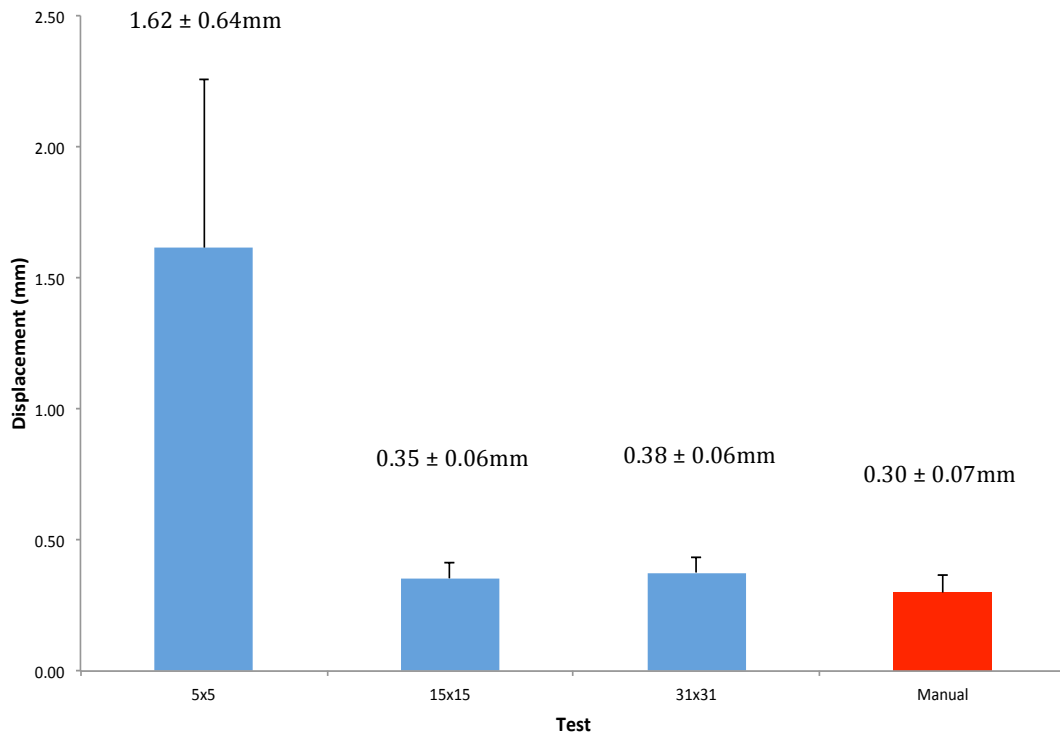


Figure 5.7: Comparisons graph between ROI size and manual tracking for passive movement at the patella.

5.3.1.1 Active Movement

The next tests involved active displacement of the tendon (where the tendon stretches). Figure 5.8 illustrates the results of the comparisons between various sizes of ROIs and compared to the manual measurement for active knee movement. As previous tests, all ROI sizes were compared to the manual method for the knee using the same method as the passive movement test. There were no significant differences ($p>0.05$) between the results, being different ROIs and the manual measurements although it can be seen that the 31x31 pixel ROI did worse in this test in comparison to the other sized ROIs. The 5x5, 15x15, and 31x31 pixels ROI giving mean values of $4.74\pm 0.39\text{mm}$, $4.82\pm 0.48\text{mm}$, and $4.36\pm 0.33\text{mm}$ respectively as compared with the manual mean value of $4.80\pm 0.45\text{mm}$.

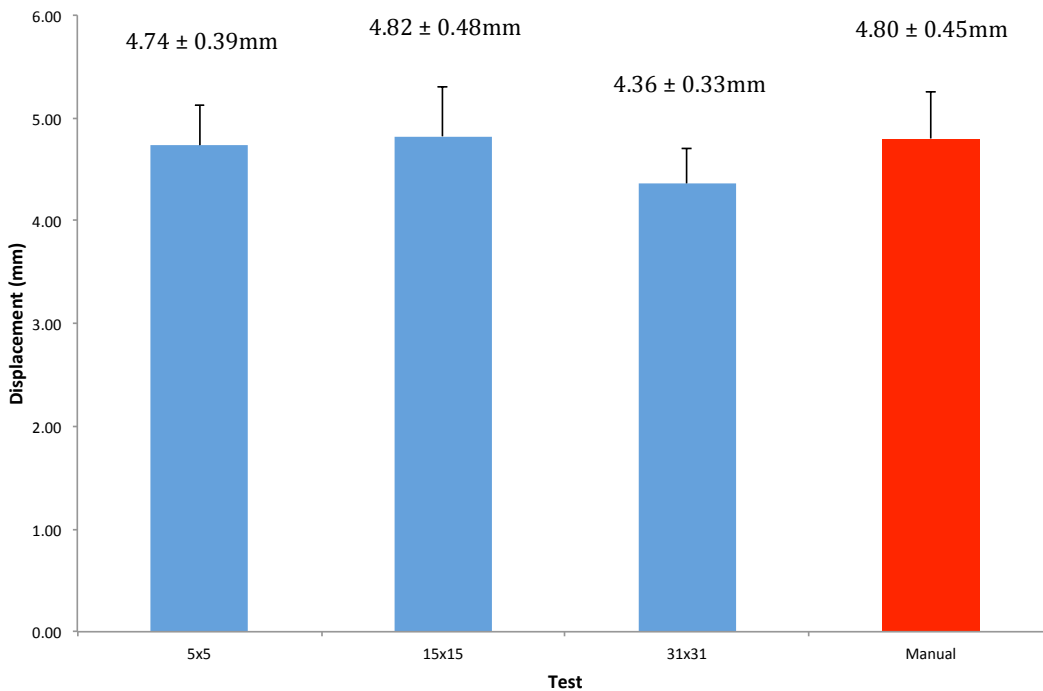


Figure 5.8: Comparisons graph between various sizes of ROI and manual tracking for active movement at the patella.

The percentage differences of 5x5 pixel ROI against the manual measurement were seen to be $0.31\pm 0.06\%$, 15x15 with $0.12\pm 0.03\%$ and 31x31 with 2.17 ± 0.12 . For the active tests, the errors were expected to be larger due to the tendon being dynamically stretched during muscle contraction hence causing some deformation.

5.3.2 Medial Gastrocnemius Tendon

The second experiment looked at the ankle area of the medial gastrocnemius tendon using the 2-ROI-experiment setup described in Chapter 3, for both passive and active muscle movement tested. The results of both tests were compared to the manual measurements.

5.3.2.1 Passive movement

The tests for the ankle (medial gastrocnemius tendon junction) showed the 15x15 pixel ROI has the closest mean value ($0.44\pm 0.09\text{mm}$) to the manual method mean displacement ($0.42\pm 0.05\text{mm}$) followed by a 31x31 pixel ROI ($0.63\pm 0.12\text{ mm}$). Here the 5x5 pixel ROI has the largest mean displacement measurement ($1.07\pm 0.36\text{ mm}$) compared to the mean value of manual measurement (see Figure 5.9). The displacement value for each algorithm and manual measurement measures the displacement relative to their starting position in the initial frame to their final position in the final frame.

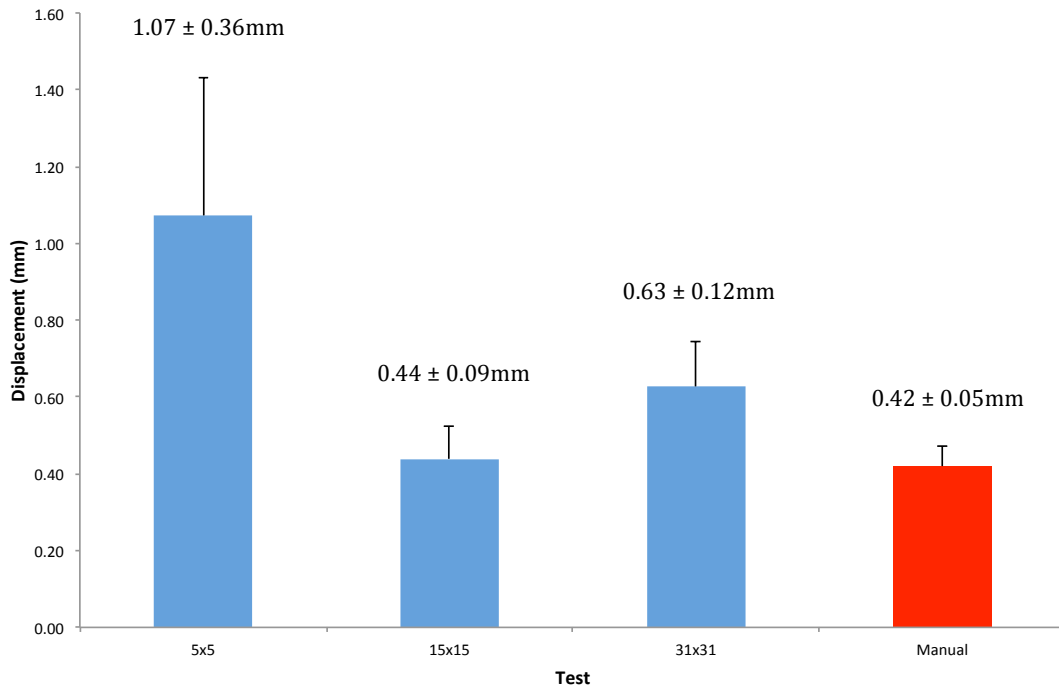


Figure 5.9: Comparisons graph between various sizes of ROI and manual tracking for passive medial gastrocnemius measurement. The displacement value for each algorithm and manual measurement measures the displacement relative to their starting position in the initial frame to their final position in the final frame.

Comparisons between manual and automated tracking indicated that there was a significant difference ($P < 0.05$) between the 5x5 pixel ROIs and the manual method. The 15x15 pixel ROI showed no significant differences ($p > 0.05$) from the manual measurement.

5.3.2.2 Active movement

Same as the active movement analysis on the knee area, the active displacement of the tendon involved the movement where the tendon stretches. As with the previous tests, all ROI sizes were compared to the manual method for the ankle using the same method as the passive movement tests. There were no significance differences ($p > 0.05$) found between the comparisons to the other sized ROIs although it can be seen that the 5x5 pixel ROI performed worse in this test in

comparison to the other pixel ROI's (see figure 5.10) with displacement value of $2.74 \pm 0.57\text{mm}$ in comparison to the manual measurement ($5.03 \pm 0.31\text{mm}$). The 15×15 gave the closest mean displacement value ($5.08 \pm 0.32\text{mm}$) to the manual measurement and 35×35 pixels gave the mean value of $4.86 \pm 0.21\text{mm}$. As discussed earlier from the knee analysis, the active tests showed larger errors due to the tendon being dynamically stretched during muscle contraction hence causing some deformation.

The whole experiments of 2-ROI analyses showed that 15×15 pixels ROI for both passive and active movement of the patella, and medial gastrocnemius tendon gave the best agreement with the manual measure. The difference found from the passive tendon movement showed that 15×15 pixel ROI gave difference of $0.05 \pm 0.09\text{mm}$ (knee) and $0.02 \pm 0.66\text{mm}$ (ankle) from the manual measurement. The active tendon movement showed that the 15×15 pixel ROI gave the differences of $0.10 \pm 0.02\text{mm}$ (knee) and $0.05 \pm 0.45\text{mm}$ (ankle) from the manual measurement. Furthermore no significance differences ($p > 0.05$) were found between 15×15 pixel ROI and manual measurement.

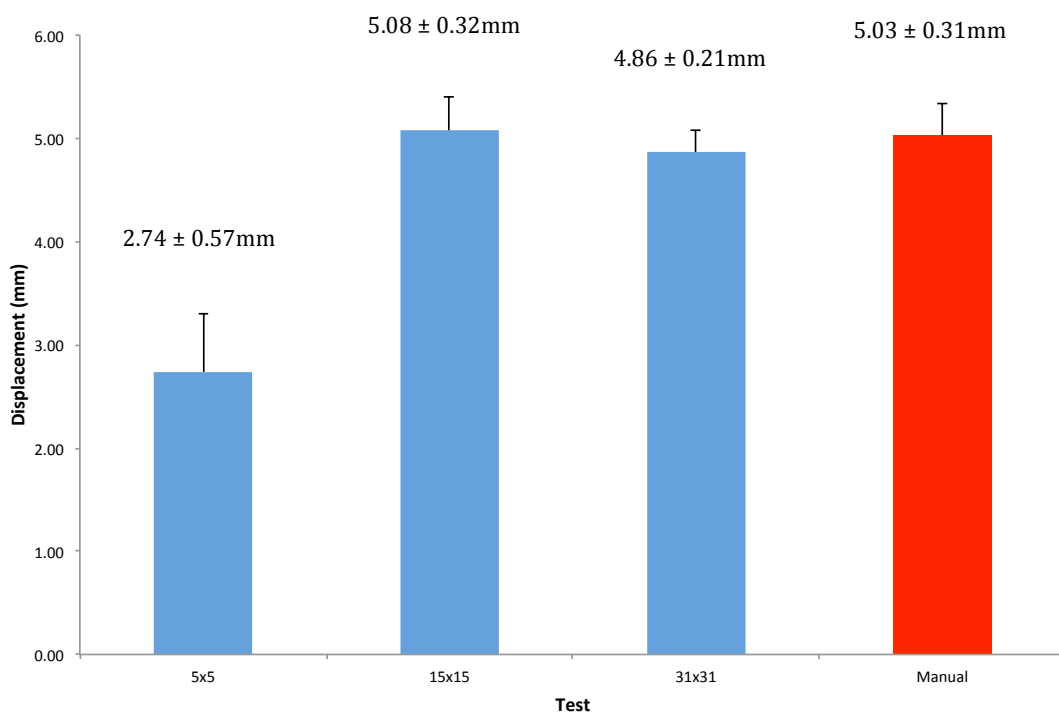


Figure 5.10: Comparisons graph between various sizes of ROI and manual tracking for active medial gastrocnemius movement.

5.4 Summary

The experiments conducted showed the effectiveness of the tracking system in comparison to the manual measurement. Experiments were divided into ROI block sizes and thresholds were observed at every level. Also, two regions of interest (2-ROI) were compared with the manual measurement. The active test of the patella and gastrocnemius tendon showed that the 15x15 pixel ROI gave the best performance. The next experiment looked at the algorithm threshold level; the experiments showed that the threshold value in the range of >0.90 gave the optimum tracking results. The last tracking analysis conducted 2-ROI with the pixel size of 15x15 were found to be nearest to the manual measurement for both active and passive movements.

In the next chapter (chapter 6), actual experiments (in-vivo) are conducted whereby the settings of the tracking analysis were based on the algorithm validation results. The methods for the experiments were explained in Chapter 3. The experiment's results that are useful and gave an insight to be used by the physiologist to understand and to describe further the mechanical properties of the tendon activity.

Chapter 6

In Vivo Experiments:

Multiple Layer Automatic Tracking to

Determine Human Tendon

Mechanical Properties

Overview

In this Chapter the results obtained when using the NCC tracking algorithm with the optimum parameters to characterize localized tendon strain at the anterior, midsection and posterior layers for both proximal and distal regions of the patella is described. The importance of these results in the improved understanding of the working aetiological of human tendon mechanical properties is then discussed.

6.1 In-Vivo Strain Comparison

The in-vivo experiments were concerned with observing and comparing the patella tendon excursion at the anterior, midsection and posterior layers for both proximal and distal regions of the patella tendon during ramped isometric voluntary contractions. For each layer, the NCC speckle tracking algorithm with the optimum parameters, and 2-ROIs was used to measure the tendon displacement and tendon strain frame-by-frame.

6.2 Proximal Strain Results

The proximal region is located at the proximal side of the patella and very close to the peninsula knee bone. The regional area was shown in Figure 3.18. The strain measurements that were derived from the speckle tracking for different force levels accumulated at every 10% interval starting from 10% of force for each of the three layers (anterior, mid section and posterior) are shown in Figure 6.1. The figure reveal that significant increased strain ($p < 0.01$) across the total range of forces levels but force levels 50-60% and 90-100% showed no significant difference ($p > 0.05$) for the anterior layer, indicated by (*) symbols. Force levels of 40-60% for the mid section layer also showed no significant difference ($p > 0.05$) and indicated by (^) symbol. The posterior layer was also found to have no significant difference ($p > 0.05$) at force levels 30-60% and 70-100%, indicated by the (~) symbols. It can be seen that at 100% of force the anterior gave the highest mean strain of $11.86 \pm 0.53\%$. The mid section gave $10.30 \pm 0.79\%$, and the posterior gave the smallest mean strain of $5.98 \pm 0.85\%$.

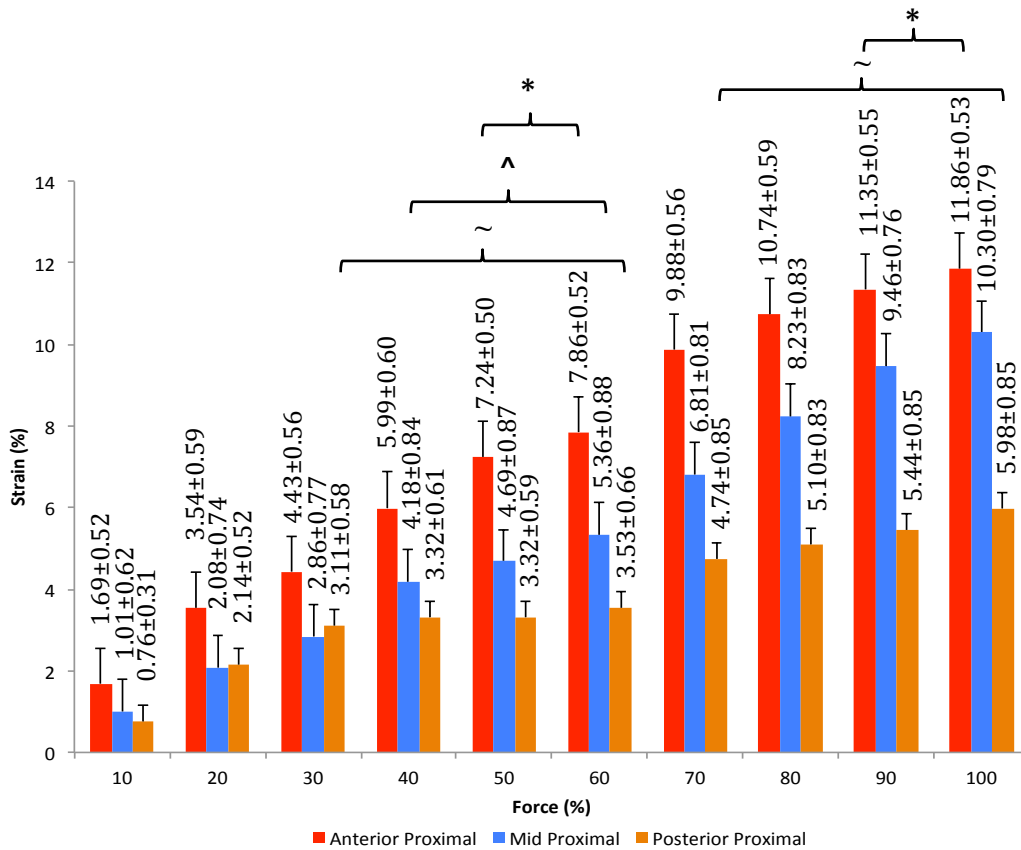


Figure 6.1: Strain value (%) for all measured proximal regions (mean \pm SEM) accumulated at 10-100% force.

6.3 Distal Strain Results

The distal region is located at the distal side of the patella as was shown in Figure 3.18. In Figure 6.2, it can be seen that all the distal layers showed a significant increase ($p < 0.01$) in strain across the force levels accumulated at each 10% interval starting from 10% of force with no interaction between layer and between forces. The mean strain of the posterior layer was seen to be significantly greater ($p = 0.01$) than both the anterior layer and the mid section for the distal region of the patella tendon. It can be seen that at 100% of force the posterior layer gave the highest mean strain of $11.96 \pm 0.62\%$, followed by the mid section ($9.55 \pm 0.79\%$) and the anterior with the mean strain of $8.96 \pm 0.89\%$.

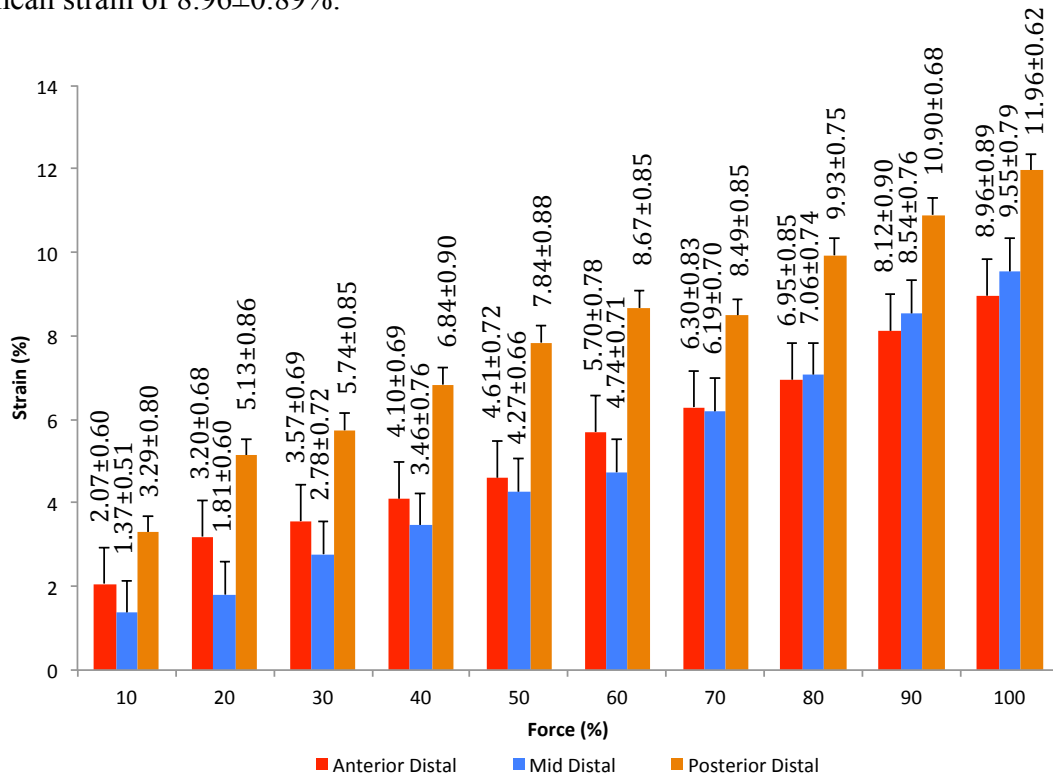


Figure 6.2: Strain values for all measured distal regions (mean ± SEM) accumulated at 10-100% force.

6.4 Comparisons Between Proximal and Distal Layers

The experiments described in the previous sections looked at the comparison between layers for both proximal and distal regions of the patella tendon at every 10% force level interval. The measurements taken were converted to a strain percentage and showed that the proximal anterior and distal posterior regions gave the largest strains. In this section, there is a comparison of overall mean strains between 50% and 100% force. Table 6.1 shows the instantaneous strain values at 50% and 100% with the relative difference and corresponding mean forces (%) for all layers at both proximal and distal regions of the patella tendon as shown in Equation 6.1:

$$d = \overline{x_{100}} - \overline{x_{50}} \quad (6.1)$$

where d is the difference between two means and x_n is the relative force level of 50% or 100%. The standard error of the difference between means is shown in equation 6.2:

$$\sigma_{100-50} = \sqrt{\sigma_{100}^2 + \sigma_{50}^2} \quad (6.2)$$

The overall mean strain was greater at 100% force with a mean strain value of $9.77 \pm 0.75\%$ compared to a mean strain value of $5.33 \pm 0.73\%$ at 50% force. The proximal strain showed a lower mean strain difference between 50 and 100% force with the posterior proximal giving the least difference at $2.66 \pm 0.24\%$, followed by anterior proximal with a difference of 4.62 ± 0.03 . The mid section gave the highest percentage difference of $5.61 \pm 0.21\%$. The distal strain results showed higher strain differences for each layer, as the anterior distal were seen to be $4.35 \pm 0.18\%$ different between 50% and 100%. The mid section gave highest difference at $5.28 \pm 0.13\%$, and the posterior distal gave the smallest difference of $4.12 \pm 0.25\%$.

Force (%)	Strain (%)						
	Proximal			Distal			Total Mean Strain (%)
	Anterior	Mid Section	Posterior	Anterior	Mid Section	Posterior	
50	7.24±0.52	4.69±0.94	3.32±0.64	4.61±0.73	4.27±0.67	7.84±0.90	5.33±0.73
100	11.86±0.55	10.30±0.73	5.98±0.88	8.96±0.91	9.55±0.80	11.96±0.65	9.77±0.75
Difference	4.62±0.76	5.61±1.19	2.66±1.09	4.35±1.17	5.28±1.04	4.12±1.11	4.44±1.05

Table 6.1: Instantaneous mean strain for all layers at both proximal and distal regions of the patella tendon at 50% and 100% force levels.

Figure 6.3 shows that all force levels and regions showed no interaction towards each other ($p>0.05$) and mean values (i.e. average of 50 & 100% force levels) for strain indicated that the proximal anterior strain (*) and the distal posterior strain (^) were greater than all other regions ($p<0.05$). The proximal mid section strain was shown to be significantly different ($p=0.02$) to the proximal posterior strain (~). These huge differences in strain between 50% and 100% force could indicate shear between the tendon boundary layers causing differential longitudinal movement between layers (shear force). In time, this relative difference in strain at different levels of force may be a factor in the development of cumulative tendon injury.

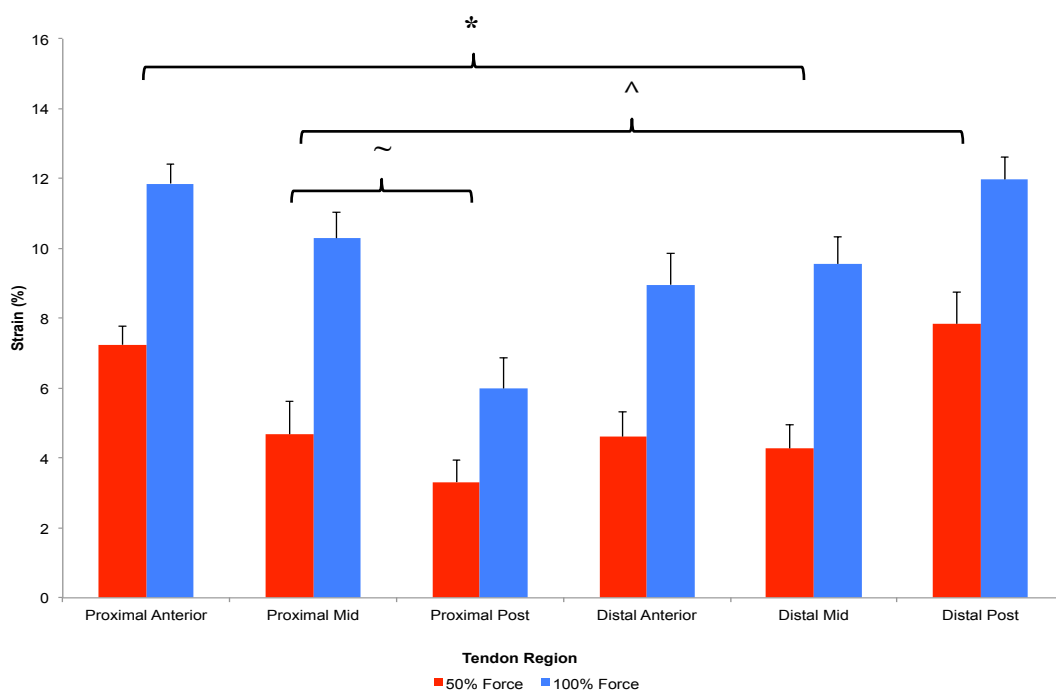


Figure 6.3: Instantaneous strain values for all layers at both proximal and distal regions of the patella tendon at 50% and 100% force.

The experiments showed that multi-layer tracking was able to estimate frame-to-frame displacements using multiple-ROI where 2-ROI end points were placed at each layer. Previous studies have validated the use of localized tracking of tendon using block-matching techniques similar to that used here (Haraldsson, et al., 2005, Pearson, et al., 2007, Kim, et al., 2011) with a small margin of errors. A recent study (Couppé, et al., 2008) reported that the tracking of tendon movement using 2-ROI end points can be achieved during twitch contraction, electrically stimulating the muscle. However, the forces in the tendon were only moderate (up to 50% of maximum), which is a significant difference to the approach in this study, where high forces were elicited and thus larger tendon deformations would be expected making tracking more difficult. In addition, previous work has indicated that contraction time can affect the amount of excursion seen in the tendon (Pearson, et al., 2007), which can be explained due to the viscoelastic nature of the tendon. It could then be speculated that the composition of the tendon at different regions may be proportionally different in terms of the viscous and elastic components, which would affect the time-course of extension under load to different degrees.

The findings showed that the patella tendon for a group of healthy young subjects, the greatest strains (100% force) during isometric ramped contractions were seen in the anterior layer at the proximal end ($11.86 \pm 0.55\%$) and posterior layer at the distal end ($11.96 \pm 0.65\%$) with significant differences ($p < 0.05$) between proximal and distal tendon. The strain calculated here were within the range of those reported for this structure in young males (Onambele, et al., 2007, Child, et al., 2010, Hansen, et al., 2010) where the previous references showing a range of 6 – 10.6% strain. It can also be concluded from the results that the proximal mid section and posterior tendon strain were at $10.30 \pm 0.73\%$ and $5.98 \pm 0.88\%$ respectively. The distal anterior and mid section showed 8.96 ± 0.91 and $9.55 \pm 0.80\%$ tendon strain respectively, which are considerably larger than those reported by others (Basso, et al., 2002).

The reason for such larger values may be due to differences in the level of load, application of load and also that here the strain was determined in the proximal and distal sections of the tendon compared to the mid-third utilised by the other study (Basso, et al., 2002). It may be that the tendon is not homogenous throughout its length and could be structurally different in terms of the collagen content, type and

extracellular matrix density. Another explanation might be related to the samples used in other study were taken from a cadaver, compared to the live specimen used in this study (Basso, et al., 2002).

The method of using 2-ROI at multiple layers of the tendon has the potential to improve clinical knowledge relating to the tendon mechanical properties. It is clear that the strain throughout the tendon structure is not equal for a given external force, lending itself to tissue shear and hence to potential for increase injury risk in specific regions of the tendon. The information generated by the tracking algorithm could help to determine how and why these differences in strain may affect the aetiology of disease and effects of training rehabilitation. These studies will give further insight into the aetiology of tendon injury, repair, response to various training interventions and the time course of tissue adaptation with disease.

6.5 Summary

The experiments described in this Chapter examined and compared localised proximal strain at both the anterior and posterior regions of the patella tendon using 2-ROI tracking on multiple layers of anterior, posterior and mid section in-vivo. The measurements obtained from the tracking were converted into mean strains, which were used to investigate the interactions between the layers of the tendon. The experimental setup for the experiments was described in Chapter 3. The algorithm used for the tracking was Normalized Cross Correlation (NCC), which was selected based on the analysis conducted in Chapter 4 and the optimal tracking settings, was based on the analysis carried out in Chapter 5.

The experiment showed that the anterior layer at the proximal end gave the highest mean strain with $11.86 \pm 0.55\%$ with mean difference between 50% and 100% force was seen to be at $4.62 \pm 0.76\%$ and posterior layer at distal end gave the highest mean strain with $11.96 \pm 0.65\%$ with mean difference between 50% and 100% force to be $4.12 \pm 1.11\%$. Significant differences were also seen ($p < 0.05$) between proximal and distal tendon. These different patterns of strain between the tendon layers at the sites measured could indicate shear of the tendon structure. It is clear that the strain

throughout the tendon structure is not equal for a given external force, lending itself to tissue shear and hence to potential for increased injury risk in specific regions of the tendon. The huge differences in strain between 50% and 100% force could also indicate shear between the tendon boundaries, which over time may develop into cumulative tendon injury. The use of multiple layer image tracking could generate valuable information that can be used to describe in detail how the tendon works at the different layers and regions by measuring the strain during ramped isometric voluntary contractions to improve clinical knowledge relating to the tendon mechanical properties to give further insight of the cause of tendon injury.

Chapter 7

Summary and Conclusions

7.1 Summary

In this thesis, an improvement to the ultrasound image-tracking algorithm was developed using various image tracking algorithms for tracking the movement of the tendon speckle image obtained using the B-mode ultrasonography. The algorithms were selected following a literature review of the tracking of images captured using ultrasound imaging. Experiments were carried out to examine these tracking algorithms and optimise them to allow the utilisation of the tracking software in human studies conducted here.

The aim of this work was to design, develop, and implement the image-tracking algorithm to track movement of the human tendon in vivo within the speckled ultrasound images. The development of the tracking software focused on solving the problems of tracking the ultrasound images, as well as analysing the tracking movement frame-by-frame to produce useful measurements that can be used to describe the mechanical properties of the human tendon.

In Chapter 1, there was a brief introduction to the fundamentals of image processing and tracking as well as its usage in various applications. Towards the end of the Chapter, the Aims and Objectives of the study were stated, and the structure of the Thesis was described in detail.

In Chapter 2, the biomedical background related to tendon structures and functions was described, as well as applications and experiments related to the ultrasound imaging and tracking in biomedical areas. The background to image tracking within the domain of ultrasound imaging was also described, with details of the main tracking algorithms that have been used for tracking biomedical ultrasound

images. This understanding of the tracking algorithms and its area of interest within the mechanical tendon was essential for the parameter identification and motion estimation for the ultrasound imaging with random speckle formations.

In Chapter 3, the experiment setup was explained in detail in order to validate the effectiveness of the tracking algorithms using the tendon muscle data in-vivo. The hardware used, and the method of image acquisition is explained, as well as the test subjects including areas of interest within the tendon muscle, and what kind of output was to be expected. The software design and implementation was also covered in Chapter 3 showing how results are achieved and what kind of algorithms were used within the software environment. Details of each tracking algorithm were described and how each data was treated from each algorithm and techniques used for each experiment were also described.

In Chapter 4, there were detailed discussions of tracking algorithms that were used in the study. These algorithms included Normalised Cross Correlation (NCC), Mean Square Error (MSE), optical flow – Lucas-Kanade (LK) and the combination of NCC and MSE (NCCMSE) selected by signal noise-to-ratio (SNR). The investigation of the algorithms lead to the best performing algorithm, in the sense of the measurements generated were approximately similar to those obtained using the manual experiments, being identified and selected for the subsequent experiments. This algorithm was the Normalised Cross Correlation (NCC) with a block matching search method (BMA). This tracking algorithm was shown to be capable of handling the randomness of the speckle pattern in any conditions (active or passive) on two different tendon areas (knee and ankle).

Furthermore, the results obtained from all the algorithms tested showed both MSE and LK to be the least accurate followed by NCCMSE. The NCC showed the closest match to the manual measurement at 100% of the frame with the mean difference of 0.44 ± 1.99 mm (passive knee). However, NCCMSE performed better than NCC when tested on passive ankle with mean difference of 0.22 ± 1.61 mm against NCC of 0.63 ± 1.54 mean differences. The active knee test showed that at 100% of the frame, NCC gave closest match (5.65 ± 1.13 mm) to manual measurement (5.67 ± 0.52 mm) and active ankle also showed that NCC gave the closest match

(5.52±0.47mm) to the manual measurement (5.37±0.61mm). Further analysis looked at the time taken for each algorithm to identify which algorithm used the most resources (costliest) during the tracking procedure. NCC was seen to take the least time to track the whole image sequences with total mean time of 13±1 seconds for passive movement and 8±1 seconds for active movements. Stationary errors analysis was also conducted to measure the number of errors that occurred during the tracking process for each algorithm tested. The NCC was found to give the least mean error count (9.40±1.07) for knee passive and ankle passive (6.00±1.12). As for the active knee and ankle, NCC still showed the least mean errors count with total mean error counts of 9.40±2.37 and 4.10±0.82 respectively. This indicated that NCC gave the least errors in relation to stationary movement errors. NCC again showed the least error counts for the irregular movements errors with error counts of 0.50±0.17 (passive knee and passive ankle), 0.60±0.22 (active knee) and 0.40±0.16 (active ankle). The results established that NCC was the best choice to be incorporated into the tracking software.

In Chapter 5, the Normalised Cross Correlation (NCC) algorithm was chosen as the algorithm to be developed further and incorporated into the tracking software for the later experiments. The analysis conducted in this Chapter looked at the ROI block size and threshold value for optimum tracking results. The results were then validated against the standard manual measurement. Similar to the analysis conducted in the previous Chapter, timing comparisons were also made for both ROI block size and threshold analysis. As for the ROI block size, 15x15 ROI block size was shown to be the optimum with active knee movement measurement of 8.69±0.55mm against manual measurement of 8.50±0.51mm. The same ROI block size was also found to be the optimum on ankle with displacement value of 8.20±0.37mm against manual measurement (8.19±0.46mm). The average time for 15x15 ROI block size was within ≈37±3 to ≈44±6 seconds on both knee and patella active movements.

Further experiments looked at the optimum threshold level, which was used to indicate that a match had been found. Active movements of the knee experiment reported that the threshold levels from 0.90 onwards gave the optimum tracking results with the displacement value of 8.51±0.51mm against manual measurement (8.50±0.51mm) while the active movements of ankle showed that the same threshold

level gave the same optimum tracking results with the displacement value of $8.18 \pm 0.46 \text{mm}$ against $8.19 \pm 0.46 \text{mm}$. The experiments validated the threshold level range of >0.90 to be the optimum threshold as it gave close approximation to the manual measurement.

The last tracking analysis that was conducted examined the two regions of interest (2-ROI), where two ROI nodes were placed along the elongation of the tendon, giving relative movement of two ROIs during muscle contraction. The passive movement of the knee proved that 15×15 pixel ROIs were found to be optimum with displacement value of $0.35 \pm 0.06 \text{mm}$ against the manual measurement ($0.30 \pm 0.07 \text{mm}$). The passive movement should give relative movements close to zero displacement. However, a slight increase or decrease within the movement was expected since the accuracy of the tracking was dependent on the clarity of the speckle image. The passive movement of the ankle also indicated that 15×15 pixels ROI to be the optimum with mean displacement value of 0.44 ± 0.09 against manual measurement ($0.42 \pm 0.05 \text{mm}$).

The active movement analysis looked at the relative movement of two ROI nodes during active muscle contractions. The 15×15 pixel ROI for both knee and ankle tendon areas was seen to give the nearest value to the manual measurements, with the active movement of the patella giving mean displacement of $4.82 \pm 0.48 \text{mm}$ against the manual measurement ($4.80 \pm 0.45 \text{mm}$) and ankle giving the mean displacement of $5.08 \pm 0.32 \text{mm}$ against the manual measurement ($5.03 \pm 0.31 \text{mm}$). Throughout the experiments, the automatic tracking was proven to be accurate enough to match the manual measurements. The differences were minimal and proved that 15×15 pixel ROI was the best for the tracking of the tendon area of the patella and medial gastrocnemius using either 1-ROI or 2-ROI modes. Finally, the validation analysis confirmed that the Normalised Cross Correlation (NCC) approach was seen to be the optimum choice of tracking algorithm for tracking highly speckled ultrasound images.

In Chapter 6, the experiments aimed at examining and comparing localised proximal strain at both the anterior and posterior layers of the patella tendon using 2-ROI tracking on multiple layers of anterior, posterior and mid section were described.

The measurements obtained from the optimum tracking were then converted into mean strain to look at the interactions between the layers of the tendon.

The first experiment used the tracking software to look at the proximal strain to compare the strains between its layers. The results showed that the proximal anterior at 100% force level gave the highest mean strain of $11.86 \pm 0.53\%$, followed by the proximal mid section layer with the mean strain of $10.30 \pm 0.79\%$, and the smallest mean strain ($5.98 \pm 0.85\%$) was found at the proximal posterior. The second experiment looked at the distal strain and as for the proximal strain analysis, several layers were analysed. The results showed that the distal posterior at 100% force level gave the highest mean strain with $11.96 \pm 0.62\%$, followed by the distal mid section with $9.55 \pm 0.79\%$ and finally the distal anterior gave the smallest mean strain at $8.96 \pm 0.89\%$. The last experiment compared each layer of proximal and distal at 50 and 100% force levels.

Overall, it was found that the mean strain value at 100% force level was $9.77 \pm 0.75\%$, which was greater than the 50% mean strain value at $5.33 \pm 0.73\%$. The mean strain difference between 50 and 100% force levels in the distal regions was seen to be greatest at the mid section layer with a $5.28 \pm 1.04\%$ difference, followed by the anterior layer with $4.35 \pm 1.17\%$ difference, and the posterior layer gave the smallest difference with $4.12 \pm 1.11\%$. The proximal regions however gave the least mean strain difference at the posterior layer with $2.66 \pm 1.09\%$, followed by the anterior layer with $4.62 \pm 0.76\%$ and highest at mid section layer with $5.61 \pm 1.19\%$. The results also indicated that the greatest mean strains during isometric ramped contraction were seen in the anterior layer at the proximal ends with $9.55 \pm 0.54\%$ and the distal posterior mean strain value of $9.90 \pm 0.78\%$.

All experiments indicated that regional layers differences exist in strain within a tendon; also, the 'twisting' of the bone attachment caused the differential strain seen here. These different patterns of strain between the tendon layers at the sites measured could indicate shear of the tendon structure. It was concluded that the use of multiple layer image tracking could generate valuable information that can be used to describe in detail on how tendon works at each layer and region.

To summarise, the aims and objectives of the study were:

- The data acquisition consists of stages where images collected using the ultrasound machine and tracked using the tracking algorithms selected for this study.
- The process of tracking the ultrasound images using the tracking software consists of three stages; input, process and output.
- The optimum similarity measurement algorithms for the tracking software showed that Normalised Cross Correlation (NCC) with the search method of block matching (BMA) gave the best tracking results with the measurements observed to be close to the standard manual measurement.
- The optimum search parameters were shown to be 15x15 ROI pixel size and threshold range of 0.90 to 0.96.
- The automatic tracking showed that both 1-ROI and 2-ROI gave measurements less than 5% different against the manual measurement in terms of accuracy with no significant difference ($p>0.05$) against the manual measurement throughout the experiments, also the experiments were conducted at both relaxed positions (passive) and 100% voluntary contractions (active) in vivo.
- A novel multilayered approach was conducted on B-mode ultrasound images on the patella tendon to investigate the interactions between layers (anterior, mid section and posterior) on both proximal and distal areas of the tendon in vivo.
- As a result, the layers measurements were converted into strain percentages to obtain its differences, and results showed that there exists shear within the tendon towards the 100% force levels.

7.2 Conclusions and Recommendations for Future Works

The method described here has the potential to improve clinical knowledge relating to the tendon's mechanical properties. It is clear that the strain throughout the tendon structure is not equal for a given external force, lending itself to tissue shear

and hence to potential for increased injury risk in specific areas of the tendon. The information generated by the tracking algorithm could help to determine how and why these differences in strain may affect the aetiology of disease and effects of training rehabilitation. These studies will give further insight into the aetiology of tendon injury, repair, response to various training interventions and the time course of tissue adaptation with disease.

The following aspects could be the subject of future works in the field of ultrasound image tracking on human mechanical tendon in vivo:

- To implement GPU parallel processing to improve the tracking speed and measure multiple points at every regions and layer of the tendon.
- Implementation of the tracking software to look at controlled subjects to determine how and why these differences in strain may affect the aetiology of disease and effects of training rehabilitation.
- To look at tendinopathy related subject to understand the disease progression ranging from various ages and genders, with the help of the tracking software.

References

- ALEXANDER, R. M. 2002. Tendon elasticity and muscle function. *Comparative Biochemistry and Physiology a-Molecular and Integrative Physiology*, 133, 1001-1011.
- ALMEKINDERS, L. C. & ALMEKINDERS, S. V. 1994. Outcome in the treatment of chronic overuse sports injuries: a retrospective study. *J Orthop.Sports Phys.Ther.*, 19, 157-161.
- ALMEKINDERS, L. C., VELLEMA, J. H. & WEINHOLD, P. S. 2002. Strain patterns in the patellar tendon and the implications for patellar tendinopathy. . *Knee Surgery Sports Traumatology Arthroscopy* 10, 2-5.
- ANDERSON, M. E. & TRAHEY, G. E. 1999. A seminar on k-space applied to medical ultrasound. *Department of Biomedical Engineering, Duke University*.
- ARAMPATZIS, A., STAFILIDIS, S., DEMONTE, G., KARAMANIDIS, K., MOREY-KLAPSING, G., & BRUGGEMANN, G.P 2005. Strain and Elongation of the Human.
- ARCHAMBAULTS, J.M., WILEY, J.P., BRAY R.C., VERHOEF, M., WISEMAN, D.A. and ELLIOTT, P.D. 1998. Can sonography predict the outcome in patients with achillodynia? *Journal of Clinical Ultrasound*, 26(7), 335-339.
- ASLAN, H., KIMELMAN-BLEICH, N., PELLED, G. & GAZIT, D. 2008. Molecular targets for tendon neoformation. *The Journal of Clinical Investigation*, 118, 439-444.
- BAKER, S. & MATTHEWS, I. 2004. Lucas-Kanade 20 Years On: A Unifying Framework. *International Journal of Computer Vision*, 56, 221-255.
- BALKE, M., DEDY, N., MUELLER-HUEBENTHAI, J., LIEM, D., HARDES, J. & HOEHER, J. 2010. Uncommon cause for anterior knee pain - Aggressive aneurysmal bone cyst of the patella. *Sports Medicine, Arthroscopy, Rehabilitation, Therapy & Technology*. 2:9, 1-5.
- BALTZOPOULOS, V. 1995. A Videofluoroscopy Method for Optical Distortion Correction and Measurement of Knee-Joint Kinematics. . *Clinical Biomechanics*, 10, 85-92.

- BAMBER, J. C. & DAFT, C. 1986. Adaptive filtering for reduction of speckle in ultrasonic pulse-echo images. *Ultrasonics*, 41-44.
- BARFOD, K. 2014. Achilles tendon rupture; assessment of nonoperative treatment. *Dan Med J*, 61, B4837.
- BARJATYA, A. 2003. Block Matching Algorithms For Motion Estimation. *Tech. Rep., Utah State University*.
- BASSO, O., AMIS, A. A., RACE, A. & JOHNSON, D. P. 2002. Patellar Tendon Fiber Strains: Their Differential Responses to Quadriceps Tension. *Clin Orthop Relat Res* 400, 246-253.
- BEAUCHEMIN, S. S. & BARRON, J. L. 1995. The computation of optical flow. *ACM Computing Surveys*, 27, 433-467.
- BENFOLD, B., & REID, I. 2009. Guiding Visual Surveillance by Tracking Human Attention. *Proceedings of the British Machine Vision Conference*.
- BENJAMIN, M. & RALPHS J.R 1995. Fibrocartilage associated with human tendons and their pulleys. *Journal of Anatomy*, 187, 625–633.
- BENJAMIN, M., RALPHS J.R & QIN, S. 1997. Tendons and ligaments--an overview. *Histology and Histopathology*, 12, 1135-44.
- BENNET, M. B., KER, R. F., DIMERY, N. J. & ALEXANDER, R. 1986. Mechanical Properties of various mammalian tendons. *Journal of Zoology*, A, 537-548.
- BIERING-SORENSEN, T., HOFFMANN, S., MOGELVANG, R., IVERSEN, A. Z., GALATIUS, S., FRITZ-HANSEN, T., BECH, T. & JENSEN, J. S. 2014. Myocardial Strain Analysis by 2-Dimensional Speckle Tracking Echocardiography Improves Diagnostics of Coronary Artery Stenosis in Stable Angina Pectoris. *Cardiovascular Imaging*, 7, 58-65.
- BOHS, L. N., GEIMAN, B. J., ANDERSONS, M. E., GEBHART, S. C. & TRAHEY, G. E. 2000. Speckle tracking for multi-dimensional flow estimation. *Ultrasonics*, 38, 369-375.
- BRUHN, A. & WEICKERT, J. 2005. Lucas/Kanade Meets Horn/Schunck: Combining Local and Global Optic Flow Methods. *International Journal of Computer Vision*, 61, 211-231.
- BUTLER, D. L., GROOD, E. S., NOYES, F. R. & ZERNICKE, R. F. 1978. Biomechanics of ligaments and tendons. *Exerc Sport Sci Rev.*, 6, 125-81.

- CAFFORIA, C., & ROCCA, F. 1976. Methods for measuring small displacements in television images. *IEEE Trans. Of Information Technology.*, 22, 573-579.
- CANNY, J., 1986. A Computer Approach to Edge Detection. *IEEE Transac. On Pattern Analysis and Machine Intelligence.*, 8(6), 679-698.
- CAROLAN, B. & CAFARELLI, E. 1992. Adaptations in Coactivation after Isometric Resistance Training. *J Appl Physiology*, 73, 911-917.
- CHAN, Y.-L. & SIU, W.-C. 1998. On Block Motion Estimation Using a Novel Search Strategy for an Improved Adaptive Pixel Decimation. *JOURNAL OF VISUAL COMMUNICATION AND IMAGE REPRESENTATION*, 9, 139-154.
- CHEN, J., JENKINS, W., HEIN, I. & O'BRIEN, W. D. Design of a residue number system digital correlator for real-time processing in ultrasonic blood flow measurements. . Proceeding of the IEEE International Symposium on Circuits and Systems, 1989. 208-211.
- CHILD, S., BRYANT, A. L., CLARK, R. A. & CROSSLEY, K. M. 2010. Mechanical Properties of the Achilles Tendon Aponeurosis Are Altered in Athletes with Achilles Tendinopathy. . *Am J Sports Med*, 38, 1885-1893.
- CHUEN, F. S., CHUK, C. Y., PING, W. Y., NAR, W. W., KIM, H. L. & MING, C. K. 2004. Immunohistochemical Characterization of Cells in Adult Human Patellar Tendons. *Journal of Histochemistry and Cytochemistry*, 52, 1151-1157.
- CLAYTON, R. A. & COURT-BROWN, C. M. 2008. The epidemiology of musculoskeletal tendinous and ligamentous injuries. *Injury*, 39, 1338-1382.
- COHEN, B. & DINSTEIN, I. 2002. New maximum likelihood motion estimation schemes for noisy ultrasound images. *16th International Conference on Pattern Recognition*. IEEE CS-Press.
- COUPPÉ, C., KONGSGAARD, M., AAGAARD, P., HANSEN, P., BOJSEN-MOLLER, J., KJAER, M. & MAGNUSSON, S. 2008. Habitual loading results in tendon hypertrophy and increased stiffness of the human patellar tendon. . *J Appl Physiol*, 105, 805-8015.
- DIAMANT, J., KELLER, A., BAER, E., LITT, M. & ARRIDGE, R. G. 1972. Collagen; ultrastructure and its relation to mechanical properties as a function of ageing. *Proceedings of the Royal Society London B.*, 180, 293-315.
- DILLEY, A., GREENING, J., LYNN, B., LEARY, R. & MORRIS, V. 2001. The Use of Cross-Correlation Analysis Between High-Frequency Ultrasound Images to

- Measure Longitudinal Median Nerve Movement. *Ultrasound in Medicine & Biology*, 27, 1211-1218.
- DRUMMOND, T., & CIPOLLA, R. 2002. Real-time visual tracking of complex structures. *IEEE PAMI*, 24(7): 932-946.
- EFFORD, N. 2000. Digital Images. *Digital Image Processing: A Practical Introduction Using Java*. University of Leeds: Addison-Wesley.
- ELTOUKHY, H. & SALAMA, K. 2001. Multiple Camera Tracking - Final Report. Electrical Engineering Department, Stanford University: Stanford image sensors group.
- FABIO, L. B. C., GEORGE, S., SHOUHAMI, L., MARIE, D., SERGIO, L. F., MARC, D., FRANK, V., ROBERT, C. & TONY, F. 2006. Ultrasound-Based Image Guided Radiotherapy for Prostate Cancer -Comparison of Cross-Modality and Intramodality Methods for Daily Localization During External Beam Radiotherapy. *Int. J. Radiation Oncology Biol. Phys.*, 1562-1567.
- FARRON, J., VARGHESE, T. & THELEN, D. G. 2009. Measurement of Tendon Strain During Muscle Twitch Contractions Using Ultrasonography. *IEEE Transaction of Ultrasonics, Piezoelectrics, and Frequency Control*, 56, 27-35.
- FORESTI, G. L. 1998. A real-time system for video surveillance of unattended outdoor environments. *IEEE Trans. Circuits and Systems for Vid. Tech*, 8, 697-704.
- FORSTNER, W. & PERTL. 1986, Photogrammetric Standard Methods and Digital Image Matching Techniques for High Precision Surface Measurements. *Elsevier Science Publication*.
- FUKUNAGA, T., ITO, M., ICHINOSE, Y., KUNA, S., KAWAKAMI, Y. & FUKASHIRO, S. 1996. Tendinous movement of a human muscle during voluntary contractions determined by realtime ultrasonography. *Journal of Applied Physiology*, 81, 1430-1433.
- FUNG, Y. C. 1993. *Biomechanics: Medical properties of living tissues*, New York, Springer-Verlag.
- GARRA, B. S., CESPEDES. E. I., OPHIR, J., SPRATT, S. R., ZUURBIER, R. A., MAGNANT, C. M. & PENNANEN, M. F. 1997. Elastography of breast lesions: initial clinical results. *Radiology*, 202, 79-86.
- GILL, R. W. 1985. Measurement of blood flow by ultrasound: Accuracy and sources of error. *Ultrasound in Med. & Biol*, 11, 625-641.

- GONZALEZ, R. C. & WOODS, R. E. 1992. Digital Image Fundamental, *Digital Image Processing*, Addison-Wesley Publishing,
- GONZALEZ, R. C. & WOODS, R. E. 2002. Digital Image Fundamentals. *Digital Image Processing*. Prentice-Hall, Inc.
- GREAVES, L. L., HECKER, A. T. & BROWN, C. H. 2008. The Effect of Donor Age and Low-Dose Gamma Irradiation on the Initial Biomechanical Properties of Human Tibialis Tendon Allografts. *American Journal of Sports Medicine*, 36, 1358-1366.
- GUAN, L., KUNG, S.Y., HE, Y., KUNG, S., LARSEN, J., Emerging Standards for Multimedia Applications. *Multimedia Image and Video Processing*, CRC PRESS, 1-34.
- HALL, T. J., JIANG, J., ZHU, Y. & COOK, L. T. Noise reduction strategies in freehand elasticity imaging. Proceedings of 2002 IEEE Int. Ultrasonics Symposiums, 2002. 1877-1957.
- HAMPSON , K., FORSYTH , N. R., EL HAJ, A. & MAFFULLI, N. 2008. Tendon Tissue Engineering. *Topics in Tissue Engineering*, 4, 44-60.
- HANSEN, P., BOJSEN-MOLLER, J. & AAGAARD, P. 2006. Mechanical properties of the human patellar tendon, in vivo. *Clin Biomech (Bristol, Avon)*, 21, 54 – 58. .
- HANSEN, P., HARALDSSON, B. T., AAGAARD, P., KOVANEN, V., AVERY, N. C., QVORTRUP, K., LARSEN, J. O., KORGSGAARD, M., KJAER, M. & MAGNUSSON, S. P. 2010. Lower Strength of the Human Posterior Patellar Tendon Seems Unrelated to Mature Collagen Cross-Linking and Fibril Morphology. *J Appl Physiol*, 108, 47-52.
- HARRIS, C. & STEPHENS, M., 1988. A Combined Corner and Edge Detector. *Proceedings of the 4th Alvey Vision Conference.*, 4: 146-151.
- HARIHARAKRISHNAN, K. & SCHONFELD, D. 2005. Fast object tracking using adaptive block matching. *IEEE TRANSACTIONS ON MULTIMEDIA*, 7, 853-859.
- HARALDSSON, B. T., AAGAARD, P., KROGSGAARD, M., ALKJAER, T., KJAER, M. & MAGNUSSON, S. P. 2005. Region-Specific Mechanical Properties of the Human Patella Tendon. *J Appl Physiol.* , 98, 1006-1018.

- HAYES, B. T., MERRICK, M. A., SANDREY, M. A. & CORDOVA, M. L. 2004. Three-MHz Ultrasound Heats Deeper Into the Tissues Than Originally Theorized. *J Athl Trai*, 39, 230–234.
- HELLE-VALLE, T., CROSBY, J., EDVARDBSEN, T., LYSEGGEN, E., AMUDSEN, B. H., SMITH, H.-J., ROSEN, B. D., LIMA, J. A., TORP, H., IHLEN, H. & SMISETH., O. A. 2005. New noninvasive method for assessment of left ventricular rotation: Speckle tracking echocardiography. *Circulation - American Heart Association*, 112, 3149-3156.
- HERZOG, W. & READ, J. L. 1993. Lines of Action and Moment Arms of the Major Force Carrying Structures Crossing the Human Kneejoint. *Journal ofAnatomy*, 182, 213-230.
- HIBON, M. & MAKRIDAKIS, S. 1995. Evaluating Accuracy (or Error) Measures Fontainebleau, France: INSEAD.
- HII, A. J. H., HANN, C. E., CHASE, J. G. & HOUTEN, V. E. E. W. 2006. Fast normalized cross correlation for motion tracking using basis function. *Computer Methods and Programs in Biomedicine*, 82, 144-156.
- HILL, A. V. 1938. The heat of shortening and the dynamic constants of muscle. *Proc.R.Soc.London Ser*, B126, 136-195.
- HORN, B. & SCHUNCK, B. 1981. Determining optical flow. *Artificial Intelligence* 17, 185-204.
- HSU, A., MILLER, N. R., EVANS, P. M., BAMBER, J. C. & WEBB, S. 2005. Feasibility of using ultrasound for real-time tracking during radiotherapy. *Med Phys*, 32, 1500-1512.
- HULMES, D. J. S. 2002. Building Collagen Molecules, Fibrils, and Suprafibrillar Structures. *Journal of Structural Biology*, 137, 2-10.
- JAN-WIEBE, H. K., SELLESA, R. W., STAMA, H. J., HOVIUSB, S. E. R. & BOSCHC, J. G. 2010. Development and validation of ultrasound speckle tracking to quantify tendon displacement. *Journal of Biomechanics*, 43, 1373-1379.
- JONATHAN, M. R., MARY, F., SCOTT, W. H., FOWLKES, J. B. & HAMILTON, J. D. 2012. Potential Use of Ultrasound Speckle Tracking for Motion Management During Radiotherapy. *J Ultrasound Med*, 31, 469-481.

- JONES, D. A. & ROUND, J. M. 1990. Skeletal Muscle Structure. *In*: JONES, D. A. (ed.) *Skeletal muscle in health and disease*. Manchester: Manchester University Press.
- KAHN, D. & WILSON, M. A. 1987. Bone scintigraphic findings in patellar tendonitis. *J Nucl Med*, 28, 1768-1838.
- KALUZYNSKI, K., CHEN, X., EMELIANOV, S., SKOVORODA, A. & O'DONNELL, M. 2001. Strain rate imaging using two-dimensional speckle tracking. *IEEE Transactions on Ultrasonics, Ferroelectrics and Frequency Control*, 48, 1111-1123.
- KANNUS, P. 2000. Structure to the tendon connective tissue. *Scandinavian Journal of Medicine & Science in Sports*, 10, 312-320.
- KARASICK, D. & SCHWEITZER, M. E., 1996. The OsTrigonum Syndrom: Imaging Features. *AJR*. 166, 125-129.
- KEHTARNAVAZ, K. & GAMADIA, M. 2006. ALGORITHM SIMPLIFICATION STRATEGIES. *Real-Time Image and Video Processing: From Research to Reality*. 1st ed. University of Texas at Dallas, USA: Morgan & Claypool.
- KELLIS, E. & BALZPOULOS, V. 1999. In Vivo Determination of the Patella Tendon and Hamstrings Moment Arms in Adult Males Using Videofluoroscopy During Submaximal Knee Extension and Flexion. *Clinical Biomechanics*, 14, 118-124.
- KIM, Y. S., KIM, J. M., BIGLIANI, L. U., KIM, H. J. & JUNG, H. W. 2011. In Vivo Strain Analysis of the Intact Supraspinatus Tendon by Ultrasound Speckles Tracking Imaging. *Journal of Orthopaedic Research*, 12, 1931-1937.
- KJAER, M. 2004. Role of Extracellular Matrix in Adaptation of Tendon and Skeletal Muscle to Mechanical Loading. *Physiological Review*, 84, 649-698.
- KJÆR, M., MAGNUSSON, P., KROGSGAARD, M., MØLLER, J. B., OLESEN, J., HEINEMEIER, K., HANSEN, M., HARALDSSON, B., KOSKINEN, S., ESMARCK, B. & LANGBERG, H. 2006. Extracellular matrix adaptation of tendon and skeletal muscle to exercise. *Journal of Anatomy*, 208, 445-450.
- KOGA, T., IINUMA, A., HIRANO, Y., IJIMA & ISHIGIRO, T. Motion compensated interframe coding for video conferencing. Proc. Nat. Telecommun. Conf, 1981. 532-535.

- KORSTANJE, J. W., SELLES, R., STAMA, H. J., HOVIUS, S. & BOSCH, J. G. 2010. Development and validation of ultrasound speckle tracking to quantify tendon displacement. *Biomech*, 43, 1373-1379.
- KREVOLIN, J. L., PANDY, M. G. & PEARCE, J. C.P., 2004. Moment Arm of the Patellar Tendon in the Human Knee. . *J Biomech*, 37, 785-8.
- KUMAR, A., MADHUSUDAN RAO, B., GHOLE, R., PATIL, A. & GHATPANDE, N. Demons based tracking for non-rigid transformed Region of Interest. TENCON 2011 - 2011 IEEE Region 10 Conference, 2011 Bali. 321 - 325.
- LEE, S., GREGORY S. L. & PIAZZA, S. J. 2008a. An algorithm for automated analysis of ultrasound images to measure tendon excursion in vivo. *Journal of Applied Biomechanics*, 24, 75-82.
- LEE, S. M. & PIAZZA, S. J. 2008b. Inversion–eversion moment arms of gastrocnemius and tibialis anterior measured in vivo. *Journal of Biomechanics*, 41, 3366-3370.
- LÈJARD, V., BRIDEAU, G., BLAIS, F., SALINGCAMBORIBOON, R., WAGNER, G., ROEHL, M.H., NODA, M., DUPREZ, D., HOUILLIER, R., ROSSER, J. 2007. Scleraxis and NFATc regulate the expression of the pro-alpha1(I) collagen gene in tendon fibroblasts. *Journal Biological Chemistry*, 282(24): 17665-17675.
- LIEBER, R. L., LEONARD, M. E., BROWN, C. G. & TRESTIK, C. L. 1991. Frog semitendinosus tendon load-strain and stress-strain properties during passive loading. *American Journal of Physiology C*, 86-92.
- LI, L. HUANG, W., GU, I.Y., TIAN, Q. 2004. Statistical Modelling of Complex Backgrounds for Foreground Object Detection. *IEEE Trans. Image Processing*. 13: 1459-1472.
- LIN, Y. C. & TAI, S. C. 1997. Fast Full Search Block Matching Algorithm for Motion-Compensated Video Compression. *IEEE Transaction on Communications*, 45, 527-531.
- LINDAHL, O. & MOVIN, A. 1967. The Mechanics of Extension of the Knee-Joint. *Acta ORTHOPAEDICA SCANDINAVICA*, 38, 226-234.
- LINGURARU, M. G., VASILYEV, N. V., MARX, G. R., TWORETZKY, W., DEL NIDO, P. J. & HOWE, R. D. 2008. Fast block flow tracking of atrial septal defects in 4D echocardiography. *Medical Image Analysis*, 12, 397-412.

- LIPPOLD, O. C. 1952. The Relationship between Integrated Action Potentials in a Human Muscle and Its Isometric Tension. . *Journal of Physiology.* , 177, 492-501.
- LIU, H., MOTODA, H. 1998. Feature Selection for Knowledge Discovery and Data Mining. *Kluwer Academic Publishers.*
- LORAM, I. D., MAGANARIS, C. N. & LAKIE, M. 2006. Use of ultrasound to make noninvasive in vivo measurement of continuous changes in human muscle contractile length. *Journal of Applied Physiology*, 100, 1311-1323.
- LU, T. W. & O'CONNOR, J. J. 1996. Lines of Action and Moment Arms of the Major Force- Bearing Structures Crossing the Human Knee Joint: Comparison between Theory and Experiment. . *Journal of Anatomy*, 189, 575-585.
- LUCAS, B. & KANADE, T. 1981. An iterative image registration technique with an application to stereo vision. *Proc. DARPA Image Understanding Workshop*, 121-130.
- MAGANARIS, C. N., BALZPOULOS, V. & SARGEANT, A. J. 1998. In Vivo measurements of the triceps surae complex architecture in man: implication for muscle function. *The Journal of Physiology*, 512, 603-614.
- MAGANARIS, C. N., REEVES, N. D., RITTWEGER, J., SARGEANT, A. J., JONES, D. A., GERRITS, K. & DE HAAN, A. 2006. Adaptive response of human tendon to paralysis. *Muscle Nerve*, 33, 85-92.
- MAGNUSSON, S. P., HANSEN, P., AAGARD, P. & KJAER, M. 2003. Tendon properties in relation to muscular activity and physical training. *Scandinavian Journal of Medicine & Science in Sports*, 13, 211-223.
- MESBAH, M. Gradient-Based Optical Flow : A Critical Review. Fifth International Symposium on Signal Processing and its Applications, 1999. 464-470.
- MEUNIER, J. 1998. Tissue motion assesement form 3D echographic speckle tracking. . *Physics in Medicine and Biology*, 43, 1241-1295.
- MOHAMMAD, D. A., TAVAKOLI, V. & NIMA, S. 2009. Optimized Noninvasive Monitoring Thermal Changes on Digital B-Mode Renal Sonography During Revascularization Therapy. *J. Ultrasound Med*, 28, 1535-1547.
- MOKONE, G. G., GAJJAR, M., SEPTEMBER, A. V., SCHWELLNUS, M. P., GREENBERG, J., NOAKES, T. D. & COLLINS, M. 2005. The guanine-thymine dinucleotide repeat polymorphism within the tenascin-C gene is associated with achilles tendon injuries. *Am J Sports Med*, 33, 1016-1037.

- MOKONE, G. G., SCHWELLNUS, M. P., NOAKES, T. D. & COLLINS, M. 2006. The COL5A1 gene and Achilles tendon pathology. *Scand J Med Sci Sports*, 16, 19-26.
- NARICI, M. V. & MAGANARIS, C. N. 2006. Adaptability of elderly human muscles and tendons to increased loading. *J. Anat.*, 208, 443-443.
- NILLIUS, P. & EKLUNDH, J. 2002. Fast block matching with normalized cross-correlation using Walsh transforms. Department of Numerical Analysis and Computer Science
- NISELL, R., NEMETH, G. & OHLSEN, H. 1986. Joint Forces in Extension of the Knee. Analysis of a Mechanical Model. *Acta ORTHOPAEDICA SCANDINAVICA*, 57, 41-46.
- OLEG, V. M. & TANNENBAUM, A. 2006. Descpeckling of Medical Ultrasound Images. *IEEE Trans. Ultrason. Ferroelectr. Freq. Control*, 53(1), 64-78.
- ONAMBELE, G., PEARSON, S. & BURGESS, K. 2007. Gender-Specific In Vivo Measurement of the Structural and Mechanical Properties of the Human Patellar Tendon. *Journal of Orthopaedic Research*, 25, 1635-1642.
- OPHIR, J., ALAM, S. K., GARRA, B., KALLEL, F., KONOFAGOU, E., KROUSKOP, T. & VARGHESE, T. 1999. Elastography: Ultrasonic estimation and imaging of the elastic properties of tissues. *Proc Inst Mech Eng H*, 213, 203-206.
- OURSELIN, S., ROCHE, A., PRIMA, S. & AYACHE, N. 2000. Block Matching: A General Framework to Improve Robustness of Rigid Registration of Medical Images. *MICCAI'2000*, 557-566.
- PEARSON, S. 2010. Tendons. In: COMFORT, P. & ABRAHAMSON, E. (eds.) *Sports Rehabilitation and Injury Prevention*. Wiley-Blackwell.
- PEARSON, S., BURGESS, K. & ONAMBELE, G. 2007. Creep and the in Vivo Assessment of Human Patellar Tendon Mechanical Properties. *Clin Biomech (Bristol, Avon)*, 22, 712-7.
- PEARSON, S., MOHAMED, A. S. A. & RITCHINGS, T. 2014. Regional Strain Variations in the Human Patellar Tendon. *Med Sci Sports Exerc*, 46, 1343-51.
- PEARSON, S. & ONAMBELE, G. 2005. Acute Changes in Knee-Extensors Torque, Fibre Penetration, and Tendon Characteristics. *Chronobiology International*, 22, 1013-1027.

- PEARSON, S. & ONAMBELE G. 2006. Tendon Compliance: Implications for the Measurement of Voluntary Activation Levels. . *Muscle & Nerve*, in press.
- PEARSON, S. & ONAMBELE, G. 2006. Influence of Time of Day on Tendon Compliance and Estimations of Voluntary Activation Levels. *Muscle Nerve*, 33, 792-800.
- PEARSON, S., RITCHINGS, T. & MOHAMED, A. S. A. 2013. The Use of Normalized Cross Correlation Analysis for Automatic Tendon Excursion Measurement in Dynamic Ultrasound Imaging. *Journal of Applied Biomechanics*. 29(2), 165-173.
- PELLERITO, J. S. & POLAK, J. F. 2012. Color Flow Ultrasound Imaging. *Introduction to Vascular Ultrasonography*. 6th ed.: Elsevier.
- PURWAR, R. K. & RAJPAL, N. 2010. TWO LEVEL BLOCK MATCHING CRITERION FOR MOTION ESTIMATION USING INTEGRAL FRAMES FEATURES. *International Journal of Engineering and Management Science*, 1, 73-78.
- REVELL, J., MIRMEHDI, M., MCNALLY, D. 2003. Strain Quantification In Ultrasound Sequences. *Proceedings of the British Machine Vision Conference*, 1-10.
- REVELL, J., MIRMEHDI, M. & MCNALLY, D. 2004. Musculoskeletal motion flow fields using hierarchical variable-sized block matching in ultrasonographic video sequences *Journal of Biomechanics*, 37: 511-522.
- REVELL, J., MIRMEHDI, M. & MCNALLY, D. 2005. Computer vision elastography: speckle adaptive motion estimation for elastography using ultrasound sequences. *IEEE transactions on medical imaging*, 24: 755-66.
- REVELL, J., MIRMEHDI, M. & MCNALLY, D. 2008. Combined Ultrasound Speckle Pattern Similarity Measures.
- RIGBY, B. J., HIRAI, N., SPIKES, J. D. & EYRING, H. 1959. The Mechanical Properties of Rat Tail Tendon. *The Journal of General Physiology*, 43, 265-283.
- ROBINSON, D. E., CHEN, F. & WILSON, L. S. 1982. Measurement of velocity of propagation from ultrasonic pulse-echo data, 3-D flow velocity vector estimation with a triple beam lens transducer - experimental results. . *Utrasound Med. Biol.*, 8, 413-420.

- RYAN, T.W., GRAY, R.T., & HUNT, B.R. 1980. Prediction of errors in stereo-pair images. *Optical Engineering*, 19(3), 312-322.
- SAHBA, N., TAVAKOLI, V., AHMADIAN, A., ABOLHASSANI, M. D. & FOTOUHI, M. 2008. Hybrid local/global optical flow and spline multi-resolution analysis of myocardial motion in B-mode echocardiography images. *Electronic Journal of Technical Acoustics*, 12.
- SCHATZKER, J. & BRÅNEMARK, P. I. 1969. Intravital observations on the microvascular anatomy and microcirculation of the tendon. *ACTA ORTHOPAEDICA SCANDINAVICA. SUPPLEMENTUM*, 126.
- SEHGAL, C. M., 1993 Quantitative relationship between tissue composition and scattering of ultrasound. *J. Acoust. Soc. Amer*, 94, 1944-1952.
- SEITZ, A. L., MCCLURE, P. W., FINUCANE, S., BOARDMAN, N.D. III. & MICHENER, L. A. 2011. Mechanisms of rotator cuff tendinopathy: Intrinsic, extrinsic, or both? *Clinical Biomechanics*, 26, 1-12.
- SHARMA, N. & AGGARWAL, L. M. 2010. Automated medical image segmentation techniques. *J Med Phys.* , 35, 3-14.
- SHARMA, P. & MAFFULI, N. 2006. Biology of tendon injury: healing, modeling and remodeling. *Journal of musculoskeletal & neuronal interactions.*, 6, 181-190.
- SHARMA, P. & MAFFULLI, N. 2005. Tendon Injury and Tendinopathy: Healing and Repair. *J Bone Joint Surg Am*, 87, 187-202.
- SHI, J., & TOMASI, C. 1994. Good features to track. *IEEE Conference on Computer Vision and Pattern Recognition*, 593-600.
- SODE, J., OBEL, N., HALLAS, J. & LASSEN, A. 2007. Use of fluroquinolone and risk of Achilles tendon rupture: a population-based cohort study. *Journal of Clinical Pharmacology*, 63, 499-503.
- STAUFER, C., & GRIMSON, W. 2000. Learning patterns of activity using real-time tracking. *IEEE Trans. On Pattern Analysis and Machine Intelligence*, 22: 747-757.
- STØYLEN, A. 2010. *Basic ultrasound, echocardiography and Doppler for clinicians* [Online]. Norwegian University of Science and Technology. Available: <http://fold.ntnu.no/stoylen/strainrate/Ultrasound/>.

- STØYLEN, A., HEIMDAL, A., BJORNSTAD, K., TORP, H. G. & SKJAERPE, T. 1999. Strain Rate Imaging by Ultrasound in the Diagnosis of Regional Dysfunction of the Left Ventricle. *Echocardiography*, 16, 321-329.
- SUHLING, M., ARIGOVIDAN, M. & JANSEN, C. 2005. Myocardial motion analysis from B-mode echocardiograms. *IEEE Trans Image Process*, 14, 525-536.
- SUHLING, M., ARIGOVINDAN, M., JANSEN, C. & HUNZIKER, P. 2004. Bimodal myocardial motion analysis from B-mode and tissue Doppler ultrasound. *IEEE International Symposium on Biomedical Imaging: Nano To Macro*, 1, 308-311.
- SUN, X., JIN, G., HUANG, M. & XU, G. 2003. A novel partial block matching motion estimation algorithm. *Third International Symposium on Multispectral Image Processing and Pattern Recognition*, 593-600.
- SWILLENS, A., SEGERS, P., LOVESTAKKEN, L., 2010. Two-Dimensional Flow Imaging in The Carotid Bifurcation Using a Combined Speckle Tracking and Phase-Shift Estimator: A Study Based on Ultrasound Simulations and in vivo Analysis. *Ultrasound in Medicine & Biology*, 36(10) : 1722-1735.
- TRAHEY, G. E., HUBBARD, S. M. & VON RAMM, O. T. 1988. Angle independent ultrasonic blood flow detection by frame-to-frame correlation of b-mode images,. *Ultrasonics*, 26, 271-277.
- TSAOPOULOS, D. E., BALZPOULOS, V. & MAGANARIS, C. N. 2006. Human Patellar Tendon Moment Arm Length: Measurement Considerations and Clinical Implications for Joint Loading Assessment. *Clin Biomech (Bristol, Avon)*, 21, 657-67.
- TWOMEY, J. M. & SMITH, A. E. 1996. Validation and Verification. In: KARTAM, N., FLOOD, I. & GARRETT, J. (eds.) *Artificial Neural Networks for Civil Engineers: Fundamentals and Applications*. ASCE Press.
- ULYSSES, J. N. & CONEI, A. 2010. Measuring Similarity in Medical Registration. *IWSSIP 2010 - 17th International Conference on Systems, Signals and Image Processing*.
- VAHID, T., ALIREZA, A. & ALBOHASSANI, M. D. 2007. An evaluation of moment based optical flow techniques for myocardial motion analysis in B-mode Echocardiography Images. *Journal of Technical Acoustics*.

- VAHID, T., SAHBA, N., AHMADIAN, A. & ALBOHASSANI, M. D. 2008. Adaptive multi-resolution myocardial motion analysis of B-mode echocardiography images using combined local/global optical flow. *2nd International Conference on Bioinformatics and Biomedical Engineering Engineering ICBBE*.
- VERMAUT, F., DEVILLE, Y., MARICHAL, X. & MACQ, B. 2001. A distributed adaptive block matching algorithm: Dis-ABMA. *Signal Processing: Image communication*, 16, 431-444.
- VRAY, D., NEEDLES, A., YANG, V. X. D. & FOSTER, F. S. High frequency B-mode ultrasound blood flow estimation in the microvasculature. Proceedings of the 2004 IEEE Ultrasonic Symposium, 2004. 466-460.
- WAGNER, R.F., SMITH, S.W., SANDRIK, J.M & LOPEZ, H. 1983. Statistics of speckle in ultrasound B-scans. *IEEE Trans. Sonics. Ultrason*, 30, 156-163.
- WHITTING, W. C. & ZERNICKE, R. F. 2008a. Basic Biomechanics. *Biomechanics of Musculoskeletal Injury*. 2nd ed. USA: Human Kinetics.
- WHITTING, W. C. & ZERNICKE, R. F. 2008b. Concepts of Injury and Healing. *Biomechanics of Musculoskeletal Injury*. 2nd ed. USA: Human Kinetics.
- WRETENBERG, P., NEMETH, G., LAMONTAGNE, M. & LUNDIN, B. 1996. Passive Knee Muscle Moment Arms Measured in Vivo with Mri. *Clinical Biomechanics*, 11, 439-446.
- YAMAGUCHI, G. T. & ZAJAC, F. E. 1989. A Planar Model of the Knee Joint to Characterize the Knee Extensor Mechanism. *Journal of Biomechanics*, 22, 1-10.
- YEUNG, F., LEVINSON, S. F., FU, D. & PARKER, K. J. 1998. Feature-adaptive motion tracking of ultrasound image sequences using a deformable mesh. *IEEE Transactions on Medical Imaging*, 17, 945-956.
- YOSHII, Y., VILLARRAGA, H. R., HENDERSON, J., ZHAO, C., AN, K. & AMADIO, P. 2011. Ultrasound assessment of the motion patterns of human flexor digitorum superficialis and profundus tendons with speckle tracking. *J Orthop Res.*, 29, 1465-1469.
- ZHANG, D. & LU, G. An Edge and Color Oriented Optical Flow Estimation Using Block Matching. Signal Processing Proceedings, 2000 WCCC-ICSP 2000 5th International Conference On, , 2000. 1-8.

ZHU, S. & MA-, K. K. 1997. A new diamond search algorithm for fast block matching motion estimation. , *Proc Int. Conf. Inform. Commun. Signal Process*, 292-296.

Appendix A

Publication I

Journal of Applied Biomechanics. 2013 Apr; 29(2): 165-73. Epub 2012 May 8.

THE USE OF NORMALIZED CROSS CORRELATION ANALYSIS FOR AUTOMATIC TENDON EXCURSION MEASUREMENT IN DYNAMIC ULTRASOUND IMAGING

Stephen J. Pearson¹, Tim Ritchings², A.S.A Mohamed²

¹Centre for Health, Sport and Rehabilitation Sciences Research, University of Salford, Greater Manchester M6 6PU, United Kingdom

²Control & Systems Engineering Research Centre, University of Salford, Greater Manchester, M5 4WT, United Kingdom

Abstract

The work describes an automated method of tracking dynamic ultrasound images using a normalised cross correlation algorithm, applied to the patellar and gastrocnemius tendon. Displacement was examined during active and passive tendon excursions using B-mode ultrasonography. In the passive test where two regions of interest (2-ROI) were tracked, the automated tracking algorithm showed insignificant deviations from relative zero displacement for the knee (0.01 ± 0.04 mm) and ankle (-0.02 ± 0.04 mm), ($p > 0.05$). Similarly, when tracking 1-ROI the passive tests showed no significant differences ($p > 0.05$) between automatic and manual methods, 7.50 ± 0.60 vs. 7.66 ± 0.63 mm for the patellar and 11.28 ± 1.36 vs. 11.17 ± 1.35 mm for the gastrocnemius tests. The active tests gave no significant differences ($p > 0.05$) between automatic and manual methods with differences of 0.29 ± 0.04 mm for the patellar and 0.26 ± 0.01 mm for the gastrocnemius. This study showed that automatic tracking of in vivo displacement of tendon during dynamic excursion under load is possible and valid when compared to the standardised method.

This approach will save time during analysis and enable discrete areas of the tendon to be examined.

Keywords: Normalized Cross-Correlation, Speckle Tracking, Tendon, Ultrasound.

Introduction

Detailed characterisation of the tendon allows for insight into the aetiology of tendon injury, repair and response to various training interventions. There have been a number of previous works that has detailed the in vivo tendon mechanical properties (Fukunaga et al. 1996; Kubo et al. 2000; Hansen et al. 2006; Onambele et al., 2007). However, these properties, due to the limitations of the methods have been related to the whole tendon and not specific to any given region. The method described here allows for the quantification of the mechanical properties of regions of interest (ROI) along the tendon length. Thus it may allow for the sensitive identification of changes to the tendon prior to injury or during rehabilitation, which cannot be identified using the method outlined in previous work.

The randomness of the speckle pattern in ultrasound ensures that each region of the tissue within the imaging frame has its own unique pixel pattern that can differentiate a region from other regions. The aim of any tracking algorithm is to attempt to identify the pixel 'signature' between subsequent image frames. Under ideal conditions the tissue would not change its ultrasound echo from frame to frame i.e. as during a passive movement where the tissue is not expected to distort. However, as the tissue is stretched under load, so it deforms and its density changes, altering the ultrasound pattern produced. Hence the pixel signature of a region of interest in any given frame may in fact change in the subsequent frames.

The tendon extension seen during muscle contraction is a factor of the loading and loading rate and potentially can be large over a typical acquisition period (3-4 seconds) dependant on the tendon mechanical characteristics. Hence in order to get a 'best match' between subsequent frames the loading rate must be relatively low and/or frame acquisition high so that frame to frame tendon displacement is relatively small, hence reducing potential for mismatch. A number of approaches have previously been utilised in an attempt to track nerve and tendon displacement (Dilley et al. 2001; Lee et al. 2008; Kim et al. 2011). Of these none have utilised maximal force efforts where the tendon would be expected to develop high levels of strain. Farron et al (2009), utilised a block matching, normalised cross correlation (NCC) method whereby tendon strain was estimated, and here at only up to 50% of maximal effort. Here we utilise a more efficient method of searching in conjunction with the (NCC) algorithm by implementing the Three Steps Searching (TSS) algorithm developed by Koga et al (1981).

None of the previous tracking papers have related their measurements with the manual method used in the literature (e.g. Onambele et al., 2007) to estimate tendon excursion. In addition, none appear to have utilised high force contractions (where tendon stretch is relatively large) to test the ability of the tracking algorithm to follow a region of interest across successive frames.

Therefore the aims of this present study were to examine a method of tracking regions of interest within the ultrasound images of in vivo human tendon tissue during both passive (probe movement) and active (highly loaded) tendon, and secondly to compare in vivo, the automated method with the established manual method to ascertain its validity.

This work will enable a much more detailed picture of the tendon mechanical properties in injury, repair and in response to various training interventions. This detailed understanding will subsequently allow for more effective rehabilitation and injury prevention strategies to be put in place.

Methods

The test subject for the study is a healthy recreationally active male aged 47 years with mass 91 kg and height 1.81m. The local Ethics Committee approved the investigation and the subject gave written informed consent to participate. The study conformed to the principles of the World Medical Association's Declaration of Helsinki.

For the comparison analysis between the automatic and manual tracking methods, two sites were chosen based on those typically utilised in the literature. These were the patellar and medial gastrocnemius tendon (Arampatzis et al., 2005; Hansen et al., 2006; Onambele et al., 2007). A 7.5 MHz 40mm linear array, B-mode ultrasound probe (AU5, Esaote Biomedica, Italy) with a depth resolution of 49.3mm was used to image the patellar and medial gastrocnemius tendons in the sagittal plane. For the patellar tendon the knee was fixed at 90° flexion, and the ankle was fixed in the neutral position (i.e. 90°) for imaging the medial gastrocnemius tendon junction. An echo-absorptive marker was placed between the probe and the skin to act as a fixed reference from which manual measures of elongation could be made. Ultrasound images were then taken in DV format via s-video output and captured into PC at 25 frames per second using Quintic Biomechanics (9.03 v 11) software. Scaling in pixels per mm was determined from ImageJ software by using the known depth of field in the ultrasound

images, (1 mm = 9.20 pixels or 1 pixel = 0.108696mm) and utilised as a calibration factor in the automated tracking programme to ensure equivalent pixel to mm ratios.

In order to examine the tracking algorithm, passive tendon movements were employed, where no tendon deformation would be expected, hence the simplest task for the algorithm. Contraction start was defined as frame zero for the passive trials. End of contraction was seen when movement stopped for the passive trials. The same criteria or frame range was used for all similar trials. The purpose of the passive probe movement experiment (Transducer probe moved proximally over the skin surface within a 20mm range. - PM) was to examine the initial measurement of the automatic tracking method, compared with the manual tracking method. Here a good match should be expected if the algorithm is able to 'template match' and hence track the speckle pattern in successive frames. These tests used one and 2 ROI for comparison purposes. For 1-ROI, the identified region was determined frame to frame and the displacement also measured manually from its position in the first frame. For the 2ROI passive tests, if the algorithm tracks successfully, any 2 regions should show a zero net movement (relative movement). A total of ten trials were carried out for both 1 and 2 ROI experiments. ROI displacements were measured at every ten percent of the total frame number for each trial.

Active movement (Applied ramped voluntary contractions at both knee and ankle with the knee flexed to an angle of 90° and ankle in neutral, transducer probe fixed static at the skin surface.- AM), examined both the patellar and medial gastrocnemius tendons, resulting in tendon stretch (See figure 1a and b). Voluntary forces were ramped manually over 3-4 seconds and recorded along with the ultrasound images. Co contraction was accounted for by recording the emg in the antagonist muscles (Hamstrings and tibialis anterior), where net torque = external torque + co contraction torque. Tendon forces were calculated by dividing all net torques by the respective moment arms. All excursion records were then determined at ten percent intervals of maximal voluntary force

up to maximum. Here only 2 ROI were examined whereby one region was put onto the echo absorptive marker and the other on identifiable landmark within the tendon (Gastrocnemius muscle tendon

junction and just distal to the inferior pole of the patellar on the inferior aspect). Again a total of ten trials were carried out for the 2 ROI experiments. For the active trials start was defined where force was zero and end where a force plateau was reached.

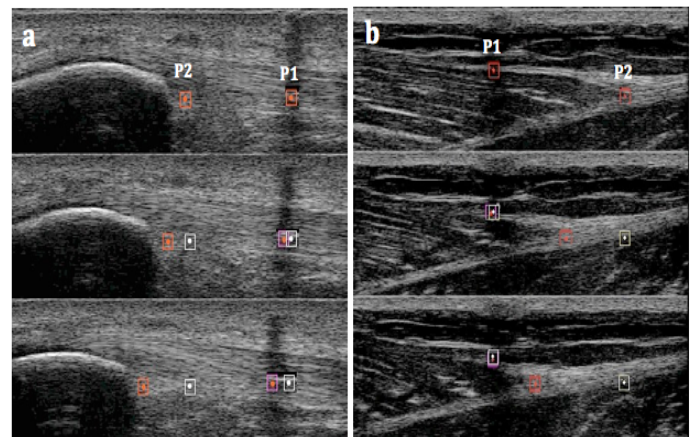


Figure 1 shows the tracking node points (ROI), a) 2-ROI nodes patellar tendon tracking b) 2-ROI nodes medial gastrocnemius. Where the first frames hold the initial points and the relative displacement of the points in subsequent frames determines the tendon displacement.

The tracking algorithm calculated the Normalised Correlation Coefficient (NCC) of the ROI and the same – sized region, centred on each pixel in a surrounding search window in the following frame (See Figure 1). The NCC was used in preference to other measures because it was found to be more sensitive to speckle tracking in ultrasound images (Revell and McNally, 2005). As this was a time consuming process, the search times were reduced by using the traditional Three Steps Searching (TSS) algorithm developed by Koga et al (1981). This algorithm was developed for motion estimation in video compression applications, where the movement could be in any direction and employed a rectangular search window of 2 x ROI size for the width and 1 x ROI size for the height. If the threshold for the NCC (0.95) was not reached or exceeded then the ROI was not moved in the subsequent frame. If the NCC

found a new region i.e. $r > 0.95$ then the process started again with the new updated position for the template match in the next frame i.e. adaptive NCC implementation. This increases the ability to match where the template changes as when the tendon deforms with stretch.

Tests used a pixel ROI area of 15×15 (2.66 mm^2), this gave optimal tracking results compared to larger and smaller areas for the structures examined (data not shown). For 1-ROI, the distance moved from the initial start point node ($P1_{\text{initial}}$) to the successive frames was determined ($P1_j$) and plotted against the manually measured displacement. For 2-ROI the position of $P1_{\text{initial}}$ and $P2_{\text{initial}}$ was then tracked until it reached the last frame. The position of the nodes relative to each other across the subsequent frames was measured ($P1_j - P2_j$), the accumulative relative displacement between nodes was plotted (manual vs. automatic tracked).

T tests were used to determine differences from zero displacement for the 2 ROI passive measures, and to compare all other automatic tracking with manual measures. Intraclass correlation coefficients (ICCs) were determined to examine the reliability of the manual measures. Bland-Altman plots were determined with 95% limits to examine the level of agreement. Alpha level was set to $p < 0.05$. All data are presented as mean \pm SEM.

Results

Repeat tests of the manual measures for tendon excursion gave an ICC of 0.991.

Passive movement of the probe allowed examination of either displacement of two ROI relative to each other or 1 ROI as the probe moved over the region. The 2-ROI automatic tracking passive test for the patellar tendon showed a mean value close to zero displacement ($0.010 \pm 0.040 \text{ mm}$), manual measures gave a mean value of $-0.005 \pm 0.040 \text{ mm}$, both results were not significantly different from zero ($p=0.53$; 0.75) for the automatic and manual

measures respectively. The 2-ROI automatic test for the medial gastrocnemius tendon, also showed a mean value close to zero displacement ($-0.020 \pm 0.040 \text{ mm}$), with manual measures giving a mean displacement of $-0.030 \pm 0.060 \text{ mm}$. Neither the automatic nor the manual measure was significantly different to zero ($p=0.14$; 0.15) respectively.

For determination of a simple tendon displacement trial during passive movement, 1 ROI was utilised. Comparisons between manual and automated tracking with 1 ROI for passive probe movement (PM) indicated that there were no significance differences ($p = 0.06$) between the tracked ROI and the manual method. For the patellar test, automatic tracking gave a total displacement of $7.50 \pm 0.60 \text{ mm}$ vs. the manual measure of $7.66 \pm 1.63 \text{ mm}$. An excellent and significant correlation between methods was shown ($r=0.99$; $p < 0.05$), with the Bland-Altman plot indicating that the mean difference or bias is very small (0.04 mm) and that within the 95% confidence limits the difference does not exceed 0.17 mm , a very small difference across the range of measurements (See Figure 2).

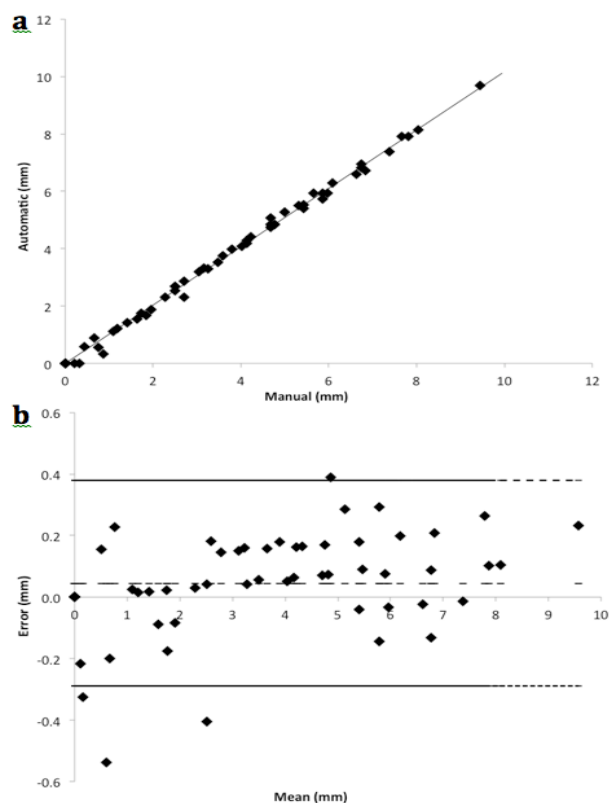


Figure 2 shows the comparisons of the 1-ROI passive tracking between automatic vs. manual measures of patellar tendon. a)

Relationship between manual and automatic tracking, compared at 10% intervals of total frame count ($r = 0.998$; $P < 0.05$). b) Bland – Altman plot showing mean difference (bias) and 95% confidence limits. (lines showing mean difference = 0.04 mm, ± 2 SD).

For the medial gastrocnemius tendon test, the automatic tracking gave a total displacement of 11.28 ± 1.36 mm vs. 11.17 ± 1.35 mm for the manual measures, again no significant differences were seen between methods ($p = 0.79$). These initial tests confirmed that the automatic tracking method is a good match to the manual method for measuring displacements, with no significance differences between the two. Figure 3 indicates for this data set the relationship between measures was significant ($r=0.99$; $p<0.05$). The mean difference was negligible (0.01mm) and the 95% confidence intervals indicated that the maximum difference was 0.5mm.

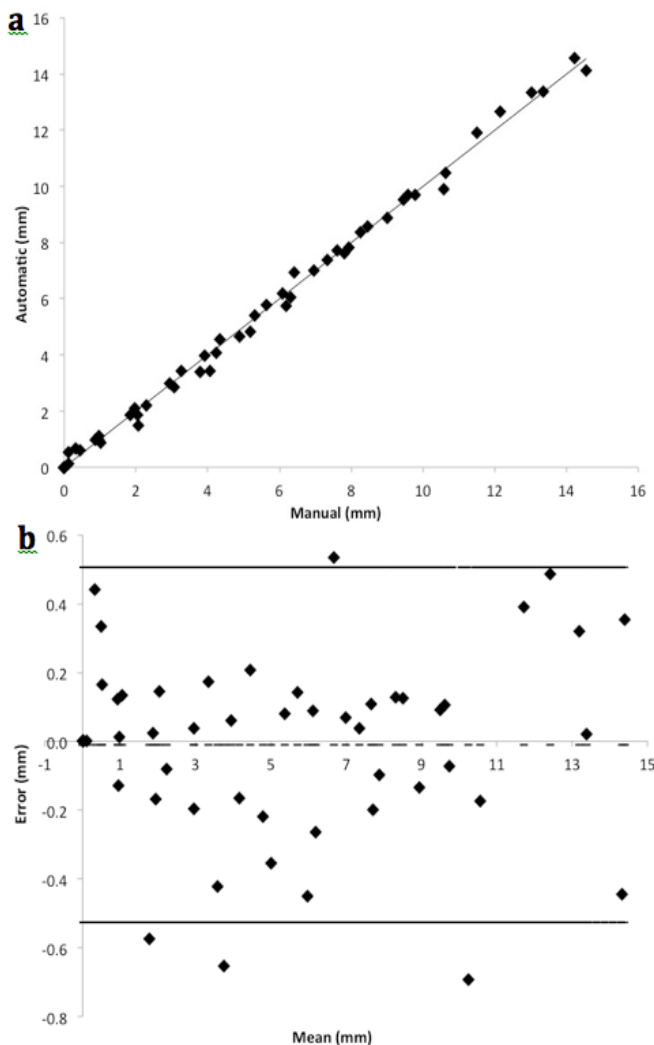


Figure 3 shows the comparisons of the 1-ROI passive tracking between automatic vs. manual measures of gastrocnemius tendon. a) Relationship between manual and automatic tracking, compared at 10% intervals of total frame count ($r = 0.998$; $P < 0.05$). b) Bland – Altman plot showing mean difference (bias) and 95% confidence limits (lines showing mean difference = -0.01 mm, ± 2 SD).

The active trials consisted of muscle contractions, the resultant muscle forces which were generated resulted in tendon stretch, and this was tracked and measured manually to determine the validity of the automated method. All active testing utilised 2-ROI. For the patellar tests, here again there were no significance differences ($p=0.85$) between the automatic and the manual measurements with a mean displacement value of 4.88 ± 0.24 mm, compared to 4.59 ± 0.28 mm for the manual measures. The scatter plot shows a very good agreement between measures ($r=0.99$; $p < 0.05$) (See figure 4). Bland-Altman plot giving a bias of 0.005mm and indicating no greater difference at a 95% confidence than 0.4mm.

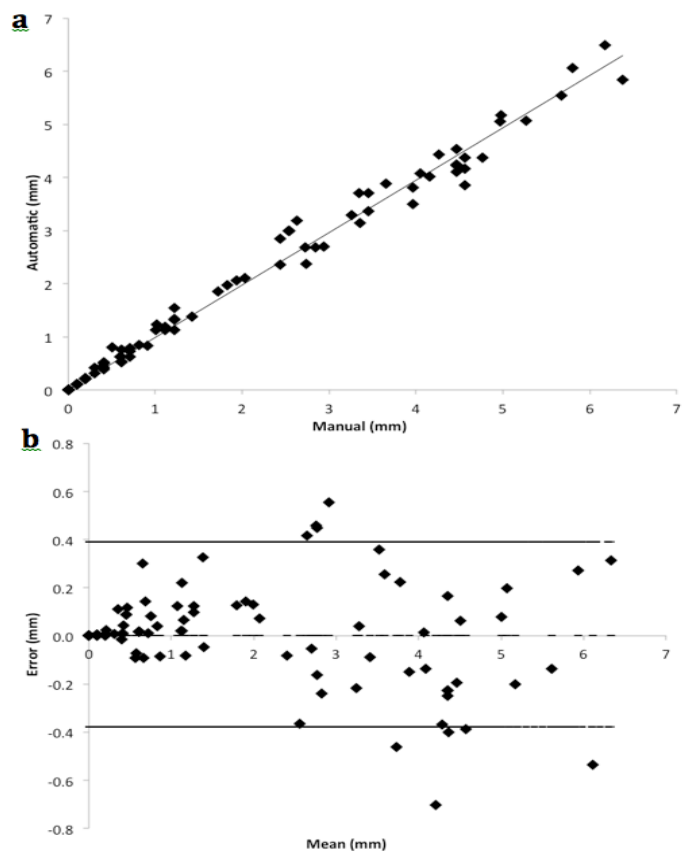


Figure 4 shows the comparisons of 2-ROI active tracking between automatic vs. manual measures of patellar tendon. a) Relationship between manual and automatic tracking, compared at 10% intervals of maximal voluntary force ($r=0.994$; $P<0.05$). b) Bland – Altman plot showing mean difference (bias) and 95% confidence limits (line showing mean difference = 0.005 mm, ± 2 SD).

For the medial gastrocnemius tendon, automated tracking gave a mean displacement value of 16.42 ± 0.85 mm, vs. 16.68 ± 0.86 mm for the manual measures. No significant differences were seen between measures ($p = 0.95$) indicating a good general agreement. The scatter plot indicates again an excellent relationship between measures ($r=0.99$; $p<0.05$) (See figure 5). Bias between measures was negligible (0.002mm), with the maximum difference of 0.81mm.

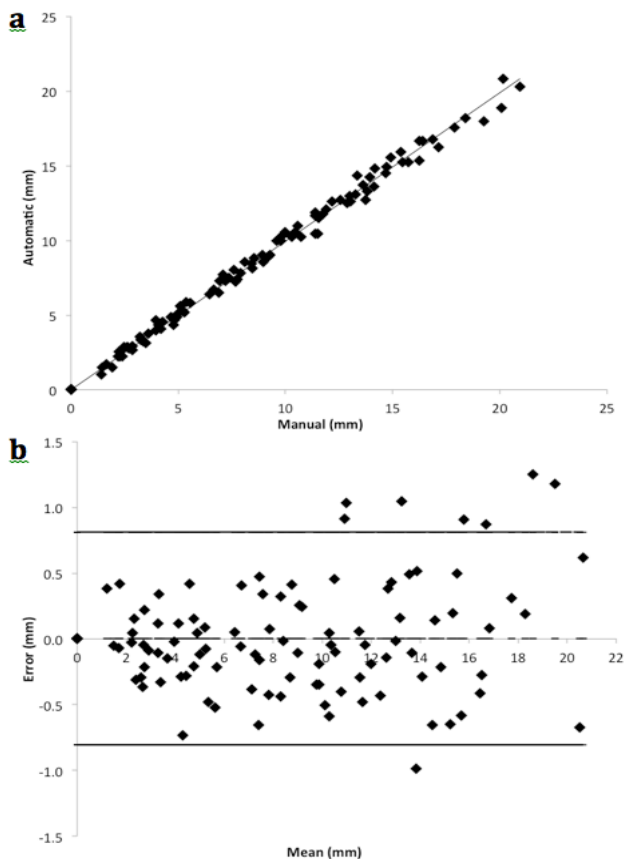


Figure 5 shows the comparisons of 2-ROI active tracking between automatic vs. manual measures of gastrocnemius tendon. a) Relationship between manual and automatic tracking, compared at 10% intervals of maximal voluntary force ($r=0.997$; $P<0.05$). b) Bland – Altman plot showing the

mean difference (bias) and 95% confidence limits (line showing mean difference = 0.002 mm, ± 2 SD).

Discussion

The results from the passive tests in this study showed that the automated algorithm enabled effective tracking of a region of interest within the image window when compared to the manually measured results. Here the net movement of 1-ROI's measured using manual and automated tracking were not significantly different from each other for both the patellar with a 2% difference in the total displacement ($p=0.06$) and medial gastrocnemius showing an approximate 1% difference ($p=0.79$). The 2-ROI passive tests showed no significant differences to zero for both the patellar and medial gastrocnemius tendon displacements ($p=0.53$; 0.75 and $p=0.14$; 0.15) for the automatic and manual methods respectively.

For the active tests the errors were expected to be larger due to the tendon being dynamically stretched during muscle contraction, causing some deformation and making automatic tracking more demanding. This was indeed found to be the case with the maximal differences (bias) determined for the active tests at 0.4 and 0.81mm for the patellar and medial gastrocnemius junction respectively. These were still considered relatively small differences between the methods, the correlations indicating excellent general agreement (Figures 4 and 5).

The tests carried out here are the first to directly compare automated tracking with manually measured tendon excursion during maximally loaded voluntary contractions. Lee et al. (2008) discussed comparisons of 'lightly' loaded in vivo tendon excursions using an automated tracking method and manual measures. But they did not make clear the manual approach or indeed the reliability of the manual method. This aside they reported absolute errors of ~ 0.5 mm, similar to that seen here. However, our RMS percent errors were smaller than those reported by Lee et al. (2008) with 3.2% seen here

compared to 5.9% reported by Lee and co workers. Although a limitation of the present study may be that the measures were made on only one subject, differences in image quality across subjects may affect the agreement or the ability of the algorithm to track regions effectively. However carrying out the trials on two distinct tendons with different morphologies shows the robustness of this procedure.

Fukunaga et al. (1996) were the first to utilise and validate in vivo muscle tendon movements using ultrasonography and manual tracking, this involved voluntary contraction of the dorsi- and plantar flexors whilst monitoring the associated ankle and muscle insertion displacements. The movement of the fascicle insertion point was seen to be highly correlated with the ankle angular displacement ($r=0.93$ to 0.97). Since then a number of authors have examined aspects of tendon mechanical properties using the manual method to determine tendon excursion during loading (Hansen et al. 2006; Onambélé et al. 2007; Pearson et al. 2007). The utility of having the ability to automatically track tendon displacement is seen in the limitation of the manual method which requires a known landmark to follow during tendon movement. It is not known if the tendon is homogenous with respect to its mechanical properties, as the current method only allow for an 'average' value to be determined from the total tendon excursion. Use of the automatic tracking algorithm as here, enables examination of specific areas of the tendon to ascertain for example site specific strain.

Our findings showed that for passive movements the tracking accuracy was within 1-2% of the manual values and active movements within 2.4-3.2% which is comparable to the displacement errors reported by Maganaris et al. (2000), 0.8-2.5% in the tendon and 2.1-7% in the aponeurosis. A more recent study (Farron et al., 2009) reported that the speckle tracking method was able to estimate frame-to-frame displacements using 2-ROI end points by tracking the movement of tendon during twitch contractions. However, as the tracking was carried out during twitch contractions by electrically stimulating the muscle, the forces in the tendon

were only moderate (up to 50% of maximum) which is a major difference to the approach here where high forces were elicited and thus larger tendon deformations would be expected making the tracking potentially more demanding.

Where others have utilised an automated algorithm to examine tracking there have been reported errors of <10% (Dilley et al. 2001). Here the transducer probe was moved within a 1-3 mm range over the surface of the forearm. Whilst, Magnusson et al. (2003) tracked a needle sliding 10 mm through gel with mean error of 2%, similar to the errors of 2% reported using cross-correlation to track wire oscillating in water (Loram et al., 2006). These are similar to our passive trials and give similar errors or differences to the manual method as we report here (up to 2%).

In summary, this method shows for the first time the utility of an automated tracking programme to determine tendon excursion during maximally loaded in vivo contractions by contrast with the standardised manual measurement method. Hence, it has the potential to improve clinical knowledge relating to the tendon mechanical properties by enabling discrete tendon mechanical properties to be determined.

References

- Arampatzis, A., Stafilidis, S., DeMonte, G., Karaminidis, K., Morey-Klapsing, G., & Bruggemann, G.P. (2005). Strain and elongation of the human gastrocnemius tendon and aponeurosis during maximal plantarflexion effort. *Journal of Biomechanics*, 38, 883-841.
- Dilley, A., Greening, J., Lynn, B., Leary, R., & Morris, V. (2001). The use of Cross-Correlation analysis between high-frequency ultrasound images to measure longitudinal median nerve movement. *Ultrasound in Medicine & Biology*, 27, 211-218.
- Farron J., Varghese T., & Thelen D. G. (2009). Measurement of Tendon Strain During Muscle Twitch Contractions Using Ultrasonography. *IEEE Transaction of*

- Ultrasonics, Piezoelectrics, and Frequency Control, 56, 27 - 35.
- Fukunaga, T., Ito, M., Ichinose, Y., Kuna, S., Kawakami, Y., & Fukashiro, S. (1996). Tendinous movement of a human muscle during voluntary contractions determined by realtime ultrasonography. *Journal of Applied Physiology*, 81, 1430 -1433.
 - Hansen, P., Bojsen -Moller, J., Aagaard, P., Kjaer, M., & Magnusson, S.P. (2006). Mechanical properties of the human patellar tendon, in vivo. *Clinical Biomech (Bristol, Avon)*, 21, 54 – 58.
 - Onambélé, G.N., Burgess, K., & Pearson, S.J. (2007). Gender -Specific In Vivo Measurement of the Structural and Mechanical Properties of the Human Patellar Tendon. *Journal of Orthopaedic Research*, 25, 1635 -1642.
 - Kim, Y.S., Kim, J.M., Bigliani, L.U., Kim, H.J., & Jung, H.W. (2011). In vivo strain analysis of the intact supraspinatus tendon by ultrasound speckles tracking imaging. *Journal of Orthopaedic Research*, 12,1931 -7.
 - Koga, T., Iinuma, K., Hirano, A., Iijima, Y., & Ishiguro, T. (1981). Motion Compensated Interframe Coding for Video Conferencing, in Proc. Nat. Telcommun. Conf., New Orleans, LA, Nov, 5.3.1 -5.3.5.
 - Kubo, K., Kanehisa, H., Kawakami, Y., & Fukunaga, T. (2000). Elastic properties of muscle - tendon complex in long -distance runners. *European Journal of Applied Physiology*. 81,181 -7.
 - Lee, S.S., Lewis, G.S., & Piazza, S.J. (2008). An algorithm for automated analysis of ultrasound images to measure tendon excursion in vivo. *Journal of Applied Biomechanics*, 24, 75 -82.
 - Loram, I.D., Maganaris, C.N., & Lakie, M. (2006). Use of ultrasound to make noninvasive in vivo measurement of continuous changes in human muscle contractile length. *Journal of Applied Physiology*, 100, 1311 -1323.
 - Maganaris, C. N., Baltzopoulos, V., & Sergeant, A.K. (2000). In vivo measurement -based estimations of the human Achilles tendon moment arm. *European Journal of Applied Physiology*, 83, 363 -369.
 - Magnusson, S. P., Hansen, P., Aagaard, P., Brønd, J., Dyhre - Poulsen, P., Bojsen -Moller, J. , & Kjaer, M. (2003). Differential strain patterns of the human gastrocnemius aponeurosis and free tendon, in vivo. *Acta Physiologica Scandanavica*, 177, 185–195.
 - Pearson, S.J., Burgess, K., & Onambele, G.N. (2007). Creep and the in vivo assessment of human patellar tendon mechanical properties. *Clinical Biomechanics (Bristol, Avon)*. 22,712 -7.
 - Revell, M. M., & McNally, D. (2005). Computer vision elastography: speckle adaptive motion estimation for elastography using ultrasound sequences. *IEEE transactions on medical imaging*, 24, 755.

Appendix B

Publication II

Medical Science Sports Exercise. 2014 Jan 1. [Epub ahead of print]

REGIONAL STRAIN VARIATIONS IN THE HUMAN PATELLAR TENDON

Stephen J. Pearson PhD¹, Tim Ritchings PhD², A.S.A Mohamed MSc²

¹Centre for Health, Sport and Rehabilitation Sciences Research, University of Salford, Greater Manchester M6 6PU, United Kingdom. ²Control & Systems Engineering Research Centre, University of Salford, Greater Manchester, M5 4WT, United Kingdom

Running head: In Vivo regional human patellar strain

Abstract

Purpose: Characteristics of localised tendon strain in vivo are largely unknown. The present study examines local tendon strain between the deep, middle and surface structures at the proximal and distal aspect of the patellar tendon during ramped isometric contractions.

Methods: Male subjects (aged 28.0 ± 6.3) were examined for patellar tendon excursion (anterior, midsection, posterior) during ramped isometric voluntary contractions using real time B-mode ultrasonography and dynamometry. Regional tendon excursion measurements were compared using an automated pixel tracking method. Strain was determined from the tendon delta length normalised to initial/resting segment length.

Results: Strain increased from 10-100 % force for all regions. Significantly greater mean strain was seen for the anterior proximal region compared to the posterior and mid layer of the tendon ($7.46 \pm 1.11\%$ vs. $3.74 \pm 0.51\%$ vs. $5.49 \pm 0.99\%$; $P < 0.05$). Similarly the distal posterior region showed greater mean strain compared to the mid and anterior regions ($7.88 \pm 0.85\%$ vs. $4.98 \pm 0.88\%$ vs. $5.36 \pm 0.71\%$; $P < 0.05$). Relative changes in strain differences from 50-100 % force for proximal were greatest for the anterior to midline regions ($4.62 \pm 0.61\%$,

$5.61 \pm 0.61\%$) and for the distal were also greatest for the anterior to midline regions ($4.35\% \pm 0.22\%$, $5.28 \pm 0.22\%$). The largest mean strain for the proximal region was at the anterior layer ($7.46 \pm 1.11\%$), and at the posterior layer for the distal tendon ($7.88 \pm 0.85\%$).

Conclusions: This study shows significant regional differences in strain during ramped isometric contractions for the patellar tendon. Lower proximal strains in the posterior tendon compared to the anterior region may be associated with the suggestion of 'stress shielding' as an aetiological factor in insertional tendinopathy.

Key Words: In vivo; tendon; regional structural properties; ultrasound

Introduction

Tendon is described as a viscoelastic structure and has been shown to have characteristic strain approximating linearity over a range of physiological loading (29). With increased strain there is a risk of damage to the tendon structure, leading to tears and ultimately rupture. Previous in vivo work using non invasive ultrasound imaging has described the patellar tendon properties in terms of its stiffness (extension per unit load) and associated strain values during voluntary contractions

(5, 10, 28). However the previous work has limitations in that the methods used to determine the values shown are in relation to the whole tendon and as such do not represent the mechanical properties of discrete portions of the tendon. Indeed previous studies have highlighted the non uniform nature of the human tendon with respect to cross sectional area (11, 12, 15, 25). Assuming similar forces in the tendon, this would indicate that the stress (force per unit area) is different along the tendon structure. If the tissue is homogenous then the strain may well be region specific. However, it may be that the loading is not homogenous along the tissue and that the strain may indeed be equivalent in line with the differences in cross sectional area. In any case if strain is not uniform it may indicate shear loading which could lead to excessive micro trauma or tears and cumulative damage of the tendon structure.

Tendon like muscle is able to alter its mechanical properties in response to loading. It comprises mainly of collagen fibrils and of which the predominant form is type I. These collagen fibrils play a major role in the characteristic mechanical properties of the tendon. It is known that collagen turnover is responsive to loading and will increase or decrease its turnover rates accordingly. The effect of increased loading and concomitant increased tendon collagen has been shown previously in animals (18) and also in humans in response to acute (26), and chronic exercise (20, 32).

It is not unreasonable to assume that the tissue which is metabolically active could be non homogenous in terms of the collagen turnover rates, leading to potential regional differences in mechanical properties. For example recently, Couppé et al. (7) reported differential hypertrophy of the patellar tendon along its length in comparison to the contralateral (i.e. non-dominant) tendon in athletes who had a tendency to display a dominant limb. Similarly in human subjects, Carroll and co workers reported regional differences in tendon cross sectional area (csa) with the proximal patellar tendon showing greater csa compared to the mid and distal regions (5).

It has previously been suggested that the patellar tendon is 'differentially' stimulated during loading leading to 'overuse'

type problems as in tendinopathy (24). This pattern is seen often at the proximal posterior portion of the patellar tendon. Of the few studies carried out examining regional patellar strain in cadaveric knee flexion models, one reported greater anterior strain; in contrast the other stated the posterior portion experienced greater strain (1, 3).

Tendinopathies have been described as being associated with overuse, where continued excessive loading leads to eventual tendon degradation via accumulated micro damage (21). However, 'stress shielding' has been suggested as an alternative explanation for the development of tendinopathy (24). Where insertional tendinopathies are seen there is a tendency for the pathology to occur at the posterior or joint side of the tendon. Here cartilaginous metaplasia can be seen to occur (34), typical with compressive loading, suggestive of non uniform strain or loading across the tendon. These tendon related anomalies are seen to be implicated in increasing number of tendon related functional disabilities in both the sporting and non athletic populations and which have a tendency to become chronic and degenerative. Understanding of the aetiology of tendinopathies is poor and as such treatment and rehabilitation modalities are not well defined.

To date, there are limited numbers of validated techniques to measure discrete tissue movement in vivo without the use of identifiable landmarks (9). The use of block matching techniques to measure tissue movement has been utilised previously to measure tissue movement (8, 23, 27). Dilley (8) has also shown that an optical flow technique can be used to study tissue displacement. However, optical flow performs better with smaller frame to frame displacements compared to speckle tracking. The design of tracking algorithms requires the capability of the algorithm handle both small and large frame-to-frame displacements in order to maintain accuracy. Where monitoring of tendon displacement during voluntary contractions is required, there are a number of ways to reduce frame to frame displacement; either ensure the ramped contraction is slow enough to reduce frame to frame displacement for a given frame rate, or increase the frame

acquisition rate to give a smaller frame-to-frame displacement. The region block is needed to capture a unique speckle pattern, this is important as tendons have a typical striated speckle pattern when compared to other tissue area. The size of the region of interest block has to be an optimum size, a relatively smaller block being less susceptible to deformation but local artefacts with an ambiguous pattern may be seen, whilst larger blocks may contain a less ambiguous and unique pattern, but during rapid motion, the pattern in the block may deform more leading to lower correlation.

The method described here allows for the quantification of the mechanical properties of the tendon at discrete regions of interest within the intact tendon structure. Thus it may allow for the sensitive identification of patterns of strain and associated changes within the tendon prior to injury, during rehabilitation or with disease, which cannot be identified using the method outlined in previous work. Detailed characterisation of the tendon may allow for further insight into the aetiology of tendon injury, repair and response to various training interventions.

Due to the previous observations and suggestions of differential loading of tendon structures we hypothesise that under ramped maximal isometric loads the patellar tendon will show regional differences in strain between the deep and superficial layers and that the proximal and distal tendon will exhibit characteristic differences in strain patterns.

Therefore the purpose of this present study was to:

- Examine proximal and distal localised strain across the anterior, mid and posterior patellar tendon using automated speckle tracking of dynamic ultrasound images of in vivo human patellar tendon tissue during ramped isometric loading.

The ultimate objective being for this work to contribute towards a much more detailed picture of the tendon in injury, repair and in response to various training interventions. This detailed understanding will allow for more effective screening, rehabilitation and injury prevention strategies to be put in place.

Methods

Subjects and experimental design

Sixteen healthy limbs were used for data collection in this study from healthy male subjects (age 28.0 ± 6.3 years, height 1.7 ± 0.04 m and body mass 79 ± 5.4 kg). The local Ethics Committee approved the investigation and all participants gave written informed consent to participate. The study conformed to the principles of the World Medical Association's Declaration of Helsinki.

A 7.5 MHz 100mm linear array, B-mode ultrasound probe (Mylab 70, Esaote Biomedica, Italy) with a depth resolution of 67mm was used to image the patellar tendon in the sagittal plane, the knee was fixed at 90° flexion. Ultrasound images were then taken in DV output and captured at 25 frames per second. Scaling in pixels per mm was determined from Image J software by using the known depth of field in the ultrasound images, (1 mm = 11 pixels) and utilised as a calibration factor in the automated tracking programme to ensure equivalent pixel to mm ratios.

The tendon was imaged during ramped voluntary contractions the transducer probe was fixed statically at the skin surface. Torque output during isometric quadriceps contraction was determined using a dynamometer (Kin Com, type 125 AP, Chattanooga, USA), with the participant in a seated position. The knee was fixed at 90° flexion (full extension = 0°) and hip at 85° (supine = 0°) and a lever attachment cuff was placed on the lower leg at ~3cm above the medial malleolus. Three maximal isometric quadriceps contraction efforts were carried out to ensure tendon preconditioning prior to the test. Participants were instructed to perform ramped isometric contractions from rest to maximum over a 3-4s time period. Three trials of the knee extension test were performed with 180s rest between contractions. Mean values of strain for the three contractions for each individual were used for subsequent analysis. The ultrasound output was synchronized (using an electronic square wave signal generator) with the torque records to allow temporal alignment. Electromyography determined any co contraction, which was added to the net

knee extension torque to give total torque. The EMG of the long head of the biceps femoris muscle (BF) was measured in order to ascertain the level of antagonistic muscle co-contraction during the isometric knee extension (30). Assumptions were that BF is representative of its constituent muscle group (4) and that the BF EMG relationships with knee flexors torque is linear (22). Briefly, a series of three maximal isometric knee flexion contractions were carried out to obtain the EMG at maximal flexion torque. The root mean square EMG activity corresponding to the peak torque period was analysed over 50 ms epochs and averaged for a 1 s period during the plateau of peak torque. This has previously been suggested to be acceptable in terms of signal-to noise ratio (13). Electromyographic activity of the BF during knee extension was divided by the maximal flexor EMG, and the maximal flexor torque was then multiplied by this value to determine co-contraction torque.

Patellar tendon force was determined then by dividing the total torque by the patellar lever arm (determined from the literature - (19, 33)). Captured greyscale ultrasound images gave region attributes (dimensions, position coordinates, and greyscale pixel values). In the compared frame, the coordinates of the region of interest (ROI) were offset along the horizontal and vertical image plane, and shifted by a pixel at a time.

Tracking algorithm

A block matching algorithm with normalized cross-correlation (NCC) (Eq. 1) was used as the search schema to determine similarity between subsequent frames. Multiple search blocks (regions of interests -ROIs) were placed manually on the regional layers of the tendon (proximal and distal). The ROI's on the proximal and distal tendon were divided into three layers; anterior (layer 1), mid (layer 2) and posterior (layer 3) (see figure 1). These are then utilised to determine the relative excursion from the initial start point and also to calculate strain for the specific force levels. An optimal ROI size was used (15x15 pixel based on pilot work) to track multiple layers of the tendon with the search window for each ROI fixed at 2xROI size for the width and 1xROI for the height. Multiple

ROIs (6) of the same size as the initial ROIs are distributed along the selected ROI layers to calculate the average displacements to help improve accuracy during frame-to-frame tracking. For frame to frame movements of the ROI, within each search window the ROI's were displaced by 1 pixel at a time compared with the original ROI in the previous frame and evaluated using NCC. The results of which are stored in a matrix and best matches based on peak detection (i.e. highest correlation value). To reduce the chances of the decorrelation the correlation threshold value was set to above 0.9. If the threshold value was not reached or exceeded, then the ROI was not moved in the subsequent frame. Otherwise the tracking will start with the new updated position of the template ROI blocks in the next frame.

$$\rho_{nm(k,l)} = \frac{\sum_{i=-K}^K \sum_{j=-L}^L [F_1(n+i, m+j) F_2(n+k+i, m+l+j)]}{\left[\sum_{i=-K}^K \sum_{j=-L}^L [F_1(n+i, m+j)]^2 \right]^{1/2} \left[\sum_{i=-K}^K \sum_{j=-L}^L [F_2(n+k+i, m+l+j)]^2 \right]^{1/2}} \quad (1)$$

where, F_1 refers to the image block of the initial frame and F_2 is the image block of the subsequent frame. n and m refer to the number of pixels with k and l represent the coordinate of the image block, while i and j refer to the displacements in the axial and lateral directions. $\rho_{nm(k,l)}$ represents the normalized correlation ranging from -1 to 1 and 1 being the closest match.

The test comprises of two regions of interests (2-ROI) R1 and R2 (see figure 1), tracked from the initial frame until they reach the last frame. The determined measurement of the displacement is the difference of the distance of two nodes at 10 % intervals of force up to 100 % MVC. For all repeat trials (three) the initial positions of the ROIs were the exact same reference point in the frame.

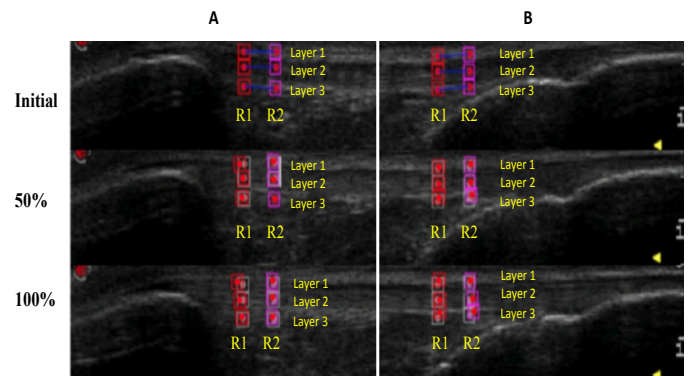


Figure 1. Regional tracking of ROIs (R1 & R2-arbitrary pixel regions in the tendon) by layer (1,2 and 3) on a typical tendon excursion on both proximal (A) and distal (B) showing shift in the ROI's from the resting tendon, at 50% force and 100% force.

The measurements taken for the tests are classified into six parts, proximal anterior tendon excursion (PS), proximal midline tendon excursion (PM), proximal posterior tendon excursion (PP), also distal anterior tendon excursion (DS), distal midline tendon excursion (DM) and distal posterior tendon excursion (DP). The movement in each layer for each frame is determined by measuring the distance of x and y for both R1 and R2 regions from initial frame (f_i) to frame (f_n). The resultant displacement for each layer is measured by subtracting the distance of the frame (f_n) with the initial frame (f_i) as formulated in (2). Strain measurement is thus the change in length divided by the initial length of the tendon (I). All initial proximal and distal regions were aligned vertically to enable quantification of any differences in regional strain within a localised site of the tendon.

$$Disp = \left(\sqrt{(x_{R2} - x_{R1})^2 + (y_{R2} - y_{R1})^2} \right)_{f_n} - \left(\sqrt{(x_{R2} - x_{R1})^2 + (y_{R2} - y_{R1})^2} \right)_{f_i} \quad (2)$$

Statistics

Intraclass correlation coefficients (ICCs) were determined to examine the reliability/robustness of the measures by carrying out repeated tracking on the full data set at each 10% increment of force. A number of tracking correlation thresholds ranging from value of 0.8 to 1.0 were tested previously and for this experiment the value of 0.9 was found to be optimal in terms of tracking the pattern correctly, which is presented as speckle. The value of 0.8 shown to be more sensitive (less robust to variation) to any changes of the speckle pattern around the searching area and prone to track other movement, while the value of 1.0 shown to be less sensitive (too robust to variation) and restricted to exactly match the initial pattern. Between region comparisons (all regions being independent) for all

strain (dependant variable) measures (at given levels of force - 10% increments) were carried out using two way ANOVA and Bonferroni post hoc pairwise tests. Alpha level was set to $P=0.05$. All data are presented as mean \pm standard error of the mean (SEM). Sample size was determined using G power (3.09, Franz, Faul, Universitat, Keil, Germany). For a power ($1 - \beta$), of 0.95, and moderate effect size (0.2), a sample size of 15 was calculated.

Results

Reliability

Repeat tests of the measures for tendon excursion at all layers and forces gave an ICC of 0.9.

Proximal tendon strain

All layers showed increased strain across the forces levels from 10-100% ($P<0.01$) (Figure 2). The analysis also revealed an interaction of force by layer. Subsequent one-way ANOVA showed no significant difference ($P>0.05$) at force levels 50-60% and 90-100% for the anterior layer. No significant difference ($P>0.05$) at force levels 40-60% for the mid layer. The posterior layer showed no significant difference ($P>0.05$) at force levels 30-60% and 70-100%.

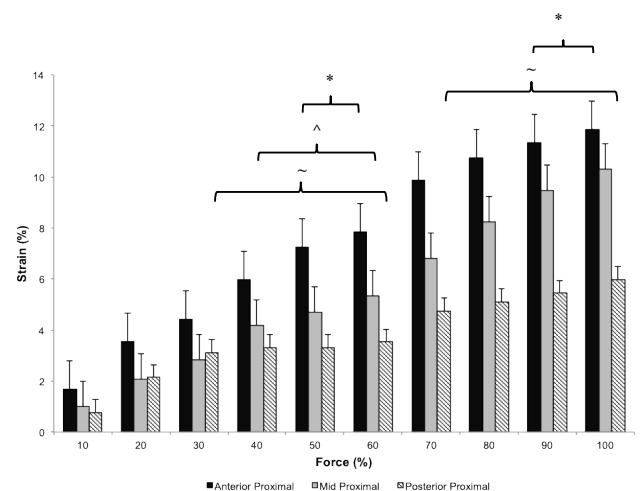


Figure 2: Strain values for all measured proximal regions (mean \pm SEM) at 10 - 100% MVC. Mean Strain anterior layer shows no significant differences ($P>0.05$) at the force levels indicated by *. Mean midline shows no significant differences

($P>0.05$) at force levels indicated by ~. Mean posterior layer shows no significant differences ($P>0.05$) at force levels marked by ^.

Distal tendon strain

Similar to the proximal strain, it can be seen in figure 3 that all distal layers showed increased strain across the forces levels from 10-100%. Analysis revealed significant increase in strain with force ($P<0.01$), the mean values for the posterior layer strain were seen to be greater than anterior strain ($7.88\pm0.62\%$ vs. $5.36\pm0.62\%$; $P=0.01$). Posterior strain was also greater than midline strain ($7.88\pm0.62\%$ vs. $4.98\pm0.62\%$; $P<0.01$). No interaction between layer and force was shown.

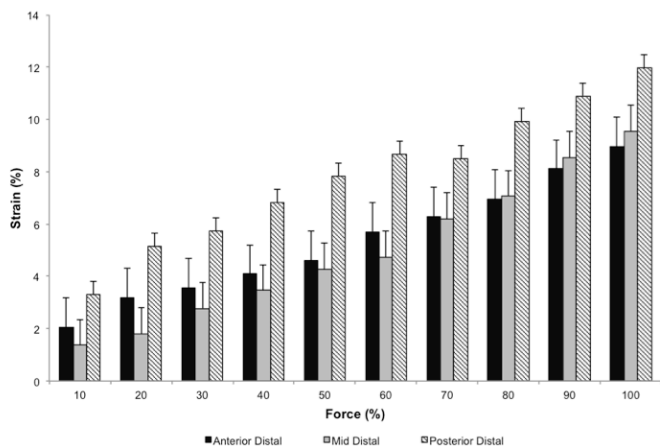


Figure 3: Mean strain significantly increased with force level ($P<0.01$). Mean anterior strain was greater than posterior strain ($P=0.01$). Mean midline strain was also greater than the mean posterior strain ($P<0.01$).

Figure 4 illustrates instantaneous regional strain values at 50% and 100% force. Overall mean strain was greater at 100% compare to 50% strain ($9.77\pm0.34\%$, $5.33\pm0.34\%$). No interaction was seen between force level and region ($p>0.05$). Pooled values for strain indicated that proximal anterior and distal posterior strains were greater than all regions ($p<0.05$). Proximal midline strain was also significantly different to proximal posterior strain (see table I).

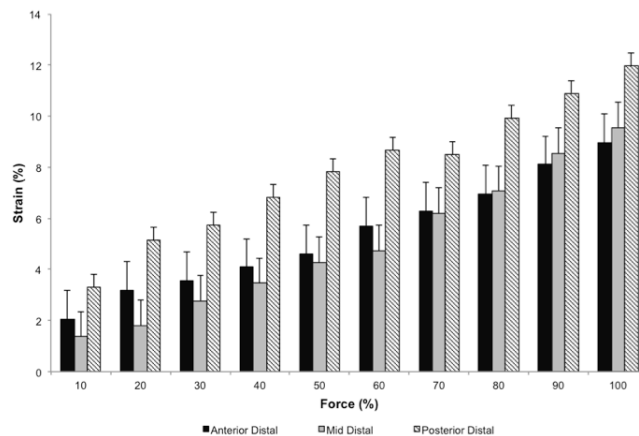


Figure 4: Instantaneous Strain values for all layers at both proximal and distal regions of the patellar tendon at 50% and 100% force. Pool means strain of proximal anterior was significantly different to regions other than distal posterior (*; $P<0.05$). Pool means strain of distal posterior was significantly different to regions other than proximal anterior (^; $P<0.05$).

Force (%)	Strain (%)					
	Proximal			Distal		
	Anterior	Midline	Posterior	Anterior	Midline	Posterior
50	7.24±1.15	4.69±1.15	3.32±1.15	4.61±1.14	4.27±1.14	7.84±1.14
100	11.86±1.76	10.30±1.76	5.98±1.76	8.96±0.92	9.55±0.92	11.96±0.92
Difference	4.62±0.61	5.61±0.61	2.66±0.61	4.35±0.22	5.28±0.22	4.12±0.22
Pooled Mean Values	9.55±0.36	7.50±0.56	4.65±0.52	6.79±0.57	6.91±0.52	9.90±0.54

Table I. Instantaneous strain values at 50% and 100% with its relative difference and corresponding pooled mean values for all layers at both proximal and distal regions of the patellar tendon. These differences in strain between 50% and 100% could indicate shear between the tendon boundary layers.

Proximal anterior and distal posterior were seen to have significantly greater total mean strain than all of the regions ($7.46\pm1.11\%$, $7.88\pm0.88\%$; $P<0.05$). Also, the distal anterior region showed greater total mean strain in comparison to the proximal posterior region ($5.49\pm0.99\%$ vs. $3.74\pm0.51\%$; $P=0.02$) (See figure 5).

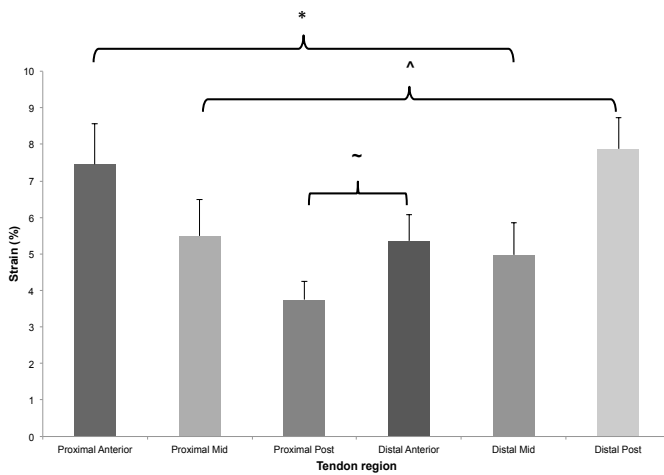


Figure 5. Total mean strain at all layers for both proximal and distal regions of the patellar tendon. Mean strain at proximal anterior was significantly different to regions other than distal posterior (*; $P < 0.05$). Distal posterior is significantly different to regions other than proximal anterior (^; $P < 0.01$). Proximal posterior was significantly different to distal anterior (~; $P = 0.02$).

Discussion

The current study aimed to examine and compare localised proximal strain at both the anterior and posterior regions of the patellar tendon. The findings show that in the patellar tendon for a group of healthy young subjects the greatest mean strains during isometric ramped contractions were seen in the anterior layer at the proximal end (7.46%) and posterior layer at the distal end (7.88%) (see figure 5).

Of particular interest was the finding that for the proximal and distal tendon, there were significant differences between the layers of tendon examined. Here the strain being greatest in the anterior layer and least in the posterior layer for the proximal tendon, and greatest in the posterior layer for the distal tendon (see figure 4).

Speckle tracking has been utilised previously to estimate tissue velocity and hence relative excursion. A number of studies have attempted to utilise commercially available speckle tracking programmes to determine tendon excursion compared

to doppler methods and reported speckle tracking to be superior (35, 36). Others have utilised a custom developed speckle tracking programme to estimate tendon movement during both active and passive movements without any mention of validation against a standard measure (16). These studies report that speckle tracking may be useful to allow for estimation of tendon movement in vivo.

Previous studies have validated the use of localised tracking of tendon using block matching techniques similar to that used here (14, 17, 31). Korstanje et al. (17) reported relatively small errors of up to 1.6% when attempting to track an in vivo structure. Here we also show very good repeatability of tracking data indicating a very good agreement with other reports of measurement. A recent study (9) reported that the speckle tracking method was able to estimate frame-to-frame displacements using 2-ROI end points by tracking the movement of tendon during twitch contractions. However, as the tracking was carried out during twitch contractions by electrically stimulating the muscle, the forces in the tendon were only moderate (up to 50% of maximum) which is a major difference to the approach here where high forces were elicited and thus larger tendon deformations would be expected making tracking more difficult. In addition, previous work has indicated that contraction time can affect the amount of excursion seen in the tendon (29), this can be explained due to the viscoelastic nature of the tendon. It could then be speculated that the composition of the tendon at different regions may be proportionally different in terms of the viscous and elastic components, which would affect the time-course of extension under load to different degrees.

The determined mean strains reported here at MVC (~ 7.5 – 7.9%) for the tendon were within the range of those reported for this structure in young males (5, 10, 28) these previous references showing a range of 6 – 10.6%. The anterior and posterior regional strains have been previously reported in cadaveric specimens (3), here strain values at a load of 1KN were 1.7 % and 3.2% for the anterior and posterior regions respectively. In the present study we report values of 7.46 and

3.74% for the proximal anterior and posterior tendon strain, while distal anterior and posterior show 5.36 and 7.88% tendon strain respectively (see figure 4), which are considerably larger than those reported by Basso and co workers. This may in part reflect differences in the level of load, application of load and also that we determined the strain in the proximal half of the tendon compared to the mid third utilised by Basso and co workers. It may be that the tendon is not homogenous throughout its length and could be structurally different in terms of the collagen content, type and extracellular matrix density. In addition to this the samples used by Basso were from cadavers, these may not accurately reflect the values for 'live' tissues as measured here.

Others have also indicated that regional layer differences exist in strain within a tendon. A study utilising speckle tracking to estimate in vivo tendon strain, examining layer differences in strain of the supraspinatus tendon during isometric and isotonic efforts, reported that the superficial layer of the tendon showed greater strain relative to the deep layers (14). Also during passive plantar dorsi flexion of the ankle it was seen that the Achilles tendon showed greater relative displacement of the deep portion of the tendon in comparison to the superficial and mid portions (2).

Recently, Hansen et al. (11) showed that tendon fascicles from the anterior tendon were in fact stiffer and stronger with less mature pyridinium type cross-links relative to fascicles from the posterior tendon region. These data however, were from ACL surgery patients and it is not known to what degree these would be representative of the 'normal' population. In spite of this suggested greater resistance to strain of the anterior tendon, due to the lever arm arrangements of the patellar relative to the tendon, it may well be that forces are greatest at the anterior region due to the lever arm advantage at the patellar surface in comparison to the deep layers leading to increased strain for a given external force.

Indeed Almekinders et al. (1) showed larger forces/strains present in cadaveric patellar specimens on the anterior portion

of the proximal tendon. In intact human muscle/tendon systems though there is the complex interplay of agonist-antagonist interaction, and differences in the mechanical tissue properties to that of cadaveric specimens. Any differences in applied force, if it is habitual should lead to adaptation of the structures under normal circumstances.

In relations to the distal tendon, it has been observed previously (unpublished observations by authors) that the tibial insertion end rotates inward (posterior) in the sagittal plane when forces are generated in the protocol as used here. Thus this 'twisting' of the bone attachment could partly cause the differential strain as seen here, both between the proximal and distal ends and also the layers of the distal end. These different patterns of strain between the tendon layers at the sites measured could indicate shear of the tendon structure. For example, we clearly show greater strain in the anterior region for the proximal tendon and posterior region for the distal tendon. In addition, the relative strain change (within layers) with increased loading (from 50-100 %) (see figure 5) force again indicated probability of shear between the tendon layers, as each region strain differently at given force levels, thus causing differential longitudinal movement between layers (shear force). This relative difference in strain at different levels of force may in fact be a factor in the development of cumulative tendon injury with time. However, here we would also draw attention to the understanding that statistical significance alone does not constitute 'clinical' or physiological significance, and further studies will have to be carried out to elucidate further. In addition all the above reported measures of in vivo tendon properties have been carried out at a knee angle of 90 degrees, it would be interesting to determine local tissue strains at a number of different knee angles to identify if the ratio's of local strains are similar to that at 90 degrees. This would present a useful insight into perhaps a more functional interpretation of the localised strains as reported here.

Tendinopathies have been reported to alter the mechanical properties of the tendon. Child et al. (6) reported in a group of runners with mid portion tendinopathy, an increased

compliance of the achilles tendon aponeurosis. If changes such as this are seen with specific degenerative states or diseases it can be seen that a sensitive marker for changes in localised tendon strain may be very useful as a predictor of disease/degeneration progression. Indeed with further testing patterns of ‘change’ or indicators of ‘risk’ may be developed to help early intervention or rehabilitation of damaged tendon.

Conclusion

The method used here has the potential to improve clinical knowledge relating to the tendon mechanical properties. It is clear that the strain throughout the tendon structure is not equal for a given external force, lending itself to tissue shear and hence to potential for increase injury risk in specific areas of the tendon. Future studies using this methodology will include testing of other tendon landmarks, to determine and describe discrete tendon mechanical properties, to examine various changes of regional tendon stiffness and strain with gender, age and in specific disease states (i.e. tendinopathies, diabetes). It is for future studies to determine how and why these differences in strain may affect the aetiology of disease and effects of training rehabilitation. These studies will give further insight into the aetiology of tendon injury, repair, response to various training interventions and the time course of tissue adaptation with disease.

Acknowledgements

The authors indebted to all our study participants without whom none of this work would have been possible. The authors are not professionally and/or financially affiliated to any institution that may be perceived as causing a bias in the presentation of their results.

References

1. Almekinders LC, Vellema JH, and Weinhold PS. Strain patterns in the patellar tendon and the implications for

patellar tendinopathy. *Knee Surg Sports Traumatol Arthrosc.* 2002;10(1):2-5.

2. Arndt A, Bengtsson AS, Peolsson M, Thorstensson A, and Movin T. Non-uniform displacement within the Achilles tendon during passive ankle joint motion. *Knee Surg Sports Traumatol Arthrosc.* 2011.
3. Basso O, Amis AA, Race A, and Johnson DP. Patellar tendon fiber strains: their differential responses to quadriceps tension. *Clin Orthop Relat Res.* 2002;(400):246-53.
4. Carolan B, and Cafarelli E. Adaptations in coactivation after isometric resistance training. *J Appl Physiol.* 1992;73(3):911-7.
5. Carroll CC, Dickinson JM, Haus JM, Lee GA, Hollon CJ, Aagaard P, Magnusson SP, and Trappe TA. Influence of aging on the in vivo properties of human patellar tendon. *J Appl Physiol.* 2008;105(6):1907-15.
6. Child S, Bryant AL, Clark RA, and Crossley KM. Mechanical properties of the achilles tendon aponeurosis are altered in athletes with achilles tendinopathy. *Am J Sports Med.* 2010;38(9):1885-93.
7. Couppé C, Kongsgaard M, Aagaard P, Hansen P, Bojsen-Moller J, Kjaer M, and Magnusson SP. Habitual loading results in tendon hypertrophy and increased stiffness of the human patellar tendon. *J Appl Physiol.* 2008;105(3):805-10.
8. Dille A, Greening J, Lynn B, Leary R, and Morris V. The use of cross-correlation analysis between high-frequency ultrasound images to measure longitudinal median nerve movement. *Ultrasound Med Biol.* 2001;27(9):1211-8.
9. Farron J, Varghese T, and Thelen DG. Measurement of tendon strain during muscle twitch contractions using ultrasound elastography. *IEEE Trans Ultrason Ferroelectr Freq Control.* 2009;56(1):27-35.
10. Hansen P, Bojsen-Moller J, Aagaard P, Kjaer M, and Magnusson SP. Mechanical properties of the human patellar tendon, in vivo. *Clin Biomech (Bristol, Avon).* 2006;21(1):54-8.

11. Hansen P, Haraldsson BT, Aagaard P, Kovanen V, Avery NC, Qvortrup K, Larsen JO, Krogsgaard M, Kjaer M, and Peter Magnusson S. Lower strength of the human posterior patellar tendon seems unrelated to mature collagen cross-linking and fibril morphology. *J Appl Physiol*. 2010;108(1):47-52.
12. Haraldsson BT, Aagaard P, Krogsgaard M, Alkjaer T, Kjaer M, and Magnusson SP. Region-specific mechanical properties of the human patella tendon. *J Appl Physiol*. 2005;98(3):1006-12.
13. Hermens HJ, Fredriks B, Disselhorst-Klug C, and Rau G. Development of recommendations for SEMG sensors and sensor placement procedures. *Journal of Electromyography and Kinesiology*. 2000;10(5):361-74.
14. Kim YS, Kim JM, Bigliani LU, Kim HJ, and Jung HW. In vivo strain analysis of the intact supraspinatus tendon by ultrasound speckles tracking imaging. *J Orthop Res*. 2011;29(12):1931-7.
15. Kongsgaard M, Reitelsheder S, Pedersen TG, Holm L, Aagaard P, Kjaer M, and SP M. Region specific patellar tendon hypertrophy in humans following resistance training. *Acta Physiol (Oxf)*. 2007;191(2):111-21.
16. Korstanje JW, Schreuders TR, van der Sijde J, Hovius SE, Bosch JG, and Selles RW. Ultrasonographic assessment of long finger tendon excursion in zone v during passive and active tendon gliding exercises. *The Journal of hand surgery*. 2010;35(4):559-65.
17. Korstanje JW, Selles RW, Stam HJ, Hovius SE, and Bosch JG. Development and validation of ultrasound speckle tracking to quantify tendon displacement. *J Biomech*. 2010;43(7):1373-9.
18. Kovanen V, and Suominen H. Age and training-related changes in the collagen metabolism of rat skeletal muscle. *Eur J Appl Physiol Occup Physiol*. 1989;58(7):765-71.
19. Krevolin JL, Pandy MG, and Pearce JC. Moment arm of the patellar tendon in the human knee. *J Biomech*. 2004;37(5):785-8.
20. Kubo K, Ikebukuro T, Maki A, Yata H, and Tsunoda N. Time course of changes in the human Achilles tendon properties and metabolism during training and detraining in vivo. *European journal of applied physiology*. 2012;112(7):2679-91.
21. Leadbetter WB. Cell-matrix response in tendon injury. *Clin Sports Med*. 1992;11(3):533-78.
22. Lippold OC. The relationship between integrated action potentials in a human muscle and its isometric tension. *Journal of Physiology*. 1952;177: 492-9.
23. Loram ID, Maganaris CN, and Lakin M. Use of ultrasound to make noninvasive in vivo measurement of continuous changes in human muscle contractile length. *J Appl Physiol*. 2006;100(4):1311-23.
24. Maganaris CN, Narici MV, Almekinders LC, and Maffulli N. Biomechanics and pathophysiology of overuse tendon injuries: ideas on insertional tendinopathy. *Sports Med*. 2004;34(14):1005-17.
25. Magnusson SP, and Kjaer M. Region-specific differences in Achilles tendon cross-sectional area in runners and non-runners. *European journal of applied physiology* 2003;90:549-53.
26. Miller BF, Olesen JL, Hansen M, Døssing S, Crameri RM, and Welling RJ. Coordinated collagen and muscle protein synthesis in human patella tendon and quadriceps muscle after exercise *J Physiol*. 2005;15(567):1021-33.
27. Ofer N, Akselrod S, Nyska M, Werner M, Glaser E, and Shabat S. Motion-based tendon diagnosis using sequence processing of ultrasound images. *J Orthop Res*. 2004;22(6):1296-302.
28. Onambele GN, Burgess K, and Pearson SJ. Gender-specific in vivo measurement of the structural and mechanical properties of the human patellar tendon. *J Orthop Res*. 2007;25(12):1635-42.
29. Pearson SJ, Burgess K, and Onambele GN. Creep and the in vivo assessment of human patellar tendon mechanical properties. *Clin Biomech (Bristol, Avon)*. 2007;22(6):712-7.
30. Pearson SJ, and Onambele GN. Influence of time of day on tendon compliance and estimations of voluntary activation levels. *Muscle Nerve*. 2006;33(6):792-800.
31. Revell J, Mirmehdi M, and McNally D. Computer vision elastography: speckle adaptive motion estimation for

- elastography using ultrasound sequences. *IEEE Trans Med Imaging*. 2005;24(6):755-66.
32. Rufai A, Ralphs JR, and Benjamin M. Structure and histopathology of the insertional region of the human Achilles tendon. *J Orthop Res*. 1995;13(4):585-93.
 33. Tsaopoulos DE, Baltzopoulos V, and Maganaris CN. Human patellar tendon moment arm length: measurement considerations and clinical implications for joint loading assessment. *Clin Biomech (Bristol, Avon)*. 2006;21(7):657-67.
 34. Vogel KG, Ordog A, Pogany G, and Olah J. Proteoglycans in the compressed region of human tibialis posterior tendon and in ligaments. *J Orthop Res*. 1993;11(1):68-77.
 35. Yoshii Y, Henderson J, Villarraga HR, Zhao C, An KN, and Amadio PC. Ultrasound assessment of the motion patterns of human flexor digitorum superficialis and profundus tendons with speckle tracking. *J Orthop Res*. 2011;29(10):1465-9.
 36. Yoshii Y, Villarraga HR, Henderson J, Zhao C, An KN, and Amadio PC. Speckle tracking ultrasound for assessment of the relative motion of flexor tendon and subsynovial connective tissue in the human carpal tunnel. *Ultrasound Med Biol*. 2009;35(12):1973-81.

Appendix C

Conference Abstract

(SPARC 2011)

Image tracking using normalized cross-correlation to track and analyse mechanical tendon properties.

Ahmad Sufril Azlan Mohamed, Professor Tim Rithcings¹, Dr. Stephen J. Pearson²

¹Control & Systems Engineering Research Centre, University of Salford, Greater Manchester, M5 4WT, United Kingdom

²Centre for Health, Sport and Rehabilitation Sciences Research, University of Salford, Greater Manchester M6 6PU, United Kingdom

The use of two-dimensional ultrasound can be optimised using image-tracking algorithm to track and observe the characteristics of the tendon muscle. Detailed characteristics of the tendon allows for insight into the aetiology of the tendon injury, repair and response to various training interventions. Although there have been numerous studies that detailed the in vivo tendon mechanical properties these properties are limited to the methods which described the whole region of the tendon and not specific to any given regions (Hansen, et al., 2006; Pearson, et al., 2007). The method described here allows for the quantification of the mechanical properties of regions of interest along the tendon length. Thus it may allow for the sensitive identification of changes to the tendon prior to injury or during rehabilitation, which cannot be identified using the method outlined in previous work.

The randomness of the speckle pattern in ultrasound ensures that each region of the tissue within the imaging frame has its own unique pixel pattern that can differentiate a region from other regions. The aim of any tracking algorithm is to attempt to identify the pixel ‘signature’ between subsequent image frames. Under ideal conditions the tissue would not change its ultrasound echo from frame to frame i.e. as during a passive movement where the tissue is not expected to distort. However, as the tissue is stretched under load, so it deforms and its density changes, altering the ultrasound pattern produced. Hence the pixel signature of a region of interest in any given frame may in fact change in the subsequent frames.

Recent work employing the Lucas-Kanade method used a synthetic material (i.e. wire often called “phantom wire” which was moved a known distance) in an attempt to validate the efficiency of measuring muscle excursion automatically (Lee, et al., 2008). The same approach was carried out using cross-correlation (Dilley, et al., 2001; Ellis, et al., 2008) to determine longitudinal medial nerve movement. Here slight artifactual movements were seen at the end of the frame. Revell, et al. (2005), utilised a normalised cross correlation (NCC) of fast fourier transformed data to track speckle signatures in ultrasound tendon images as it is suggested to be reliable and fast algorithm to track. None of the previous tracking papers have related their measurements with the manual method used in the literature (e.g. Pearson, et al., 2007) to estimate tendon excursion. In addition, none appear to have utilised high force contractions (tendon stretch is relatively large) to test the ability of the tracking algorithm to follow a region of interest across successive frames.

Therefore the aims of this present study were to:

- Examine and identify tracking algorithm without the need to use synthetic materials and able to track in real-time.
- Examine a method of tracking regions of interest within the ultrasound images of in vivo human tendon tissue during active (highly loaded) tendon movement.
- Examine and determined optimum tracking regions within the ultrasound images for strain analysis using the tracking algorithm.
- Compare the automated method with the established manual method to ascertain its validity.

This work will enable a much more detailed picture of the tendon in injury, repair and in response to various training interventions. This detailed understanding will allow for more effective rehabilitation and injury prevention strategies to be put in place.

References

- [1] Dilley, J. G., B Lynn, R Leary, V Morris, 2001. The use of Cross-Correlation analysis between high-frequency ultrasound images to measure longitudinal median nerve movement. *Ultrasound in Medicine & Biology*, 27(9), pp.1211-1218.

- [2] Ellis, W. H., Andrew Dilley, Peter McNair, 2008. Reliability of measuring sciatic and tibial nerve movement with diagnostic ultrasound during a neural mobilisation technique. *Ultrasound in Medicine & Biology*, 34(8), pp.1209-1216.
- [3] Farron J., Varghese T., Thelen D. G., 2009. Measurement of Tendon Strain During Muscle Twitch Contractions Using Ultrasonography. *IEEE Transaction of Ultrasonics, Perroelectrics, and Frequency Control*, 56(1), pp.27 - 35
- [4] Fukunaga, T., Ito, M., Ichinose, Y., Kuna, S., Kawakami, Y., & Fukashiro, S., 1996. Tendinous movement of a human muscle during voluntary contractions determined by realtime ultrasonography. *Journal of Applied Physiology*, 81, pp.1430-1433.
- [5] Hansen P, B.-M. J., Aagaard P, et al., 2006. Mechanical properties of the human patellar tendon, in vivo. *Clinical Biomech (Bristol, Avon)*, 21, pp.54 – 58. .
- [6] Lee S, G. S. L., and Stephen J. Piazza, 2008. An algorithm for automated analysis of ultrasound images to measure tendon excursion in vivo. *Journal of Applied Biomechanics*, 24(1), pp.75-82.
- [7] Maganaris, C. N., Baltzopoulos, V., & Sergeant, A.K., 2000. In vivo measurement-based estimations of the human Achilles tendon moment arm. *European Journal of Applied Physiology*, 83, pp.363-369.
- [8] Magnusson SP, Aagaard P, Rosager S, Dyhre-Poulsen P, and Kjaer M., 2001. Load-displacement properties of the human triceps surae aponeurosis in vivo. *Journal of Physiology*, 531, pp.227-288
- [9] Pearson S., G. O., K Burgess, 2007. Gender-Specific In Vivo Measurement of the Structural and Mechanical Properties of the Human Patellar Tendon. *Journal of Orthopaedic Research*, 25(12), pp.1635-1642.
- [10] Revell, M. M., Donal McNally, 2005. Computer vision elastography: speckle adaptive motion estimation for elastography using ultrasound sequences. *IEEE transactions on medical imaging*, 24(6), pp.755

Appendix D

RISE magazine column (August / September 2011)

Ultrasound image research

Ahmad S. A. Mohamed is a full time PhD student in the School of Computing, Science & Engineering.

Originally from Malaysia, Ahmad is at the University researching into developing a solution to improve the currently available motion estimation algorithm for tracking the ultrasound images of the knee's tendon tissue being contracted at maximum effort.

Ahmad said: "The images were captured using the B-mode ultrasound 2-D images, which is highly speckled and constantly changing from frame to frame. The ultrasound device used consists of a probe transducer that transmits pulses of wave signals penetrating the tissue structure; the waves are reflected back to the probe transducer to generate a digitised form of the image. The level of density of the image depends on the depth of the wave signals and

the time taken for the reflected wave signals to reach the probe transducer. The major disadvantage of ultrasound image is that the image presented is in speckle formation and the way that the probe is positioned on the skin does contribute to the changes in the resulted image. Past studies from other researchers focused on tracking the regional areas of the muscle tissue with various results. The study that I am conducting looks into the various motion estimation algorithms used on speckled images in vivo at the fibrous area of the tendon. So far we have found that Normalised Cross-Correlation (NCC) was the optimal solution. However, the algorithm alone is not able to accurately estimate the motion of a single muscle fibre because the speckle signal itself is dynamic from frame-to-frame. Therefore, the aim of the study is to devise a

solution to improve the tracking algorithm. The estimation of the next possible location in the next frame is determined by averaging the pattern of multiple points of regional areas placing on different layers of the tendon tissue to guide the search window as to where the tracking algorithm should look to perform the similarity measurement in the next frame.

The search window then uses the Block Matching Algorithm (BMA) to determine best similarity. This method is then used during dynamic excursions of the patellar tendon across subjects of various age and gender to identify the accuracy, and effectiveness of the solution to improve the tracking algorithm to produce clinical results that are useful to the practitioner. The real impact of this study allows an insight into the aetiology of the tendon injury, repair and response to various training interventions".

Name: Ahmad Mohamed

Email: a.s.a.mohamed@edu.salford.ac.uk

August/September | 53

Appendix E

Conference Paper

Int. Conf. of Global Network for Innovative Technology (IGNITE 2014)

Automated Speckle Tracking in Ultrasound Images of Tendon Movements

A.S.A Mohamed School of Computer Sciences

Universiti Sains Malaysia Penang, Malaysia sufril@cs.usm.my

T. Ritchings¹, S. J. Pearson² ¹Control & Systems Engineering Research Centre

²Centre for Health, Sport and Rehabilitation Sciences Research University of Salford Greater Manchester, United Kingdom

Abstract—The work describes an automated method of tracking dynamic ultrasound images of tendon movements using a Normalized Cross Correlation algorithm, applied to the patellar and gastrocnemius tendon. Displacement was examined during active and passive tendon excursions using B-mode ultrasonography. In the passive test, 2-ROI were tracked and showed insignificant deviation from relative zero displacement for the knee and ankle. Similarly when tracked using 1-ROI showed no significant differences. The active tests gave no significant differences between automatic and manual methods for both patellar and gastrocnemius. This study showed that automatic tracking of in vivo displacement of tendon during dynamic excursion under load is possible and valid when compared to the standardized method. This approach will save time during analysis and enable discrete areas of the tendon to be examined.

Keywords—Normalised Cross Correlation, Speckle Tracking, Tendon, and Ultrasound.

I. INTRODUCTION

Detailed characterization of the tendon allows for insight into the aetiology of tendon injury, repair and response to various training interventions. There have been a number of previous works that has detailed the in vivo tendon mechanical properties [1, 2, 5, 6]. However, these properties, due to the limitations of the methods have been related to the whole

tendon and not specific to any given region. The method described here allows for the quantification of the mechanical properties of regions of interest (ROI) along the tendon length. Thus it may allow for the sensitive identification of changes to the tendon prior to the injury or during rehabilitation, which cannot be identified using the method outlined in previous work.

The randomness of the speckle pattern in ultrasound ensured that each region of the tissue within the imaging frame has its own unique pixel pattern that can differentiate a region from other regions. The aim of any tracking algorithm is to attempt to identify the pixel 'signature' between subsequent image frames. Under ideal conditions the tissue would not change its ultrasound echo from frame to frame i.e. as during a passive movement where the tissue is not expected to distort. However, as the tissue is stretched under load, so it deforms and its density changes, altering the ultrasound pattern produced. Hence the pixel signature of a region of interest in any given frame may in fact change in the subsequent frames.

Fukunaga et al. [4] were the first to utilize and validate in vivo muscle tendon movements using ultrasonography and manual tracking, this involved voluntary contraction of the dorsi- and plantar flexors whilst monitoring the associated ankle and muscle insertion displacements. The movement of the fascicle insertion point was highly correlated with the ankle angular displacement ($r=0.93$ to 0.97). Since then a number of authors have examined aspects of tendon mechanical properties using the manual method to determine tendon excursion during

loading [5, 6, 14]. The utility of having the ability to automatically track tendon displacement is seen in the limitation of the manual method, which requires a known landmark to follow during tendon movement. It is not known if the tendon is homogenous with respect to its mechanical properties, as the current method only allow for an 'average' value to be determined from the total tendon excursion. Use of the automatic tracking algorithm as here, enables examination of specific areas of the tendon to ascertain for example site-specific strain.

The tendon extension seen during muscle contraction is a factor of the loading and loading rate and potentially can be large over a typical acquisition period (3-4 seconds) dependent on the tendon mechanical characteristics. Hence in order to get an optimum match between subsequent frames, the loading rate must be relatively low during frame acquisition so that frame-to-frame tendon displacement is relatively small, hence reducing potential for mismatch. A number of approaches have previously been utilized in an attempt to track nerve and tendon displacement [2, 7, 10]. Of these, none have utilized maximal force efforts where the tendon would be expected to develop high levels of strain. Block matching and Normalized Cross Correlation (NCC) have been previously utilized [3] whereby tendon strain was estimated, and here at only 50% of maximal effort.

This paper utilized a more efficient method of searching in conjunction with the NCC algorithm by implementing the full search algorithm. None of the previous tracking papers have related their measurements with the manual method used in the literature [6] to estimate tendon excursion. In addition, none appear to have utilized high for contractions (where tendon stretch is relatively large) to test the ability of the tracking algorithm to follow a region of interest across successive frames.

Therefore the aims of this present study were to examine a method of tracking ROI within the ultrasound images of in vivo human tendon tissue during both passive (probe movement) and active (highly loaded) tendon, and secondly to compare in vivo, the automated method with the established manual method to ascertain its validity.

This work will enable a much more detailed picture of the tendon mechanical properties in injury, repair and in response to various training interventions. This details understanding will subsequently allow for more effective rehabilitation and injury prevention strategies to be put in place.

II. METHODS

The test subject for the study is a healthy recreationally active male aged 47 years with mass 91 kg and height 1.81m. The local Ethics Committee approved the investigation and the subject gave written informed consent to participate. The study conformed to the principles of the World Medical Association's Declaration of Helsinki.

For the comparison analysis between the automatic and manual

tracking methods, two sites were chosen based on those typically utilized in the literature. These were the patellar and medial gastrocnemius tendon [1, 5, 6]. A 7.5 MHz 40mm linear array, B-mode ultrasound probe (AU5, Esaote Biomedica, Italy) with a depth resolution of 49.3mm was used to image the patellar and medial gastrocnemius tendons in the sagittal plane. For the patellar tendon the knee was fixed at 90° flexion, and the ankle was fixed in the neutral position (i.e. 90°) for imaging the medial gastrocnemius tendon junction.

An echo-absorptive marker was placed between the probe and the skin to act as a fixed reference from which manual measures of elongation could be made. Ultrasound images were then taken in DV format via s-video output and captured into PC at 25 frames per second. Scaling in pixels per mm was determined from ImageJ software (National Institute of Health, USA) by using the known depth of field in the ultrasound images, (1 mm = 9.20 pixels or 1 pixel = 0.108696mm) and utilized as a calibration factor in the automated tracking program to ensure equivalent pixel to mm ratios.

In order to examine the tracking algorithm, passive tendon movements were employed, where no tendon deformation would be expected, hence the simplest task for the algorithm. Contraction start was defined as frame zero for the passive trials. End of contraction was seen when movement stopped for the passive trials. The same criteria or frame range was used for all similar trials. The purpose of the passive probe movement (PM) experiment (Transducer probe moved proximally over the skin surface within a 20mm range.) was to examine the initial measurement of the automatic tracking method, compared with the manual tracking method. Here a good match should be expected if the algorithm is able to 'template match' and hence track the speckle pattern in successive frames.

These tests used one and 2-ROI for comparison purposes. For 1-ROI, the identified region was determined frame to frame and the displacement also measured manually from its position in the first frame. For the 2-ROI passive tests, if the algorithm tracks successfully, any 2 regions should show a zero net movement (relative movement). A total of ten trials were carried out for both 1 and 2-ROI experiments. ROI displacements were measured at every ten percent of the total frame number for each trial. Active movement (AM) where applied ramped voluntary contractions were conducted at both knee and ankle with the knee flexed to an angle of 90° and ankle in neutral, transducer probe fixed static at the skin surface), examined both the patellar and medial gastrocnemius tendons, resulting in tendon stretch (Fig. 1).

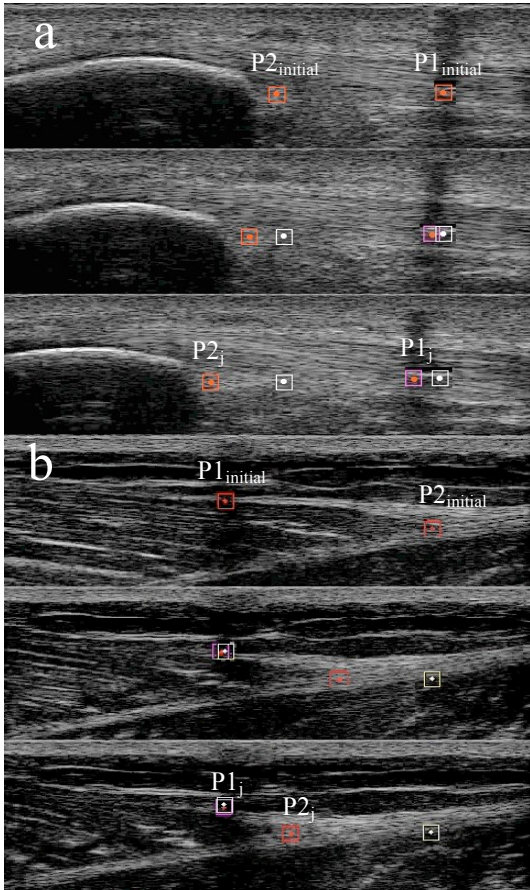


Fig. 1. Shows the tracking node points (ROI), a) 2-ROI nodes patellar tendon tracking b) 2-ROI nodes medial gastrocnemius. Where the first frames hold the initial points and the relative displacement of the points in subsequent frames determines the tendon displacement.

Voluntary forces were ramped manually over 3-4 seconds and recorded along with the ultrasound images. Co contraction was accounted for by recording the EMG in the antagonist muscles (hamstrings and tibialis anterior), where net torque (T) is calculated (1):

$$T = T_e + T_c \quad (1)$$

where, T_e is the external torque and T_c is the co contraction torque.

Tendon forces were calculated by dividing all net torques by the respective moment arms. All excursion records were then determined at ten percent intervals of maximal voluntary force up to maximum. Here only 2-ROI were examined whereby one region was put onto the echo absorptive marker and the other on identifiable landmark within the tendon (Gastrocnemius muscle tendon junction and just distal to the inferior pole of the patellar on the inferior aspect). Again a total of ten trials were carried out for the 2-ROI experiments. For the active trials start was defined where force was zero and end where a force plateau was reached. The tracking algorithm calculated the Normalized Correlation Coefficient (NCC) of the ROI and the

same – sized region, centered on each pixel in a surrounding search window in the following frame (Fig. 1). The NCC was used in preference to other measures because it was found to be more sensitive to speckle tracking in ultrasound images [16]. This algorithm (2) was developed for motion estimation in video compression applications:

$$NCC(u,v) = \frac{\sum_{x=0}^M \sum_{y=0}^N [I(x,y) - \bar{I}_{u,v}] \sum_{x=0}^M \sum_{y=0}^N [T(x-u,y-v) - \bar{T}_{u,v}]}{\left\{ \sum_{x=0}^M \sum_{y=0}^N [I(x,y) - \bar{I}_{u,v}]^2 \sum_{x=0}^M \sum_{y=0}^N [T(x-u,y-v) - \bar{T}_{u,v}]^2 \right\}^{\frac{1}{2}}}, \quad (2)$$

$$-w \leq u,v \leq w$$

where x,y are the pixel locations, $M \times N$ is the size of the template, and \bar{I} is the mean feature of I within the search area w of the template T shifted to (u,v) . As the template T is shifted to n -th positions (u,v) where at every position, the zero mean image I and the zero mean of the template T have to be recalculated simultaneously. Due to the zero mean, NCC measures the similarity between -1 to 1, where -1 is assumed as a poor match and 1 to be the best match.

The movement could be in any direction and employed a rectangular search window of $2 \times$ ROI size for the width and $1 \times$ ROI size for the height. If the threshold for the NCC (0.95) was not reached or exceeded then the ROI was not moved in the subsequent frame. If the NCC found a new region i.e. $r > 0.95$ then the process started again with the new updated position for the template match in the next frame i.e. adaptive NCC implementation. This increases the ability to match where the template changes as when the tendon deforms with stretch.

Tests used a pixel ROI area of 15×15 (2.66mm^2), this gave optimal tracking results compared to larger and smaller areas for the structures examined (data not shown). For 1-ROI, the distance moved from the initial start point node ($P1_{\text{initial}}$) to the successive frames was determined ($P1_j$) and plotted against the manually measured displacement. For 2-ROI the position of $P1_{\text{initial}}$ and $P2_{\text{initial}}$ was then tracked until it reached the last frame. The position of the nodes relative to each other across the subsequent frames was measured (3)

$$(P1_j - P2_j) \quad (3)$$

where the accumulative relative displacement between nodes was plotted (manual vs. automatic tracked).

T-tests were used to determine differences from zero displacement for the 2-ROI passive measures, and to compare all other automatic tracking with manual measures. Intraclass correlation coefficients (ICCs) were determined to examine the reliability of the manual measures. Bland-Altman plots were determined with 95% limits to examine the level of agreement. Alpha level was set to $p < 0.05$. All data are presented as mean \pm SEM.

III. RESULTS AND DISCUSSIONS

Repeat tests of the manual measures for tendon excursion gave an ICC of 0.991. Passive movement of the probe allowed examination of either displacement of two ROI relative to each other or 1-ROI as the probe moved over the region. The 2-ROI automatic tracking passive test for the patellar tendon showed a mean value close to zero displacement (0.010 ± 0.040 mm), manual measures gave a mean value of -0.005 ± 0.040 mm, both results were not significantly different from zero ($p=0.53$; 0.75) for the automatic and manual measures respectively. The 2-ROI automatic test for the medial gastrocnemius tendon, also showed a mean value close to zero displacement (-0.020 ± 0.040 mm), with manual measures giving a mean displacement of -0.030 ± 0.060 mm. Neither the automatic nor the manual measure was significantly different to zero ($p=0.14$; 0.15) respectively.

For determination of a simple tendon displacement trial during passive movement, 1-ROI was utilized. Comparisons between manual and automated tracking with 1-ROI for passive probe movement (PM) indicated that there were no significance differences ($p = 0.06$) between the tracked ROI and the manual method. For the patellar test, automatic tracking gave a total displacement of 7.50 ± 0.60 mm vs. the manual measure of 7.66 ± 1.63 mm. An excellent and significant correlation between methods was shown ($r=0.99$; $p<0.05$), with the Bland-Altman plot indicating that the mean difference or bias is very small (0.04 mm) and that within the 95% confidence limits the difference does not exceed 0.17 mm, a very small difference across the range of measurements (Fig. 2).

Fig. 2. Shows the comparisons of the 1-ROI passive tracking between automatic vs. manual measures of patellar tendon. a) Relationship between manual and automatic tracking, compared at 10% intervals of total frame count ($r = 0.998$; $P<0.05$). b) Bland – Altman plot showing mean difference (bias) and 95% confidence limits. (lines showing mean difference = 0.04 mm, ± 2 SD).

For the medial gastrocnemius tendon test, the automatic tracking gave a total displacement of 11.28 ± 1.36 mm vs. 11.17 ± 1.35 mm for the manual measures, again no significant differences were seen between methods ($p = 0.79$). These initial tests confirmed that the automatic tracking method is a good match to the manual method for measuring displacements, with no significance differences between the two. Fig. 3 indicates for this data set the relationship between measures was significant ($r=0.99$; $p<0.05$). The mean difference was negligible (0.01 mm) and the 95% confidence intervals indicated that the maximum difference was 0.5 mm.

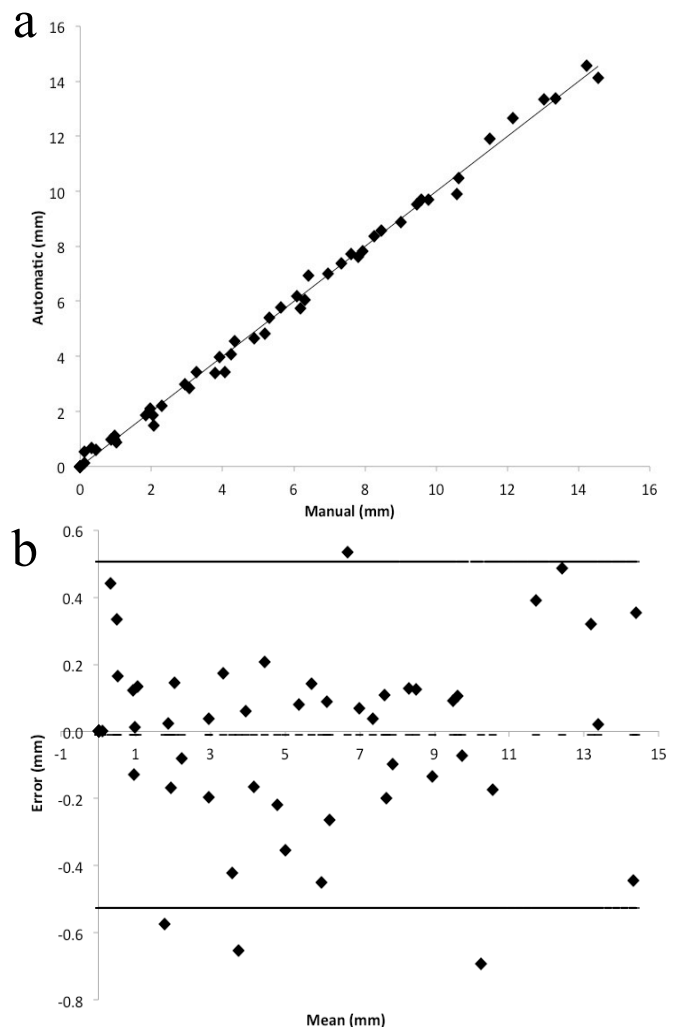
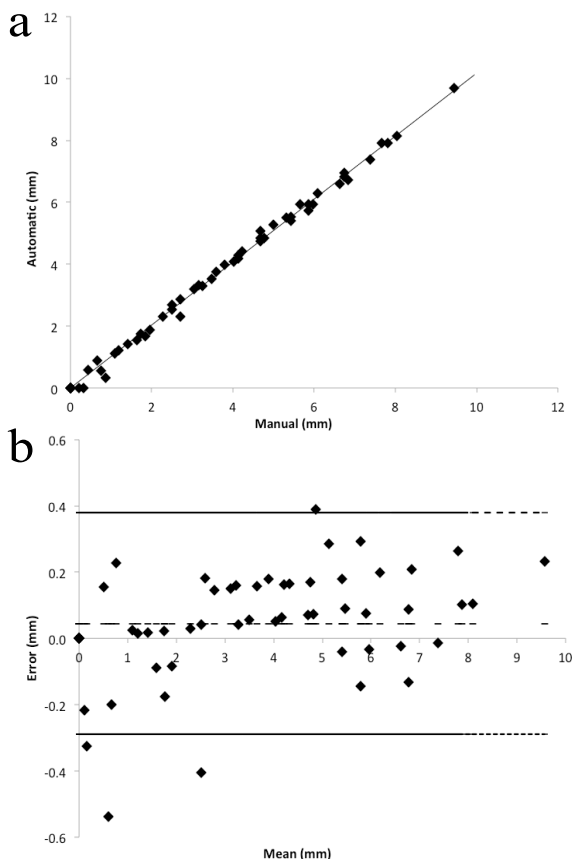


Fig. 3. Shows the comparisons of the 1-ROI passive tracking between automatic vs. manual measures of gastrocnemius

tendon. a) Relationship between manual and automatic tracking, compared at 10% intervals of total frame count ($r = 0.998$; $P < 0.05$). b) Bland – Altman plot showing mean difference (bias) and 95% confidence limits (lines showing mean difference = -0.01 mm, ± 2 SD).

The active trials consisted of muscle contractions, the resultant muscle forces, which were generated, resulted in tendon stretch, and this was tracked and measured manually to determine the validity of the automated method. All active testing utilized 2-ROI. For the patellar tests, here again there were no significance differences ($p=0.85$) between the automatic and the manual measurements with a mean displacement value of 4.88 ± 0.24 mm, compared to 4.59 ± 0.28 mm for the manual measures. The scatter plot shows a very good agreement between measures ($r=0.99$; $p < 0.05$) (Fig. 4). Bland-Altman plot gave a bias of 0.005 mm, indicating no greater difference at a 95% confidence than 0.4 mm.

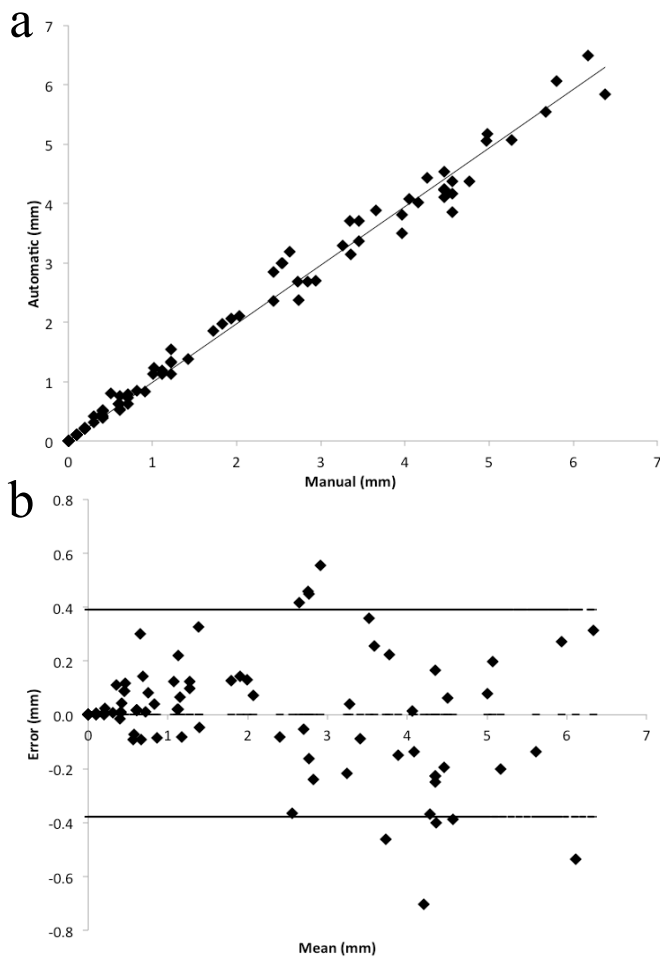


Fig. 4. shows the comparisons of 2-ROI active tracking between automatic vs. manual measures of patellar tendon. a) Relationship between manual and automatic tracking, compared at 10% intervals of maximal voluntary force ($r=0.994$; $P < 0.05$). b) Bland – Altman plot showing mean

difference (bias) and 95% confidence limits (line showing mean difference = 0.005 mm, ± 2 SD).

For the medial gastrocnemius tendon, automated tracking gave a mean displacement value of 16.42 ± 0.85 mm, vs. 16.68 ± 0.86 mm for the manual measures. No significant differences were seen between measures ($p = 0.95$) indicating a good general agreement. The scatter plot indicates again an excellent relationship between measures ($r=0.99$; $p < 0.05$) (Fig. 5). Bias between measures was negligible (0.002 mm), with the maximum difference of 0.81 mm.

The results from the passive tests in this study showed that the automated algorithm enabled effective tracking of a region of interest within the image window when compared to the manually measured results. Here the net movement of 1-ROI's measured using manual and automated tracking were not significantly different from each other for both the patellar with a 2% difference in the total displacement ($p=0.06$) and medial gastrocnemius showing an approximate 1% difference ($p=0.79$). The 2-ROI passive tests showed no significant differences to zero for both the patellar and medial gastrocnemius tendon displacements ($p=0.53$; 0.75 and $p=0.14$; 0.15) for the automatic and manual methods respectively.

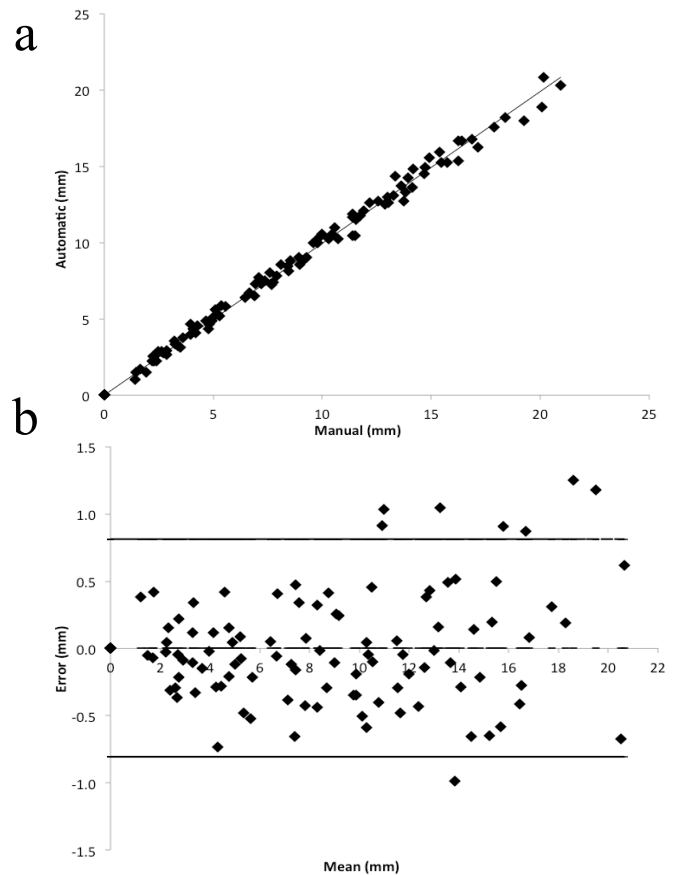


Fig. 5. shows the comparisons of 2--ROI active tracking between automatic vs. manual measures of gastrocnemius tendon. a) Relationship between manual and automatic tracking, compared at 10% intervals of maximal voluntary

force ($r=0.997$; $P<0.05$). b) Bland – Altman plot showing the mean difference (bias) and 95% confidence limits (line showing mean difference = 0.002 mm, ± 2 SD).

For the active tests the errors were expected to be larger due to the tendon being dynamically stretched during muscle contraction, causing some deformation and making automatic tracking more demanding. This was indeed found to be the case with the maximal differences (bias) determined for the active tests at 0.4 and 0.81mm for the patellar and medial gastrocnemius junction respectively. These were still considered relatively small differences between the methods, the correlations indicating excellent general agreement (Fig. 4 and 5).

The tests carried out here are the first to directly compare automated tracking with manually measured tendon excursion during maximally loaded voluntary contractions. Lee et al. [10] discussed comparisons of 'lightly' loaded in vivo tendon excursions using an automated tracking method and manual measures. But they did not make clear the manual approach or indeed the reliability of the manual method. This aside they reported absolute errors of ~ 0.5 mm, similar to that seen here. However, our RMS percent errors were smaller than those reported by Lee et al. [10] with 3.2% seen here compared to 5.9% reported by Lee and co workers. Although a limitation of the present study may be that the measures were made on only one subject, differences in image quality across subjects may affect the agreement or the ability of the algorithm to track regions effectively. However carrying out the trials on two distinct tendons with different morphologies shows the robustness of this procedure.

Our findings showed that for passive movements the tracking accuracy was within 1-2% of the manual values and active movements within 2.4-3.2% which is comparable to the displacement errors reported by Maganaris et al. [12], 0.8-2.5% in the tendon and 2.1-7% in the aponeurosis. A more recent study [3] reported that the speckle tracking method was able to estimate frame-to-frame displacements using 2-ROI end points by tracking the movement of tendon during twitch contractions. However, as the tracking was carried out during twitch contractions by electrically stimulating the muscle, the forces in the tendon were only moderate (up to 50% of maximum) which is a major difference to the approach here where high forces were elicited and thus larger tendon deformations would be expected making the tracking potentially more demanding.

Where others have utilized an automated algorithm to examine tracking there have been reported errors of $<10\%$ [2]. Here the transducer probe was moved within a 1-3 mm range over the surface of the forearm. Whilst, Magnusson et al. [13] tracked a needle sliding 10 mm through gel with mean error of 2%, similar to the errors of 2% reported using cross- correlation to track wire oscillating in water [11]. These are similar to our passive trials and give similar errors or differences to the manual method as we report here (up to 2%).

In summary, this method shows for the first time the utility of

an automated tracking program to determine tendon excursion during maximally loaded in vivo contractions by contrast with the standardized manual measurement method. Hence, it has the potential to improve clinical knowledge relating to the tendon mechanical properties by enabling discrete tendon mechanical properties to be determined [15].

REFERENCES

- [1] A. Arampatzis, S.Stafilidis, G. DeMonte, K. Karaminidis, G. Morey- Klapsing and G.P, Bruggemann, "Strain and elongation of the human gastrocnemius tendon and aponeurosis during maximal plantar flexion effort," *Journal of Biomechanics*, vol. 38, pp. 883-841, 2005.
- [2] A. Dilley, J. Greening, B. Lynn, R. Leary and V. Morris, "The use of Cross-Correlation analysis between high-frequency ultrasound images to measure longitudinal median nerve movement," *Ultrasound in Medicine & Biology*, vol. 27, pp 211-218, 2001.
- [3] J. Farron, T. Varghese and D.G. Thelen, "Measurement of Tendon Strain During Muscle Twitch Contractions Using Ultrasonography," *IEEE Transaction of Ultrasonics, Perroelectrics and Frequency Control*, vol. 56, pp 27-35, 2009.
- [4] T. Fukunaga, M. Ito, Y. Ichinose, S. Kuna, Y. Kawakami and S. Fukashiro, "Tendinous movement of a human muscle during voluntary contractions determined by realtime ultrasonography," *Journal of Applied Physiology*, vol. 81, pp. 1430-1433, 1996.
- [5] P. Hansen, J. Bojsen-Moller, P. Aagaard, M. Kjaer and S.P. Magnusson, "Mechanical properties of the human patellar tendon, in vivo," *Clinical Biomechanics*, vol. 21, pp 54-58, 2006.
- [6] G. Onambele, K. Burgess and S. Pearson, "Gender specific In Vivo Measurement of the structural and mechanical properties of the human patellarr tendon," *Journal of Orthopaedic Research*, vol. 25, pp. 1635- 1642. 2007
- [7] Y.S. Kim, J.M. Kim, L.U. Bigliani, H.J. Kim and H.W. Jung, "In vivo strain analysis of the intact suprastinatus tendon by ultrasound speckles tracking imaging," *Journal of Orthopaedic Research*, vol. 12, pp. 1931- 1937, 2011.
- [8] T. Koga K. Iinuma, A. Hirano, Y. Iijima and T. Ishiguro, "Motion compensated interframe coding for video conferencing," *Proc. Nat. Telcommun Conf*, vol. 5, pp 31- 35, 1981.
- [9] K. Kubo, H. Kanehisha, Y. Kawakami and T. Fukunaga, "Elastic properties of muscle-tendon complex in long-distance runners," *European Journal of Applied Physiology*, vol. 81, pp 181-187, 2000.

- [10] S. Lee, G. Lewis and S. Piazza, "An algorithm for automated analysis of ultrasound images to measure tendon excursion in vivo," *Journal of Applied Biomechanics*, vol. 24, pp. 75-82, 2008.
- [11] I.D. Loram, C. Maganaris and M. Lakie, "Use of ultrasound to make noninvasive in vivo measurement of continuous changes in human muscle contractile length," *Journal of Applied Physiology*, vol. 100, pp. 1311-1323, 2006.
- [12] C. Maganaris, V. Baltzopoulos and A. Sergeant, "In vivo measurement based estimations of the human Achilles tendon moment arm," *European Journal of Applied Physiology*, vol. 83, pp. 363-369, 2000.
- [13] S. Magnusson, P. Hansen, P. Aagaard, J. Brond, P.D. Poulsen, J. Bojsen-Moller and M. Kjaer, "Differential strain patterns of the human gastrocnemius aponeurosis and free tendon in vivo," *Acta Physiologica Scandinavica*, vol. 177, pp. 185-195, 2003.
- [14] S. Pearson, K. Burgess and G. Onambele, "Creep and the in vivo assessment of human patellar tendon mechanical properties," *Clinical Biomechanics*, vol. 22, pp. 712-717, 2007.
- [15] S. Pearson, A.S.A. Mohamed and T. Ritchings, "Regional strain variations in the human patellar tendon," *Med Sci Sports Exerc*, vol. 46, pp 1343-51, 2014.
- M. Revell and D. McNally, "Computer vision elastography: speckle adaptive motion estimation for elastography using ultrasound sequences," *IEEE transactions on medical imaging*, vol. 25, pp. 755, 2005.

Appendix F

Matlab Source Code (Normalised Cross Correlation)

```
function [reg] = AlgoNCC1( hObject, eventdata, handles, ~ )
delete itemp/*.*
tic;
global h_tracker;
xyinit = h_tracker.xy(1,:);
%% Start from first frame
count = 0;
for i=1:h_tracker.numFrames

    set(h_tracker.Text_Status,'string',sprintf('Processing (%i/%i) ...',i,h_tracker.numFrames)); %drawnow;
    set(h_tracker.Slider_frames,'value',i);

    imnum = i;

    if i == 1
        h_tracker.xy(1,:) = xyinit(1,:);
        if h_tracker.endFrame1 == 0
            set(h_tracker.Text_Status,'string','Copying frames into memory for faster processing. '); %drawnow;

            h_tracker.im = read(h_tracker.readerobj, [1 h_tracker.numFrames]);
            clear h_tracker.readerobj;
            h_tracker.endFrame1 = 1;
            set(h_tracker.Text_Status,'string','Copying done. Starting tracking process. '); %drawnow;
        end

        if h_tracker.endFrame1 == 0
            imT = im2double(read(h_tracker.readerobj,1));
        else
            imT = im2double(h_tracker.im(:,:,1));
        end

        %% Display to Axis
        image(imT, 'Parent', h_tracker.axes_display);

    hold off;
```

```

%% Assign Initial Refpatch & xy
refpatch1(:,:)=imT(h_tracker.xy(1,2):h_tracker.xy(1,4),h_tracker.xy(1,1):h_tracker.xy(1,3));

rectangle('position',[h_tracker.xy(1,1) h_tracker.xy(1,2) h_tracker.xy(1,3)-h_tracker.xy(1,1)
h_tracker.xy(1,4)-h_tracker.xy(1,2)],'edgecolor',[1 0 1]); hold on;

% Assign to main patch and temporary patch
refpatch = refpatch1;
refpatchtemp = refpatch1;

%% Record first frame for video capture
[reg1]=trackAlgo2(hObject, eventdata, i,refpatch(:,:),imT, refpatchtemp(:,:), refpatch1(:,:), handles);
else
cla;
if h_tracker.endFrame1 == 0
imT = im2double(read(h_tracker.readerobj,i));
else
imT = im2double(h_tracker.im(:,:i));
end

image(imT, 'Parent', h_tracker.axes_display);
[reg1]=trackAlgo2(hObject, eventdata, i-1,refpatch(:,:),imT, refpatchtemp(:,:), refpatch1(:,:), handles);
end

reg = reg1;

if reg(7) > -1
h_tracker.xy(i,:) = [reg(1,1) reg(1,2) reg(1,3) reg(1,4) reg(1,5) reg(1,6) reg(1,7)];
refpatch(:,:) = (imT(reg(1,2):reg(1,4),reg(1,1):reg(1,3)));
refpatchtemp(:,:) = refpatch(:,:);
end

moviefilenameT = fix(clock);

text('Position',[20,size(imT,1)-50,1],'FontSize',10,'Color','Yellow','String',['Frame No= ',num2str(i)])

```

```

text('Position',[20,size(imT,1)-
80,1],'FontSize',10,'Color','Yellow','String',[num2str(moviefilenameT(3)),'\ ',num2str(moviefilenameT(2)),'\ ',num2s
tr(moviefilenameT(1))]);
set(h_tracker.uipanel_main,'title',sprintf('Filename: %s  Frame Number: %i  Total Frames:
%i',h_tracker.readerobj.name,num2str(1),h_tracker.numFrames));

rectangle('position',[h_tracker.xy(i,1) h_tracker.xy(i,2) h_tracker.xy(i,3)-h_tracker.xy(i,1) h_tracker.xy(i,4)-
h_tracker.xy(i,2)],'edgecolor',[1 0 1]);

line([h_tracker.xy(1,5) h_tracker.xy(i,5)], [h_tracker.xy(1,6) h_tracker.xy(i,6)], 'LineWidth',4); hold on;

if i > 1
    a1 = abs(h_tracker.xy(i,5) - h_tracker.xy(1,5));
    b1 = abs(h_tracker.xy(i,6) - h_tracker.xy(1,6));
else
    a1 = abs(h_tracker.xy(1,5) - h_tracker.xy(1,5));
    b1 = abs(h_tracker.xy(1,6) - h_tracker.xy(1,6));
end
dispix1(i) = round(sqrt(a1^2+b1^2));
distant1(i) = dispix1(i)/h_tracker.unit3;

text('Position',[20,size(imT,1)-30,1],'FontSize',10,'Color','Yellow','String',['Displacement= ',num2str(distant1(i))])

set(h_tracker.uipanel_main,'title',sprintf('Filename: %s  Frame Number: %i  Total Frames:
%i',h_tracker.readerobj.name,imnum,h_tracker.numFrames));

h_tracker.check = 1;
end

set(h_tracker.Btn_Results,'enable','on');
set(h_tracker.Btn_Measure,'enable','on');

h_tracker.distant1 = distant1;
allTimes = toc;
timesinmin = allTimes;

h_tracker.trackingstatus = 1;

save temp/regions1_1.dat distant1 -tabs;

```

```
moviefilename=sprintf('temp/movie/%s%s%s%s%s%s%s.s.avi',num2str(moviefilenameT(6)),num2str(moviefilenameT(5)),num2str(moviefilenameT(4)),num2str(moviefilenameT(3)),num2str(moviefilenameT(2)),num2str(moviefilenameT(1)));
```

```
save temp/moviefilename.dat moviefilename;
```

```
clear imT;
```

```
clear imT0;
```

```
clear axes_display;
```

```
set(h_tracker.Text_Status,'string',sprintf('Processing...done Time Taken is %0.2f,timesinmin)); %drawnow;
```

```
guidata(hObject, handles);
```

```
% generic error metric between two image patches
```

```
function err= errfun(im1 ,im2,algorithm)
```

```
    [h w]=size(im1);
```

```
    switch(algorithm)
```

```
        case 'bmamse',
```

```
            err = sqrt(mean(mean((im1-im2).^2,2),1));
```

```
        case 'bmance',
```

```
            err = im1(:)*im2(:) / (sqrt(im1(:)*im1(:))*sqrt(im2(:)*im2(:)));
```

```
    end
```

```
end
```

Appendix G

Matlab Source Code (Mean Square Error)

```
function [reg] = AlgoNCC1(hObject, eventdata, handles, ~)
delete itemp/*.*
tic;
global h_tracker;
xyinit = h_tracker.xy(1,:);

%% Start from first frame
for i=1:h_tracker.numFrames
    %cla ;

    set(h_tracker.Text_Status,'string',sprintf('Processing (%i/%i) ...',i,h_tracker.numFrames)); %drawnow;
    set(h_tracker.Slider_frames,'value',i);

    imnum = i;

    if i == 1
        h_tracker.xy(1,:) = xyinit(1,:);
        if h_tracker.endFrame1 == 0
            set(h_tracker.Text_Status,'string','Copying frames into memory for faster processing. '); %drawnow;

            h_tracker.im = read(h_tracker.readerobj, [1 h_tracker.numFrames]);
            clear h_tracker.readerobj;
            h_tracker.endFrame1 = 1;
            set(h_tracker.Text_Status,'string','Copying done. Starting tracking process. '); %drawnow;
        end

        if h_tracker.endFrame1 == 0
            imT = read(h_tracker.readerobj,1);
        else
            imT = h_tracker.im(:,:,i);
        end

        %% Display to Axis
        image(imT, 'Parent', h_tracker.axes_display);
    end
end
```

```

hold off;

%% Assign Initial Refpatch & xy
refpatch1(:,:)=double(imT(h_tracker.xy(1,2):h_tracker.xy(1,4),h_tracker.xy(1,1):h_tracker.xy(1,3)));
    rectangle('position',[h_tracker.xy(1,1) h_tracker.xy(1,2) h_tracker.xy(1,3)-h_tracker.xy(1,1)
h_tracker.xy(1,4)-h_tracker.xy(1,2)],'edgecolor',[1 0 1]); hold on;

% Assign to main patch and temporary patch
refpatch = refpatch1;
refpatchtemp = refpatch1;

%% Record first frame for video capture
[reg]=trackAlgo5(hObject, eventdata, i,refpatch(:,:),imT, refpatchtemp(:,:), refpatch1(:,:), handles);
else
    cla;
    if h_tracker.endFrame1 == 0
        imT = read(h_tracker.readerobj,i);
    else
        imT = h_tracker.im(:, :, i);
    end

    image(imT, 'Parent', h_tracker.axes_display);
    imT = double(imT);

    [reg]=trackAlgo5(hObject, eventdata, i-1,refpatch(:,:),imT, refpatchtemp(:,:), refpatch1(:,:), handles);
end

if reg(7) > -1
    h_tracker.xy(i,:) = [reg(1,1) reg(1,2) reg(1,3) reg(1,4) reg(1,5) reg(1,6) reg(1,7)];
    refpatch(:,:) = (imT(reg(1,2):reg(1,4),reg(1,1):reg(1,3)));
    refpatchtemp(:,:) = refpatch(:,:);
end

moviefilenameT = fix(clock);

text('Position',[20,size(imT,1)-50,1],'FontSize',10,'Color','Yellow','String',['Frame No= ',num2str(1)])
text('Position',[20,size(imT,1)-
80,1],'FontSize',10,'Color','Yellow','String',[num2str(moviefilenameT(3)),'/',num2str(moviefilenameT(2)),'/',num2s
tr(moviefilenameT(1))]);

```

```

set(h_tracker.uipanel_main,'title',sprintf('Filename: %s  Frame Number: %i  Total Frames:
%i',h_tracker.readerobj.name,num2str(1),h_tracker.numFrames));

rectangle('position',[h_tracker.xy(i,1) h_tracker.xy(i,2) h_tracker.xy(i,3)-h_tracker.xy(i,1) h_tracker.xy(i,4)-
h_tracker.xy(i,2)],'edgecolor',[1 0 1]);

rectangle('position',[(h_tracker.xy(i,1)+h_tracker.limL) (h_tracker.xy(i,2)+h_tracker.limU)
((h_tracker.xy(i,3)+h_tracker.limR)-(h_tracker.xy(i,1)+h_tracker.limL)) ((h_tracker.xy(i,4)+h_tracker.limD)-
(h_tracker.xy(i,2)+h_tracker.limU))],'edgecolor',[1 1 0]); hold on;

line([h_tracker.xy(1,5) h_tracker.xy(i,5)], [h_tracker.xy(1,6) h_tracker.xy(i,6)], 'LineWidth',4); hold on;

if i > 1
    a1 = abs(h_tracker.xy(i,5) - h_tracker.xy(1,5));
    b1 = abs(h_tracker.xy(i,6) - h_tracker.xy(1,6));
else
    a1 = abs(h_tracker.xy(1,5) - h_tracker.xy(1,5));
    b1 = abs(h_tracker.xy(1,6) - h_tracker.xy(1,6));
end
distant1(i) = round(sqrt(a1^2+b1^2));
distant1(i) = distant1(i)/h_tracker.unit3;

text('Position',[20,size(imT,1)-30,1],'FontSize',10,'Color','Yellow','String',['Displacement=
',num2str(distant1(i))])

set(h_tracker.uipanel_main,'title',sprintf('Filename: %s  Frame Number: %i  Total Frames:
%i',h_tracker.readerobj.name,imnum,h_tracker.numFrames));

h_tracker.check = 1;
end

set(h_tracker.Btn_Results,'enable','on');
set(h_tracker.Btn_Measure,'enable','on');

h_tracker.distant1 = distant1;

h_tracker.trackingstatus = 1;

save temp/regions1_1.dat distant1 -tabs;

```

```

moviefilename=sprintf('temp/movie/%s%s%s%s%s%s.s.avi',num2str(moviefilenameT(6)),num2str(moviefilename
T(5)),num2str(moviefilenameT(4)),num2str(moviefilenameT(3)),num2str(moviefilenameT(2)),num2str(moviefile
nameT(1)));
save temp/moviefilename.dat moviefilename;

clear imT;
clear imT0;
clear axes_display;

allTimes = toc;
timesinmin = allTimes;

set(h_tracker.Text_Status,'string',sprintf('Processing...done Time Taken is %0.2f',timesinmin)); %drawnow;

guidata(hObject, handles);

```

```

% generic error metric between two image patches
function err= errfun(im1 ,im2,algorithm)
    [h w]=size(im1);
    switch(algorithm)
        case 'bmamse',
            err = sqrt(mean(mean((im1-im2).^2,2),1));
        case 'bmance',
            err = im1(:)*im2(:) / (sqrt(im1(:)*im1(:))*sqrt(im2(:)*im2(:)));
    end
end
end

```

Appendix H

Matlab Source Code (NCCMSE)

```
function [reg] = AlgoMSENCC1( hObject, eventdata, handles, ~ )
delete itemp/*.*
tic;
global h_tracker;
xyinit = h_tracker.xy(1,:);
%% Start from first frame
count = 0;
for i=1:h_tracker.numFrames
    set(h_tracker.Text_Status,'string',sprintf('Processing (%i/%i) ...',i,h_tracker.numFrames)); %drawnow;
    set(h_tracker.Slider_frames,'value',i);

    imnum = i;

    if i == 1
        h_tracker.xy(1,:) = xyinit(1,:);
        if h_tracker.endFrame1 == 0
            set(h_tracker.Text_Status,'string','Copying frames into memory for faster processing. '); %drawnow;

            h_tracker.im = read(h_tracker.readerobj, [1 h_tracker.numFrames]);
            clear h_tracker.readerobj;
            h_tracker.endFrame1 = 1;
            set(h_tracker.Text_Status,'string','Copying done. Starting tracking process. '); %drawnow;
        end

        if h_tracker.endFrame1 == 0
            imT = im2double(read(h_tracker.readerobj,1));
        else
            imT = im2double(h_tracker.im(:,:,1));
        end

        %% Display to Axis
        image(imT, 'Parent', h_tracker.axes_display);

        %% Set image to double
        %     imT0 = double(imT);
    end
end
```

```

hold off;

%% Assign Initial Refpatch & xy
refpatch1(:,:)=(imT(h_tracker.xy(1,2):h_tracker.xy(1,4),h_tracker.xy(1,1):h_tracker.xy(1,3)));

rectangle('position',[h_tracker.xy(1,1) h_tracker.xy(1,2) h_tracker.xy(1,3)-h_tracker.xy(1,1)
h_tracker.xy(1,4)-h_tracker.xy(1,2)],'edgecolor',[1 0 1]); hold on;

% Assign to main patch and temporary patch
refpatch = refpatch1;
refpatchtemp = refpatch1;

%% Record first frame for video capture
[reg1, reg2]=trackAlgo2MN(hObject, eventdata, i,refpatch(:,:),imT, refpatchtemp(:,:), refpatch1(:,:),
handles);
else
cla;
if h_tracker.endFrame1 == 0
imT = im2double(read(h_tracker.readerobj,i));
else
imT = im2double(h_tracker.im(:, :, i));
end

image(imT, 'Parent', h_tracker.axes_display);
[reg1 , reg2]=trackAlgo2MN(hObject, eventdata, i-1,refpatch(:,:),imT, refpatchtemp(:,:), refpatch1(:,:),
handles);
end

aa(:,:) = (imT(reg1(1,2):reg1(1,4),reg1(1,1):reg1(1,3)));
bb(:,:) = (imT(reg2(1,2):reg2(1,4),reg2(1,1):reg2(1,3)));
aa1 = mean(aa(:).^2);
bb1 = mean(bb(:).^2);
cc1 = mean(refpatch(:).^2);
y = awgn(refpatch,30);

y1 = mean(y(:).^2);
SNR = cc1/y1;

if SNR > 1
reg = reg1;

```

```

else
    reg = reg2;
end

if reg(7) > -1
    h_tracker.xy(i,:) = [reg(1,1) reg(1,2) reg(1,3) reg(1,4) reg(1,5) reg(1,6) reg(1,7)];
    refpatch(:, :) = (imT(reg(1,2):reg(1,4), reg(1,1):reg(1,3)));
    refpatchtemp(:, :) = refpatch(:, :);
end

moviefilenameT = fix(clock);

text('Position',[20,size(imT,1)-50,1],'FontSize',10,'Color','Yellow','String',['Frame No= ',num2str(i)])
text('Position',[20,size(imT,1)-
80,1],'FontSize',10,'Color','Yellow','String',[num2str(moviefilenameT(3)), '/', num2str(moviefilenameT(2)), '/', num2s
tr(moviefilenameT(1))]);
set(h_tracker.uipanel_main,'title',sprintf('Filename: %s  Frame Number: %i  Total Frames:
%i',h_tracker.readerobj.name,num2str(1),h_tracker.numFrames));

rectangle('position',[h_tracker.xy(i,1) h_tracker.xy(i,2) h_tracker.xy(i,3)-h_tracker.xy(i,1) h_tracker.xy(i,4)-
h_tracker.xy(i,2)],'edgecolor',[1 0 1]);

line([h_tracker.xy(1,5) h_tracker.xy(i,5)], [h_tracker.xy(1,6) h_tracker.xy(i,6)], 'LineWidth',4); hold on;

if i > 1
    a1 = abs(h_tracker.xy(i,5) - h_tracker.xy(1,5));
    b1 = abs(h_tracker.xy(i,6) - h_tracker.xy(1,6));
else
    a1 = abs(h_tracker.xy(1,5) - h_tracker.xy(1,5));
    b1 = abs(h_tracker.xy(1,6) - h_tracker.xy(1,6));
end
dispix1(i) = round(sqrt(a1^2+b1^2));
distant1(i) = dispix1(i)/h_tracker.unit3;

text('Position',[20,size(imT,1)-30,1],'FontSize',10,'Color','Yellow','String',['Displacement=
',num2str(distant1(i))])

set(h_tracker.uipanel_main,'title',sprintf('Filename: %s  Frame Number: %i  Total Frames:
%i',h_tracker.readerobj.name,imnum,h_tracker.numFrames));

```

```

    h_tracker.check = 1;
end
set(h_tracker.Btn_Results,'enable','on');
set(h_tracker.Btn_Measure,'enable','on');

h_tracker.distant1 = distant1;

h_tracker.trackingstatus = 1;

save temp/regions1_1.dat distant1 -tabs;
moviefilename=sprintf('temp/movie/%s%s%s%s%s%s.s.avi',num2str(moviefilenameT(6)),num2str(moviefilename
T(5)),num2str(moviefilenameT(4)),num2str(moviefilenameT(3)),num2str(moviefilenameT(2)),num2str(moviefile
nameT(1)));
save temp/moviefilename.dat moviefilename;

clear imT;
clear imT0;
clear axes_display;

allTimes = toc;
timesinmin = allTimes;

set(h_tracker.Text_Status,'string',sprintf('Processing...done Time Taken is %0.2f',timesinmin)); %drawnow;

guidata(hObject, handles);

```

```

% generic error metric between two image patches
function err= errfun(im1 ,im2,algorithm)
    [h w]=size(im1);
    switch(algorithm)
        case 'bmamse',
            err = sqrt(mean(mean((im1-im2).^2,2),1));
        case 'bmance',
            err = im1(:)*im2(:) / (sqrt(im1(:)*im1(:))*sqrt(im2(:)*im2(:)));
    end
end

```

Appendix I

Matlab Source Code (Lucas Kanade)

```
function [regtt]=AlgoLK1( hObject, eventdata, handles, ~ )
delete itemp/*.*
tic;
global h_tracker;

set(h_tracker.Text_Status,'string',sprintf('Processing (%i/%i) ...!',1,h_tracker.numFrames)); %drawnow;

h_tracker.regionsErr=0;
h_tracker.ROI_sizeT = h_tracker.ROI_size / 2;
h_tracker.ROI_size2T =h_tracker.ROI_size / 2;
h_tracker.post = 0;

if h_tracker.endFrame1 == 0
    set(h_tracker.Text_Status,'string','Copying frames into memory for faster processing. '); %drawnow;

    h_tracker.im = read(h_tracker.readerobj, [1 h_tracker.numFrames]);
    clear h_tracker.readerobj;
    h_tracker.endFrame1 = 1;
    set(h_tracker.Text_Status,'string','Copying done. Starting tracking process. ');
end

clear count;
moviefilenameT = fix(clock);
moviefilename=sprintf('temp/movie/%s%s%s%s%s%s%s.s.avi',num2str(moviefilenameT(6)),num2str(moviefilenameT(5)),num2str(moviefilenameT(4)),num2str(moviefilenameT(3)),num2str(moviefilenameT(2)),num2str(moviefilenameT(1)));
save temp/moviefilename.dat moviefilename;

if h_tracker.endFrame1 == 0
    imT0 = read(h_tracker.readerobj,1);
else
    imT0 = h_tracker.im(:,:,1);
end
image(imT0, 'Parent', h_tracker.axes_display);
```

```

imT0 = double(imT0);
hold off;

text('Position',[20,size(imT0,1)-50,1],'FontSize',10,'Color','Yellow','String',['Frame No= ',num2str(1)])
text('Position',[20,size(imT0,1)-
80,1],'FontSize',10,'Color','Yellow','String',[num2str(moviefilenameT(3)),'/',num2str(moviefilenameT(2
)), '/',num2str(moviefilenameT(1))]);
set(h_tracker.Slider_frames,'value',1);
set(h_tracker.uipanel_main,'title',sprintf('Filename: %s  Frame Number: %i  Total Frames:
%i',h_tracker.readerobj.name,num2str(1),h_tracker.numFrames));

refpatchinit(:,:)=(imT0(h_tracker.xy(1,2):h_tracker.xy(1,4),h_tracker.xy(1,1):h_tracker.xy(1,3)));
rectangle('position',[h_tracker.xy(1,1) h_tracker.xy(1,2) h_tracker.xy(1,3)-h_tracker.xy(1,1)
h_tracker.xy(1,4)-h_tracker.xy(1,2)],'edgecolor',[1 0 1]); hold on;

refpatch = refpatchinit;
refpatchtemp = refpatchinit;
im = imT0;

[m, n] = size(refpatch);
h_tracker.A = zeros(m,n);
h_tracker.B = zeros(m,n);

starts = 1;
ends = h_tracker.numFrames;

reg = h_tracker.xy(1,:);
sig = 1;

if h_tracker.endFrame1 == 0
    F1 = read(h_tracker.readerobj,1);
else
    F1 = h_tracker.im(:,:,1);
end

F = double(rgb2gray(F1));
[rows,cols] = size(F);
[X,Y] = meshgrid(1:cols,1:rows);

```

```

G = gauss(sig);
dG = dgauss(sig,G);
kernelx = G'*dG;
kernely = dG'*G;
u = 0; u2 = 0; v = 0; v2 = 0;

w = reg(3)-reg(1);
h = reg(4)-reg(2);
xmin = max(reg(1),1); xmax = min(reg(3),size(im,2));
ymin = max(reg(2),1); ymax = min(reg(4),size(im,1));
rectangle('position',[xmin ymin xmax-xmin ymax-ymin],'edgecolor',[1 0 0]);
c= [xmax xmax xmin xmin]; r= [ymin ymax ymax ymin];
mask = double(roipoly(rows,cols,c,r)); inds = find(mask);
min_x = min(X(inds)); max_x = max(X(inds));
min_y = min(Y(inds)); max_y = max(Y(inds));

imwrite(uint8(F1), 'temp/tempimfirst.jpg');

err = 0;
for i = 1:ends
    set(h_tracker.Text_Status,'string',sprintf('Processing (%i/%i) ...',i,ends));

    if h_tracker.endFrame1 == 0
        IM = double(rgb2gray(read(h_tracker.readerobj,i)));
    else
        IM = double(rgb2gray(h_tracker.im(:,:,i)));
    end

    Fx = conv2(F,kernelx,'same');
    Fy = conv2(F,kernely,'same');

    tester = 9*10^9;

    j=0;
    while j<10
        Gwarp = interp2(X,Y,IM,X+u,Y+v, 'cubic');
        inds_nan = isnan(Gwarp);
        Gwarp(inds_nan) = 0;
        Fx2 = sum(Fx(inds).^2);

```

```

Fy2 = sum(Fy(inds).^2);
Fxy = sum(Fx(inds).*Fy(inds));
Ft = Gwarp - F;
Ftx = sum(Ft(inds).*Fx(inds));
Fty = sum(Ft(inds).*Fy(inds));
C = [Fx2 Fxy; Fxy Fy2];
D = [Ftx; Fty];
uv = C\D;
u = u - uv(1);
v = v - uv(2);
err_old = err;
err = sum((Fx(inds)*u + Fy(inds)*v - Ft(inds)).^2);
tester_old = tester;
tester = abs(err_old - err);
if ((tester > tester_old) || (tester < .1))
    break;
end

j = j+ 1;
end

new_min_x = round(min_x+u);
new_max_x = round(max_x+u);
new_min_y = round(min_y+v);
new_max_y = round(max_y+v);
imshow(uint8(IM)); axis image;
rectangle('position',[new_min_x new_min_y new_max_x-new_min_x new_max_y-
new_min_y],'edgecolor',[1 0 0]);

if i == 1
    h_tracker.xy(i,:) = [reg(1,1) reg(1,2) reg(1,3) reg(1,4) reg(1,5) reg(1,6) reg(1,7)];
else
    h_tracker.xy(i,:) = [new_min_x new_min_y new_max_x new_max_y new_min_x+(w/2)
new_min_y+(h/2), 1];
    line([h_tracker.xy(1,5) h_tracker.xy(i,5)], [h_tracker.xy(1,6) h_tracker.xy(i,6)], 'LineWidth', 4);
hold on;
end

set(handles.Slider_frames,'value',i);
inum = round(get(handles.Slider_frames,'value'));

```

```

set(handles.uipanel_main,'title',sprintf('Image Panel (%i/%i)',imnum,ends));
imnumT = starts+imnum-1;
text('Position',[20,size(h_tracker.im,1)-50,1],'FontSize',12,'Color','Yellow','String',['Frame No=
',num2str(imnumT)]);

if i > 1
    a1 = abs(h_tracker.xy(i,5) - h_tracker.xy(1,5));
    b1 = abs(h_tracker.xy(i,6) - h_tracker.xy(1,6));
else
    a1 = abs(h_tracker.xy(1,5) - h_tracker.xy(1,5));
    b1 = abs(h_tracker.xy(1,6) - h_tracker.xy(1,6));
end
dispix1(i) = round(sqrt(a1^2+b1^2));
distant1(i) = dispix1(i)/h_tracker.unit3;

text('Position',[20,size(im,1)-30,1],'FontSize',10,'Color','Yellow','String',['Displacement=
',num2str(distant1(i))])
drawnow;
end
allTimes = toc;
timesinmin = allTimes;
set(h_tracker.Text_Status,'string',sprintf('Processing...done Time Taken is %0.2f',timesinmin));
%drawnow;

format short;
save temp/regions1_1.dat distant1 -tabs;

regtt = h_tracker.xy;
guidata(hObject, handles);

```